Modeling and prediction of near wall turbulent flows

Sricharan Srinath

N° d'ordre : 350

CENTRALE LILLE

THESE

Présentée en vue
d'obtenir le grade de

DOCTEUR

En

Spécialité : Mécanique

Par

Sricharan SRINATH

DOCTORAT DELIVRE PAR CENTRALE LILLE

Titre de la thèse :

Prédiction et modélisation d'écoulements turbulents proches de parois

Modeling and prediction of near wall turbulent flows

Soutenue le 19 Décembre 2017 devant le jury d'examen:

Président	**Thomas GOMEZ**	**Professeur, Université de Lille**
Rapporteur	**Denis SIPP**	**Directeur de Recherche ONERA, Meudon**
Rapporteur	**Bérengére PODVIN**	**Chargé de Recherche CNRS, HDR, LIMSI, Orsay**
Examinateur	**Gerrit ELSINGA**	**Associate Professor, Delft University of Technology**
Directeur de thèse	**Jean-Marc FOUCAUT**	**Professeur, Ecole Centrale de Lille**
Directeur de thèse	**Jean-Philippe LAVAL**	**Chargé de Recherche CNRS, HDR, LML, Lille**
Invité	**Michel STANISLAS**	**Professeur émirité, Ecole Centrale de Lille**
Invité	**Christophe CUVIER**	**Maître de Conférences, Ecole Centrale de Lille**

Thèse préparée au Laboratoire de Mécanique de Lille

Ecole Doctorale SPI 072 (Lille I, Lille Ill, Artois, ULCO, UVHC, Centrale Lille)

Contents

Acknowledgements

First and foremost, I express my sincere gratitude to my advisers Prof. Jean-Marc Foucaut and Dr. Jean-Philippe Laval for giving me the opportunity to conduct this research and increase my understanding of turbulent flows. The guidance, support and patience they provided during the course of this work is deeply appreciated.

I am indebted to Prof. Christos Vassilicos for his ideas in developing the model described in Chapter 3 and his help in shaping this chapter. I also thank Prof. Michel Stanislas and Dr. Christophe Cuvier for their help in setting up the experiments and Dr. Christophe Cuvier for analysing the PIV fields, and with whom I learned a lot scientifically and technically.

I would also like to thank Dr. Bérengère Podvin and Dr. Denis Sipp for having accepted to be the reporters of my thesis. I also thank Dr. Geritt Elsinga and Dr. Thomas Gomez for having accepted to be part of my thesis jury.

To my collegues at LML: Ilkay, Linh, Raoul, Robin and Florian; You have provided an invaluable set of resources both inside and outside the lab. Your company has really made my time in Lille enjoyable and memorable.

Finally, I would like to thank my parents and friends and for their love and support over the course of my life and their patience over the last three years.

Without financial support, the study would not be possible. I would like to thank Centrale Lille, the Nord-pas-de-Calais region and EuHIT for the financial support that made this study possible.

Résumé

Le but de ce travail est d'étudier une couche limite soumise à un gradient de pression et de la comparer avec une couche limite de plaque plane à grands nombres de Reynolds. Dans ce cadre, l'accent est mis sur le comportement des structures cohérentes à grande échelle. En raison de leur grande longueur, ces structures ne sont pas faciles à extraire et à caractériser en utilisant des techniques de mesure standard. Pour cette raison, des dispositifs expérimentaux spécifiques utilisant la PIV dans les plans longitudinaux et parallèles à la paroi ont été conçus pour capturer les structures à grande échelle et pour mieux comprendre les mécanismes régissant la dynamique de ces écoulements. La présente thèse est organisée en quatre parties, pour un total de cinq chapitres. Ceux ci se résument comme suit:

- La première partie donne le contexte du présent travail. Le premier chapitre contient une courte introduction motivant l'objectif de la thèse,qui est une caractérisation expérimentale de l'écoulement en vue de sa modélisation et de sa prédiction. Les écoulements avec gradient de pression adverse sont importants pour de nombreux enjeux industriels, mais restent encore mal connus.

- Le chapitre 2 commence par une brève description de la turbulence de paroi: équations moyennées de Reynolds, équations de Prandtl qui régissent une couche limite turbulente, structure d'une couche limite turbulente sans gra-

dient de pression (région interne, région externe, zone de recouvrement logarithmique, effet d'un gradient de pression sur la sous-couche visqueuse, équations de transport des tensions de Reynolds et de l'énergie cinétique turbulente. Suit ensuite une description détaillée de l'état de l'art des connaissances sur l'organisation des structures cohérentes dans une couche limite sans et avec gradient de pression.. L'accent est mis sur l'organisation de l'coulement en structures cohrentes. Pour la couche limite sans gradient de pression, le modèle de Townsend-Perry s'appuyant sur des tourbillons attachés à la paroi est détaillé. Pour un gradient de pression adverse, différentes théories et scalings pour le profil de vitesse moyenne sont présentés.

- La deuxième partie (le chapitre 3) revisite les résultats obtenus sur une couche limite plaque plane en sondant l'origine d'une décroissance spectrale en k_x^{-1} dans la couche limite turbulente. Dans cette perspective, un modèle simpliste basé sur le modèle de Townsend-Perry est proposé. On s'intéresse particulièrement au spectre longitudinal en vitesse. Ce modèle est une généralisation du modèle de Perry-Townsend. On stipule que l'intensité des stries dépend de la longueur de celles-ci suivant une loi de puissance paramétré par un coefficient p (le modèle de Perry-Townsend étant obtenu à nouveau pour p = 0). L'intérêt de ce modèle généralisé est que le spectre énergétique de la fluctuation de vitesse longitudinale se comporte maintenant comme $E_{11}(k_x) \sim k_x^{-1-p}$, ce qui pourrait permettre de donner un cadre théorique conceptuel pour comprendre pourquoi E_{11} ne se comporte pas strictement comme k_x^{-1}, comme cela a été observé dans de nombreuses expériences. Ce modèle peut, en principe, être appliqué à n'importe quel écoulement turbulent de paroi.

- La troisième partie (le chapitre 4) se concentre sur l'amélioration de la compréhension de la turbulence en gradient de pression adverse en effectuant une caractérisation complète d'un écoulement académique au dessus

d'une géométrie. Une description du dispositif est tout d'abord donnée. Les mesures de pression le long de la rampe permettent d'établir que la couche limite turbulente est soumise sur une partie de la rampe à un gradient de pression favorable, puis à un gradient de pression adverse. Le caractère bi-dimensionnel de l'écoulement moyen (pas de variation dans la direction transverse) est établi. Une analyse des statistiques turbulente dans la zone de gradient de pression favorable est également effectuée. L'accent est mis sur les caractéristiques des structures (longueur, loi d'échelle, contribution énergétique et distribution selon la normale à la paroi) ainsi que sur l'influence du gradient de pression adverse sur les structures des grandes échelles. L'analyse permet de comparer le comportement d'une couche limite en présence de gradient de pression adverse avec le cas d'une plaque plane à grands nombres de Reynolds.

- La dernière partie (le chapitre 5) présente les conclusions de l'étude et propose des directions de recherche futures, telles que le calcul du spectre de vitesse, l'extension à des gradients de pression plus intenses, l'analyse de la structure de l'écoulement dans la direction transverse. Plusieurs annexes fournissent des informations supplémentaires sur la méthodologie utilisée dans cette analyse et des résultats statistiques supplémentaires.

Nomenclature

Latin Symbols

C_1, C_2, p, q, r	Values of the constants in the form $-C_1 + C_2(\lambda/\delta)^{-r}$;
C_f	Friction coefficient;
C_p	Pressure coefficient;
E_{11}	Streamwise energy spectra;
$F()$	Flatness;
H	Shape factor;
k_x	Streamwise wavenumber;
O	Origin, fixed at the ramp apex and at the middle of the wind tunnel;
P	Pressure;
Q_1	Event with $u' > 0$ and $v' > 0$;
Q_2	Event with $u' < 0$ and $v' > 0$;
Q_3	Event with $u' < 0$ and $v' < 0$;
Q_4	Event with $u' > 0$ and $v' < 0$;
Re_θ	Momentum Reynolds number;
R_{uu}	Two point correlation of fluctuating streamwise velocity;
R_{vv}	Two point correlation of fluctuating wall-normal velocity;
$S()$	Skewness;
s	Curvilinear abscissa of the ramp, origin at O;
T	Temperature;
t	Time;
u_{th}	Threshold for low and high speed regions;
u^*	Gaussian filtered field of the streamwise fluctuating velocity component;
u, v	Streamwise, wall-normal fluctuating velocities;
U, V	Streamwise, wall-normal mean velocities;
u', v'	Streamwise, wall-normal turbulence intensities;
U_τ	Friction velocity;
U_e	Local free-stream velocity;
U_∞	Free-stream velocity upstream the ramp;
U_{ZS}	Zagorala and Smits reference velocity, $\frac{U_e \delta^*}{\delta}$;
X	Streamwise coordinate, attached to the lower wall of the wind tunnel;
x	Wall-parallel coordinate;
Y	Wall-normal coordinate of the wind tunnel;
y	Wall-normal coordinate;
Z	Spanwise coordinate of the wind tunnel;
z	Spanwise coordinate;

Greek Symbols

α	Average streamwise fluctuating velocity of the detected wall-attached structures;
β	Pressure gradient Clauser's parameter;
δ	Boundary layer thickness;
δ^*	Displacement thickness;
κ	Von Kàrmàn constant;
Λ	Castillo and George's similarity parameter;
λ	Streamwise length of the detected wall-attached structures;
μ	Dynamic viscosity;
ν	Kinematic viscosity;
ρ	Mass density;
$-\rho\overline{u_i u_j}$	Reynolds stresses ;
σ	Standard deviation;
τ, τ_w	Wall shear stress;
θ	Momentum thickness;

Abbreviations

2D	Two dimensional;
3D	Three dimensional;
2D2C	Two dimensions, two components;
2D3C	Two dimensions, three components;
APG	Adverse Pressure Gradient;
CS	Castillo-George scaling (Castillo and George (2001));
DNS	Direct numerical simulations;
FP	Flat Plate;
FPG	Favourable Pressure Gradient;
HW	Hot-Wire;
LES	Large Eddy simulations;
LFSt	Large field streamwise PIV;
LSM	Large-scale motions;
PIV	Particle Image Velocimetry;
SPIV	Stereo PIV;
TRHM	Time resolved high magnification;
TBL	Turbulent Boundary Layer;
VLSM	Very large-scale motions;
ZPG	Zero Pressure Gradient;
ZS	Zagarola-Smits scaling (Zagarola and Smits (1998b));

Others

$(.)^+$	Wall units (u_τ,ν);
$\overline{(.)}$	Mean;

List of Figures

List of Tables

CHAPTER 1

Introduction

A large majority of natural flows and flows encountered in engineering applications are in fact turbulent e.g. flows of water in rivers, seas, oceans, motions of the air in the Earth's atmosphere, in water pipes, the nozzles of jet engines, etc. Most of these turbulent flows are bounded by one or more solid surfaces along which a boundary layer develops. This thin layer is responsible for the skin friction drag of bodies and thus understanding and modelling of the boundary layer can help in improving the design of transport vehicles in order to increase safety, decrease fuel consumption and green house gas emissions.

In the study of turbulence, devising methods to segregate the complex turbulent motions into simplified events called "coherent structures" has been a challenging task. This is especially so in the past two decades as in the case of canonical turbulent wall flows, where a comprehensive research based on experimental and numerical analysis has been undertaken to understand the pattern of coherent structures. Over the last several years, the observation of large-scale coherent structures in turbulent boundary layers has sparked great experimental and numerical interest, as they are known to play a significant role in the production of turbulent kinetic energy (Ganapathisubramani et al. (2005)). While the occurrence and length of these structures have been documented, the relation between these large-scale structures and the energy spectrum has not yet been fully understood. One of the goals of this thesis is to gain a better understanding by bridging the gap between both. To

achieve this goal we show that the scaling of the streamwise energy spectrum in a wavenumber range directly affected by the wall, are determined by wall-attached eddies.

Although many studies have been conducted on zero pressure gradient (ZPG) flows (see Smits et al. (2011) for a recent review on ZPG flows), most engineering devices like airfoils, compressors, diffusers, turbine blades to name a few, encounter boundary layers exposed to pressure gradients. So fundamentally, the study of APG boundary layers may act as a catalyst for deeper understanding of real turbulent flows. Furthermore, the APG boundary layer is usually the most difficult to predict using computational fluid dynamics (CFD). Most of these applications mentioned above occur at high Reynolds numbers, significantly higher than can be examined even in large scale laboratory experiments. Direct numerical simulation (DNS) can provide highly reliable data as all the relevant turbulent length and time scales are resolved. However, due to the limitations of computational power, only low or moderate Reynolds numbers and simple geometries have been investigated by DNS so far. For this reason, alternative numerical methods like Reynolds-Averaged Navier Stokes (RANS) models and Large-Eddy Simulations (LES) have been approached. RANS models have been primarily used in industrial flows. They are based on averaged equations describing the mean flow with all the scales of the turbulence being modelled. Although fast and reliable for simple flows, RANS models perform poorly in complex turbulent separated/vortical flows and are often calibrated for geometry specific flows. When these models calibrated with low and moderate Reynolds number for specific flows are used for more complex flows, the results are inaccurate. While LES provides a possible alternative of resolving the flow structures and achieving better predictions for high Reynolds numbers, requirement of a fine mesh in the inner region of the boundary layer to resolve the near wall flow accurately, makes LES computationally expensive as well. The study of adverse pressure gradient (APG) boundary layers is therefore still a significant challenge to advanced computational schemes.

Additionally, understanding of wall turbulence especially in a decelerating situation through experiments is also quite limited due to the lack of

sufficiently high Reynolds number data and large test facilities. These are necessary to reach some state of an equilibrium boundary layer where theoretical approaches can be relevant. Also, the length of these large-scale structures, up to 14 times the boundary layer thickness (Kim and Adrian (1999), Hutchins and Marusic (2007), Lee and Sung (2011)) requires a large field of view and a high spatial resolution. An experimental database at high Reynolds number subjected to an APG was built, in the framework of a EuHIT (European High-Performance Infrastructures in Turbulence) project to investigate the problem. The fundamental aim of this project was to improve the understanding of turbulence under APG by performing a complete characterisation of the flow. Emphasis is laid on the characteristics of the structures (length, scaling, energetic contribution and their wall normal distribution). The analysis is also extended to compare the behaviour of APG with the ZPG case at high Reynolds numbers.

Organization of the thesis

The present thesis is organized in four parts, for a total of five chapters. Its content is summarized as follows:

The first part gives the context of the present work. **Chapter 1** introduces the background of the thesis and presents the motivation and objective of the study. **Chapter 2** begins with a brief description of wall turbulence. This is followed by a literature review focussing on turbulence structures in wall-bounded flows, particularly the ZPG and APG turbulent boundary layer flows.

The second part (**chapter 3**) is devoted to the analysis of an experiment on ZPG turbulent boundary layer flow at high Reynolds number. A simple model relating the attached flow structures and the streamwise energy spectra is first presented. The experimental facility and measurement techniques used to validate the model are described followed by a discussion of the turbulence statistics and the large-scale structures.

Part three (**Chapter 4**) describes the results of an experiment dedicated to the study of APG turbulent boundary layer flow. The extensive set of

experiments that were performed in the framework of a EuHIT project to improve the understanding of APG flows is described first. Then, the characterization of the flow over the APG region is covered in detail along with the influence of the adverse pressure gradient on the large-scale structures.

The last part (**chapter 5**) summarizes the main conclusions of the study and highlights further research opportunities to continue this investigation. Several appendices provide additional information on the methodology used in this analysis and additional statistical results.

Publications and communications

Journal Articles

- Cuvier, C., Srinath, S., Stanislas, M., Foucaut, J.-M., Laval, J.-P., Kahler, C. J., Hain, R., Scharnowski, S., Schrder, A., Geisler, R., Agocs, J., Rose, A., Willert, C., Klinner, J., Amili, O., Atkinson, C., and Soria, J. (2017). Extensive characterisation of a high reynolds number decelerating boundary layer using advanced optical metrology. *Journal of Turbulence*, 18(10):929-972.

- Srinath. S., Vassilicos. J. C., Cuvier. C., Laval. J.-P., Stanislas. M., and Foucaut. J.-M. (2017). Attached flow structure and streamwise energy spectra in a turbulent boundary layer. *Submitted to the Journal of fluid mechanics.* arXiv:1706.07774

Communications

- Srinath. S., Cuvier. C., Foucaut. J.-M. and Laval. J.-P. (2015, May). *Large-scale structures in high Reynolds number turbulent boundary layers.* Presented at the Workshop on Wall Turbulence and Advanced Measurement Techniques, Lille, France.

- Srinath. S., Cuvier. C., Foucaut. J.-M. and Laval. J.-P. (2015, August). *Experimental Characterisation of large-scale structures in a high Reynolds number turbulent boundary layer.* Presented at 15th European Turbulence Conference, Delft, The Netherlands.

- Srinath, S., Cuvier, C., Stanislas, M., Foucaut, J.-M., Laval, J.-P., Kahler, C. J., Hain, R., Scharnowski, S., Schrder, A., Geisler, R., Agocs, J., Rose, A., Willert, C., Klinner, J., Amili, O., Atkinson, C., and Soria, J. (2017, August). *Experimental characterisation of a high Reynolds number turbulent boundary layer subjected to an adverse pressure gradient.* Presented at 16th European Turbulence Conference, Stockholm, Sweden.

- Srinath, S., Cuvier, C., Stanislas, M., Foucaut, J.-M., Laval, J.-P., Kahler, C. J., Hain, R., Scharnowski, S., Schrder, A., Geisler, R., Agocs, J., Rose, A., Willert, C., Klinner, J., Amili, O., Atkinson, C., and Soria, J. (2017, September). *Coherent large-scale structures in adverse pressure gradient turbulent boundary layers.* Presented at 23rd Congrès Français de Mécanique , Lille, France.

CHAPTER 2

Literature review

2.1 Wall turbulence

Fluid flow can be classified as laminar or turbulent. In laminar flows, the motion of fluid particles is very orderly with the fluid moving in parallel layers. Turbulent flows on the other hand lose the orderly flow pattern with sharp and irregular space and time fluctuating motion. Transition to turbulence is generated due to the development of instabilities from a laminar flow. These instabilities continue to develop when inertial forces in the flow grow larger than the viscous forces, ultimately resulting in the flow field becoming unstable. The ratio of the inertial forces to the viscous forces is known as the Reynolds number ($Re = \frac{L_s U_s}{\nu}$, where U_s and L_s are a chosen length and velocity scale and ν is the kinematic viscosity of the fluid).

Regarded as one of the most complex problem of applied mathematics and physics, there is perhaps not a conventional way to define turbulence. Instead of giving a standard definition, Tennekes and Lumley (1972) listed out the main characteristics of turbulent flows :

- Non-linear: turbulence arises from the coupling between the viscous terms and the non-linear inertial terms in the Navier-Stokes equations.

- Chaotic: a small perturbation introduced at any point of the field can affect the entire flow making turbulent flows difficult to predict.

- Rotational and three-dimensional: turbulence is characterised by high levels of fluctuating vorticity that are maintained through three-dimensional vortex stretching.

- Diffusive: turbulence causes rapid mixing and increased rates of momentum, heat and mass transfer along but also across mean streamlines.

- Dissipative: the kinetic energy gets converted into heat due to viscous shear stresses. This process is enhanced for turbulent flows because of the higher deformation rate.

- Multiscale: a wide range of length scales exists in turbulent flows ranging from the dimensions of the flow field to the action of molecular viscosity (Kolmogorov scales)

According to Hinze (1938), turbulence can be categorised into two types: (a) *wall turbulence* where flows remain "attached" to the surface and evolve entirely under the influence of it and (b) *free shear flows* where mean velocity gradients develop in the absence of boundaries. In this thesis, we focus on wall-bounded flows i.e the ZPG and APG turbulent boundary layer flows.

2.1.1 Reynolds Average Navier Stokes Equations

The Navier-Stokes equations (equation 2.1) govern the flow of incompressible fluids. Throughout this dissertation, we assume the flow to be incompressible and isothermal so that the fluid properties such as the density, ρ and dynamic viscosity, μ in the Navier-Stokes equation are not affected by temperature.

$$\begin{cases} \dfrac{\partial \tilde{u_i}}{\partial x_i} = 0. \\ \\ \rho(\dfrac{\partial \tilde{u_i}}{\partial t} + \tilde{u_j}\dfrac{\partial \tilde{u_i}}{\partial x_j}) = -\dfrac{\partial \tilde{p}}{\partial x_i} + \mu\dfrac{\partial^2 \tilde{u_i}}{\partial x_j^2}. \end{cases} \tag{2.1}$$

where $\tilde{u_i}$ is i-th component of the instantaneous fluid velocity at the position (x_1, x_2, x_3), t is the time and $\tilde{p}$ is the instantaneous pressure field.

Along this document, x_1 or just x denotes the streamwise, x_2 or y the wall-normal and x_3 or z the spanwise directions repectively. The equations are written using the Cartesian tensor notation and the Einstein summation convention. Also, u_1 or u, u_2 or v and u_3 or w can be used in reference to the streamwise, wall-normal and spanwise velocities respectively.

Through Reynolds decomposition, the instantaneous flow quantities can be expressed by the sum of their mean (U_i, P) and fluctuating parts (u_i, p) as shown in equation 2.2.

$$\begin{cases} \tilde{u_i} = U_i + u_i. \\ \tilde{p} = P + p_i. \end{cases} \tag{2.2}$$

The Reynolds decomposition can be then introduced in the Navier-Stokes equation (equation 2.1) to obtain the basic equations for the averaged turbulent flow known as the Reynolds Averaged Navier Stokes equations (RANS) as shown in equation 2.3.

$$\begin{cases} \dfrac{\partial U_i}{\partial x_i} = 0 \\ \rho(\dfrac{\partial U_i}{\partial t} + U_j \dfrac{\partial U_i}{\partial x_j}) = -\dfrac{\partial P}{\partial x_i} + \mu \dfrac{\partial^2 U_i}{\partial x_j^2} - \rho \dfrac{\partial \overline{u_i u_j}}{\partial x_j} \end{cases} \tag{2.3}$$

where $\overline{u_i u_j}$ is the Reynolds stress tensor. It is a symmetric tensor, the trace of which is equal to twice the turbulent kinetic energy, k.

$$k = \frac{1}{2}\overline{u_i' u_i'} \tag{2.4}$$

2.1.2 Turbulent boundary layer equation

The conservation equations can be reduced to simpler forms by examining the relative magnitude of the terms in the equations. The respective length and velocity scales are used to evaluate the order of magnitude of the various terms in the equations. Considering a 2D flow over a wall at high Reynolds number, it is common to introduce two length scales L and δ which are the parallel and normal length scales to the wall. Near the wall, as the length

scale δ is much smaller than the longitudinal scale ($\delta << L$), equation 2.3 reduces to the boundary layer equations (2.5).

$$\begin{cases} \dfrac{\partial U}{\partial x} + \dfrac{\partial V}{\partial y} = 0. \\ \rho(U\dfrac{\partial U}{\partial x} + V\dfrac{\partial U}{\partial y}) = -\dfrac{\partial P}{\partial x} + \mu\dfrac{\partial^2 U}{\partial y^2} - \rho\dfrac{\partial \overline{uv}}{\partial y}. \\ \dfrac{\partial P}{\partial y} + \rho\dfrac{\partial \overline{v^2}}{\partial y} = 0. \end{cases} \tag{2.5}$$

2.1.2.1 ZPG turbulent boundary layer

In canonical wall-bounded flows (i.e. two-dimensional, smooth-wall, ZPG turbulent boundary layer and fully developed pipe and channel flows) at sufficiently high Reynolds number, two overlaping regions with different physical processes can be distinguished i.e. inner and outer regions (Panton (2001)). For a ZPG turbulent boundary layer flow, the boundary layer equations are obtained by taking $\frac{\partial P}{\partial x} = 0$ in equations 2.5. Conventionally, the turbulent flow can be characterized with two regions; An inner region and an outer region:

Inner region: This region extends from the wall until a height of about 0.1δ (George (2013); Pope (2001)) with δ being the boundary layer thickness. The flow is affected by the wall shear stress and in the case of a smooth wall, by the fluid viscosity only. Here, the convective terms are negligible compared to the viscous term and the turbulent shear stress. Thus for a ZPG turbulent boundary layer, equation 2.5 can be simplified to

$$\mu\frac{\partial^2 U}{\partial y^2} - \rho\frac{\partial \overline{uv}}{\partial y} = \frac{\partial}{\partial y}(\mu\frac{\partial U}{\partial y} - \rho\overline{uv}) = \frac{\partial \tau}{\partial y} = 0 \tag{2.6}$$

Integrating equation 2.6 and applying the boundary condition at the wall, the equation for the inner region (equation 2.7) can be obtained with U_τ the friction velocity given by $U_\tau = \sqrt{\frac{\tau_{y=0}}{\rho}}$.

$$\tau = \mu \frac{\partial U}{\partial y} - \rho \overline{uv} = \tau_{y=0} = \rho U_\tau^2 \tag{2.7}$$

From equation 2.7, the streamwise mean velocity, U can depend only on y, U_τ, ρ and μ. Dimensional analysis leads to a scaling of the mean velocity profile in the form

$$U^+ = f(y^+) \tag{2.8}$$

where $U^+ = \frac{U}{U_\tau}$ and $y^+ = \frac{yU_\tau}{\nu}$

The inner region is generally thought to comprise of three layers:

• At $y^+ \leq 5$, viscosity dominates the flow and thus $\rho\overline{uv}$ is negligible. This layer is called the viscous sublayer or linear sublayer as the velocity profile exhibits a linear relation between U^+ and y^+ ($U^+ = y^+$).

• Above the linear sublayer, the two stresses are of comparible magnitude. This region is called the buffer layer and extends up to $y^+ \leq 30$

• Beyond $y^+ > 30$ and up to $y \leq 0.1\delta$, the turbulent shear stress becomes dominant compared to the viscous stress.

Outer region: The region beyond $y > 0.1\delta$ is called the outer region and here, the streamwise velocity profile can be considered as independent of viscosity. The characteristic length and velocity scales are δ and U_τ respectively. In this region, a velocity defect law (equation 2.9) is generally used to describe the mean velocity profile.

$$\frac{U_e - U}{U_\tau} = f\left(\frac{y}{\delta}\right) \tag{2.9}$$

The 'wake law' proposed by Coles (1956) is generally used to describe this region. Recently, George (2006) and George (2007) questioned the validity of the outer region velocity defect law (equation 2.9) for boundary layer flows and proposed an alternative form where the velocity deficit is scaled by the freestream velocity U_e rather than U_τ. They argued that this alternative form is a similarity solution of the Reynolds-averaged equations giving rise to a power law equation of the overlap region. However, George (2006)

and George (2007) admit that the logarithmic law provides a good empirical description of the overlap region indistinguishable from the power-law solution.

Overlap region: At sufficiently high Reynolds number, an overlap region exists where the scaling laws for both the inner and outer regions simultaneously hold. It is often called the 'logarithmic region' and is reputed to be valid not only for boundary layers, but also for pipe and channel flows. Matching equations 2.8 and 2.9, Millikan (1939) obtained an expression to describe the mean velocity profile. Also referred to as the log-law, in inner variables it is given by

$$U^+ = \frac{1}{\kappa} \ln y^+ + C \tag{2.10}$$

where κ is the Von Karman constant and C is an additive constant. For ZPG boundary layers, the generally accepted values for these constants are $\kappa = 0.41$ and $C = 5$ (Cuvier et al. (2014); George (2013)). Conventionally this overlap region is considered to be equivalent to an inertial sublayer, indicating that neither viscous nor energetic scales are relevant.

George (2006) introduced a region called the 'mesolayer' in the inner part of the overlap region ($30 \leq y^+ \leq 300$) and described it as the region where the viscous stresses are negligible, but in which viscosity acts directly on the turbulence scales producing the Reynolds stresses.

In summary, a typical mean streamwise velocity profile showing the different regions of a turbulent boundary layer is shown in figure 2.1.

2.1.2.2 Turbulent boundary layer subjected to a pressure gradient

For turbulent boundary layers where the pressure gradient, i.e. the first term on the right hand side of equation 2.5 is non-zero and positive, the flow is said to be subjected to an APG, which can lead to separation of the boundary layer from the surface. Flow separation in many applications is generally undesirable. An APG causes the boundary layer thickness, δ to increase in the streamwise direction. In addition to the boundary layer, other quantities

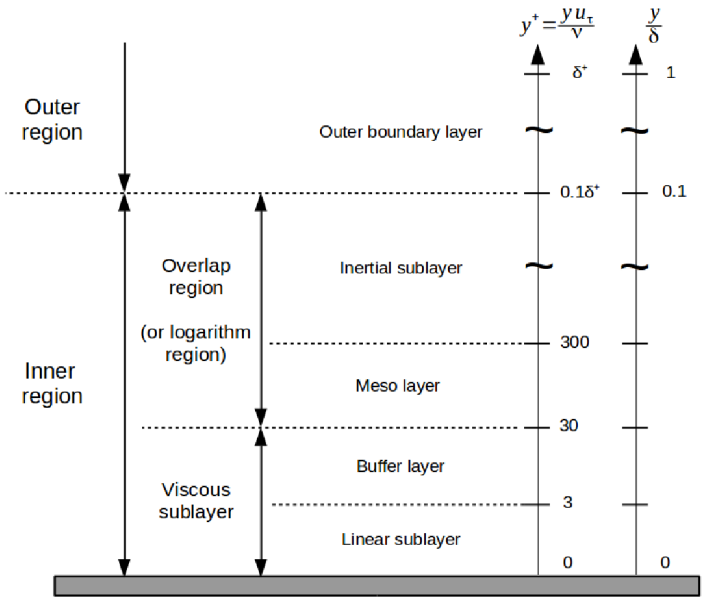

Figure 2.1: Sketch showing the various regions of a turbulent boundary layer flow adapted from George et al. (1997)

are defined to characterise the boundary layer. The displacement thickness δ^* (equation 2.11), the momentum thickness θ (equation 2.12) and the shape factor H (equation 2.13) generally increase while the skin friction coefficient C_f (equation 2.14) generally decreases.

$$\delta^* = \int_0^\delta \left(1 - \frac{U(y)}{U_e}\right) dy \tag{2.11}$$

$$\theta = \int_0^\delta \frac{U(y)}{U_e}\left(1 - \frac{U(y)}{U_e}\right) dy \tag{2.12}$$

$$H = \frac{\delta^*}{\theta} \tag{2.13}$$

$$C_f = \frac{\tau_w}{\frac{1}{2}\rho {U_e}^2} \tag{2.14}$$

For boundary layers with pressure gradients ($\frac{\partial P}{\partial x} \neq 0$ in equation 2.5), the

inner region is governed by

$$\frac{\partial P}{\partial x} = \mu\frac{\partial^2 U}{\partial y^2} - \rho\frac{\partial \overline{uv}}{\partial y} = \frac{\partial}{\partial y}(\mu\frac{\partial U}{\partial y} - \rho\overline{uv}) = \frac{\partial \tau}{\partial y} \tag{2.15}$$

Integrating the previous equation and applying the boundary condition at the wall leads to

$$\tau = \mu\frac{\partial U}{\partial y} - \rho\overline{uv} = \frac{\partial P}{\partial x}y + \rho U_\tau^2 \tag{2.16}$$

Neglecting the turbulent shear stress near the wall and integrating equation, the viscous sublayer equation (2.17) is obtained.

$$U^+ = \frac{1}{2}\frac{\partial P^+}{\partial x}y^{+2} + y^+ \tag{2.17}$$

where

$$\frac{\partial P^+}{\partial x} = \frac{\nu}{\rho U_\tau^3}\frac{\partial P}{\partial x} \tag{2.18}$$

Equation 2.17 shows that the effect of the pressure gradient on the mean velocity profile starts very close to the wall. If the term involving the pressure gradient is negligibly small compared to the other terms, the equation reduces to the equation governing the inner part of a ZPG layer, i.e. when $\frac{\partial P^+}{\partial x}y^{+2} \ll 1$ in equation 2.17, $U^+ = y^+$ can be used to describe the viscous sublayer. However, for strong APG flows at finite Reynolds, this term cannot be neglected.

The scaling of the mean velocity will be presented in section 2.3.2.

2.1.3 Reynolds shear stress transport

The transport equation for the Reynolds shear stress $\overline{u_i u_j}$ can be obtained by manipulating the Navier-Stokes equations. By decomposing the momentum equation for the total velocity and subtracting the equation of the mean, a transport equation for the momentum of the fluctuations is obtained. This is then multiplied by fluctuating velocity components, u_j. The subscripts i and j are then exchanged. These last two equations are added together and the

result is then averaged and simplified to obtain the transport equation for the Reynolds stress tensor given by equation 2.19 where $\tau_{ij} = \mu\left(\frac{\partial u_i}{\partial x_j} + \frac{\partial u_j}{\partial x_i}\right)$

$$\underbrace{\rho\frac{\partial\overline{u_iu_j}}{\partial t}}_{1} + \underbrace{\rho U_k\frac{\partial\overline{u_iu_j}}{\partial x_k}}_{2} = \underbrace{-\rho\overline{u_iu_k}\frac{\partial U_j}{\partial x_k} - \rho\overline{u_ju_k}\frac{\partial U_i}{\partial x_k}}_{3} + \underbrace{\frac{\partial(\overline{u_i\tau_{jk}e} + \overline{u_j\tau_{ik}})}{\partial x_k}}_{4} - \underbrace{\frac{\partial(\overline{u_ip}\delta_{jk} + \overline{u_jp}\delta_{ik})}{\partial x_k}}_{5} - \underbrace{\rho\frac{\partial\overline{u_iu_ju_k}}{\partial x_k}}_{6} + \underbrace{\overline{p\frac{\partial u_i}{\partial x_j}} + \overline{p\frac{\partial u_j}{\partial x_i}}}_{7} - \underbrace{\overline{\tau_{ik}\frac{\partial u_j}{\partial x_k}} - \overline{\tau_{jk}\frac{\partial u_i}{\partial x_k}}}_{8} \tag{2.19}$$

The terms under the curly braces will be described in the next sub-section.

2.1.4 Turbulent kinetic energy transport

The transport equation for the turbulent kinetic energy is obtained from the Reynolds stress equation (2.19) by contracting the free indices (i.e by taking $j = i$).

$$\underbrace{\rho\frac{\partial\overline{k}}{\partial t}}_{1} + \underbrace{\rho U_k\frac{\partial\overline{k}}{\partial x_k}}_{2} = \underbrace{-\rho\overline{u_iu_k}\frac{\partial U_i}{\partial x_k}}_{3} + \underbrace{\frac{\partial\overline{u_i\tau_{ik}}}{\partial x_k}}_{4} - \underbrace{\frac{\partial\overline{u_kp}}{\partial x_k}}_{5} - \underbrace{\frac{1}{2}\rho\frac{\partial\overline{u_iu_iu_k}}{\partial x_k}}_{6} - \underbrace{\overline{\tau_{ik}\frac{\partial u_i}{\partial x_k}}}_{8} \tag{2.20}$$

Both equations 2.19 and 2.20 can be explored for understanding the dynamics of turbulent motion. Each numbered term in equations 2.19 and 2.20 has a distinct role in the overall energy balance as described in George (2013).

Term (1) is the rate of change of kinetic energy per unit mass due to non-stationarity. Term (2) is the rate of change of kinetic energy per unit mass due to convection by the mean flow. Term (3) is the production term that takes kinetic energy from the mean flow to feed turbulence. Terms (4), (5) and (6) correspond to the viscous diffusion, diffusion by pressure fluctuations and

diffusion by velocity fluctuations respectively. They transport the turbulent kinetic energy from one place to another. Term (7) in the Reynolds shear stress equation is the pressure-strain rate term. It redistributes energy among normal stresses and makes them more isotropic. Term (8) is the rate of dissipation of turbulence kinetic energy due to viscous stresses.

2.2 Zero pressure gradient turbulent boundary layer

2.2.1 Organisation of coherent structures

Wall turbulence is characterized by the presence of eddy structures or coherent motions over a wide range of scales (Adrian et al. (2000)). Robinson (1991) defined coherent motions as *three dimensional region(s) of the flow over which at least one fundamental flow variable exhibits significant correlation with itself or with another flow variable over a range of space and/or time that is significantly larger than the smallest local scales of the flow.* The presence of coherent structures in turbulent flow has been evidenced statistically in the non-zero Reynolds shear stress and two point space-time correlations and they are believed to play a role in the production and dissipation of turbulence in boundary layers. The importance of coherent structures was initially highlighted by Theodorsen (1952); Townsend (1956); Kline et al. (1967). Efforts have since been taken by various research groups to characterize and classify them using flow visualization and measurement techniques. In the following, a literature review of coherent structures is presented in two separate frames. First, the near wall coherent structures in the inner region that have been characterized extensively are presented. This is followed by a review of the large and very large-scale motions that have been found to populate the logarithmic region (refer 2.1.2.1) at high Reynolds numbers.

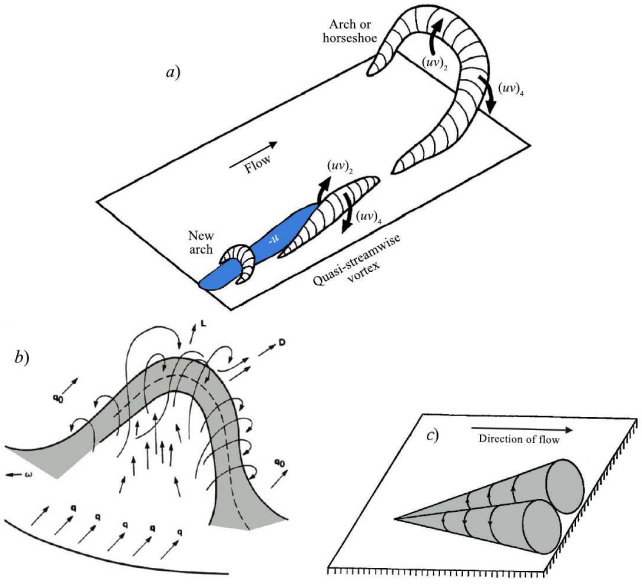

Figure 2.2: (a) Conceptual model of the kinematical relationships between ejection/sweep motions, streaks and quasi-streamwise vortices proposed by Robinson (1991) for low Reynolds number boundary layer flows. (b) sketch of a horseshoes vortex by Theodorsen (1952). (c) attached vortices concept of Townsend (1976). Figure is taken from Rahgozar (2013)

2.2.1.1 Near wall coherent structures

The organisation of turbulence in the near wall region has been studied extensively using dedicated experiments and more recently by DNS, through which full 3D time resolved information are available. The near wall cycle of turbulence can be explained in terms of well identified coherent structures that are listed below.

- **Low-speed and high-speed streaks**: They appear as alternating low and high momentum regions generally observed in the near wall region ($0 < y^+ < 40$) of the boundary layer. They were first studied from hydrogen bubble visualizations (Kline et al. (1967)). Within the sublayer, low speed streaks tend to be longer than their high-speed counterparts and this difference is more pronounced at high Reynolds numbers (Robinson (1991)). Apart from their length that varies widely, there has been an agreement

on their characteristics (Carlier and Stanislas (2005)). Low speed streaks appear below $y^+ < 10$ and are between 500^+ and 2000^+ long, 20^+ and 40^+ wide and up to 50^+ high. The streaks interact with the outer portions of the flow through a process of gradual lift-up, followed by a sudden oscillation, bursting and ejection (Kline (1978)).

- **Ejections and sweeps**: Wallace et al. (1972) defined the Reynolds shear stress events in terms of quadrant motions according to the signs of the streamwise and wall-normal velocity fluctuations. The second quadrant (Q_2) events ($u < 0, v > 0$) were termed "ejections" while the fourth quadrant (Q_4) events ($u > 0, v < 0$) were called "sweeps". The product of the Reynolds shear stress is negative in the second and fourth quadrants and thus these events produce turbulent energy (recall equation). From hot-wire anemometry and conditional averaging, Wallace showed that sweeps contribute more to the production of turbulent kinetic energy compared to ejections in the region ($y^+ < 15$) and less as we move away from the wall $y^+ > 15$.

- **Vortices** Robinson et al. (1989) defined a vortex as a coherent structure that exhibits circular or spiral instantaneous streamlines in a plane normal to its core when viewed in a reference frame moving with the centre of the vortex core. It is shown by several researchers that the near-wall region of turbulent flows is populated with quasi-streamwise vortices (also called rolls) which are associated with ejections and sweeps (refer figure 2.2). Using conceptual ideas based on the vorticity transport equations, Theodorsen (1952) postulated that boundary layers are populated by horseshoe structures originating from the stretching of perturbed spanwise vorticity. This structure is often described as having two counter-rotating streamwise oriented legs connected to a spanwise oriented head through a neck and straddling low speed fluid with their heads inclined at 45° to the wall. In agreement with Theodorsen (1952), Robinson et al. (1989) using DNS data showed that the wall layers contain counter-rotating vortices oriented and tilted downstream and Robinson suggested that these vortices create and lift the streaks in the sublayer by creating cross flows near the

wall. The shape and size of hairpins near the wall strongly depend on the Reynolds number (Head and Bandyopadhyay (1981); Smith (1984); Zhou et al. (1997, 1999); Adrian et al. (2000)).

A model of the organization of coherent structures in the inner region was built by Lin (2006) from spatial correlations analyses and structure parameters (size, orientation, etc.). A recent review of near wall turbulence can be found in Stanislas (2016). These studies could be referred to get a current picture of the near-wall organization in ZPG flows.

2.2.1.2 Large and very large-scale motions

Large scale coherent motions in the inner and outer regions have been observed in boundary layer, pipe and channel flows. Usually categorised into large-scale motions (LSM) and very large-scale motions (VLSM), they are generally referred to elongated regions of velocity fluctuations having a streamwise extent of $1 \sim 3\delta$ for LSM and larger than 3δ for VLSM (Kim and Adrian (1999); Guala et al. (2006); Balakumar and Adrian (2007)) and exist in the logarithmic and lower wake regions of a turbulent boundary layer (Hutchins and Marusic (2007); Dennis and Nickels (2011a); Lee and Sung (2011)). Much focus has been laid on these LSM and VLSM as they contribute to a significant amount of turbulent kinetic energy and Reynolds shear stress in turbulent flows (Ganapathisubramani et al. (2003); Jiménez et al. (2004); Wu (2014)). The study and organization of these structures is thus imperative for understanding the physics of wall turbulence and for the development of reliable turbulence models.

Early studies on the outer intermittent region of a turbulent boundary layer with zero pressure gradient by Kovasznay et al. (1970) was carried out to throw some light on the shape and motion of the interface separating the turbulent and non-turbulent regions as well as on nature of the LSM existing in the turbulent regime. Implementing conditional averaging and space-time correlations showed LSM in the form of turbulent bulges (see figure 2.3), that they concluded to be three dimensional and elongated in the streamwise

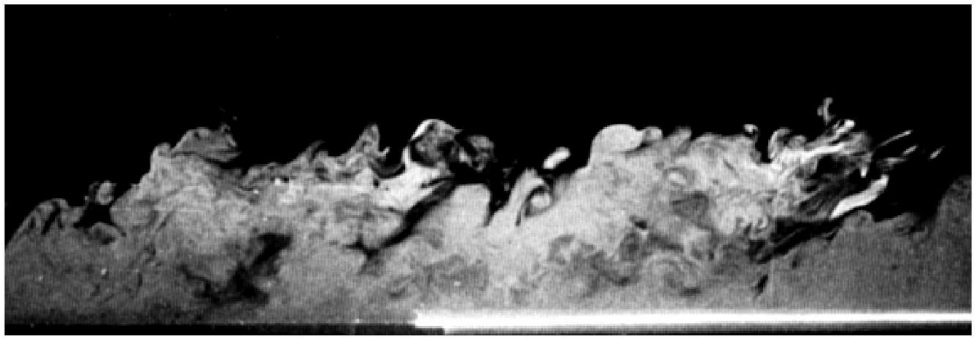

Figure 2.3: Large-scale turbulent bulges visualised by in the streamwise wall-normal plane by illuminating oil vapour with a light sheet performed by Falco (1977)

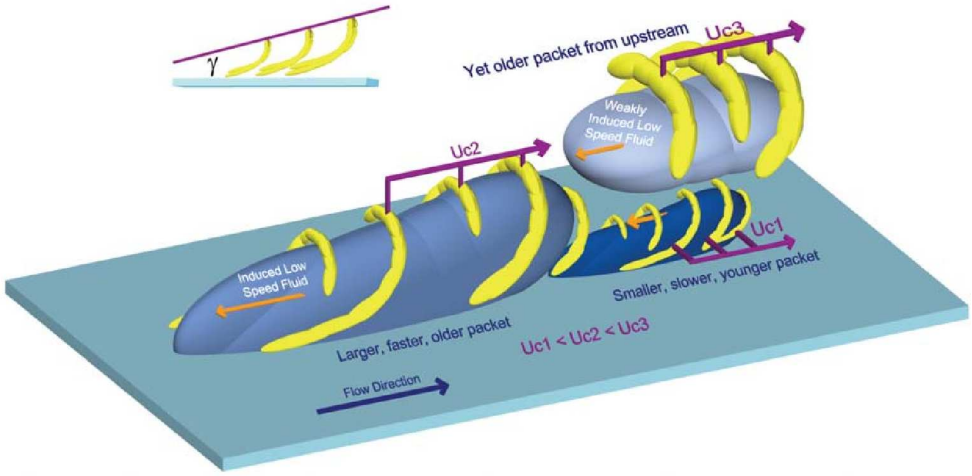

Figure 2.4: Conceptual model of the nested packets of hairpins from the PIV measurements of Adrian et al. (2000). U_{c1}, U_{c2} and U_{c3} are the convection velocities of each hairpin packet respectively.

direction, having a streamwise characteristic length of δ. From time scales of wall shear velocity correlations, Brown and Thomas (1977) found LSM of the order of 2δ related to the bursting phenomenon near the wall. They found these structures to be inclined at 18° similar to Falco (1977).

With the improvement in measuring techniques, Adrian et al. (2000) used

Particle Image Velocimetry (PIV) in a streamwise-wall-normal plane of the near wall region of a ZPG turbulent boundary layer at three Reynolds numbers in the range $930 \leq Re_\theta \leq 6845$. They attributed the origins of LSM to the streamwise alignment of hairpin vortices to form packets moving with the same convection velocity and inducing a low speed zone beetween their legs (see figure 2.4). These packets grow upwards in the streamwise direction at a mean angle of approximately 12° contributing to about 25% of $-\overline{uv}$, even though they occupy less than 4% of the total area. Ganapathisubramani et al. (2003) observed that their streamwise coherence breaks down beyond the logarithmic layer. PIV measurements in the streamwise-spanwise plane at a Reynolds numbers in the range $1015 \leq Re_\theta \leq 7705$ by Tomkins and Adrian (2003) in a ZPG turbulent boundary layer revealed that long low momentum regions with a streamwise length of over 2δ and a typical width of 0.3δ to 0.5δ are the dominant LSM in the upper buffer layer and in the logarithmic region. They also suggested that the streamwise separation between packets increases with the wall normal direction and ranges in $200^+ - 250^+$ at $Re_\theta = 7750$ and the spanwise spacing of counter rotating haipin legs ranges in $100^+ - 120^+$ at $y^+ = 100$ and $y^+ = 220$

Although the origin of VLSM is not certain, Kim and Adrian (1999) from hot-film measurements in pipe flows suggested that hairpin packets align coherently to form these VLSM. The pre-multiplied spectra $k_x E_{11}$ of the streamwise velocity fluctuations showed a bimodal behaviour and the maximum associated with the low wavenumber mode was interpreted to be the VLSM extending up to $14 - 16R$ (R is the pipe radius) in the outer layer of the fully developed turbulent pipe flow at different Reynolds numbers. They termed the structures VLSM (such as individual packets of hairpins and bulges) to distinguish them from LSM that have a typical scale of the order of δ. They suggest that these large structures may be a concatenation of hairpin packets (see figure 2.5). VLSM $20h$ long (h is the channel half-width) have also been observed in channel flows by del Álamo and Jiménez (2003); del Álamo et al. (2004); Balakumar and Adrian (2007); Monty et al. (2007). In boundary layers, Hutchins and Marusic (2007) used hot-wire rake measurements of an atmospheric surface layer at $Re_\tau \simeq 6.6 \times 10^5$ and found

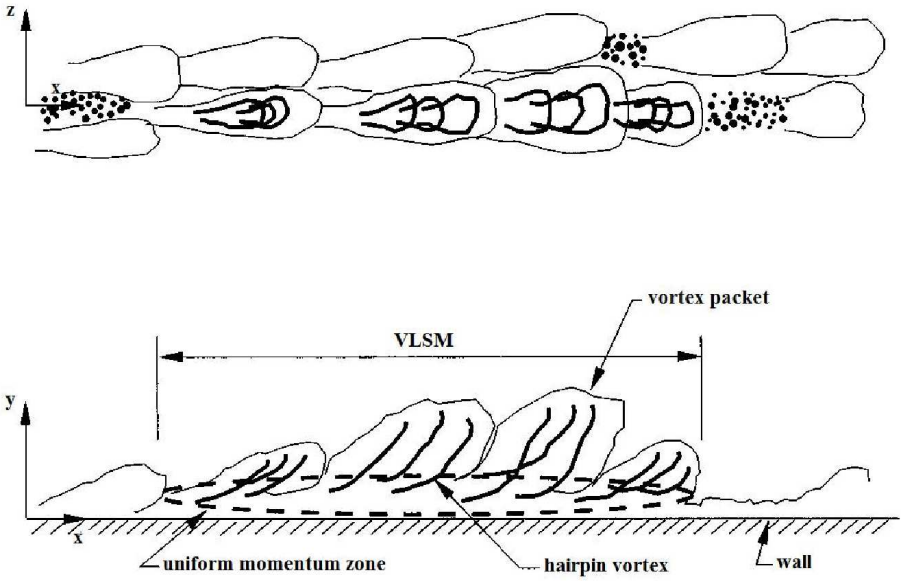

Figure 2.5: Conceptual model of Kim and Adrian (1999) showing the process that creates VLSM. The hairpins align coherently in groups to form long packets and packets align coherently to form VLSM.

very long meandering structures extending up to 20δ that they term superstructures, populating the log layer. However, when viewed from single point statistics, the meandering tendency masks the true length of these structures resulting in shorter length scales up to 6δ. Performing high-speed stereo PIV at $Re_\theta = 4700$, Dennis and Nickels (2011b) noticed structures 7δ long. In general, VLSM in pipe and channel flows are longer than the corresponding scales in boundary layer flows (Balakumar and Adrian (2007)) and in channel flows they grow with distance from the wall. By comparison in the log region, the structures were 1.6 times wider in the pipe and channel compared to those found in the boundary layer (Monty et al. (2007)). Furthermore, the low-speed regions were observed to be longer than their high-speed counterparts (Dennis and Nickels (2011b)) and in channels, the low-speed regions were longer compared to pipe and boundary layer flows (Sillero et al. (2014)).

VSLM carry substantial portions of the Reynolds shear stress (30-50%)

and kinetic energy (40-65%) in channel, pipe and boundary layer flows (Jiménez et al. (2004); Guala et al. (2006); Balakumar and Adrian (2007); Lee and Sung (2013)) making them vital while modelling turbulence. Additionally, the VSLM maintain a footprint in the near-wall region seeming to modulate the small scales (Hutchins and Marusic (2007); Mathis et al. (2009)).

These LSM and VSLM have been interpreted to account for the long correlation tails and responsible for the k_x^{-1} scaling range in the turbulence spectrum (Smits et al. (2011)) and thought to be the attached eddies discussed by Townsend (1976), the subject of which will be discussed in the following section.

2.2.2 An overview of the Townsend-Perry theory

The traditional scaling of the components of the Reynolds shear stress tensor ($\overline{u_i u_j}$) in wall bounded flows was developed by Townsend (1976). This was, in part, inspired by an earlier work (Townsend (1951)) from hot-wire measurements in a turbulent boundary layer. In particular, he examined the terms in the equation for kinetic energy of the velocity fluctuations and noted that there was a surprisingly strong flow of turbulent energy towards the wall. He postulated that turbulence consists mostly of superimposed eddies and the bulk of the energy-containing eddies are, in a sense, attached to the wall, and that the dependence of scale with distance from the wall is not a local effect but due to this attachment of most of the eddies. In this paper he also suggested a possible form of these eddies where these eddies may be thought of as velocity fields of some representative vortex structures. Thus, in the sense of Townsend (1976), any eddy with a size that scales with its distance from the wall may be considered attached to the wall. Eddies farther from the wall are larger in size and hence their velocity fields still extend to the wall. These eddies form the basis of the attached eddy hypothesis. The hypothesis itself is that the main energy containing motion of a turbulent wall bounded flow may be described by a random superposition of such eddies of different sizes, but with a similar velocity distributions. These eddies are considered as statistically representative structures in that their geometry and strength

are derived from an ensemble average of many different structures of similar scale.

Townsend (1951) then went on to form expressions for the contributions of a random superposition of attached eddies of different sizes to the correlation fuctions and derived the distribution of eddy sizes with wall distance necessary to produce invariance of the Reynolds shear stress ($-\overline{uv}/U_\tau^2 \approx 1$) with distance from the wall as observed in the equilibrium layer. This analysis effectively leads to a population density of eddies that varies inversely with size and hence with distance from the wall. That is, the number of eddies of size y per unit wall area is A/y, where A is a constant. These distributions of eddies also lead to predictions for the variation of the other components of the Reynolds shear stress tensor:

$$\begin{aligned} \overline{u^2}/U_\tau^2 &= B_1 + A_1 \ln(\delta/y) \\ \overline{v^2}/U_\tau^2 &= B_3, -\overline{uv}/U\tau^2 = \quad 1 \\ \overline{w^2}/U_\tau^2 &= B_2 + A_2 \ln(\delta/y) \end{aligned} \tag{2.21}$$

where the terms A_1, A_2, B_1, B_2 and B_3 are constants which depend on the shape and details of the representative eddy.

In the past forty years, the turbulence spectrum of velocity fluctuations in wall turbulence has received considerable attention as it gives valuable insight into the behaviour of wall-bounded flows by indicating the distribution of energy across scales. Spectral scaling laws built on ideas initiated by Townsend (1976), in particular the attached eddy hypothesis, have seen consistent development over the years (Perry and Chong (1982); Perry et al. (1986); Perry and Li (1990); Marusic et al. (1997); Marusic and Kunkel (2003)). Perry and Abell (1977), Perry and Chong (1982) and Perry et al. (1986) showed how Townsend's attached eddy hypothesis implies that the energy spectrum $E_{11}(k_x)$ of the turbulent streamwise fluctuating velocity at a distance y from the wall scales as $E_{11}(k_x) \sim U_\tau^2 k_x^{-1}$ in the range $1/\delta \ll k_x \ll 1/y$ where U_τ is the friction velocity and δ is the boundary layer thickness. Perry and Chong (1982) also made the connection between the energy spectra and the stresses and pointed out that a k_x^{-1} spectrum integrates to give a logarithmic

dependence of the streamwise stress on the wall-normal position as given in equation 2.21. Nickels et al. (2005) stressed the use of overlap arguments to deduce the -1 power law behaviour. That is, a k_x^{-1} region in the spectra would exist where the inner scaling (based on y and U_τ) and outer scaling (based on δ and U_τ) are simultaneously valid over the same wavenumber range. Nickels et al. (2007) stated that it is necessary to take measurements surprisingly close to the wall to observe a k_x^{-1} behaviour and thought this was the reason why Morrison et al. (2004) and McKeon and Morrison (2007) did not observe any -1 region in their spectra as their measurements were not close enough to the wall. However, recent experiments by Vallikivi et al. (2015) do not show an overlap region and these authors infer that the k_x^{-1} region cannot be expected even at very high Reynolds numbers.

Chapter 3 looks at the basis for the k_x^{-1} range in flat plate turbulent boundary layers from a new perspective. Using Particle Image Velocimetry (PIV) and a simple model which can in principle be applied to various wall-bounded turbulent flows, it will be shown how in the turbulent boundary layer, a power-law spectral range exists but is not a Townsend-Perry k_x^{-1} range and how it can be accounted for by taking only streamwise lengths and intensities of wall-attached structures into account.

2.3 APG turbulent boundary layers

2.3.1 Equilibrium boundary layers

The challenge in attempting to study turbulent flows has been attributed to the complex, nonlinear or multiscale phenomenon of the flow. To reduce the complexity of the problem, Clauser (1954) introduced the idea of an "equilibrium turbulent layer". In general terms, an equilibrium layer is one in which non-dimensional parameters such as H, C_f etc., vary only slowly with distance from the origin. The self-preserving character of the outer regions of such layers then makes it possible to adopt plausible assumptions that would greatly simplify the analysis.

Clauser (1954) defined a non-dimensional pressure gradient parameter, $\beta = \delta^*(dP/dx)/\tau_w$. For equilibrium boundary layers, β would then be a constant and Clauser expected such equilibrium layers to be dynamically similar at all stations in both the mean and fluctuating velocity fields. Working on the ZPG which is a boundary layer in the equilibrium sense of Clauser, where $dP/dx = 0$ and consequently $\beta = 0$, he showed that the mean velocity defect (or deficit) law given by equation 2.22 made the turbulent velocity data to fall together in a very satisfactory way.

$$\frac{u - U}{U_\tau} = f\left(\frac{y}{\delta}\right) \tag{2.22}$$

He introduced a form parameter, G given in equation 2.23 to give a measure of the velocity defect defined by

$$G = \frac{\int_0^\infty \left(\frac{U-u}{U_\tau}\right)^2 dy}{\int_0^\infty \left(\frac{U-u}{U_\tau}\right) dy} \tag{2.23}$$

which is related to the shape factor, $H = \delta^*/\theta$ by equation 2.24

$$G = \frac{\frac{H-1}{H}}{\left(\frac{C_f}{2}\right)^{1/2}} \tag{2.24}$$

Now, if G is to remain constant with downstream distance, the pressure force acting on the boundary layer must remain in a constant ratio to the skin-friction force, i.e., the parameter β must remain constant. Clauser reasoned that a velocity defect law of the same form should apply to equilibrium layers in pressure gradients for non zero constant values of β however concluding that equilibrium flows are hard to maintain and that most flows are non-equilibrium flows.

Since Clauser (1954), there have been many studies that have extended his analysis and proposed new definitions for equilibrium turbulent boundary layers while improving certain forthcomings of his theory for equilibrium layers for flows near separation where U_τ approaches zero which consequently made β approach infinity.

Analysing Clauser's flow, Townsend (1961) developed a self-preserving flow such that the distribution of mean velocity was

$$U = U_e - u_0 f\left(\frac{y}{l_0}\right) \tag{2.25}$$

and the Reynolds stress was given by

$$\overline{uv} = u_0^2 g\left(\frac{y}{l_0}\right) \tag{2.26}$$

l_0 and u_0 were the length and velocity scales depending only on the downstream distance and the functions f and g were characteristics of the whole flow. According to Townsend, a turbulent flow is self-preserving if the motions at different sections of the flow differ only in scales of velocity and length. He then substituted these distributions in the usual boundary layer equation for the two-dimensional mean flow that gave an ordinary differential equation. He then concluded that the only possibility for this equation to be compatible with the scales of the equilibrium layer (l_0 and u_0) if

$$U_e \propto (x)^{-1}, l_0 \propto (x) \tag{2.27}$$

$$U_e \propto (x)^{-0.23}, l_0 \propto (x) \tag{2.28}$$

The first possibility shown in equation 2.27 is an accelerating flow in a converging wedge while the second shown in equation 2.28 is a zero stress flow in an adverse pressure gradient. Thus Townsend (1961) showed that self-similarity for equilibrium boundary layers in pressure gradients is obtained if the freestream velocity variation has the form of a power law in the downstream direction, $U_e \sim x^m$ ('m' is an exponent describing the distribution of the freestream velocity) and the length scale varies linearly with the downstream co-ordinate (refer equation 2.28).

Extending the work of Clauser (1954) and Townsend (1961), Mellor and Gibson (1966) hypothesized an effective or eddy viscosity function presumed to be independent of pressure gradient and valid for the entire boundary layer. Clauser (1954) discovered that in the outer 80% of the boundary layer, the

eddy viscosity, ν_e could be considered constant with respect to the coordinate perpendicular to the wall. Thus following Clauser (1954), in the outer layer he defined $\nu_e = RU\delta^*$ where R was an inverse of the Reynolds number that had to be determined empirically. For the overlap layer, Prandtl's mixing length theory was used to define the eddy viscosity, $\nu_e = \kappa^2 y^2 \left|\frac{\partial u}{\partial y}\right|$. This eddy viscosity function predicted the whole range of equilibrium boundary layers ($-0.5 \leq \beta \leq \infty$) and overcame Clauser's limiting case for layers with U_τ near 0 (i.e $\beta = \infty$).

Tennekes and Lumley (1972) assumed a high Reynolds number flow and analysed the momentum integral equation. This was done in order to linearize the equations in the velocity defect with which they proceeded to obtain a relation between the exponent 'm' and 'β' which read $m = -\frac{\beta}{1+3\beta}$ with $U \sim x^m$. Skote et al. (1998) argued that this linear analysis based on the assumption of asymptotically high Reynolds number was not applicable to finite Reynolds number flows and so they carried out a non-linear approach to obtain a useful relation between 'm' and 'β' such that $m = -\frac{\beta}{H(1+\beta)+2\beta}$ with $U \sim x^m$ and $\delta^* \sim x$. The pressure gradient parameter, β was found to be a constant when the freestream velocity varied according to this power law.

Head (1976) used an integral method to calculate the turbulent boundary layer development where $U \sim x^m$ for m = -0.15, -0.255 and -0.35. The results of this study showed that for the first case, a unique equilibrium profile developed while for the second case, multiple solutions existed as long as the momentum thickness at the initial reference location didn't exceed some critical value for both. No equilibrium condition was obtained in the third case.

Perry and Schofield (1973) and Schofield (1981) argued that U_τ and velocity scales based on the local pressure gradient are inappropriate for layers in moderate to strong adverse pressure gradients. Rather than using the wall shear stress they instead introduced a velocity scale U_m that related to the maximum shear stress in the layer $\left(U_m = \sqrt{\frac{\tau_m}{\rho}}\right)$. This velocity scale was favoured as it accurately described the half-power distributions of the

mean velocity profile that have been observed in moderate to strong adverse pressure gradient layers (Perry and Schofield (1973)). The validity of this analysis was however restricted to equilibrium layers under a moderate to strong adverse pressure gradient flow and in which the maximum value of the shear stress was at least 1.5 times larger than the wall shear stress.

Skåre and Krogstad (1994) reported experimental results for an equilibrium boundary layer in a strong pressure gradient. The equilibrium region extended for about 1.0 m where the skin friction coefficient was maintained at a constant level of about $C_f = 5.7 \times 10^{-4}$ and the mean velocity profiles were documented to be self-similar. It was also shown that in this region, the length scales grow linearly with distance in accordance with the equilibrium requirements and that the non-dimensional pressure gradient, β, as well as the Clauser parameter G were constant. Townsend (1961) pointed out that equilibrium in the mean velocity might only be obtained if the turbulent stresses also show similarity. In this study, similarity was obtained in all the turbulent stresses as well as in the triple correlations. Although the Reynolds stress distribution across the layer was entirely different from the ZPG flow, the ratios between the different turbulent stress components were found to be similar, showing that the mechanism for distributing the turbulent energy between the different components remain unaffected by the mean flow pressure gradient. Close to the surface, the gradient of the mixing length was found to increase by almost twice as high as for the ZPG case. The gradient of the mixing length was found to increase from $k_m \sim 0.41$ at the beginning of the logarithmic layer to $k_m \sim 0.78$ where the layer merges with the wake. This did not influence the mean velocity which followed the law of the wall closely with the conventional von Karman constant of $K = 0.41$. This agreed with the findings of Perry et al. (1966) that the pressure gradient only defined the region of applicability of the logarithmic profile for a flow, but did not distort it.

2.3.2 Scaling of the mean velocity

For the scaling of wall bounded turbulent flows, the velocity field is usually categorized into an inner region and an outer region where a suitable length and velocity scale may be defined. The near wall region is dominated by viscous forces and is scaled by a characteristic velocity known as the friction velocity U_τ. The friction velocity is defined as based on the wall shear stress. The outer region is usually scaled by the free stream velocity (U_e). Since viscosity plays an important role near the wall, the length scale is constructed using the kinematic viscosity ν and friction velocity (U_τ) leading to a length scale given by ν/U_τ. For the outer region the length scale is generally defined by the boundary layer thickness, δ.

However in the case of a boundary layer under an APG, U_τ is not the relevant scale. This is true especially for strong APGs and low Reynolds numbers and obviously for a separating boundary layer since U_τ reaches zero. In cases of a strong APG and separation, a velocity scale based on the pressure gradient can be defined as

$$u_p \equiv \left(\nu \frac{1}{\rho}\frac{dP}{dx}\right)^{1/3} \tag{2.29}$$

Using the inner length (ν/U_τ) and velocity scales U_τ, the total shear stress in the inner region can be written as

$$\tau^+ \equiv \frac{dU^+}{dy^+} - \overline{uv}^+ = 1 + \frac{\nu}{U_\tau^3}\frac{1}{\rho}\frac{dP}{dx}y^+ \tag{2.30}$$

From studies by Bradshaw (1967); Samuel and Joubert (1974); Skåre and Krogstad (1994); Spalart and Watmuff (1993) and Skote et al. (1998), it was observed that the pressure gradient term in equation 2.30 is important for the shear stress distribution in the inner part of the boundary layer. The pressure gradient term decreases with increasing Reynolds number and is thus important for low Reynolds number flows. However, close to separation where U_τ approaches zero, it is clear that the pressure gradient term becomes infinite even for large Reynolds numbers. Skote and Henningson (2002) used a velocity scale u_p to avoid the singularity mentioned above. The authors

developed an expression for the shear stress $\left(\tau^p \equiv \frac{\tau}{\rho u_p^2}\right)$ as a function of $y^p \equiv \frac{y u_p}{\nu}$

$$\tau^p = y^p + \left(\frac{U_\tau}{u_p}\right)^2 \tag{2.31}$$

where y_p is y scaled by u_p/ν. τ^p has an asymptotic form $\tau^p = y^p$ when separation is approached. Thus in this rescaled form, the singularity using the traditional scaling is avoided. In the viscous sublayer, the Reynolds shear stress approaches zero so equation 2.31 can be integrated to give

$$u^p = \frac{U}{u_p} = \frac{1}{2}(y^p)^2 + \left(\frac{U_\tau}{u_p}\right)^2 y^p \tag{2.32}$$

where u^p is the velocity scaled by u_p For the overlap region, neither U_τ nor u_p as a velocity scale results in a self-similar expression. However, equation 2.30 can be formulated as

$$\tau^* \equiv \frac{1}{U_*^2}\left(\nu\frac{\partial U}{\partial y} - \overline{uv}\right) = 1 \tag{2.33}$$

where u_* is a velocity scale that depends on y and can be expressed in either viscous or pressure gradient units,

$$u_*^2 = U_\tau^2 + \frac{u_p^3}{U_\tau} y^p = U_\tau^2 + u_p^2 y^p \tag{2.34}$$

Based on DNS data, Manhart et al. (2008) proposed a new extended inner scaling for the wall layer of wall-bounded flows under the influence of a streamwise pressure gradient. This scaling accounted for the effect of both, the wall shear stress and the streamwise pressure gradient, which plays an important role for separated flows. Non-dimensional velocity U^* and non-dimensional length y^* were defined by

$$U^* = \frac{U}{u_{\tau p}}, y^* = \frac{y u_{\tau p}}{\nu} \tag{2.35}$$

where $u_{\tau p} = \sqrt{U_\tau^2 + u_p^2}$ is a combined velocity using the classical friction velocity at the wall, U_τ and an additional velocity based on the streamwise

pressure gradient, u_p proposed by Simpson (1983). With this scaling, the velocity profile in the viscous region including the pressure gradient effects can be written in non-dimensional form as a function of only two non-dimensional parameters

$$U^* = f(y^*, \alpha) \tag{2.36}$$

where $\alpha = \frac{U_\tau^2}{u_{\tau_p}^2}$ is used to quantify the relative importance of each of the two velocity scales, i.e., $\alpha = 0$ would correspond to a zero shear stress flow (flow with a separation point) and $\alpha = 1$ would correspond to a zero pressure gradient flow.

Angele and Muhammad-Klingmann (2006) studied a weakly separating and reattaching turbulent boundary layer flow subjected to an APG using PIV. The authors then examined the applicability of various velocity scalings on the acquired data. They found that the mean velocity profiles in the outer layer of the boundary layer and to some extent the Reynolds shear-stress are self-similar when using both a velocity scale based on the pressure gradient, u_p originally suggested by Mellor and Gibson (1966) and the scaling suggested by Perry and Schofield (1973). They thus reported these two scaling to be closely comparable contrary to the findings of Alving and Fernholz (1996). The authors also interpreted the similarity of the Reynolds shear stress as experimental evidence supporting the claimed relation between the Perry-Schofield velocity scale and the Reynolds shear-stress.

An alternative scaling approach was developed by Castillo and George (2001) for the outer region and is based on their Asymptotic Invariance Principle (AIP). AIP means that "*in the limit as the Reynolds number dependence goes to infinity, the equations of motion become independent of Reynolds number; thus any function or scale must also be independent of Reynolds number*". They started their study with the turbulent boundary layer equations given by Townsend (1961) for high Reynolds number and pressure gradient. The authors applied a similarity type solution, which showed that the outer equations permitted full similarity. The appropriate length scale was chosen as δ, and the appropriate velocity scale was deter-

mined by requiring that the differential equation should be independent of the downstream direction. It was concluded that U_e is the appropriate velocity scale (for a flow with fixed upstream conditions) if $\delta \propto U_e^{-\frac{1}{\Lambda}}$ is a constant where $\Lambda = -\frac{\delta}{\rho U_e^2 d\delta/dx}\frac{dP_\infty}{dx}$. Upon reviewing experimental data, they claimed that Λ only can have three different values, one for the case of a favorable pressure gradient (FPG), one for APG and one for ZPG, the constant however, depending on the upstream initial conditions.

Zagarola and Smits (1998a) determined an empirical scaling parameter, $U_e\frac{\delta^*}{\delta}$ for the velocity profile in the outer region of a developing pipe or channel flow. Extending their study to turbulent boundary layers, Zagarola and Smits (1998b) showed that the velocity profiles successfully collapse to one for a ZPG turbulent boundary layer with this scaling. Castillo (2000) showed that when the mean velocity deficit profiles are normalized by the Zagarola and Smits (1998b) scaling parameter in APG flows, the profiles collapse to a single curve.

Using PIV, Maciel et al. (2006) studied a very strong APG turbulent boundary layer leading to separation, transitioning from strong favourable pressure gradient to strong APG. They showed that the scaling of Zagarola and Smits (1998a) $(U_e\frac{\delta^*}{\delta})^2$ scales all the Reynolds stresses in the outer region of the flows, while U_e and U_τ were not appropriate outer scales for the Reynolds stresses. They also reviewed APG data from several experiments and they reported that the Zagarola and Smits (1998a) scaling works well.

Indinger and el Hak (2006) analysed the inner and outer scaling of mean velocity profiles and Reynolds shear stress profiles for turbulent boundary layers approaching separation. They found out that the outer scaling proposed by Zagarola and Smits (1998a) is the most suitable for the mean velocity profile, even for strong APGs. The shear stress scaling proposed by Castillo and George (2001) showed a reasonably good collapse of the data in the outer region. However very close to separation it failed due to the effect of backflow. Lögdberg et al. (2008) focussed on the mean velocity distribution of turbulent boundary layers near, at and after separation. They found that the mean velocity defect profiles are self-similar in the regions between separation and the position of maximum reverse flow. They also found out

that the Zagarola-Smits velocity scaling for mean velocity defect profiles is useful not only for the region near separation but also for cases of different adverse pressure gradients.

With regards to these results, since the Zagarola-Smits scaling can be used in all flow conditions of turbulent wall flows, it appears to be more universal. In the present work, we also apply the Zagarola-Smits scaling on the acquired data from PIV (Chapter 4) and compare it to the Castillo-George scaling.

2.3.3 Turbulent structures in APG flows

The understanding of canonical turbulent wall bounded flows has steadily improved over the past several decades. However, information about coherent structures in APG turbulent boundary layers are lacking in literature as expressed recently in Lee and Sung (2008); Rahgozar and Maciel (2011) and Harun et al. (2013). The studies conducted have generally focussed on the statistical properties of these flows; an overview of which is presented below.

Krogstad and Skåre (1995) examined the turbulence satistics and structure of an APG equilibrium boundary layer. The equilibrium region extended for about 1m with the non-dimensional pressure gradient parameter held constant at $\beta \simeq 20$. They showed that the APG significantly affects the time scales of the turbulent events, and also alters the contributions to $-\overline{uv}$ from the various quadrants. In contrast to the ZPG boundary layer, strong contributions from the first and fourth quadrant develop in the region between the outer production peak and the wall. Events in these quadrants were shown to be characterized by in-rushing turbulent fluid which is reflected back from the wall. Hence, when an adverse pressure gradient is present, they concluded that the turbulent flow in the outer layer may interact more efficiently with the inner flow than is normally the case for the ZPG layer. Following this, Krogstad and Kaspersen (2002) studied the effect of a strong adverse pressure gradient on the turbulent structure in an equilibrium boundary layer using two-point correlations. They observed that the APG correlations are higher and shorter than those of the ZPG boundary layer. This was in agreement with the reduced vortex stretching expected by the strong negative dU/dx

term in the APG flow. The two-point streamwise velocity correlations from APG were found to be inclined at a considerably higher angle with respect to the wall in the inner region than ZPG. A wavelet analysis of the correlation data showed that differences in the inclination angle existed at all length scales larger than the boundary layer thickness. They observed two maxima in the main production term; one close to the surface and a second which moved towards the middle of the layer with increasing pressure gradient. This outer peak significantly affected the turbulence field. They concluded that when APG is present, the turbulent flow in the outer layer might interact more efficiently with the inner flow than is normally the case for the zero pressure gradient layers.

Laval et al. (2012) performed a direct numerical simulation (DNS) of a converging-diverging turbulent channel flow at a Reynolds number $Re_\tau \approx 617$ based on the inlet. They found regions of strong kinetic energy production at both the upper and lower walls, just after the beginning of the APG region. While performing a stability analysis of these streaks and by looking at the velocity field, conditioned by the streaks they were able to explain that the peak of turbulent kinetic energy was a result of the enhancement of instability of streaks in the APG region. Shah et al. (2011) suggested that the outer peak found in the streamwise Reynolds stress was triggered by the APG and had its origin in an instability in the turbulent boundary layer which developed soon after the pressure gradient changed its sign. This may explain the reason for not being able to find a universal scaling for APG turbulent boundary layers. George et al. (2012) said that the position of the outer peak in the streamwise Reynolds stress depended on the initial conditions and the manner in which the APG is imposed. They also found out that far enough downstream, an inflection point of the mean velocity profile occurs very close to the observed peak in streamwise Reynolds stress.

Lee and Sung (2008) found out that the coherent structures in the outer layer in APG turbulent boundary layers are more activated than those in ZPG turbulent boundary layer. This might be due to the higher turbulence intensities in APG flows and which leads to the development of a second peak in the turbulent energy. The pressure gradient which intensifies the low

speed streaky structures are present in the outer regions of APG flows and can be related to the outer maximum observed in the turbulent kinetic energy. Lee et al. (2010) while investigating the response of coherent structures in the turbulent boundary layer subjected to APG found that the strength of the low-speed streaks decreased and the spanwise spacing between two adjacent streaks became irregular and increased four times larger than that of a ZPG flow. Also, dominance of low momentum regions in the buffer and inner log layers were found and the enhancement of the turbulent kinetic energy in the outer layer was attributed to the presence of large scale outer layer hairpin vortices. Monty et al. (2011) performed a parametric study on the effects of increasing APG in many cases with constant conditions of matching Reynolds number and viscous scaled sensor length. Studying the energy content of the flow, they found that the large scale events in the log region are strongly increased by the APG which contributes to the increasing streamwise turbulent profile across the boundary layer.

CHAPTER 3

Low and high momentum regions in a zero pressure gradient turbulent boundary layer

The current chapter looks at the basis and requirement for the k_x^{-1} spectral range in a turbulent boundary layer. To this end, a modified but rather simple model, which can in principle be applied to various wall-bounded turbulent flows is proposed from a new perspective based on the work of Townsend-Perry. This proposed model is then validated using experimental results obtained from Particle Image Velocimetry (PIV) data with a large field of view and good spatial resolution

3.1 A model for the spectral signature of the attached eddies

As already mentioned in section 2.2.2, Perry and Abell (1977) and Perry et al. (1986) showed how Townsend's attached eddy hypothesis implies $E_{11}(k_x) \sim U_\tau^2 k_x^{-1}$ in the range $1/\delta \ll k_x \ll 1/y$. Perry et al. (1986) also developed a flow structure model for this spectral range in terms of specific attached eddies of varying sizes randomly distributed in space and with a number density that is inversely proportional to size. Here we attempt to distill such a type of model to its bare essentials. In this section we show that it is sufficient to consider simple on-off representations of elongated streaky structures of varying sizes as long as their number density remains inversely proportional

to size.

We assume that the attached eddies responsible for the k_x^{-1} spectral range have a long streaky structure footprint on the 1D streamwise fluctuating velocity signals at a distance 'y' from the wall. We also assume that these streaky structures can be modeled as simple on-off functions and that it is sufficient to represent the streamwise velocity fluctuations $u(x)$ at a given height y from the wall as follows

$$u(x) = \sum_{nm} a_{nm} \Pi(\xi) \tag{3.1}$$

where $\Pi(\xi) = 1$ if $-1 < \xi < 1$ with $\xi = \frac{x - x_{nm}}{\lambda_n}$ and $\Pi(\xi) = 0$ otherwise. The on-off function $\Pi(\xi)$ is our cartoon model of a streaky structure. Streaky structures of length λ_n are present at random positions x_{nm} and their intensity is given by the coefficients a_{nm}. For each subscript n, the subscript m counts the spatial positions where cartoon structures of size λ_n can be found. The sum in (3.1) is over all structures lengths λ_n and all their positions x_{nm}.

The energy spectrum of $u(x)$ will be the average of the square of the Fourier transform of this model, given by equation 3.2

$$E_{11}(k_x) = \frac{(2\pi)^2}{L_x} \overline{|\hat{u}(k_x)|^2} \tag{3.2}$$

where L_x is the length of the record, $\hat{u}(k_x)$ is the Fourier transform of $u(x)$, and the overbar signifies an average over realisations. The Fourier transform of $\Pi(\frac{x - x_{nm}}{\lambda_n})$ being

$$\hat{\Pi}(k_x, \lambda_n, x_{nm}) = 2ik_x^{-1} e^{ik_x x_{nm}} \sin(k_x \lambda_n) \tag{3.3}$$

it follows that,

$$\hat{u}(k_x) = 2ik_x^{-1} \sum_{nm} a_{nm} e^{ik_x x_{nm}} \sin(k_x \lambda_n) \tag{3.4}$$

which implies that the energy spectrum is given by

$$E_{11}(k_x) = 4\frac{(2\pi)^2}{L_x}k_x^{-2}\overline{\sum_{nm} a_{nm}e^{ik_x x_{nm}}\sin(k_x\lambda_n)\sum_{pq} a_{pq}e^{-ik_x x_{pq}}\sin(k_x\lambda_p)}. \tag{3.5}$$

We introduce two assumptions which were also used by Perry et al. (1986) in their more intricate model. The first assumption is that the positions and amplitudes of our cartoon stuctures are uncorrelated and that different positions are not correlated to each other either, i.e. $\overline{e^{ik_x x_{nm}}e^{ik_x x_{pq}}} = \delta_{pn}\delta_{qm}$. As a result, the expression for the energy spectrum simplifies as follows:

$$E_{11}(k_x) = 4\frac{(2\pi)^2}{L_x}k_x^{-2}\sum_{nm}\overline{(a_{nm})^2}\sin^2(k_x\lambda_n). \tag{3.6}$$

Let us say that there is a number N_n of spatial positions where cartoon stuctures of size λ_n can be found. The expression for $E_{11}(k_x)$ simplifies even further:

$$E_{11}(k_x) = 4\frac{(2\pi)^2}{L_x}k_x^{-2}\sum_{n}\overline{a_n^2}N_n\sin^2(k_x\lambda_n) \tag{3.7}$$

where $\overline{a_n^2} \equiv \overline{(a_{nm})^2}$ is the same irrespective of position x_{nm}.

We now consider a continuum of different structure sizes λ rather than discrete length-scales λ_n and the previous expression for $E_{11}(k_x)$ must therefore be replaced by

$$E_{11}(k_x) = 4\frac{(2\pi)^2}{L_x}k_x^{-2}\int d\lambda\overline{a^2}(\lambda)N(\lambda)\sin^2(k_x\lambda) \tag{3.8}$$

in terms of easily understandable notation. At this point, we introduce a generalised form of the second assumption which was also used by Perry et al. (1986): we assume a power-law form for $N(\lambda)$ in the range $\lambda_i < \lambda < \lambda_o$ where $\lambda_i \sim y$ and $\lambda_o \sim \delta$, and $N(\lambda) = 0$ outside this range for simplicity. This power law form is

$$N(\lambda) = (-N_M + N_o(\lambda/\delta)^{-1-D})/\delta \tag{3.9}$$

where N_M and N_o are positive dimensionless numbers which increase

proportionally to L_x so as to keep number densities constant. The number N_M is introduced to allow for the possibility of an upper bound on streaky structure size given by $N(\lambda_o) = 0$, i.e. $N_M = N_o(\lambda_o/\delta)^{-1-D}$ which should be small given that LSM and VLSM streaky structures have been observed with lengths greater than δ (Smits et al. (2011)).

Vassilicos and Hunt (1991) proved that, if $0 \leq D \leq 1$, then the set of points defining the edges of the on-off functions $\Pi(\xi)$ is fractal and D is effectively the fractal dimension of this set of points. The case where this fractal dimension is $D = 1$ is the case where these points are space-filling. The population density assumption of Perry et al. (1986) corresponds to $D = 1$ which is also the choice we make in this work. We now show that this choice can lead to $E_{11}(k_x) \sim k_x^{-1}$ in the range $1/\lambda_o \ll k_x \ll 1/\lambda_i$.

We calculate the energy spectrum by carrying out the integral in (3.8). This requires a model for $\overline{a^2}(\lambda)$ which, in this section, we chose to be $\overline{a^2}(\lambda) = A^2/\delta$ for $\lambda_i < \lambda < \lambda_o$ where A^2 is a constant. Using our models for $N(\lambda)$ and $\overline{a^2}(\lambda)$ and the change of variables $\lambda k_x = l$, (3.8) becomes

$$E_{11}(k_x) = A^2\delta(C_o(k_x\delta)^{-2+D} - C_m(k_x\delta)^{-2}) \tag{3.10}$$

where

$$C_o = 4(2\pi)^2\frac{N_o}{L_x}\int_{\lambda_i k_x}^{\lambda_o k_x} dl\,\sin^2(l)l^{-1-D}$$

and

$$C_M = 4(2\pi)^2\frac{N_M}{L_x}(k_x\delta)^{-1}\int_{\lambda_i k_x}^{\lambda_o k_x} dl\,\sin^2(l)$$

which is bounded from above by $\frac{N_M}{L_x}\frac{\lambda_o-\lambda_i}{\delta}$.

In the attached eddy range $1/\lambda_o \ll k_x \ll 1/\lambda_i$,

$$C_o \approx 4(2\pi)^2\frac{N_o}{L_x}\int_0^{\infty} dl\,\sin^2(l)l^{-1-D} \tag{3.11}$$

which means that C_o is approximately independent of k_x in this range.

Substituting the value $D = 1$ in equation (3.10), we get

$$E_{11}(k_x) = A^2(C_o k_x^{-1} - C_M\delta^{-1}k_x^{-2}) \tag{3.12}$$

which is well approximated by

$$E_{11}(k_x) \approx C_o A^2 k_x^{-1} \tag{3.13}$$

for wavenumbers $k_x\delta \gg C_M/C_o$ (i.e. $C_o k_x^{-1} \gg C_m \delta^{-1} k_x^{-2}$).

Note that C_M/C_o is much smaller than 1 because N_M is much smaller than N_o and that equation (3.13) is valid in the range $1/\lambda_o \ll k_x \ll 1/\lambda_i$ where λ_o scales with but is much larger than δ. For a good correspondence with the scalings of the Townsend-Perry attached eddy model one needs to take $\lambda_i \sim y$ and $A^2 \sim U_\tau^2$.

A straightforward generalisation

It is worth generalising the previous section's model by assuming that $\overline{a^2}(\lambda)$ is not constant but varies with λ in the range $\lambda_i < \lambda < \lambda_o$, for example as $\overline{a^2}(\lambda) = (A^2/\delta)(\lambda/\delta)^p$ where p is a real number with bounds which we determine below. The arguments of the previous section can be reproduced till equation (3.8) which now becomes

$$E_{11}(k_x) \;=\; A^2\delta[c_o(k_x\delta)^{-2+D-p} - c_m(k_x\delta)^{-2}] \tag{3.14}$$

where

$$c_o = 4(2\pi)^2 \frac{N_o}{L_x} \int_{\lambda_i k_x}^{\lambda_o k_x} dl \sin^2(l) l^{-1-D+p}$$

and

$$c_M = 4(2\pi)^2 \frac{N_M}{L_x} (k_x\delta)^{-1-p} \int_{\lambda_i k_x}^{\lambda_o k_x} dl\, l^{+p} \sin^2(l)$$

which is bounded from above by $\frac{N_m}{(1+p)L_x}[(\frac{\lambda_o}{\delta})^{1+p} - (\frac{\lambda_i}{\delta})^{1+p}]$.

In the attached eddy range $1/\lambda_o \ll k_x \ll 1/\lambda_i$,

$$c_o \approx 4(2\pi)^2 \frac{N_o}{L_x} \int_0^{\infty} dl \sin^2(l) l^{-1-D+p} \tag{3.15}$$

which means that c_o is approximately independent of k_x in this range if $0 < D - p < 2$.

Substituting the value $D = 1$ in equation (3.14), we obtain the following

leading order approximation in the parameter range $-1 < p < 1$:

$$E_{11}(k_x) \approx c_0 A^2 \delta (k_x \delta)^q \tag{3.16}$$

where

$$p + q = -1 \tag{3.17}$$

for wavenumbers $k_x\delta \gg (c_M/c_o)^{\frac{1}{1-p}}$. Note that c_M/c_o is much smaller than 1 if p is not too close to 1 because N_M is much smaller than N_o.

The spectral shape (3.16) is potentially significantly different from what the classical Townsend-Perry attached eddy model predicts. We emphasize that in this and the previous sections we have developed a simple model based on on-off functions representing long streaky structures which returns a wavenumber dependency of $E_{11}(k_x)$ which is either identical to the Townsend-Perry spectral shape if $p = 0$, or different but in some ways comparable if $p \neq 0$. In the remainder of this chapter we present experimental evidence in support of $D = 1$ and equations (3.16)-(3.17) rather than (3.13)

3.2 Experimental validation of the model

In the previous section, we developed a model for attached flow structures in a turbulent boundary layer. To test its behaviour at a fairly high Reynolds number, we had the possibility to set up experiments at the boundary layer wind tunnel facility at LML (Laboratoire de Mécanique de Lille). The facility and the experiment that was set-up will be presented in the following section.

3.2.1 Description of the experiment

3.2.1.1 The LML wind tunnel facility

The front view and top view of the LML boundary layer wind tunnel is pictured in figure 3.1. The wind tunnel is powered by a fan and driven by a 37kW electric motor that allows the free-stream velocity at the entrance of

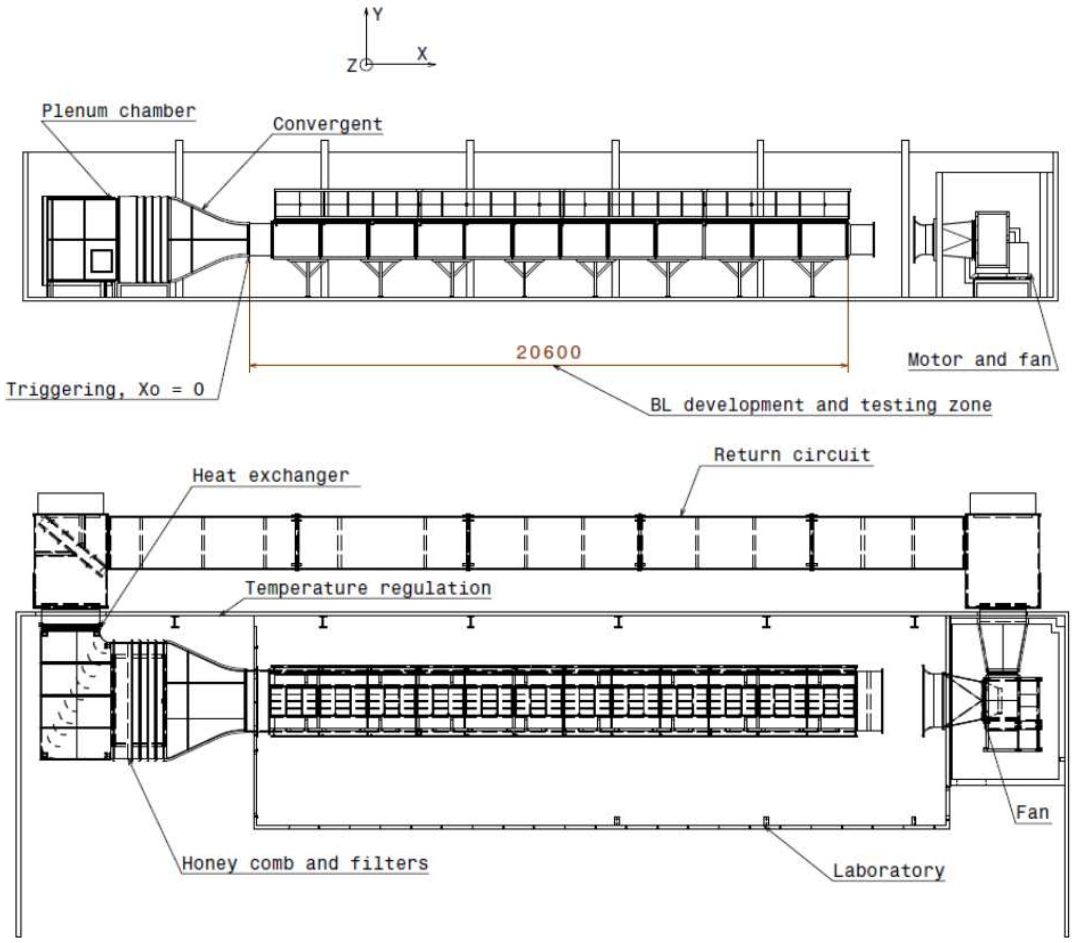

Figure 3.1: Schematic of the LML boundary layer wind tunnel

the test section to be varied continuously from 3 m/s up to 10 m/s with a stability better than 0.5%. The level of turbulence is less than 0.3% and the temperature is regulated within $0.15°C$ with the help of a heat exchanger located in the plenum chamber.

The test section is 20.6 m long in the streamwise direction (X direction) and has a constant cross-section, 2 m wide (Z direction) and 1m high (Y direction). The test section is fully transparent and this provides easy access to optical measurements and allows for excellent model viewing. The boundary layer is tripped at the wind tunnel entrance on both the top and bottom

walls to fix the boundary layer transition. It is tripped at the bottom wall using a cylinder rod, 4 mm in diameter followed by a 93 mm wide grit size 40 sandpaper while the upper wall was tripped only using sandpaper of the same grit classification as the bottom wall.

The very long test section allows the Reynolds number based on the momentum thickness to reach up to $Re_\theta = 20600$ with a boundary layer thickness of about 0.24m at 19.6m from the trip (refer Carlier and Stanislas (2005) for more details), allowing detailed near wall measurements. In the present studies, the wind tunnel was used in a closed loop configuration.

3.2.1.2 PIV set-up

At LML, the possibility of conducting stereo PIV experiments exists, thereby gaining access to all the three components of the velocity. However, to test our model in section 3.1 , it is of interest to have a large field of view through which we aim to capture the long structures in the boundary layer along the direction of flow. Thus it would suffice to have a standard (Two-dimensional two-component) 2D2C PIV set-up with cameras arranged in series overlooking a large field of view; the experiment of which is described below:

The tests on the flat plate boundary layer were conducted at two free stream velocities of 3 m/s and 10 m/s corresponding to Reynolds numbers $Re_\theta = 8100$ and $Re_\theta = 20600$ respectively. To capture the large streamwise wall-normal field, four 12bits Hamamatsu cameras having a resolution of 2048x2048 pixels were installed in series to observe a region between 19.26 m and 20.42 m from the inlet which is 1.16 m long ($\approx 3.36\delta$ and $\approx 3.85\delta$ for $Re_\theta = 8100$ and $Re_\theta = 20600$ respectively) and 0.3 m high ($\approx 0.86\delta$ and $\approx 1\delta$ for $Re_\theta = 8100$ and $Re_\theta = 20600$ respectively). Nikon lenses of 50 mm focal length were set on the cameras and the magnification obtained was M = 0.05. The aperture was set at $f_\# = 5.6$, which allowed a particle image diameter slightly larger than one pixel. The Software HIRIS was used to acquire the images of the four cameras simultaneously. The flow was seeded with $1\mu m$ Polyethylene glycol and illuminated by a double-pulsed NdYAG laser at 400 mJ/pulse. A set of mirrors and lenses allowed generating a light

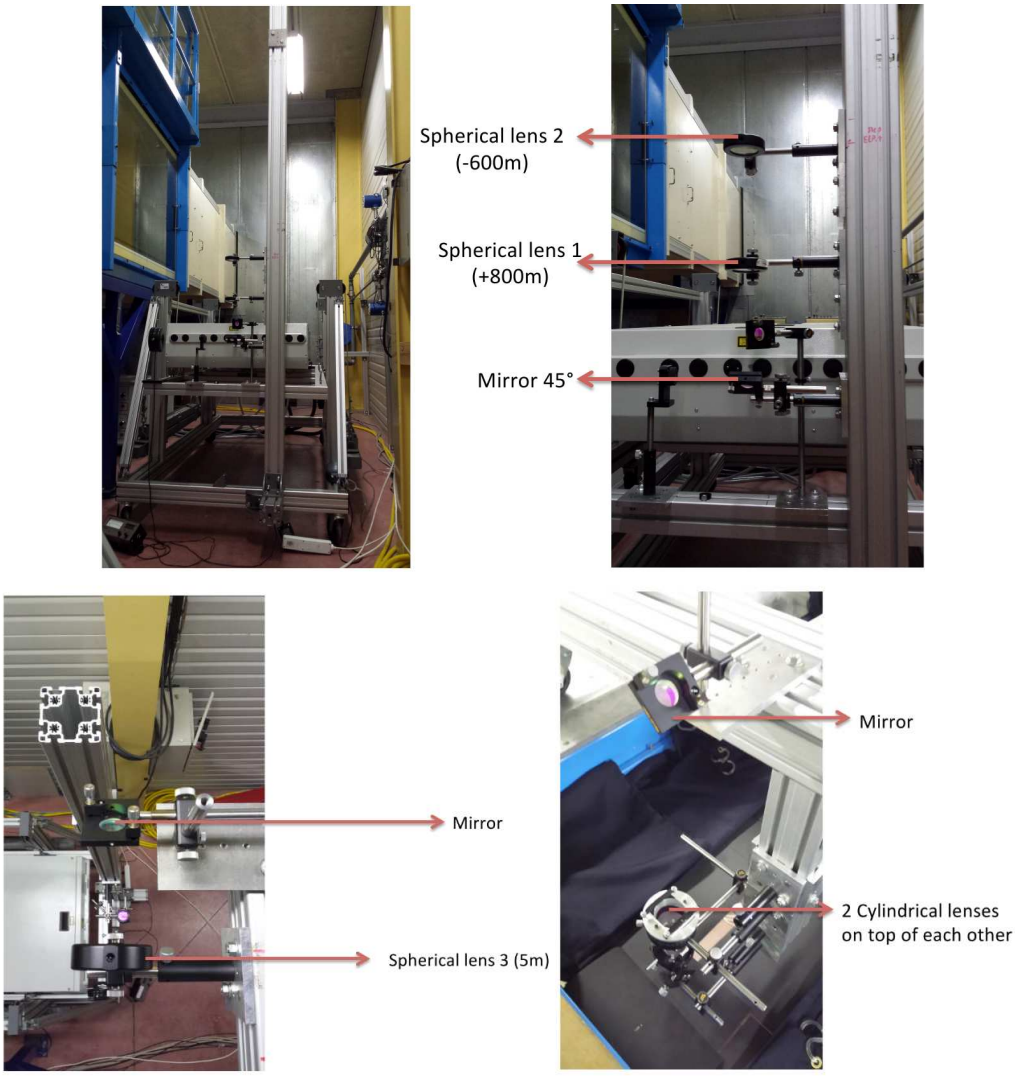

Figure 3.2: Set-up of the optics for the PIV experiment

sheet approximately 1mm in thickness in the full field.

Figure 3.2 shows the optical set-up of the PIV experiment. A mirror inclined at 45° was used to direct the beam from the laser output perpendicularly upwards through a telescope with a converging spherical lens of 800 mm focal length and 200 mm after which a diverging spherical lens of 600 mm focal length was placed to obtain a parallel laser beam of 6 mm in diam-

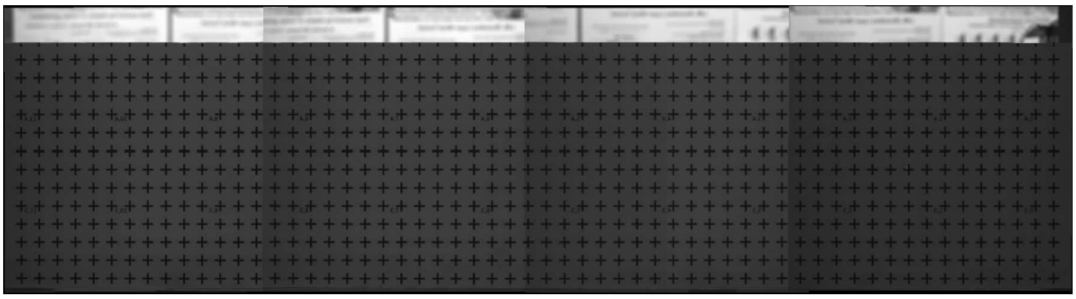

Figure 3.3: Picture of the calibration target reconstructed from the four camera images.

eter. A mirror at the top then directed the beam through another spherical lens of 5 m focal length and two cylindrical lenses of 40 mm focal length were used to generate a light sheet approximately 1 mm in thickness and 650 mm wide at the beginning of the field of view.

The calibration needed to obtain the magnification for each camera and the merging regions was obtained by placing a wall normal plate with crosses covering the entire field of view desired. The images obtained of this target by the four cameras was then processed with a home-made software to obtain the coefficients of a pinhole model for each camera. Then the four camera target pictures are merged into one (see figure 3.3) for checking the calibration parameters. The magnification of each camera together with the coordinates of the four extreme points of the fields of view of each camera are also given by the software with the help of the pinhole models obtained. The meshing program then used the entire picture of the target and these output parameters.

Several sources of uncertainty are present in a 2D2C PIV set-up (Adrian (1991); Richard and Adrian (1992); Raffel et al. (2007); Foucaut et al. (2004b), etc.). The main sources are the out of plane motion of particles, the non-uniform displacement of the particles in the interrogation windows (i.e. due to velocity gradient), the non-uniform particles concentration and the particles displacement too large compared to the interrogation window size.

To obtain good PIV measurements, Richard and Adrian (1992) and Fou-

caut et al. (2004b) have given the following recommendations: the particle image diameter has to be around 2 pixels, the particles concentration has to be about 0.04 particles per pixel (to obtain a minimum of 10 particles per interrogation window), the maximum difference in particle displacement in the interrogation windows has to be less than half the particle's image diameter and the out of plane displacement has to be less than 20% of the laser sheet thickness.

The estimation of PIV accuracy is a complex topic. Kostas et al. (2005) and Herpin et al. (2008) estimated the accuracy with the merging regions of the PIV field, i.e., the PIV uncertainty can be obtained from the same velocity overlooking a common region by two independent PIV systems. In the merging region, the random PIV uncertainty with a 95% confidence index is estimated by $\sigma_u = \pm(u_{syst1} - u_{syst2})_{RMS}$ for the streamwise component (u) and by $\sigma_v = \pm(v_{syst1} - v_{syst2})_{RMS}$ for the wall-normal component (v), where RMS refers to the root mean square value.

With respect to the mean velocity components, as the random error goes to zero by definition by taking enough samples, only the bias error affects the accuracy. The PIV uncertainty on the mean streamwise velocity U is then estimated by $\Delta U = \pm(\overline{u_{syst1} - u_{syst2}})$ and on the wall-normal velocity component by $\Delta V = \pm(\overline{v_{syst1} - v_{syst2}})$.

The uncertainties on the mean streamwise velocity and streamwise turbulence intensities are plotted as a percentage of the freestream velocity, $U_\infty = 10$ m/s in figures 3.4 and 3.5, respectively. The position of the merging regions between the respective cameras in the field of view is shown. Globally, the uncertainty is quite good at 1% or lower. Similar estimates for the uncertainty at $U_\infty = 3$m/s was obtained and is not shown here.

It is important to ensure that a good connection of the respective velocity fields is made between cameras. As we will see later on, a threshold on the turbulence intensities will be applied and if two cameras report different intensity levels, having a single threshold would distort the detected structures, if present, between these two cameras. Plotting the turbulence intensity field merging the cameras could give us a clear picture to gauge the connection in this region. This is presented in figure 3.6 where the streamwise turbulence

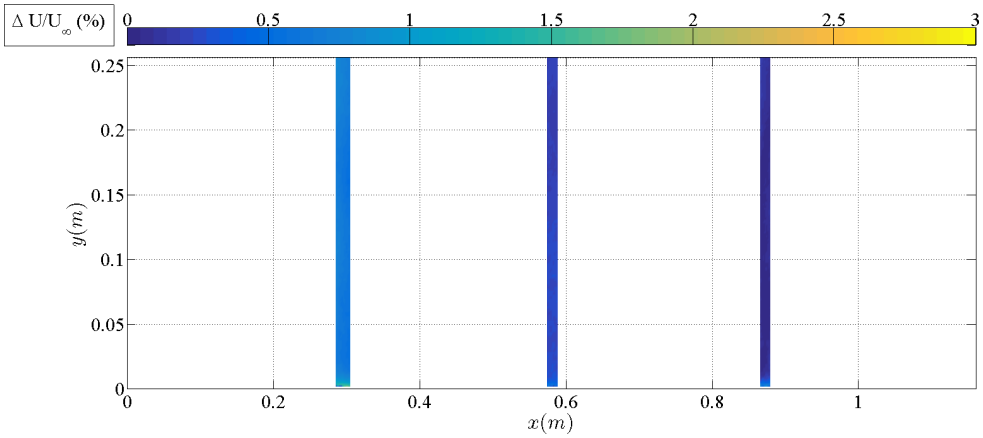

Figure 3.4: PIV uncertainty on the streamwise velocity component, U at $U_\infty = 10$ m/s

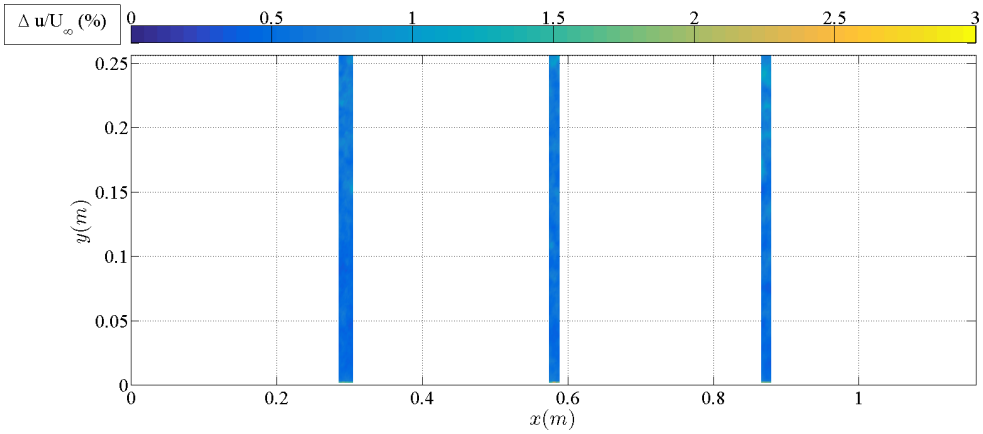

Figure 3.5: PIV uncertainty on the turbulence intensity u' at $U_\infty = 10$ m/s

intensity field is fairly uniform in the field of view thus conforming a good quality of data acquired.

The LML database for the current study is validated through an analysis of some of the single point statistics such as the mean flow, the turbulence intensity and the energy spectra of streamwise fluctuating velocity. For each flow configuration, these quantities were obtained through an ensemble average over the number of records acquired, and also through an average along

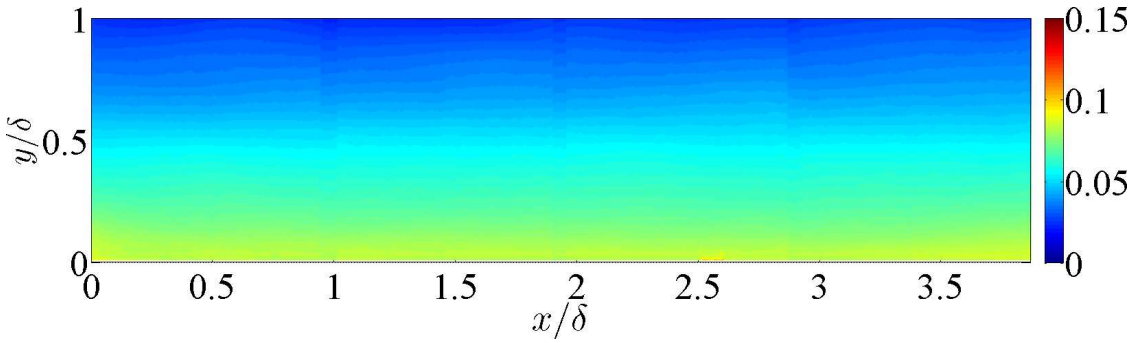

Figure 3.6: Streamwise turbulence intensity field (u'/U_∞) for $Re_\theta = 20600$ where $U_\infty = 10$ m/s.

the quasi-homogeneous directions of the measurement planes (the streamwise direction for the XY plane). Note that the homogeneity assumption along the streamwise direction can be assumed as the flow is fairly constant over the field of interest of this experiment (refer figure 3.6).

Figure 3.7 shows profiles of the mean streamwise velocity U and the streamwise turbulence intensity u' obtained from PIV at $Re_\theta = 8100$ and $Re_\theta = 20600$ and compared with the hot-wire anemometry results of Carlier and Stanislas (2005). The mean velocity profiles are in good agreement with the hot-wire data and are well resolved from $y^+ = 30$ and $y^+ = 90$ upwards for $Re_\theta = 8100$ and 20600 respectively. Comparisons of the profiles of u'^+ (u' scaled with inner variables) show a fairly good match with the hot-wire data. A plateau of u'^+ is present in the range $100 < y^+ < 300$ for the higher Reynolds number case. Close to the wall, the u'^+ values obtained from our PIV are slightly underestimated, in particular for $Re_\theta = 20600$, demonstrating some filtering of the PIV at this resolution (Foucaut et al. (2004a)). To compute from PIV the energy spectra used in this paper, we used the method of Foucaut et al. (2004a). As seen in figure 3.8 for the particular case of wall distance $y^+ = 200$ at $Re_\theta = 20600$, the agreement between the spatial spectrum from the PIV and the temporal spectrum from the hot-wire anemometry of Carlier and Stanislas (2005) is good up to wavenumbers $k_x \approx 500$ corresponding to length-scales of 2 mm.

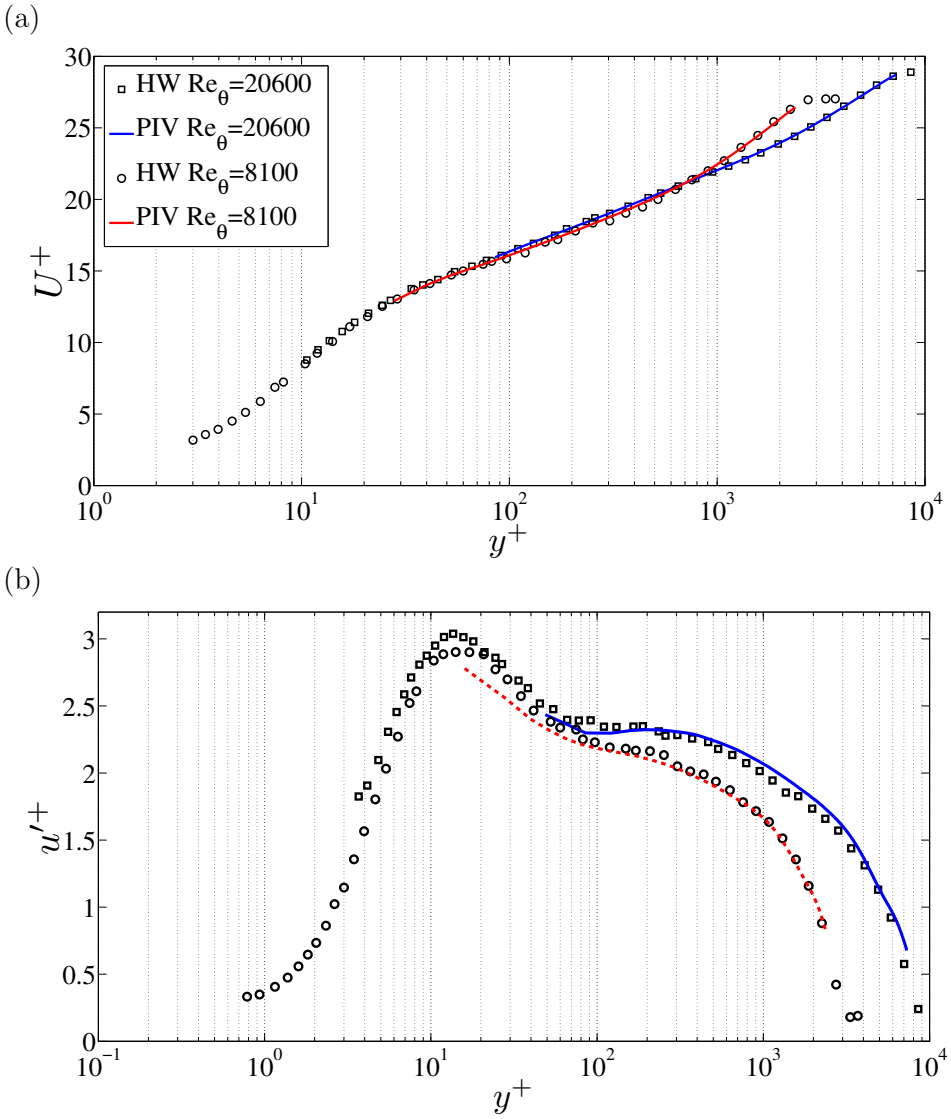

Figure 3.7: (a) Mean and (b) rms streamwise fluctuating velocity profiles at $Re_\theta = 8100$ ($U_\infty = 3$ m/s) and $Re_\theta = 20600$ ($U_\infty = 10$ m/s) obtained with PIV and compared with the hot wire anemometry results of Carlier and Stanislas (2005).

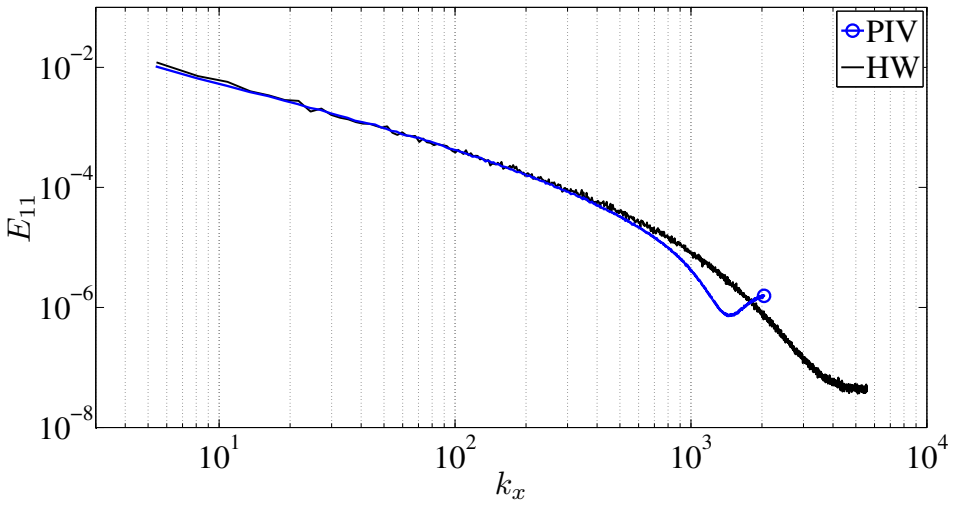

Figure 3.8: Comparison of the streamwise energy spectra obtained from PIV and hot-wire anemometry at $y^+ = 200$ for $Re_\theta = 20600$. The hot-wire anemometry was made by Carlier and Stanislas (2005) at 19.6m from the test section entrance of the same wind tunnel.

3.2.2 Results and discussion

3.2.2.1 Two-point spatial correlation

While instantaneous flow fields may give some insights about the presence and formation of various flow structures, quantitative information about the average shape and size of these structures may be obtained from the two-point spatial correlation function introduced by Stanislas et al. (1999) without invoking Taylor's frozen turbulence hypothesis (Taylor (1938)). The two-point correlation coefficient, R_{uu} is given by:

$$R_{uu} = \frac{u(x_0, y_0).u(x_0 + \Delta x, y_0 + \Delta y)}{\sqrt{(u^2(x_0, y_0))}.\sqrt{(u^2(x_0 + \Delta x, y_0 + \Delta y))}} \tag{3.18}$$

where x_0 and y_0 are the positions of the fixed points in space, Δx and Δy are the distances between the moving point and the fixed point and u is the streamwise turbulent velocity fluctuation.

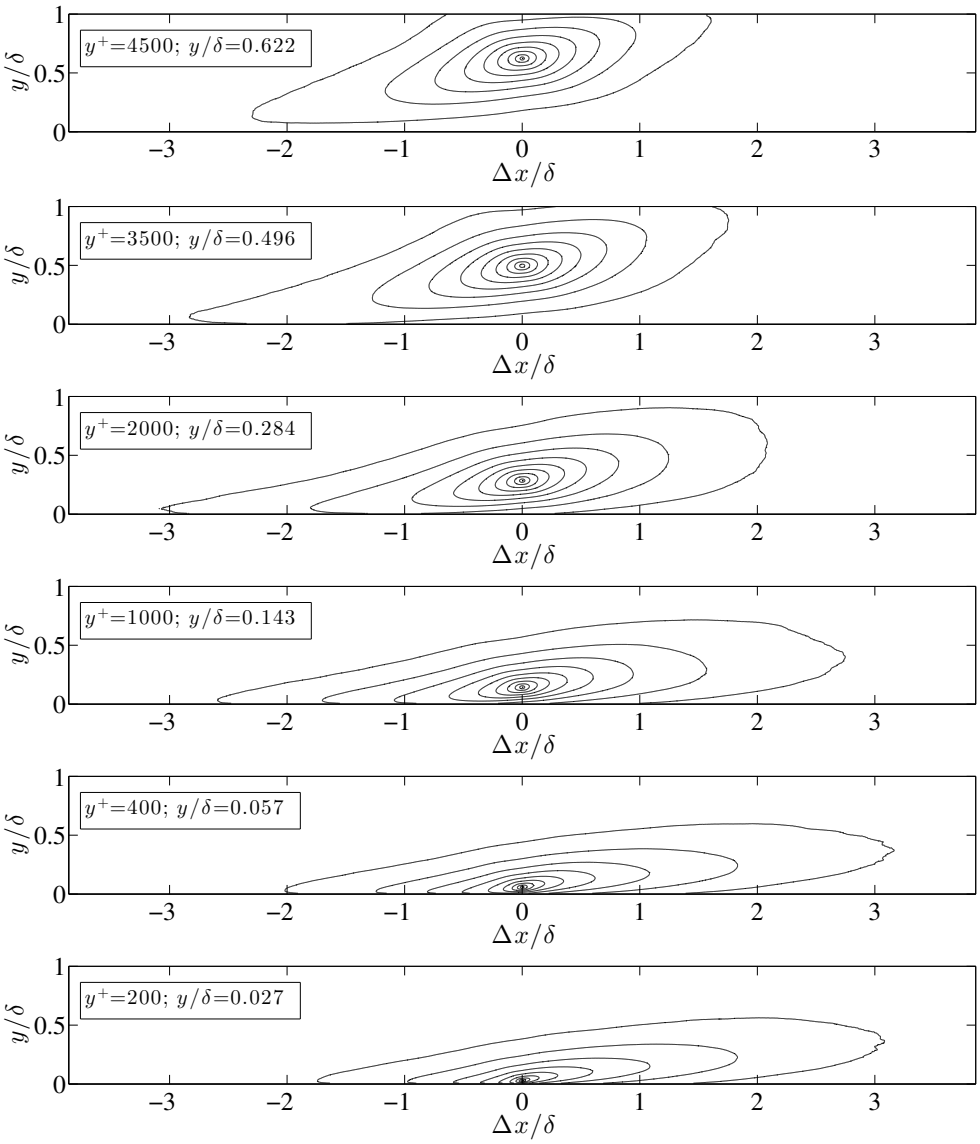

Figure 3.9: Two-point spatial correlation function of the streamwise velocity fluctuations with varying wall distance at $Re_\theta = 20600$. The contours range from 0.1 to 1 with an increment of 0.1.

Figures 3.9 and 3.10 show the correlation map of the streamwise velocity fluctuations at various wall distances in the streamwise-wall-normal plane at $Re_\theta = 20100$ and $Re_\theta = 8100$ respectively. The correlation iso-contours

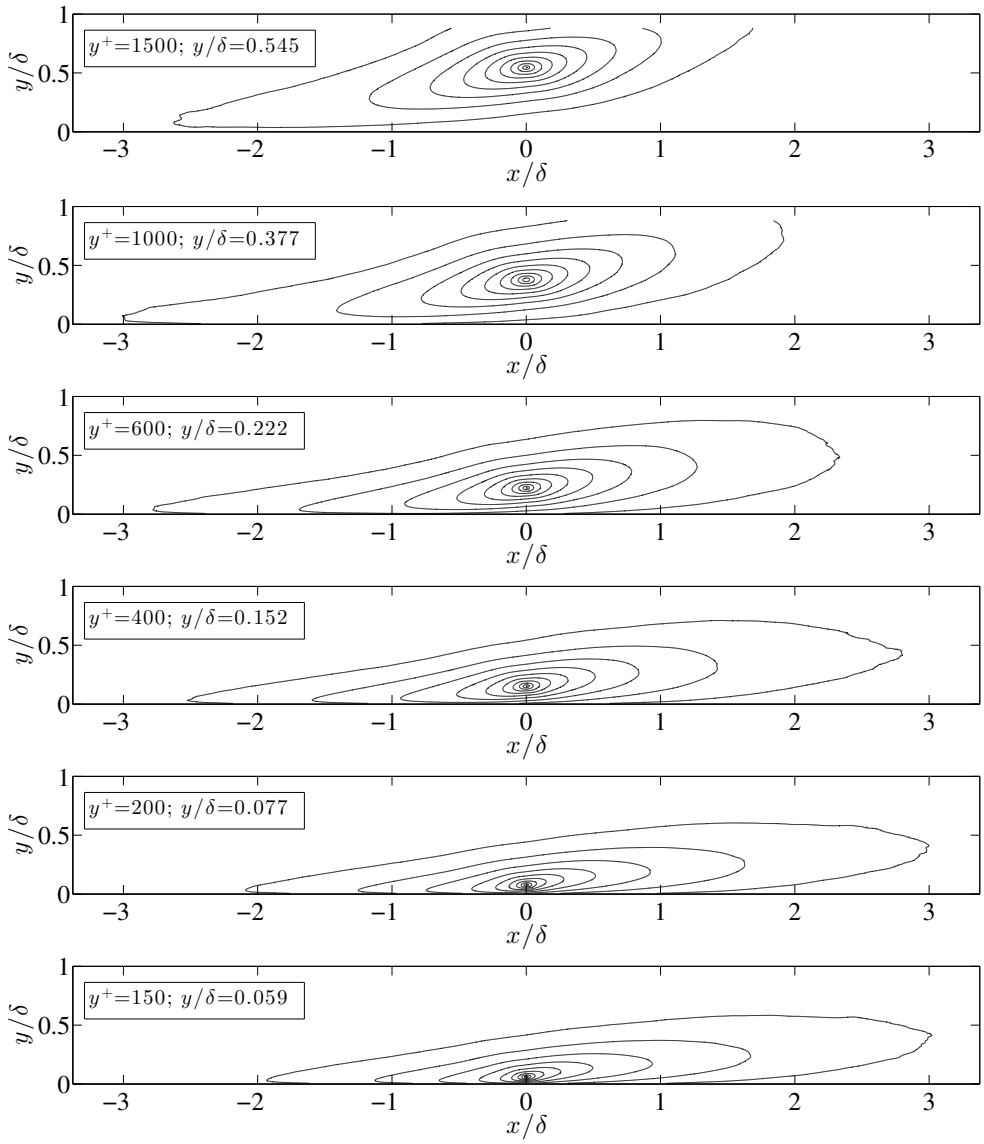

Figure 3.10: Two-point spatial correlation function of the streamwise velocity fluctuations with varying wall distance at $Re_\theta = 8100$. The contours range from 0.1 to 1 with an increment of 0.1.

are plotted as functions of $\Delta x/\delta$ and y/δ and the iso-contours range from 0.1 to 1 with a 0.1 increment. Homogeneity in the streamwise direction is assumed Foucaut et al. (2011) enabling a larger sample size and doubling of

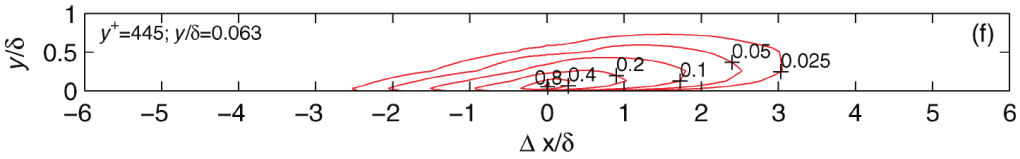

Figure 3.11: Two-point correlation function of the streamwise velocity fluctuations at $Re_\theta = 8100$ from Tutkun et al. (2009)

the correlation domain.

As seen in figures 3.9 and 3.10, the spatial correlation extends over a distance of up to 5δ at $y^+ = 200$ when looking at the 0.1 correlation value for both the Reynolds numbers. The correlation function appears shaped approximately as an ellipse and is strongly elongated in the streamwise direction with a slight inclination to the horizontal. The overall streamwise extent of the correlation grows with distance from the wall in the logarithmic region but drops (and also broadens in the wall normal direction) beyond that region in agreement with Ganapathisubramani et al. (2005).

Two-point correlations computed using hot-wire rakes obtained by Tutkun et al. (2009) at a relatively similar Reynolds number ($Re_\theta \approx 19100$) show a similar picture (refer figure 3.11) when the reference wall-normal position in the computation was placed at y/δ of 0.063, which is close to y/δ of 0.057 in figure 3.9 in this study. The time series data from Tutkun et al. (2009) was converted to space using Taylor's frozen field hypothesis. Their correlations shows a similar shape and also extends from the near-wall region to about 0.8δ, as shown in figure 3.9.

3.2.2.2 Detection of streamwise large-scale structures

In section 3.1 we developed a spectral model of the streamwise turbulence fluctuating velocity based on the concept of elongated streaky structures which are part of attached eddies and can be modeled as simple on-off functions. In this and the next subsections we use our PIV data to test this concept and assess its potential as an hypothesis for understanding near-wall turbulence spectra.

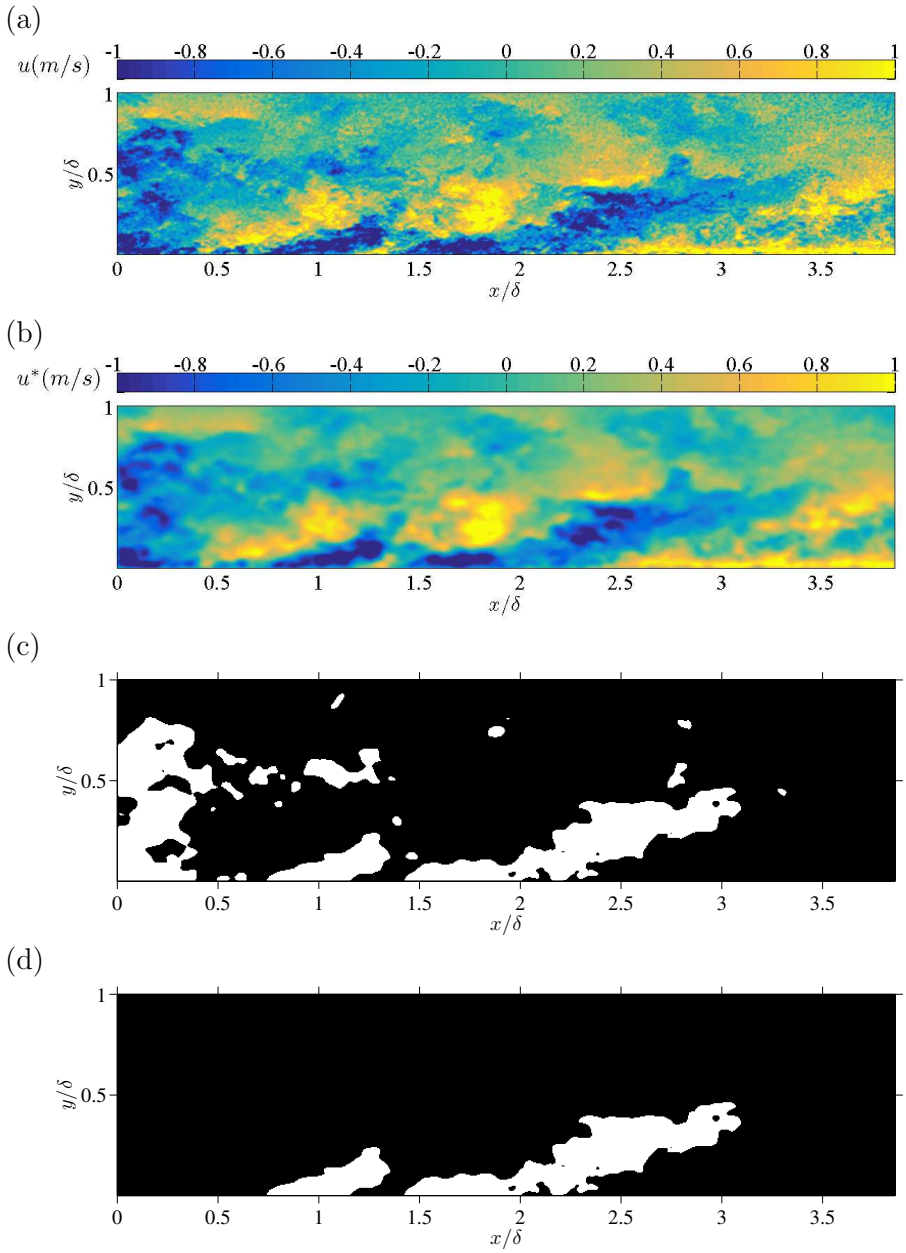

Figure 3.12: Wall-attached elongated streaky structure eduction method applied on a sample instantaneous streamwise velocity field at $Re_\theta = 20600$. From top: (a) Raw instantaneous streamwise fluctuating velocity component field (b) The same field after application of a Gaussian filter (c) Binary image obtained after thresholding negative streamwise fluctuating momentum regions. (d) Final image obtained after cleaning as described in subsection 3.2.2.2

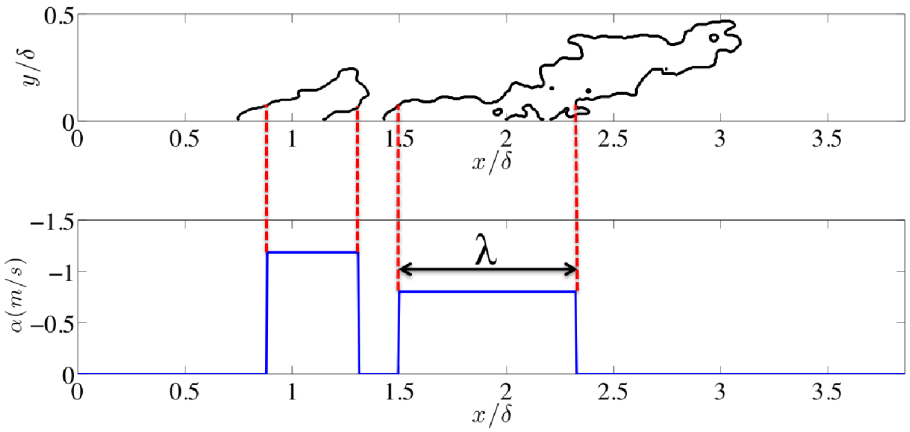

Figure 3.13: Figure 3.12(d) reproduced in the top plot, with, in the bottom plot, the average streamwise fluctuating velocity α and the streamwise length λ of the detected wall-attached structures at $y/\delta = 0.03$.

To detect and quantify the large-scale structures from the instantaneous velocity fields obtained from PIV, the following steps were employed:

1. Treatment of raw images.
2. Detection function.
3. Thresholding.
4. Structures extraction.

Treatment of raw images:

A first look at the instantaneous velocity fields showed the presence of single structures split in many parts (refer figure 3.12a). Therefore, the primary aim before analysing these structures was to implement a method to connect and smoothen out these structures while at the same time not modifying the shape and statistics at large scales. To do this, a few sample snap shots obtained from PIV was taken and a set of mathematical morphological operations were performed after converting the images to binary while a Gaussian filter was tested on the raw images.

Re_θ	20600	8100
$0.2\sigma_u$	13517	17338
$0.4\sigma_u$	14493	19576
$0.6\sigma_u$	13366	19290

Table 3.1: Number of structures detected over a set of thresholds for $Re_\theta = 20600$ and $Re_\theta = 8100$

A two-dimensional Gaussian filter was found to be sufficient to capture and connect the structures while retaining their overall shape. The standard deviation of the Gaussian filter was three pixels which corresponds to approximately 0.015δ for both Reynolds numbers, i.e. 105 wall units for $Re_\theta = 20600$ and 33 wall units for $Re_\theta = 8100$. The result of this operation on figure 3.12(a) leads to figure 3.12(b). Further details on the Gaussian filters that were tested has been included in Appendice A.1.

Detection function:

The existence of well-defined elongated and tilted wall-attached regions of relatively high (positive or negative) u values is clear from 3.12, where a sample field of instantaneous streamwise fluctuating velocity components, u is shown. It is these regions that we need to target in relation to the elongated streaky structures of our model. Thus, u is chosen as our detection function.

Thresholding:

To educe on-off functions such as the ones required by our model, we apply a threshold u_{th} on the gaussian-filetered u^* to obtain binary images which distinguish between $u^* < u_{th}$ and $u^* > u_{th}$. Effects of the threshold on the statistics of educed structures were investigated in the range $0.1u'_{300^+} < |u_{th}| < u'_{300^+}$ where u'_{300^+} is u' at $y^+ = 300$.

The number of structures educed by the algorithm described in subsection 3.2.2.2 for the three negative threshold values $-0.2u'_{300^+}$, $-0.4u'_{300^+}$ and $-0.6u'_{300^+}$ are reported in table 3.1. A threshold u_{th} equal to $-0.4u'_{300^+}$ (refer figure 3.14) was finally chosen to detect low momentum structures in the present study as it corresponds to the value that leads to least threshold-

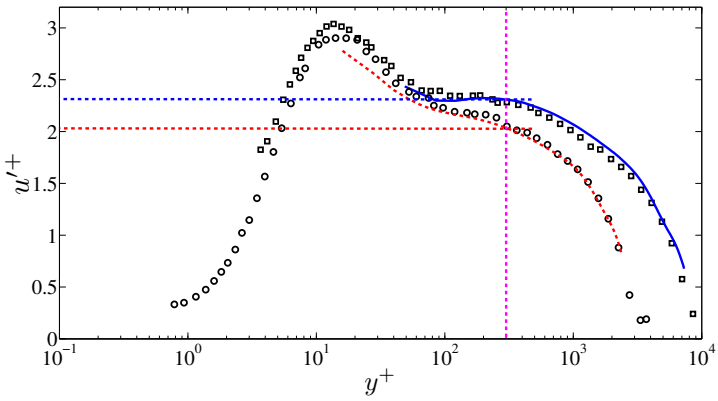

Figure 3.14: Figure 3.7(b) reproduced to explain the threshold parameter, $u_{th} = \pm 0.4 u'_{300^+}$. The horizontal dash lines indicate u' at the respective Re_θ while the vertical dash line in magenta indicates $y^+ = 300$

dependency of our statistics for a negative u_{th}. This thresholding operation leads to figure 3.12(c) when applied to figure 3.12(b). The white structures in figure 3.12(c) correspond to $u^* < u_{th}$.

Structures extraction:

One more step is required before comparing with our model. White structures which cut through the vertical borders of the figure are discarded because their streamwise extent is unknown; and white stuctures which are not attached to the bottom wall (at $y = 0$ but in fact as close to $y = 0$ as allowed by our PIV data) are also discarded because we are concerned with wall-attached structures only. With this extra step, figure 3.12(c) gives rise to figure 3.12(d).

All the steps leading from raw fluctuating streamwise velocity fields to the binary fields which we use in our statistical analysis are depicted in figure 3.12. The current study's effort is concentrated on wall-attached elongated structures of negative streamwise fluctuating velocity as in figure 3.12(d), but the analysis can be repeated equally well on structures of positive streamwise fluctuating velocity and is reported in Appendix A.3. The general behaviours of positive and negative fluctuating streamwise velocity structures are similar, the negative velocity structures being slightly longer in agreement with

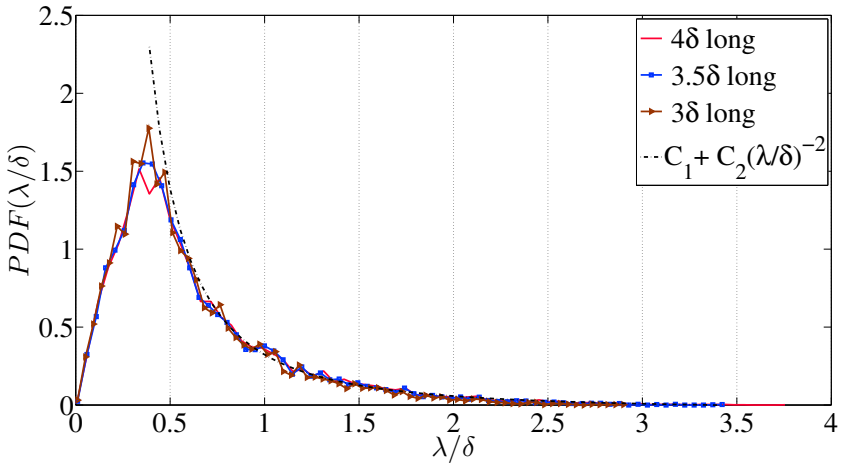

Figure 3.15: PDFs of streamwise lengths λ (see figure 3.13) for varying domain lengths at wall distance $y^+ = 195$ for $Re_\theta = 20600$

Dennis and Nickels (2011b).

3.2.2.3 Lengths of wall-attached streamwise velocity structures

We now need to obtain statistics of wall-attached elongated streaky structures represented as on-off functions in our model and as binary structures in the final stages of our structure eduction method. We first label the connected components of the binary images using image processing tools. Then we compute the streamwise length λ of each labelled structure at a distance y from the wall, i.e. the difference between the smallest and the largest values of streamwise coordinate x in this labelled structure at height y. Finally we compute the average value α of the streamwise fluctuating velocity component u inside this labelled structure at height y. Thus we obtain a pair (λ, α) for each labelled structure at each height y considered. This procedure is illustrated in figure 3.13 where the streamwise extent λ and the corresponding amplitude α of two labelled structures at wall distance $y/\delta = 0.03$ is shown. A total of 14493 and 19576 wall-attached binary structures were detected at $Re_\theta = 20600$ and $Re_\theta = 8100$ respectively.

The model in section 3.1 assumes that the number density of wall-attached

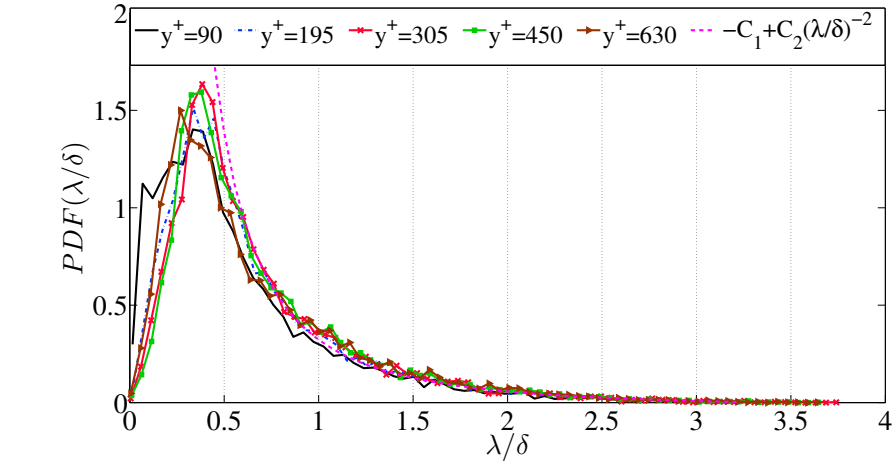

(b)

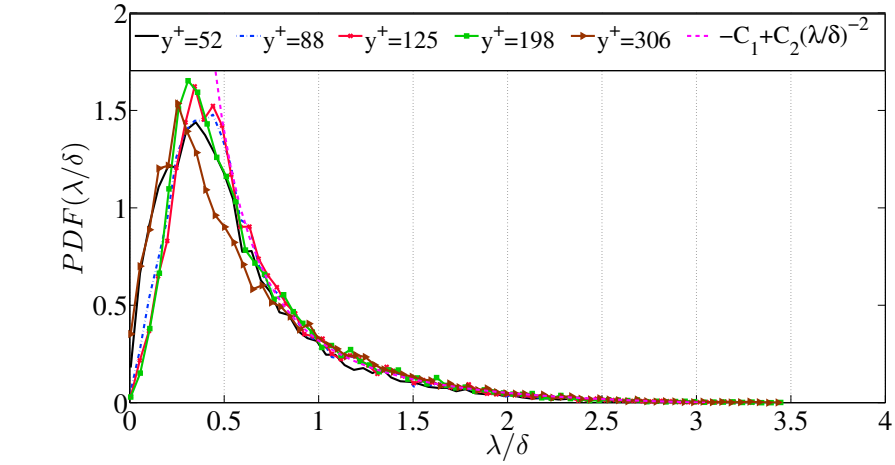

Figure 3.16: PDFs of streamwise lengths λ of wall-attached structures (see figure 3.13) at selected wall distances for $Re_\theta = 20600$ (top) and $Re_\theta = 8100$ (bottom). The fits shown here are for $y^+ = 195$ at $Re_\theta = 20600$ and $y^+ = 198$ at $Re_\theta = 8100$.

elongated streaky structures of size λ has a decreasing power-law dependence on λ in a certain range of λ values. Following Perry et al. (1986), we expect the spatial distribution of such structures to be space-filling, which implies (see Vassilicos and Hunt (1991)) that the exponent of this power law should be -2. Figures 3.15 and 3.16 show the probability distribution function (PDF) of lengths λ at various wall distances. The most probable length λ lies be-

Re_θ	20600					8100				
y^+	90	195	305	450	630	52	88	125	198	306
C_1	0.03	0.03	0.03	0.03	0.03	0.04	0.04	0.04	0.03	0.03
C_2	0.32	0.35	0.35	0.37	0.37	0.32	0.35	0.35	0.35	0.33
lower bound	0.49	0.55	0.54	0.58	0.78	0.54	0.53	0.53	0.56	0.65
upper bound	3.8	3.8	3.8	3.8	3.8	3.4	3.4	3.4	3.4	3.4

Table 3.2: Values of the constants C_1 and C_2 in the form $-C_1 + C_2(\lambda/\delta)^{-2}$ of the PDF of λ/δ. The fit is over a range of λ/δ with the lower and upper bounds for the two Reynolds numbers indicated in the table.

tween 0.3δ and 0.5δ and lengths λ longer than 3.5δ occur very rarely.

We tested for finite size effects of the field of view by computing the PDF on smaller domains, namely 3.5δ and 3δ long in the streamwise direction but same in the wall normal direction. As shown in figure 3.15 there is no significant differences caused by the three fields of view except that the smallest field returns a slightly more noisy PDF. Indeed, a reduced field of view leads to a smaller number of detected wall-attached elongated binary structures and therefore to reduced statistical convergence.

Figures 3.15 and 3.16 show a power law dependence on λ between about 0.5δ and 3δ with power law exponent -2, i.e. $D = 1$, in all cases. Given the form of $N(\lambda)$ hypothesised in section 3.1, we fit the PDF of λ/δ with a functional form $-C_1 + C_2(\lambda/\delta)^{-2}$ (where $C_1/N_M = C_2/N_o$). The fit is shown in figures 3.15 and 3.16 and is effectively the same for both Reynolds numbers and all values of y^+ in the mean flow's approximate log region. The constants C_1 and C_2 are reported in table 3.2. They are indeed fairly constant over the range of wall distances and for both Reynolds numbers. It is worth noting, though, that the lower bound of the range where the PDF of λ/δ is well approximated by $-C_1 + C_2(\lambda/\delta)^{-2}$ seems to increase slightly with increasing y^+. The dependence on threshold on the results obtained in figures 3.15 and 3.16 was tested and is reported in Appendix A.2

3.2.2.4 Energy spectra of streamwise fluctuating velocities

Figure 3.17 shows log-log plots of premultiplied energy spectra of streamwise fluctuating velocities $u(x)$ which have been obtained from our PIV data at various normalised wall distances y^+ for both Reynolds numbers. These plots might suggest that $E_{11}(k_x) \sim U_\tau^2 k_x^{-1}$ in a range of wavenumbers $0.25/\delta \lesssim k_x \lesssim 0.63/y$

for y^+ larger than about 88 and smaller than the value of y^+ where this range of wavenumbers no longer exists. The apparent k_x^{-1} wavenumber range is close to a decade long at $y^+ = 90$ for $Re_\theta = 20600$ and shorter for higher wall normal distances and for the lower $Re_\theta = 8100$. One would be justified to conclude that this is indeed experimental support for the Townsend-Perry k_x^{-1} spectrum if the only available theoretical glasses through which to look at these spectral plots were those of the Townsend-Perry attached eddy model.

However the situation is subtler and, in effect, quite different.

A closer look at the spectra in the lin-log plot of figure 3.18 suggests the possibility for small corrections to this conclusion, particularly at the lower of the two Re_θ values, but the result in equations (3.16)-(3.17) of our model in section 3.1 may pave the way for a significantly different interpretation. This model leads to $E_{11}(k_x) \sim (k_x\delta)^q$ with $p + q = -1$ if $D = 1$. Support for $D = 1$ has been obtained and reported in the previous subsection in the range of lengths λ between about 0.5δ and 3δ. It is therefore worth taking a closer look at our energy spectra in the corresponding wavenumber range. For our data, this wavenumber range turns out, in fact, to be comparable to the wavenumber range $0.25/\delta \lesssim k_x \lesssim 0.63/y$ mentioned in the previous paragraph as a candidate for Townsend-Perry scaling. Specifically, $k_x = 2/\delta$ corresponds to $k_x y = 0.25$, 0.41, 0.58, 0.91 and 1.41 in increasing order of the y^+ values in figures 3.17 and 3.18 for $Re_\theta = 8100$; and to $k_x y = 0.15$, 0.33, 0.53, 0.78 and 1.1 in increasing order of the y^+ values in figures 3.17 and 3.18 for $Re_\theta = 20600$. The wavenumber range $0.5/\delta \leq k_x \leq 2/\delta$ where the analysis is carried out is therefore not radically different for our data from the wavenumber range $0.25/\delta < k_x < 0.63/y$ where one would interpret our spectra to have a Townsend-Perry scaling for $y^+ \geq 88$.

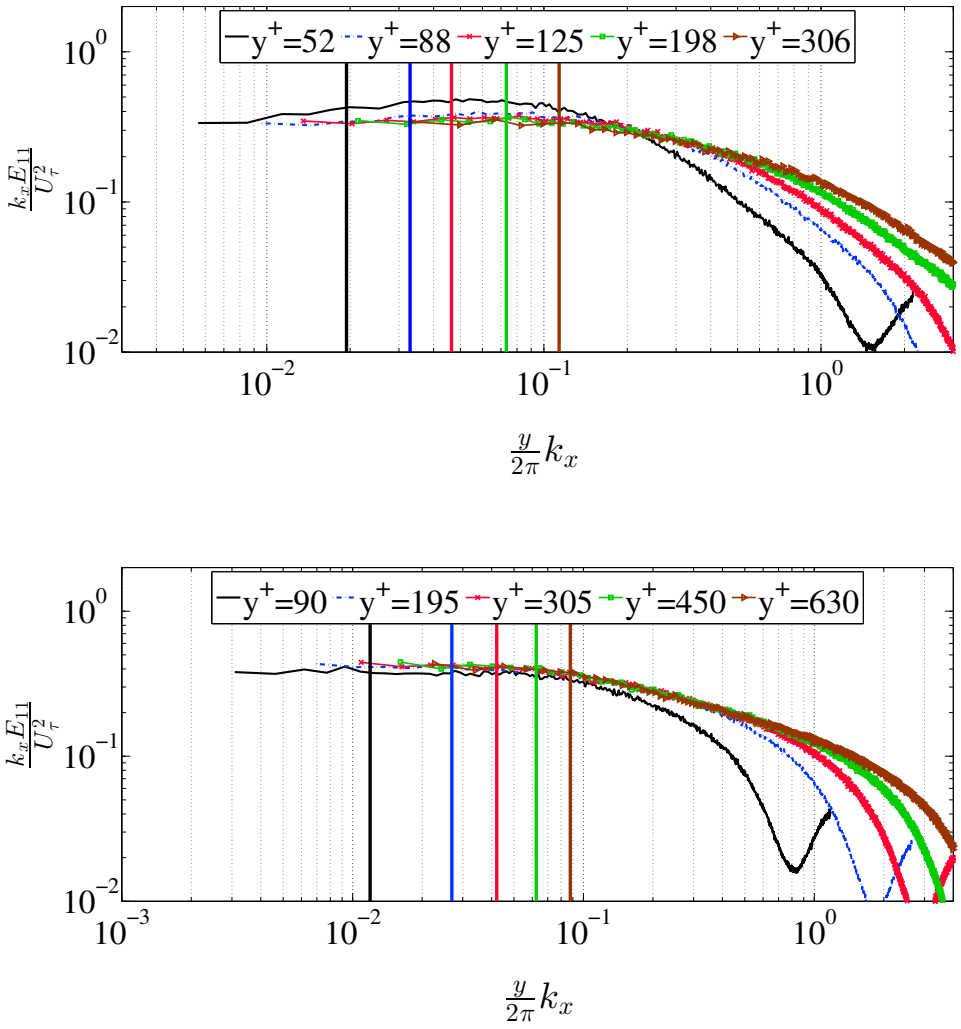

Figure 3.17: Log-log plots of pre-multiplied streamwise energy spectra at selected wall distances for $Re_\theta = 8100$ (top) and $Re_\theta = 20600$ (bottom). Vertical lines indicate the wavenumbers corresponding to the length scale $\frac{1}{\delta}$ with the same color code as the legend of the figure.

In figures 3.19 to 3.22 we plot $\overline{a^2}$ versus λ/δ where $\overline{a^2}$ is the average of $\alpha^2/\Delta\lambda$ conditional on the streamwise length of a labelled structure being between λ and $\lambda + \Delta\lambda$ (α and λ being obtained as explained in the first paragraph of subsection 3.2.2.3). The upper values of λ/δ in these plots

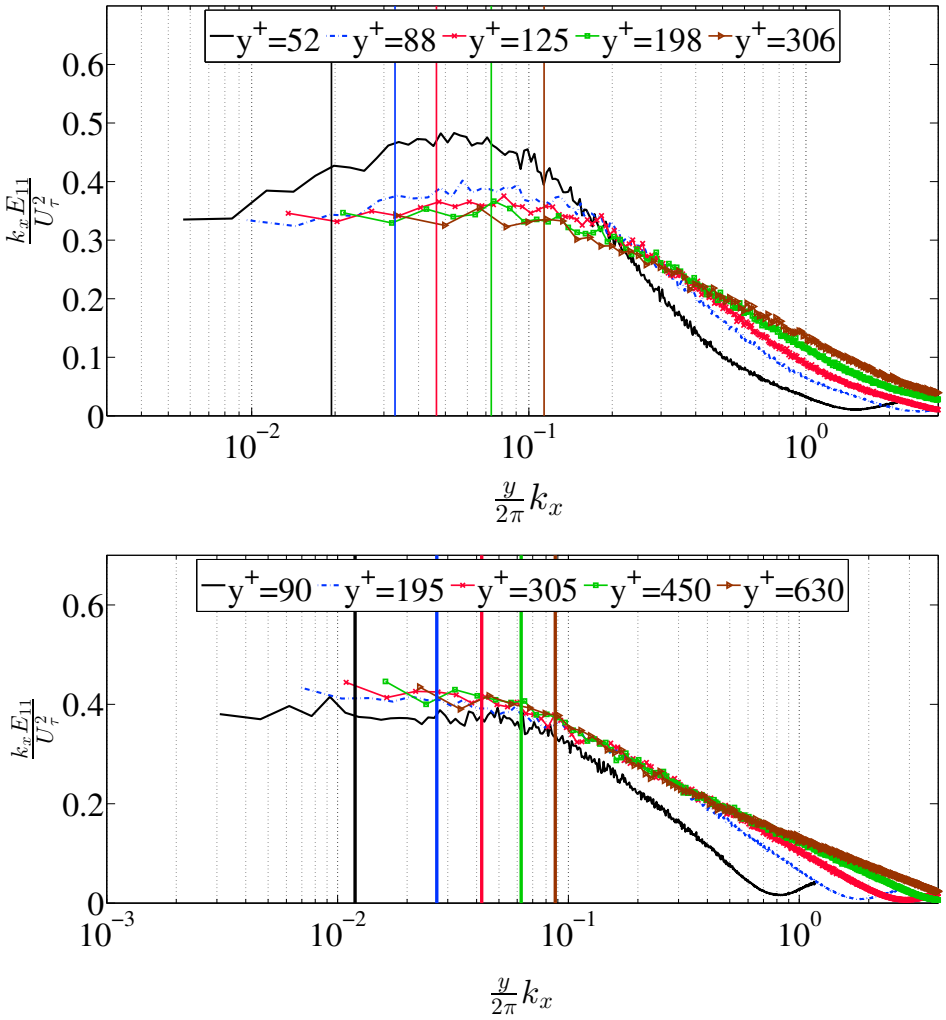

Figure 3.18: Same as figure 3.17 in lin-log plots.

are all below about 2.3 because we do not have enough samples of educed structures beyond $\lambda/\delta \approx 2.3$ to obtain values of $\overline{a^2}$ which are statistically converged. The lower values of λ/δ in these plots are all close to $\delta/2$ because the range where the PDF of λ/δ has been found in the previous subsection to be well approximated by $-C_1 + C_2(\lambda/\delta)^{-2}$ is bounded from below by about 1/2 in all our y^+ and Re_θ cases. In figures 3.19 to 3.22 we also plot $E_{11}(k_x)$ in the corresponding wavenumber range $0.5/\delta \leq k_x \leq 2/\delta$ which, as

discussed in the previous paragraph, may be close to the wavenumber range $0.25/\delta < k_x < 0.63/y$ that one could interpret as a Townsend-Perry range. We do not have enough data and high enough Reynolds numbers to clearly distinguish between these two ranges in the present work.

As an aside for the moment, note that the large-scale motions (LSMs) and very large-scale motions (VLSMs), which have been found to exist in the logarithmic and lower wake regions of a turbulent boundary layer (Kovasznay et al. (1970); Brown and Thomas (1977); Hutchins and Marusic (2007); Dennis and Nickels (2011a); Lee and Sung (2011)), generally refer to elongated regions of streamwise velocity fluctuations having a streamwise extent from about 2δ to 3δ for LSMs and larger than 3δ for VLSMs (Kim and Adrian (1999); Guala et al. (2006); Balakumar and Adrian (2007)) as described in chapter 2. The LSMs near the wall and the VLSMs have been interpreted to account for long correlation tails such as the ones in figure 3.12 and responsible for the k_x^{-1} scaling range of the turbulence spectrum Smits et al. (2011). The range of scales we concentrate on, in figures 3.19 to 3.22, just about includes some LSMs at its upper range.

Returning now to figures 3.19 to 3.22, we have included best fits of power law curves in the plots of $\overline{a^2}$ versus λ/δ and of E_{11} versus k_x. These best fits are indicated in the inserts of each plot and provide an estimation of the exponents p and q in $\overline{a^2} \sim (\lambda/\delta)^p$ and $E_{11}(k_x) \sim k_x^q$. Figure 3.23 summarizes the information with plots of p, q and $p+q$ as functions of y^+. It is perhaps remarkable that $p+q$ is very close to -1 (see figure 3.23) as predicted by equations (3.16)-(3.17) for all examined values of y^+ and for both Reynolds numbers Re_θ. Whereas this subsection's initial interpretation in terms of the Townsend attached eddy model is limited to y^+ larger or equal to 88 (based on the log-log plots of figure 3.17), the lin-lin plots of figures 3.19 to 3.22 present a different and consistent picture which covers both Reynolds numbers and all our y^+ positions, including y^+ smaller than 88.

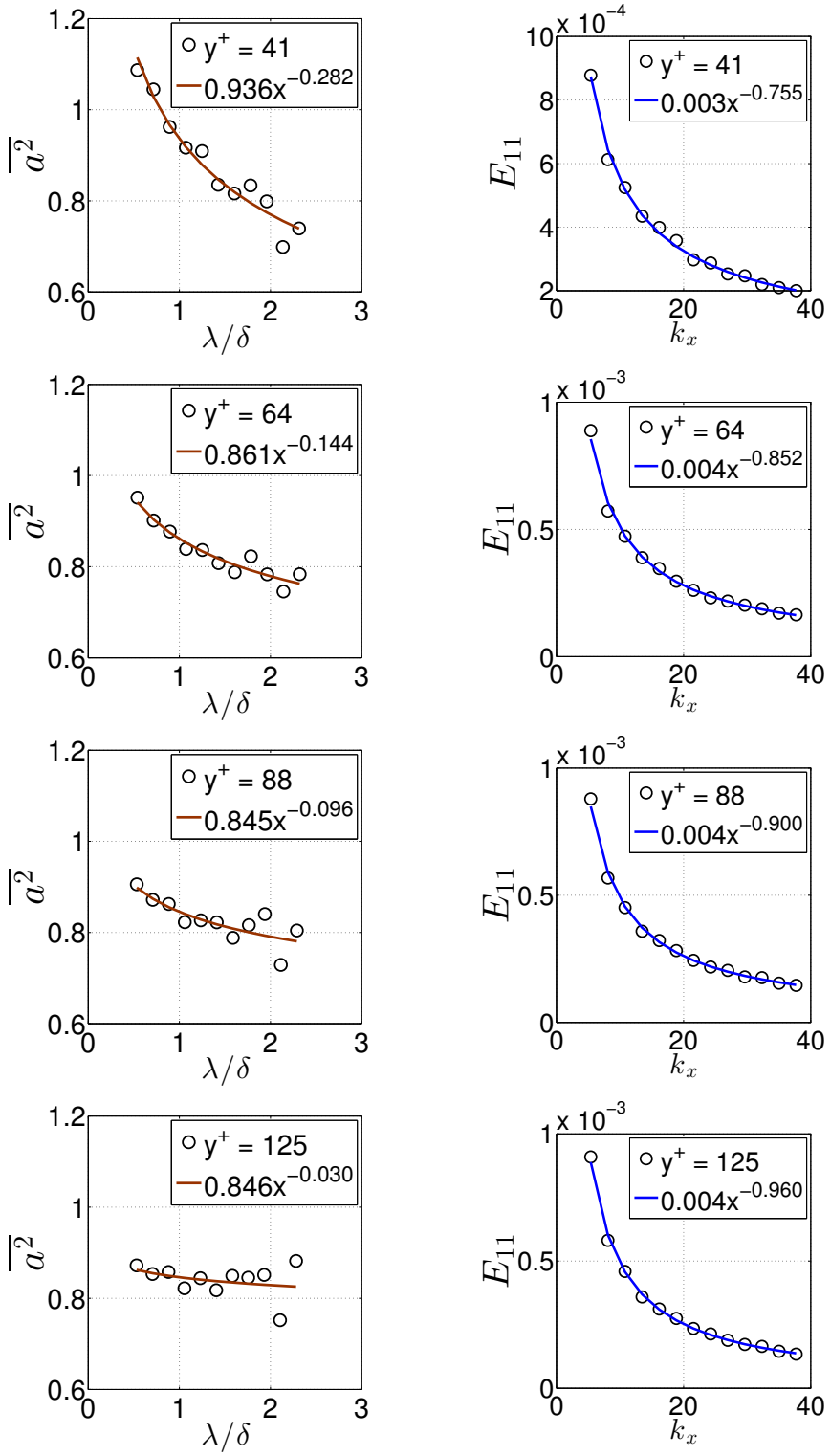

Figure 3.19: Lin-lin plots of $\overline{a^2}$ versus λ/δ (left) and streamwise energy spectra plotted at wall distances $y^+ = 41$, 64, 88 and 125 (from top to bottom) at $Re_\theta = 8100$.

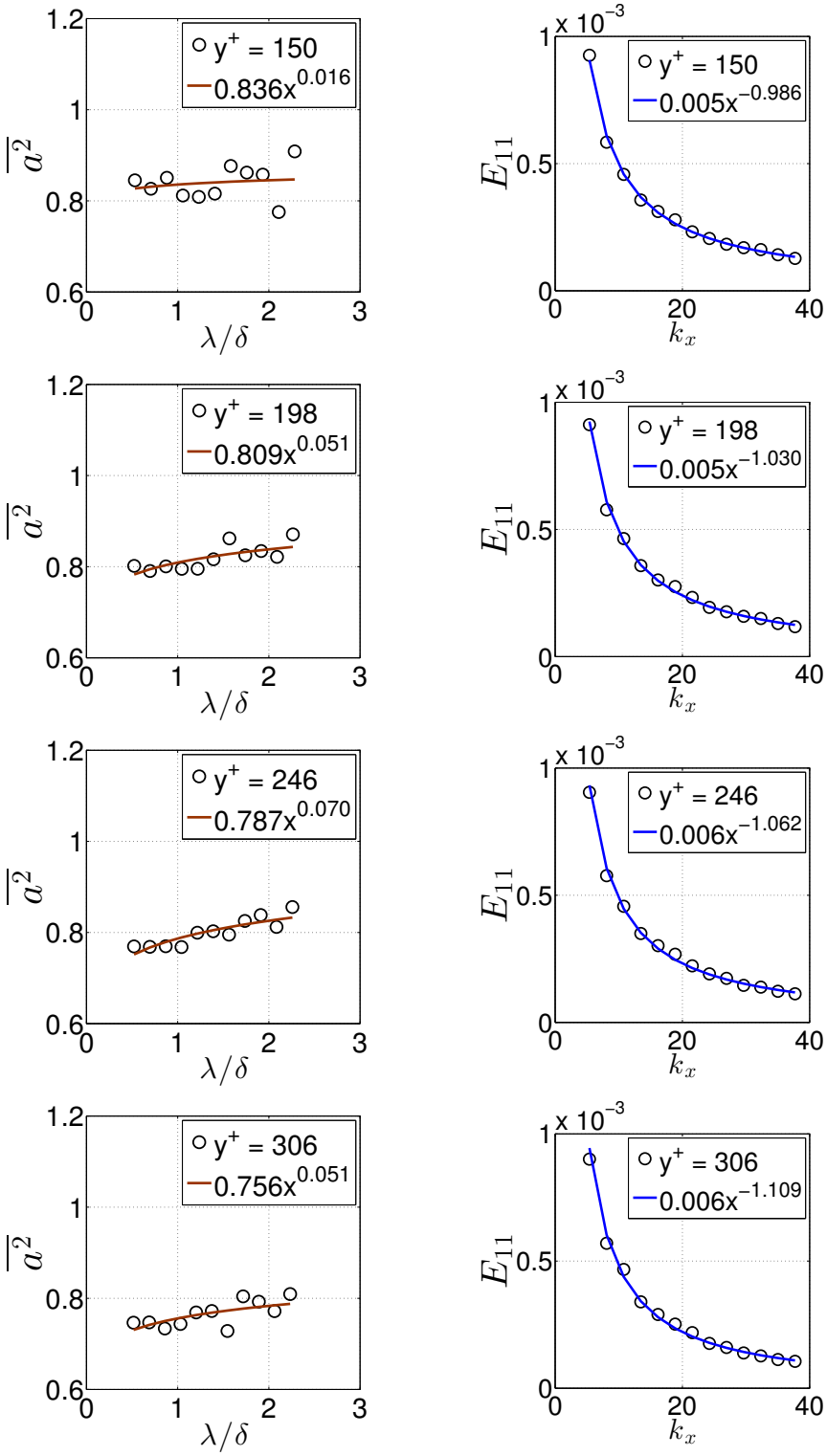

Figure 3.20: Lin-lin plots of $\overline{a^2}$ versus λ/δ (left) and streamwise energy spectra plotted at wall distances $y^+ = 150$, 198, 246 and 306 (from top to bottom) at $Re_\theta = 8100$.

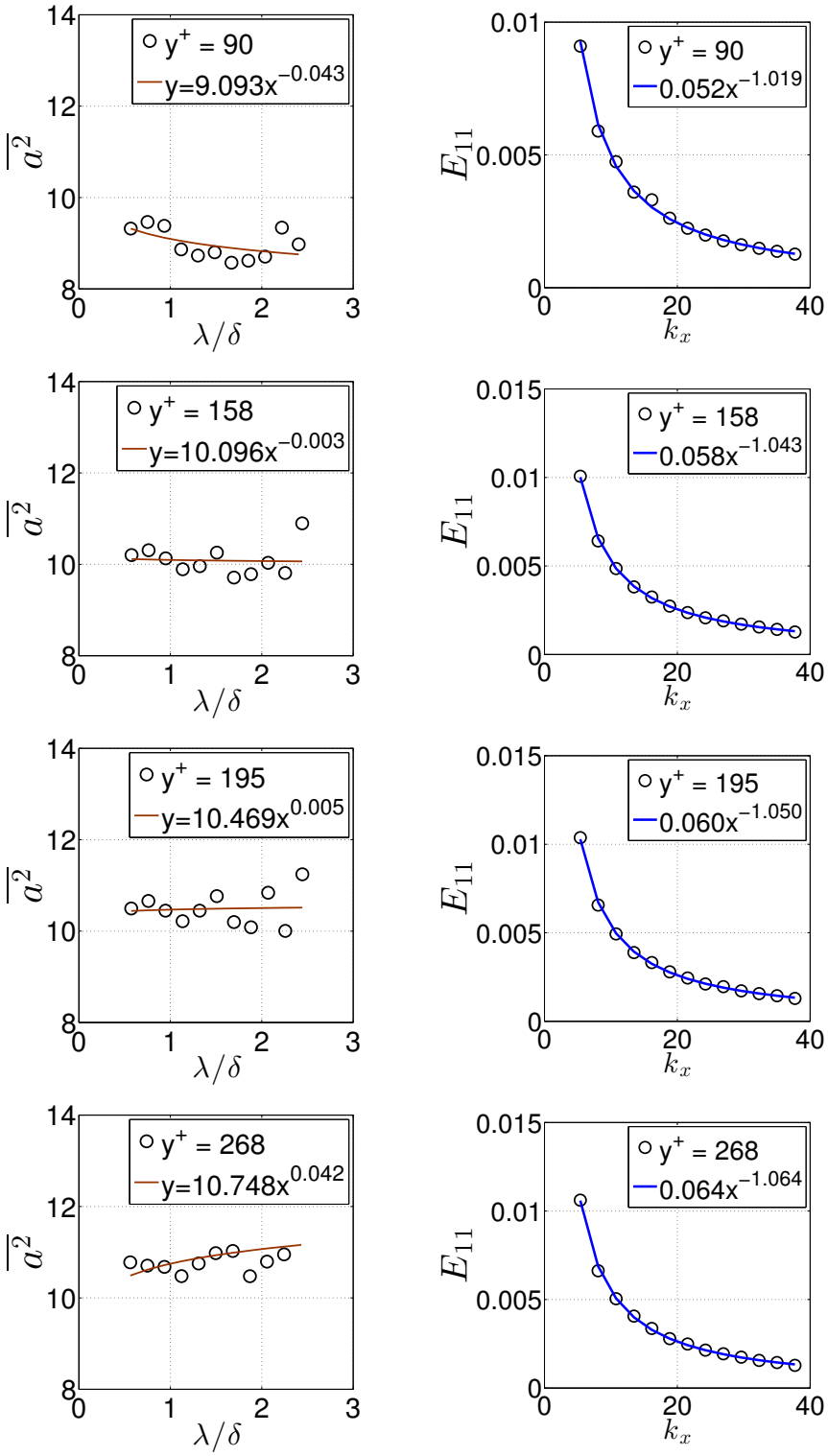

Figure 3.21: Lin-lin plots of $\overline{a^2}$ versus λ/δ (left) and streamwise energy spectra plotted at wall distances $y^+ = 90$, 158, 195 and 268 (from top to bottom) at $Re_\theta = 20600$.

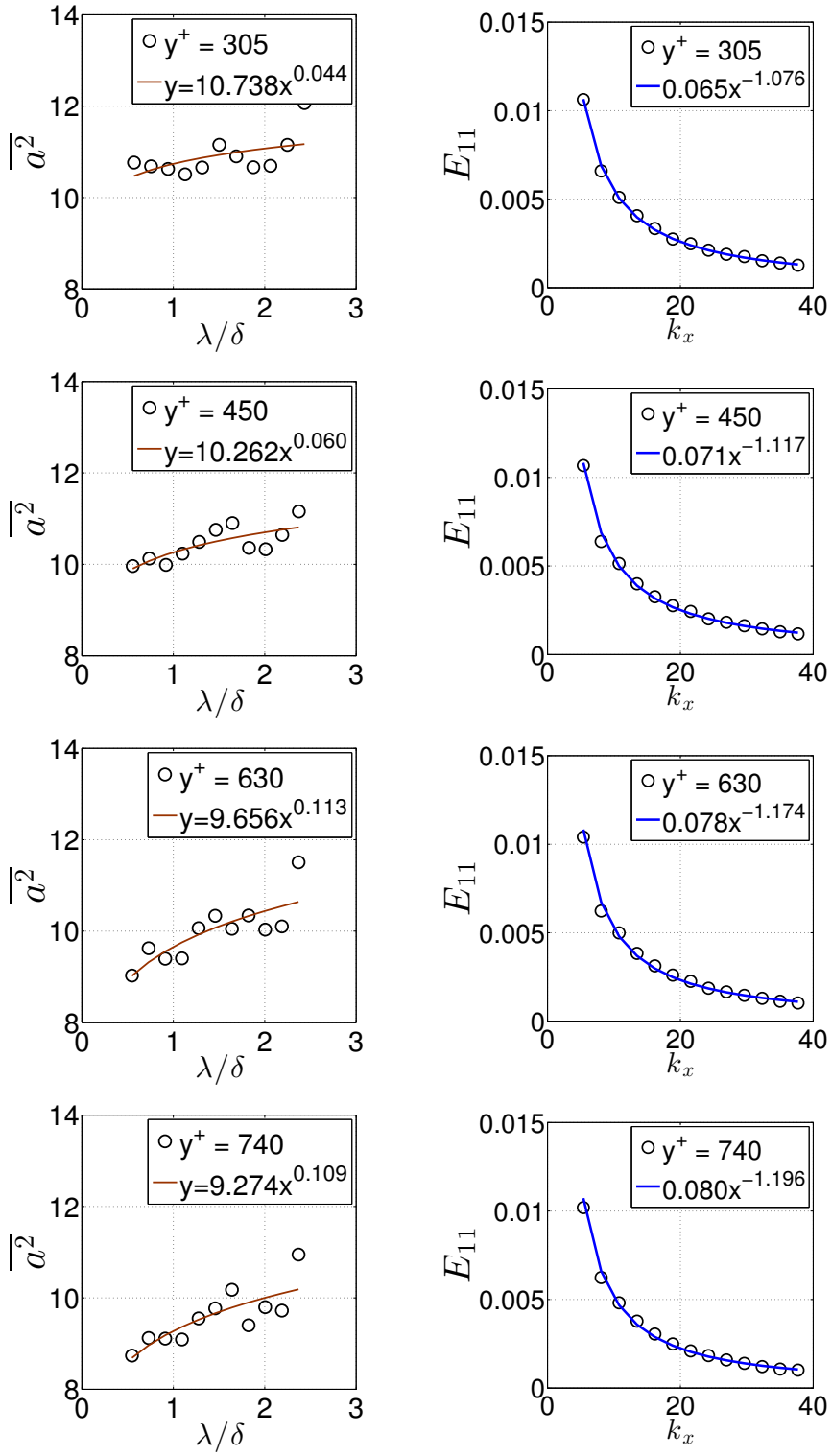

Figure 3.22: Lin-lin plots of $\overline{a^2}$ versus λ/δ (left) and streamwise energy spectra plotted at wall distances $y^+ = 305$, 450, 630 and 740 (from top to bottom) at $Re_\theta = 20600$.

3.3 Discussion

It is important to stress that the support for equations (3.16)-(3.17) in figures 3.19 to 3.22 cannot be obtained without the crucial last step of our structure detection algorithm in subsection 3.2.2.2 which discards structures that are not attached to the wall. The structures which do not touch the wall are in fact less elongated and less intense (i.e. smaller $\overline{a^2}$) on average. We have checked that if we only consider them, we do not find anything close to $p + q = -1$, i.e. equation (3.17).

The attached eddy concept introduced by Townsend (1976) is therefore important for explaining $E_{11}(k_x)$ but the results of our analysis suggest that the Townsend-Perry model does not hold because the turbulent kinetic energy content in these wall-attached flow structures does not just scale with U_τ. At different y inside such a structure, the level of turbulent kinetic energy depends both on U_τ and on the streamwise length of the structure at that height. Furthermore, this dependence varies with height: $\overline{a^2}$ decreases with increasing λ/δ very close to the wall, in the buffer layer, and increases with increasing λ further up. As $\overline{a^2}$ transits smoothly from one dependence to the other, a particular height exists where $\overline{a^2}$ is independent of λ and therefore depends only on U_τ. At that very particular height, $E_{11}(k_x) \sim k_x^{-1}$. However this is not a Townsend-Perry spectrum, it is just the spectrum at that particular distance from the wall where the turbulent kinetic energy inside the streaky structures transits from a decreasing to an increasing dependence on the length of these structures. Our conclusion agrees with Nickels et al. (2007) in their statement that it is necessary to take measurements close to the wall to observe a k_x^{-1} behaviour, in fact at y^+ between 100 and 200 as they also found. However, these authors were not in possession of equations (3.16)-(3.17) and therefore did not measure $\overline{a^2}$ at various heights and for various values of λ/δ which now allows us to see that the k_x^{-1} behaviour at the edge of the buffer layer is not the Townsend-Perry spectrum but just a transitional instance of a more involved spectral structure. In fact, the spectral picture which emerges from our analysis is a unified picture which brings together the buffer and inertial layers in a seemless way.

In figure 3.24 we plot examples of measured streamwise velocity fluctuations and the on-off signals with which we model them at various heights from the wall. Our model on-off signals are clearly a drastic simplification of the data but one gets the impression from these plots that they capture the sharpest gradients in the signal and therefore much of its spectral content at the length-scales considered here. The lengths of the non-zero parts of the model signals correspond to λ and the actual values of the on-off signal in these non-zero parts correspond to the average value α of the streamwise fluctuating velocity component inside each part.

It is clear that a wider range of Reynolds numbers needs to be examined to establish the scalings of the lower and upper bounds of the range of wavenumbers where equations (3.16)-(3.17) holds. One might expect the upper bound to scale as $1/y$ because of the recent evidence (Hultmark et al. (2012); Laval et al. (2017)) that a Townsend-like approximately logarithmic (or very weak power law) dependence on y exists for the rms streamwise turbulent velocity in the outer part of the inertial range of wall-distances. If one assumes the lower bound to scale as $1/\delta$ and therefore an energy spectrum $E_{11}(k_x)$ of the form (i) $E_{11}(k_x) \sim U_\tau^2 \delta$ for $0 \leq k_x \leq B_1/\delta$, (ii) $E_{11}(k_x) \sim U_\tau^2 \delta (k_x \delta)^{-1-p}$ for $B_1/\delta \leq k_x \leq B_2/y$ (where B_1 and B_2 are dimensionless constants and p may be a function of y as in figure 3.23a comparatively negligible energy at wavenumbers $k_x > B_2/y$, then we should have

$$(u'^+)^2 \sim 1 + \frac{B_1^p}{p}(B_1^{-p} - (B_2\delta/y)^{-p}). \tag{3.19}$$

If $p \equiv 0$ then this expression for $(u'^+)^2$ becomes

$$(u'^+)^2 \sim 1 + (\ln B_1 - \ln(B_2\delta/y)) \tag{3.20}$$

which is the Townsend logarithmic dependence on y (Townsend (1976); Perry and Abell (1977); Perry et al. (1986)). This logarithmic dependence (3.20) results from the assumption that the upper bound of the range of wavenumbers where equations (3.16)-(3.17) may hold with $p \equiv 0$ scales as $1/y$. Slightly non-zero values of p give slight deviations from this logarithmic dependence,

of the form (3.19).

Using the values of p obtained in this work and plotted versus y^+ in figure 3.23 for our two values of Re_θ, it is not possible to fit (3.19) to the data in the lower plot of figure 3.7 from $y^+ = 41$ to 306 in the $Re_\theta = 8100$ case and from $y^+ = 90$ to 742 in the $Re_\theta = 20600$ case as shown in figure 3.25. These are the y^+ ranges where equations (3.16)-(3.17) has been established for our data and they should therefore also be the ranges where (3.19) holds if the spectral model of the previous paragraph is good enough. However, in spite of the three adjustable dimensionless constants (B_1, B_2 and an overall constant of proportionality), (3.19) cannot fit the entire y^+ range for which this model has been designed, that is a y^+ range which includes both the $p < 0$ and the $p > 0$ regions.

A most suspect part of the spectral model used to derive (3.19) is its low wavenumber part. Vassilicos et al. (2015) showed that the second peak or plateau part of the u'^+ profile can be reproduced by a spectral range between the very low wavenumber range where $E_{11}(k_x) \sim U_\tau^2 \delta$ and the wavenumber range where $E_{11}(k_x) \sim U_\tau^2 \delta (k_x \delta)^{-1-p}$. In fact, Vassilicos et al. (2015) also showed that this extra intermediate spectrum is necessary for a sufficiently fast growth of the integral scale with distance from the wall. A complete model of $E_{11}(k_x)$ would therefore require the spectral range introduced by Vassilicos et al. (2015) as well as the spectral range studied here. It is interesting that equations (3.16)-(3.17) has been established in this work for length-scales up to about 3δ which therefore includes LSMs, suggesting that VLSMs might be linked with the low wavenumber spectral range introduced by Vassilicos et al. (2015).

(a)

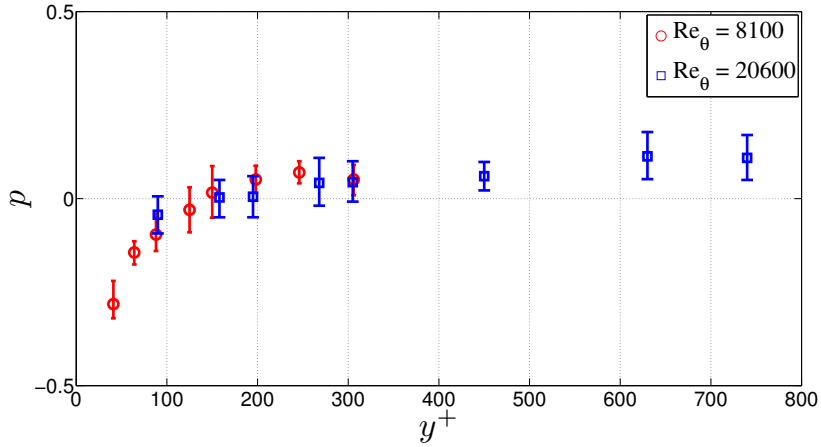

(b)

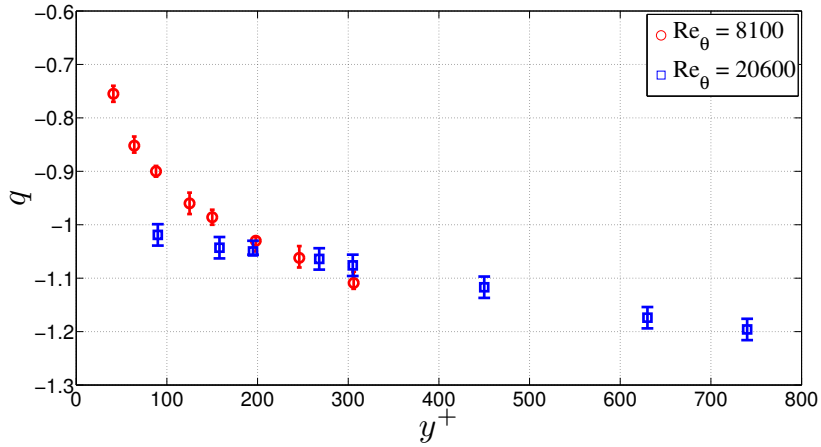

(c)

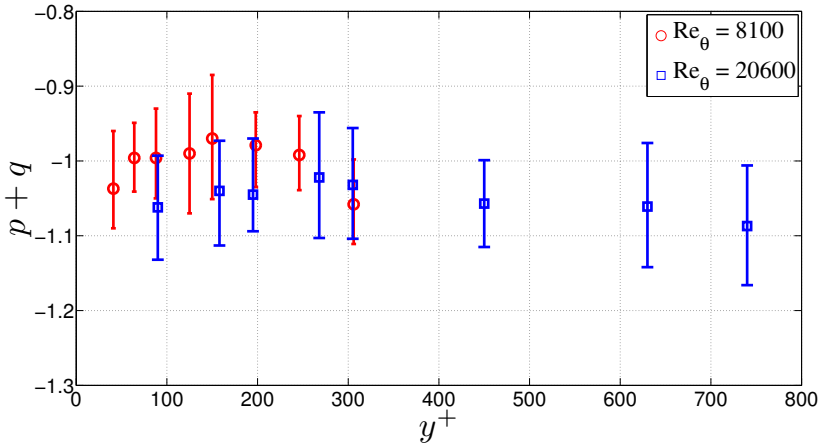

Figure 3.23: (a) Exponents p obtained from the best power-law fit of $\overline{a^2} \sim (\lambda/\delta)^p$. (b) Exponents q obtained from the best power-law fit of $E_{11} \sim k_x^q$. (c) $p+q$ versus y^+. These fits are obtained over the range of scales investigated in figures 3.19 to 3.22 and the resulting exponents are plotted with the 95% confidence intervals for these fits. The y^+ positions and the two Reynolds numbers Re_θ are those in figures 3.19 to 3.22.

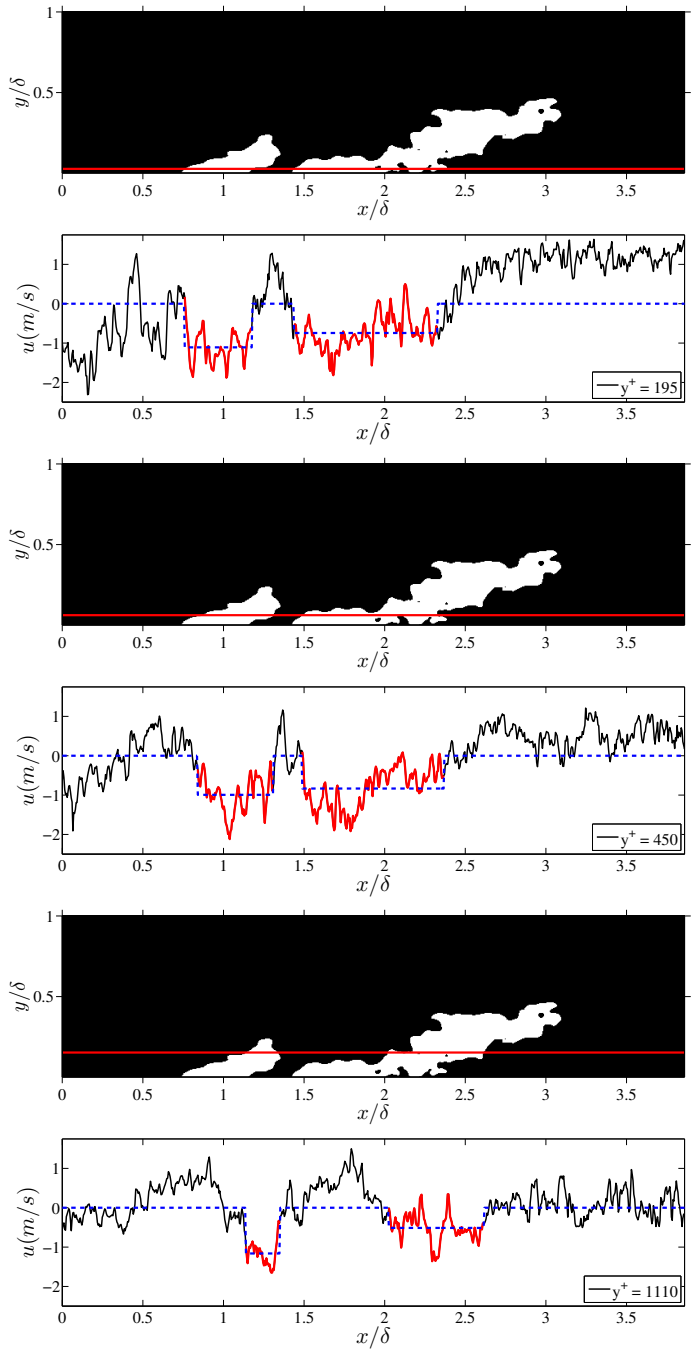

Figure 3.24: An example of a detected wall-attached flow structure for $Re_\theta = 20600$ and the $u(x)$ signal through this structure at three different y^+ positions. The red line in the repeated binary image indicates the y^+ position where the signal $u(x)$ is recorded ($y^+ = 195, 450, 1110$). The black/red line in the $u(x)$ versus x/δ plots is the raw (un-filtered) PIV fluctuating streamwise fluctuating velocity outside/inside the detected flow structures. The dashed blue line is our model signal, equal to 0 outside and to the average value of u inside the detected structures.

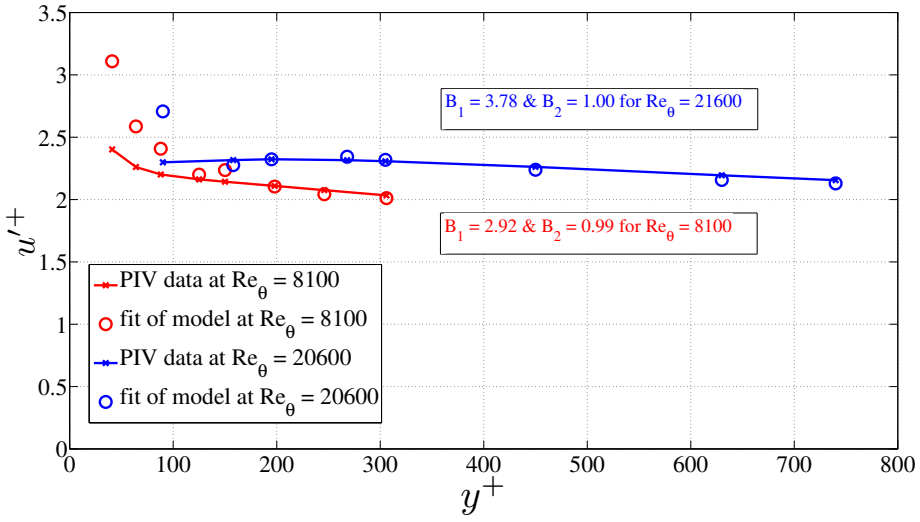

Figure 3.25: Fit of u'^+ from equation 3.19 over the PIV data shown in figure 3.7(b). Solid lines correspond to the fit given by equation 3.19 and circles are obtained from the PIV data at the two Re_θ.

CHAPTER 4

Adverse pressure gradient turbulent boundary layer flow

4.1 Introduction

In the previous chapter, the case of a ZPG turbulent boundary layer was studied. Although theoretically speaking, it simplifies the study of the turbulence problem, it seldom occurs in practical situations as most engineering applications encounter boundary layers exposed to pressure gradients. At present, turbulence models fail to predict the flow behaviour of an APG boundary layer (Manceau (2015)). This is due to the fact that the near wall region of all turbulence models is mostly based on the physics of the ZPG boundary layer and still, little is known about the physics of these APG boundary layers (Stanislas (2016)). Furthermore, understanding of wall turbulence especially in a decelerating situation is still quite limited due to the lack of sufficiently high Reynolds number data and large facilities. These are necessary to reach some state of an equilibrium turbulent boundary layer where theoretical approaches can be relevant (George et al. (2012)). Also, the length of these structures extending up to 14δ (in ZPG turbulent boundary layers Hutchins and Marusic (2007)) requires a large field of view and a high spatial resolution. In a bid to overcome these challenges, an extensive set of experiments Cuvier et al. (2017) were conducted in the boundary layer wind tunnel at LML under the framework of EuHIT (European High-Performance Infras-

tructures in Turbulence). The following section of this chapter describes the experiment that was performed. This includes the rationale behind the choice of the APG ramp, the metrology used such as pressure measurements and Particle Image Velocimetry (PIV). The final section presents the characterisation of the flow developing along the APG ramp model and the results are compared to a ZPG case whenever possible to compare the different physics between the two type of flows.

4.2 Description of the experiment

To thus improve our understanding on APG flows, a set of experiments under the framework of EuHIT were conducted at the LML boundary layer wind tunnel.

In addition to the main 2C2D PIV measurements in a streamwise wall-normal plane with 16 sCMOS cameras on the $-5°$ flat plate generating the APG, the flow above the $1.5°$ flat plate generating a FPG was also characterised through 2C2D PIV at two free-stream velocities ($U_\infty = 5$ and 9 m/s). Furthermore, to complement these large field of view measurements, time resolved near wall velocity profiles were obtained in order to determine the wall-shear stress and its fluctuations at some specific locations along the wall. This would also enable us to get an overall picture of the turbulence quantities at these measurement stations right from the wall up to the edge of the boundary layer.

The aim of the subsequent subsections of this chapter is to describe the various metrologies used followed by providing the main results of this unique experiment with an emphasis on the statistics and the boundary conditions. One objective is in fact to provide turbulence modellers with information pertaining to a carefully characterised flow which will then allow them either to validate their RANS model on a challenging test case or to be able to compare their LES predictions of the flow organisation with the experiment. For that purpose, pressure distributions along the ramp model and along the upper wall were measured. The upstream boundary conditions are also provided and the 2D character of the flow has been checked by performing

measurements near the side walls and complementary measurements have been performed in the streamwise plane of symmetry, upstream of the APG in order to provide the modellers with as complete picture of the flow as possible.

4.2.1 The ramp model

Before deciding to design experiments on such a large scale, several points pertaining to nature of APG flow we wish to study needs to be addressed:

- The strength of the APG we wish to study (either strong or mild).
- The angle the plate should be set at, to generate the desired APG case.
- The length of the plate for the flow to develop and reach a state of an equilibrium APG turbulent boundary layer.

Addressing the first point, the case of a strong adverse pressure gradient quickly leads to separation and the flow in this region is dominated by pressure effects. The case of mild APGs acting over a considerable streamwise distance results in history effects becoming important and this poses a challenge for turbulence modellers. One common physical fact that has been observed by several authors and recently summarized by Stanislas (2016) has been the development of an intense second peak of turbulence which, as opposed to the standard near wall peak, spreads and moves away from the wall as it progresses downstream. Thus, it was decided to develop a ramp model that would lead to a mild APG study case.

To design the desired ramp and to answer points 2 and 3, numerical simulation using the commercial CFD package, StarCCM+ was performed enabling us to have a first estimation of the resulting flow by varying the angle of the plate on the ramp. Test were conducted for a range of ramp angles from -3° to -5° with respect to the horizontal, in 1° increments to analyse the development of pressure coefficient and the skin friction coefficient in particular. A -5° ramp was finally chosen as this ensured a mild APG flow in equilibrium that would not separate. The details of the simulation pertaining

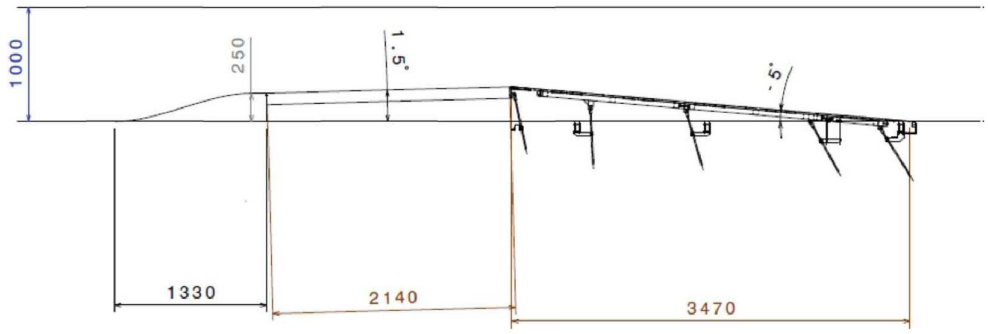

Figure 4.1: Sketch of the ramp model showing the main dimensions.

Figure 4.2: The ramp model placed in the LML boundary layer wind tunnel

to the current ramp model (refer figure 4.1) has been included in Appendix B.

A sketch of the finalized model geometry is shown in figure 4.1 where the flow is from left to right. The current geometry of the ramp was chosen to represent the most general case of an aeroplane wing; A region of accelerating mainstream flow (favourable pressure gradient (FPG)) after a leading edge up to the point of maximum thickness followed by a region of decelerating mainstream flow (APG) beyond the point of maximum thickness of a wing. The LML-AVERT ramp (Cuvier et al. (2014)) was used as the model on which the final flap was replaced by a 3.5m long plate.

Figure 4.2 shows the ramp model used for the EuHIT experiments placed in the LML boundary layer wind tunnel with the arrows in red indicating the flow direction. The leading edge of the ramp was placed at 9.4 m from the beginning of the test section. The platform consisted of a 1.33 m long

converging part, having a contraction ratio of 0.75. It was followed by a 2.2 m flat plate inclined at +1.5° to the horizontal that generated a small FPG and a second plate of length 3.5 m inclined at -5° to the horizontal where an APG region developed. This 3.5 m flat plate is made of 7 individual pieces connected together. Of these, the first is a 240 mm long Aluminium plate; the following five are in plexiglass (four of 625 mm in length and one of 515 mm in length) and the last is an Aluminium plate (210 mm long and 2 mm thick). The adjustments between plates are better than 0.1 mm and the surface quality of this 3.5 m plate is below ±0.1° on 20 cm. To minimize leaks, the junctions between plates are taped by a 0.05 mm thick black Aluminium tape. Also to minimize the vortex that developed on the sidewalls, a gasket is fixed between the sidewalls and the ramp model. Each plexiglass plate is equipped with a 240 mm by 625 mm insert to allow specific near wall measurements during the test campaign.

The exact ramp coordinates in the (X, Y, Z) global wind tunnel frame are given below (X = 0 corresponding to wind tunnel entrance). X_r is defined as $X_r = X - X_{le}$, with X_{le} the ramp leading edge position (X_{le} = 9400 mm). The converging part is defined by equation 4.1 with X_r and Y in mm,

$$\begin{cases} Y = -\dfrac{500}{1200^3}X_r^3 + \dfrac{750}{1200^2}X_r^2 & \text{for} \quad 0 \leq X_r \leq 1200\text{mm} \\ \\ Y = 250\text{mm} & \text{for} \quad 1200 \leq X_r \leq 1330\text{mm} \end{cases} \tag{4.1}$$

At the end of the converging part, the articulation has a radius of 10 mm which can be modelled by a sharp corner. This articulation is followed by a flat plate at +1.5° from the floor on a length of 2140 mm. At the end of this flate plate, the articulation corresponds to a circular arc of radius 10.25 mm with the centre at X_r = 3470 mm, Y = 295.77 mm and a $-6.5°$ rotation to join the 3486 mm flat plate which follows at $-5°$ from the floor. the connection with the wind tunnel floor at the end of this plate was done with a curvature radius of about 7.27 mm centered at X_r = 6949.04 mm, Y = 5.14 mm.

The ramp was also equipped with 51 pressure taps; 27 pressure taps for the streamwise pressure distribution and 24 for four transverse pressure distribution stations. Two transverse stations located on the 1.5° plate and two on the -5° plate. The large field experiment carried out to characterise the flow along the APG ramp is described below.

4.2.2 Static pressure distribution

The pressure distribution on the model was measured for two free-stream velocities ($U_\infty = 5$ m/s and 9 m/s, both measured at the entrance of the wind tunnel). This was done using scanivalves and a Furness FCO 14 manometer having a range of 0 to 10 mm H_2O and an uncertainty of ±0.5% of the reading value. The pressure tap number 17, located just before the 3.5 m plate was chosen as reference as it corresponded to the smallest pressure on the model. The pressure coefficient, $C_p = \frac{P-P_{17}}{\frac{1}{2}\rho U_\infty^2}$ was computed with P_{17} being the reference pressure, ρ the density of air and U_∞ the free stream velocity upstream of the ramp located 10 cm downstream of the test section entrance. In the following figures, $'s'$ will refer to the curvilinear abscissa along the ramp, with the leading edge of the ramp set as origin as defined in Cuvier et al. (2014).

The pressure coefficients along the model for the two free stream velocities (5 and 9 m/s) are shown in figure 4.3(a) while figure 4.3(b) shows the corresponding distributions of the pressure gradient. As seen in figure 4.3(a), the flow accelerates in the converging part $0 \leq s \leq 1360$ mm of the ramp causing a decrease in the pressure coefficient until the suction peak at $s = 1146$ mm corresponding to pressure tap '6'. This suction peak then induces a locally strong adverse pressure gradient (see Figure 4.3(b)). Behind this suction peak, a region of pressure recovery occurs after which the flow begins to accelerate again due to the favourable pressure gradient caused by the 2.14 m long flat plate inclined at 1.5° to the wind tunnel floor. A second suction peak is observed at the articulation of the $-5°$ plate at $s = 3500$ mm close to the reference pressure tap 17. The 3.5 m long plate inclined at $-5°$ to the wind tunnel floor then causes a region of relatively constant adverse pressure

(a)

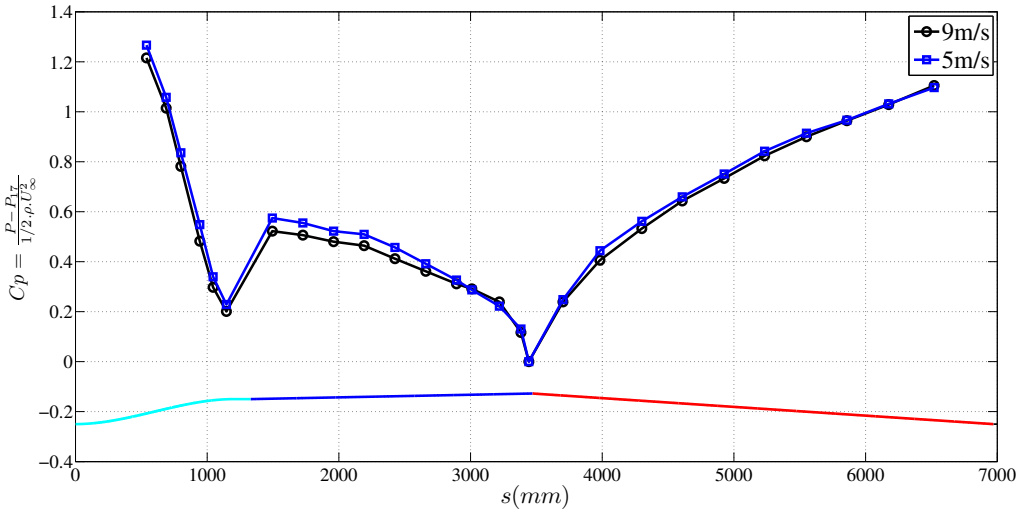

(b)

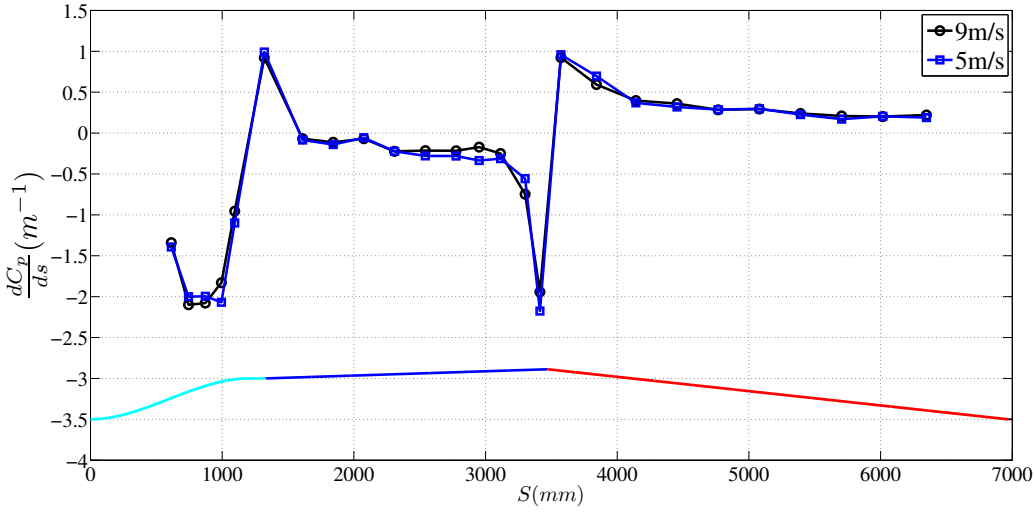

Figure 4.3: (a) Distribution of the streamwise pressure coefficient and (b) the streamwise pressure gradient along the ramp

gradient with a pressure gradient coefficient, β of about 2. To ensure that the 45° mirror inside the tunnel and the slot in the wall had limited effects on the flow upstream, the streamwise pressure distribution along the ramp

(a)

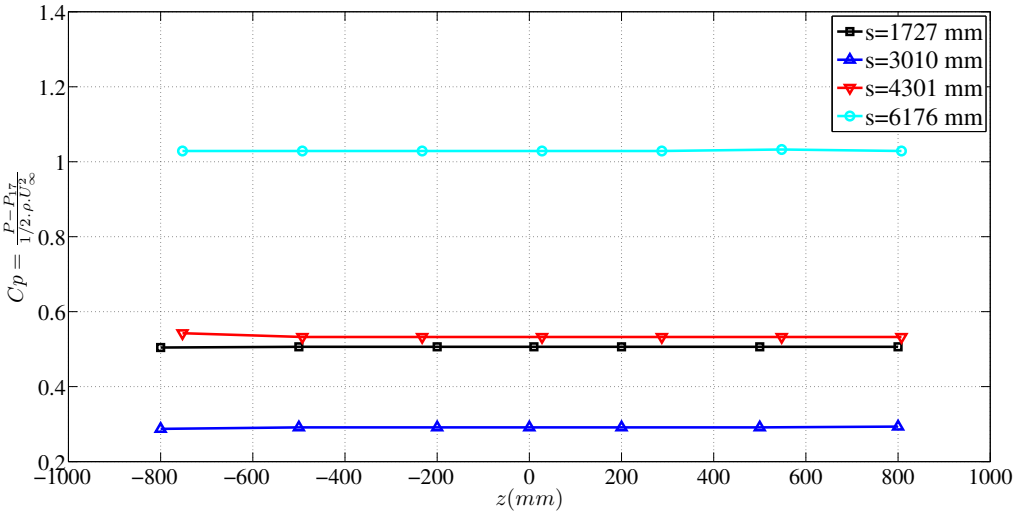

(b)

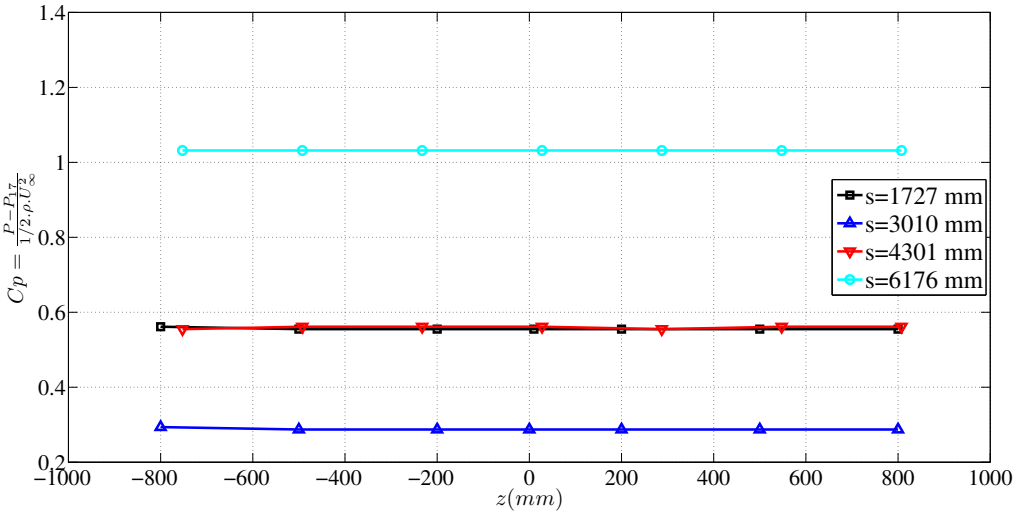

Figure 4.4: Spanwise pressure distribution along the ramp. (a) 9 m/s (b) 5 m/s

was also acquired with the mirror and the slot. No difference was observed which indicates that the flow was not affected until the last pressure tap on the model which is 460 mm upstream of the end of the ramp.

Spanwise pressure measurements were carried out at four locations to check the spanwise homogeneity and the two dimensionality of the flow. The first two stations were located on the 1.5° plate at $s = 1727$ mm and $s = 3010$ mm while the last two stations were located on the -5° plate at $s = 4301$ mm and $s = 6176$ mm. As seen in figure 4.4 where z is the transverse direction with $z = 0$ corresponding to tunnel centreline, the pressure distribution is almost constant at the 4 stations for both velocities except slight variations close to $z = -800$ mm and +800mm. This confirms the two dimensionality of the flow for at least $-600 \leq z \leq 600$ mm.

To provide complete boundary conditions, the pressure distribution on the top wall of the wind tunnel was measured using a wooden window equipped with three pressure taps. The distribution was acquired by moving this wooden window from port to port along the upper wall. The effect of the ramp becomes visible around $X = 8$ m (See Figure 4.5). Thus, the mean velocity and Reynolds stress profiles at $X = 6.8$ m (2.6m upstream of the ramp meading edge), which can serve as inlet boundary conditions for computational fluid dynamics (CFD) are then not affected by the presence of the model. The smoothness of the C_p curve shows the very good repeatability of the flow. The pressure distribution starts with a slight favourable pressure gradient (see Figure 4.5(b)) due to the boundary layer development on each wall of the test section. It is -0.44 Pa/m for $U_\infty = 9$ m/s and -0.19 Pa/m for $U_\infty = 5$ m/s close to the values found by Carlier and Stanislas (2005). Then a trend similar to the pressure distribution on the model is observed. The presence of the contraction and the flat plate at 1.5° creates a flow acceleration which induces a strong FPG until X = 12.54 m after which the flow switches to adverse pressure gradient caused by the 3.5 m plate. It should be noted that the pressure gradient contains some fluctuations due to measurement uncertainties.

Uncertainties

To ensure accurate measurements, the time constant of the Furness was set at its maximum value and a 2-3 minute waiting period was observed for the measurement to stabilize. The zero offset was checked before every reading to avoid voltage drift over time. The uncertainty for both the pressure

(a)

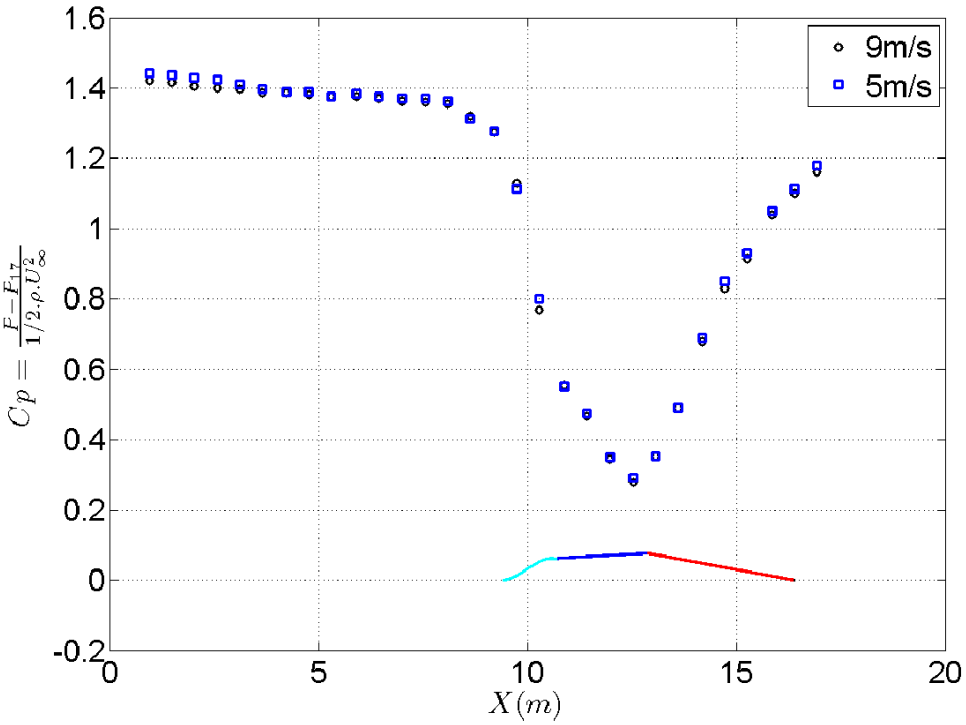

(b)

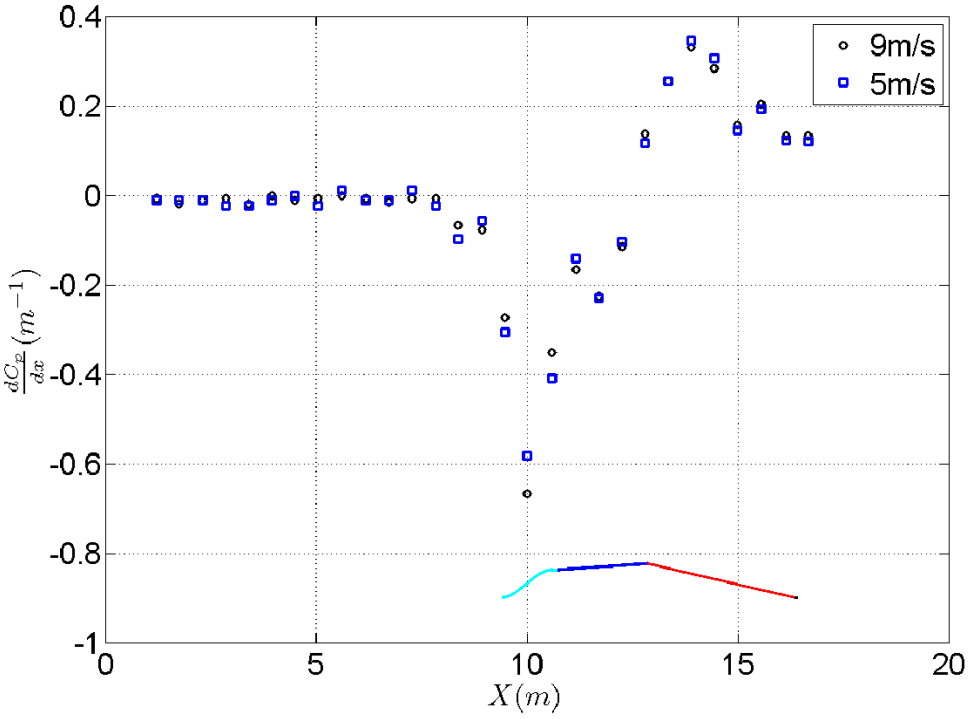

Figure 4.5: (a) Distribution of the streamwise pressure coefficient and (b) the streamwise pressure gradient along the roof

coefficient and the pressure gradient were determined using the quadratic mean estimation. With $C_p = \frac{P-P_{17}}{\frac{1}{2}\rho U_\infty^2}$ and $\rho = \frac{P_a}{rT}$ where P_a is the atmospheric pressure, r the ideal gas constant ($r = 287 J/kg/K$) and T the temperature, the error on C_p is given by

$$\frac{\triangle C_p}{C_p} = \sqrt{\left(\frac{\triangle(P-P_{17})}{P-P_{17}}\right)^2 + \left(\frac{\triangle P_a}{P_a}\right)^2 + \left(\frac{\triangle T}{T}\right)^2 + \left(2\frac{\triangle U_\infty}{U_\infty}\right)^2 + \left(\frac{\triangle r}{r}\right)^2} \quad (4.2)$$

The estimation of $\triangle(P - P_{reference})$ is given by the Furness uncertainty which should be $\pm 0.5\%$ of the value (P - $P_{reference}$) . As (P - $P_{reference}$) is read on the Furness scale, the accuracy is slightly lower. The real Furness uncertainty is estimated at $\pm 0.6\%$ of the measuring value. The other uncertainties are $\triangle Pa = 100Pa$, $\triangle T = \pm 0.2°C$ and $\triangle U_\infty = \pm 0.5\%$ of U_∞. The uncertainty on r was neglected. The uncertainty on C_p was thus found to be 1.2% of the local value.

The uncertainty on the pressure gradient could be estimated using the same method mentioned above. As $(\frac{dC_p}{ds})_{i+1/2} = \frac{C_{p_{i+1}} - C_{p_i}}{\Delta s} = \frac{P_{i+1}-P_i}{\frac{1}{2}\rho U_\infty^2 \Delta s}$ (i is the position of the pressure tap), the error on $\frac{dC_p}{ds}$ is given by equation 4.3.

$$\left(\frac{\Delta\frac{dC_p}{ds}}{\frac{dC_p}{ds}}\right)^2 = \left(\frac{\Delta(P_{i+1}-P_i)}{P_{i+1}-P_i}\right)^2 + \left(\frac{\Delta(s_{i+1}-s_i)}{s_{i+1}-s_i}\right)^2 + \left(\frac{\Delta P_a}{P_a}\right)^2 + \left(\frac{\Delta T}{T}\right)^2 + \left(2\frac{\Delta U_\infty}{U_\infty}\right)^2 + \left(\frac{\Delta r}{r}\right)^2 \quad (4.3)$$

As the real Furness uncertainty is estimated at $\pm 0.6\%$ of the measuring value, the uncertainty $\Delta(P_{i+1} - P_i)$ is estimated with a quadratic mean of the two errors as $\frac{0.6}{100}\sqrt{(P_{i+1} - P_{reference})^2 + (P_i - P_{reference})^2}$. The uncertainty was found to be 6.5% on the pressure gradient.

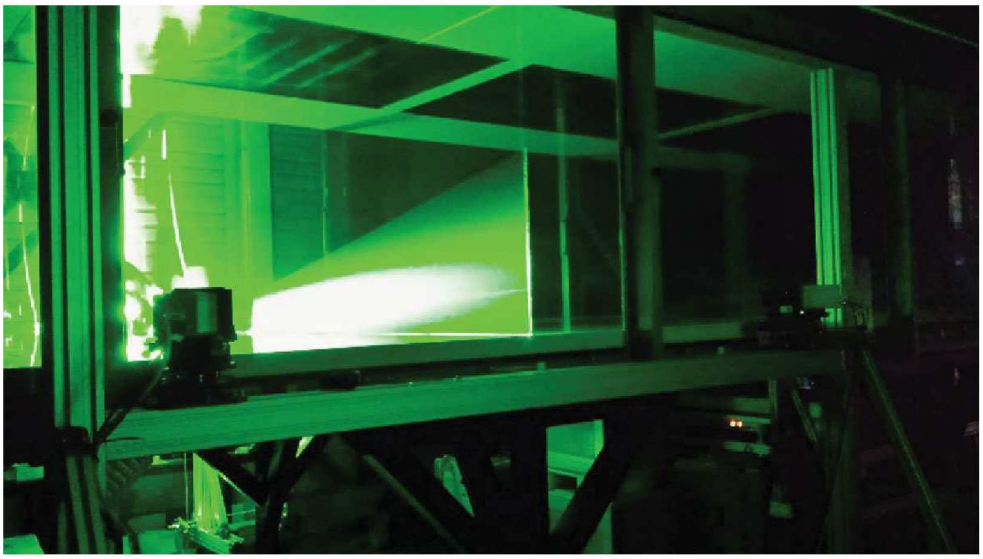

Figure 4.6: Picture of the SPIV set-up used to obtain inlet boundary conditions at x = 6.8 m.

4.2.3 Upstream boundary conditions

In order to characterize the upstream boundary conditions, a stereo PIV (SPIV) experiment was carried out at 6.8 m from the entrance of the wind tunnel.

Figure 4.6 shows the SPIV set-up and the laser light-sheet used to characterise the upstream conditions. The set-up comprised of a spanwise wall-normal plane centered at the wind tunnel test section. The field of view was imaged using two Hamamatsu 2k by 2k cameras equipped with 105mm Nikon lenses at $f_{\#} = 8$ in forward scattering (refer to figure 4.6). The tests were performed at the two velocities of the EuHIT campaign i.e 5m/s and 9m/s, measured at the wind tunnel entrance. A total of 10000 velocity fields were acquired for each test case to ensure good convergence of the mean flow and turbulence intensities. The data was processed by the modified version of the Matpiv toolbox by LML. For 2D2C mapping, only a planar target is required however for 2D3C mapping in the case of a SPIV set-up, Soloff et al. (1997) have suggested to translate the 2D target in order to recover depth information. A self-calibration similar to that proposed by Wieneke (2005)

was applied with the Soloff reconstruction method (Soloff et al. (1997)). The analysis was done with four passes starting with 48 x 64 pixels and ending with 16 x 24 pixels which was found to be the optimal final interrogation window size. Image deformation was used to improve the quality of the results. The final interrogation window size corresponds to 2.4 x 2.4 mm^2 in the physical space. The mesh spacing was 1 mm in both directions corresponding to an overlap of about 60%. This resulted in 180 points in the wall normal direction and 299 in the transverse direction. The maximum displacement was about 11 pixels in the external region.

Figure 4.7 shows the mean streamwise velocity field for both free-stream velocities investigated. The local free-stream velocity was found to be nearly constant (difference between minimum and maximum less than 0.3%),however the difference is more pronounced on the boundary layer thickness, δ as the extraction of this quantity is very sensitive to small variations in the local free-stream velocity. At 5 m/s, the mean BL thickness was 10.7 cm with a minimum value of 9.9 cm and a maximum of 11.3 cm. At 9 m/s, δ was 10.0 cm with a minimum of 9.4 cm and a maximum of 10.5 cm. These slight variations were attributed to the remains of the wake of the turning vanes in the settling chamber.

Figure 4.8 shows the mean streamwise velocity profile in the plane of symmetry for the two cases. The profiles obtained from the TRHM PIV have also been included to get a complete picture of the mean streamwise velocity in the boundary layer. The mean velocity profile at 9 m/s has been compared to hot wire data, obtained previously by Carlier and Stanislas (2005). A small adjustment in the friction velocity, U_τ was necessary to connect and match the SPIV and the TRHM PIV data. A friction velocity $U_\tau = 0.203$ m/s was used for SPIV compared to 0.204 m/s for TRHM PIV at 5 m/s and 0.351 m/s and 0.350 m/s respectively at 9 m/s. This was because the two experiments were not conducted at the same time (about one month between both experiments) which could change the viscosity marginally due to variations in atmospheric pressure. The collapse with the hot-wire data is good for the 9 m/s case as it corresponds to almost the same Reynolds number based on the momentum thickness ($Re_\theta \approx 7750$ compared to $Re_\theta \approx 7500$).

(a)

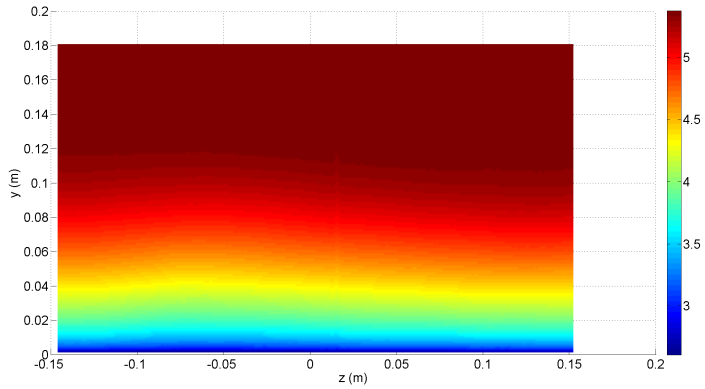

(b)

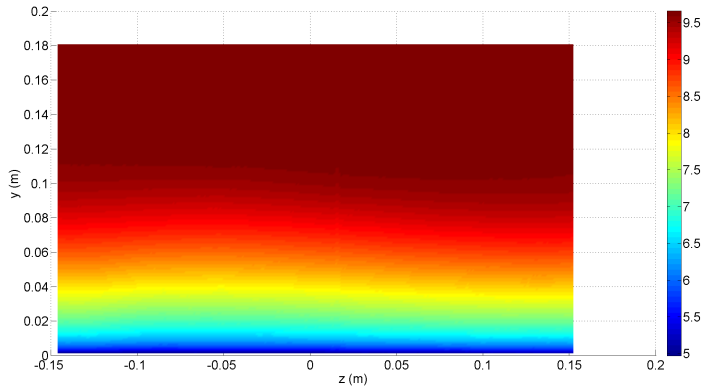

Figure 4.7: Mean streamwise velocity field U in m/s for (a) $U_\infty = 5$ m/s and (b) $U_\infty = 9$ m/s in a spanwise-wall normal plane at X = 6.8 m (2.6 m upstream of the ramp).

The boundary layer characteristics are provided in Table 4.1.

Also, a characterisation of the corner vortices developing on the side walls of the wind tunnel was performed using a spanwise/wall-normal SPIV plane. The effects of the corner flow is found to be negligible at about 200 mm from the side wall of the wind tunnel. Additional details about this experiment has been included in Appendix C.

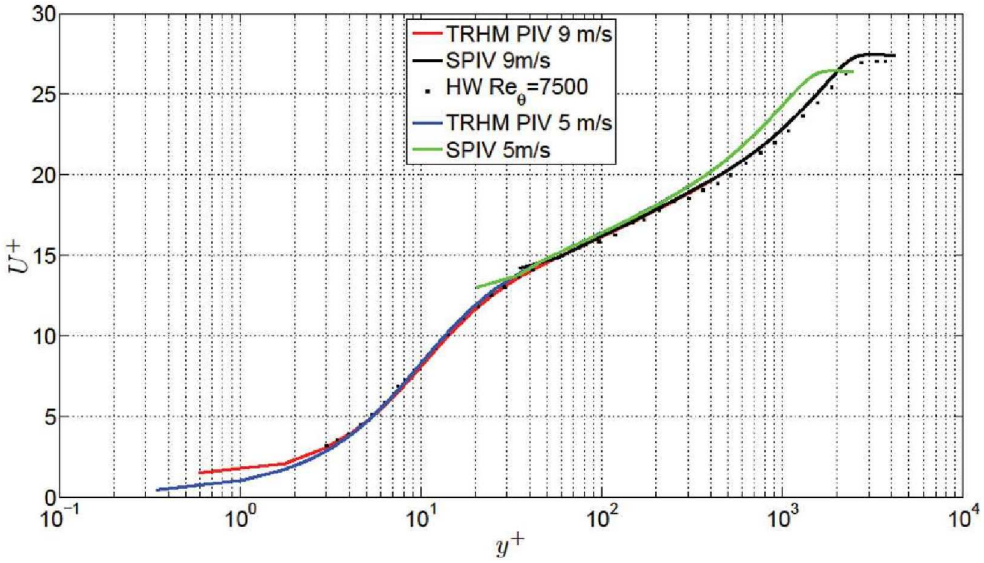

Figure 4.8: Mean streamwise velocity profile obtained 2.6 m upstream of the ramp, along the plane of symmetry for both free stream velocities. Data obtained from TRHM (time resolved high magnification) PIV and hot-wire data (HW) at $Re_\theta = 7500$ from Carlier and Stanislas (2005) are included to get a global picture of the mean streamwise velocity profile.

U_∞ (m/s)	U_e (m/s)	δ (mm)	δ^* (mm)	θ (mm)	H	Re_θ	U_τ (m/s)	β
5	5.36	109	18.0	13.1	1.37	4700	0.203	-0.069
9	9.64	102	16.4	12.0	1.37	7750	0.350	-0.049

Table 4.1: Inlet boundary layer characteristics.

Station s (m)	U_e (m/s)	δ (mm)	δ^* (mm)	θ (mm)	H	Re_θ	β
1.362	7.17	101	9.8	7.6	1.30	3630	1.28
2.392	7.33	118	12.1	9.6	1.26	4680	-0.42
3.050	7.68	117	12.1	9.6	1.27	4920	-0.50
3.497	7.80	78	05.5	4.3	1.28	2230	-0.32

Table 4.2: Boundary layer characteristics at different stations on the 1.5° plate at $U_\infty = 5$ m/s.

Station s (m)	U_e (m/s)	δ (mm)	δ^* (mm)	θ (mm)	H	Re_θ	β
1.362	12.93	95	9.0	7.0	1.29	6000	1.41
2.392	13.20	110	11.0	8.7	1.26	7630	-0.37
3.050	13.79	113	11.3	8.9	1.27	8170	-0.33
3.497	14.03	71	04.5	3.5	1.29	3280	-0.24

Table 4.3: Boundary layer characteristics at different stations on the 1.5° plate at $U_\infty = 9$ m/s.

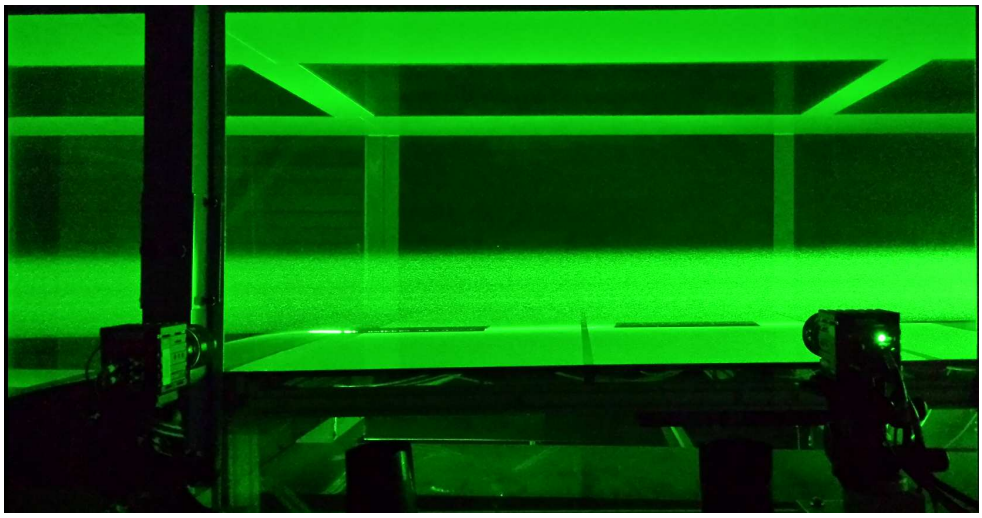

Figure 4.9: Picture of the 2D2C set-up used to characterise the FPG flow on the 1.5° plate.

4.3 Flat plate FPG flow

4.3.1 PIV Analysis

The flow above the 2.14 m long flat plate inclined at 1.5° with respect to the horizontal was characterised through 2D2C PIV for the two free-stream velocities (U_∞ = 5 and 9 m/s). The aim was to characterise the accelerating flow upstream of the APG. The light sheet was introduced in the same manner as the large field 2D2C PIV in the APG region also using the same optics. The mirror inside the wind tunnel located downstream of the model was raised by 50 cm. The light sheet was 1 mm in thickness on the 2.14 m of the 1.5° plate.

The experiment was conducted in two set-ups. The first was with two sCMOS cameras close to the end of the 1.5° plate with an overlap of 10 mm between both fields of view forming a global field of view of 46.5 cm long and 19.8 cm in height above the wall. This field of view was positioned to get a 7 mm overlap with the large field APG-TBL set-up. The second set-up (refer figure 4.9) also used two sCMOS cameras, however without any

overlap between them. The field of view of each camera was 23.6 cm along the wall and 19.5 cm in the wall-normal direction. The field of view of the first camera began at 1.5° plate and the second was located close to the middle of this plate. For both cases, the cameras were equipped with Nikon 105 mm lenses at $f_{\#} = 5.6$. The time interval between frames was tuned to obtain 12 pixels of displacement in the free-stream region to ensure sufficient velocity dynamic range for the turbulence intensity measurements. For the first set-up, 30,000 PIV fields were recorded for the two velocities and 10,000 for the second set-up. The data were processed in the same way similar to the previous subsection by the modified version of the Matpiv toolbox by LML. The final interrogation window size corresponded to 2.25 mm by 2.25 mm in the physical space. The grid spacing was selected as 0.94 by 0.94 mm leading to an overlap of 58%.

4.3.2 Statistical results

Figure 4.10 shows the evolution of the mean streamwise velocity profiles for both velocities along the 1.5° plate normalised with the respective reference velocities, U_∞. The wall-normal distance, $'y'$ is normalised by the boundary layer thickness, δ_0 taken at s = 1.362 m, which is 101 mm at 5 m/s and 95 mm at 9 m/s (refer tables 4.2 and 4.3). The first profile at s = 1.362 m located just after the beginning of the 1.5° plate exhibits a small peak close to $y/\delta_0 = 0.15$. The external velocity is about 1.4 U_∞ due to the contraction upstream. At the second station, the peak is still visible but is strongly attenuated and is located further away from the wall ($y/\delta_0 = 0.4$). After this station, the peak disappears. The mean velocity is increasing continuously from the beginning of the plate to its end due to the FPG encountered, with an external velocity reaching 1.55 U_∞ at the last station. At the last station located very close to the ramp articulation, the acceleration is highly marked due to the strong FPG generated by the sudden change of flow direction. Tables 4.2 and 4.3 show the boundary layer characteristics on the 1.5° plate at the stations depicted in figure 4.10 for $U_\infty = 5$ and 9 m/s respectively. The evolution of the shape factor indicates a similar behaviour of the boundary

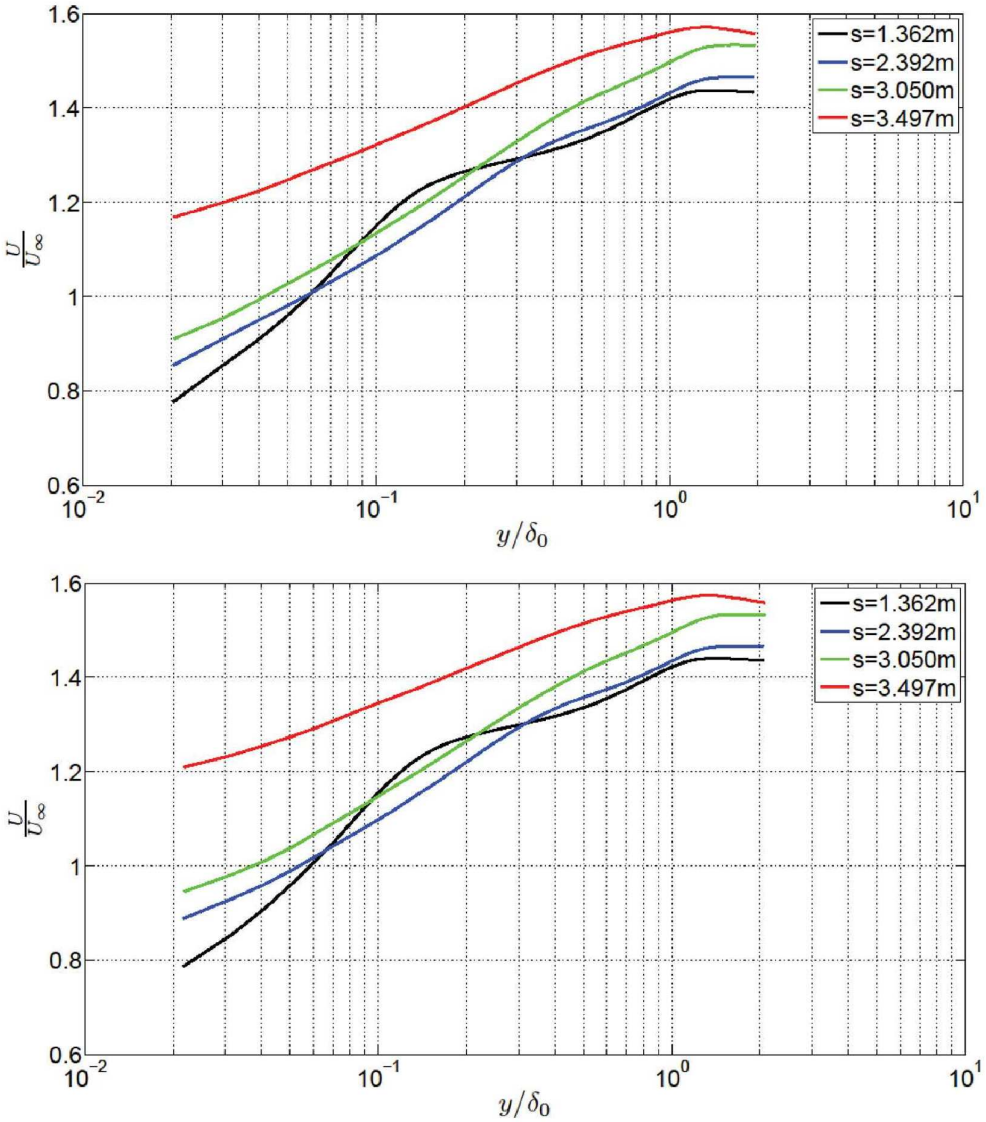

Figure 4.10: Evolution of the mean streamwise velocity profiles along the 1.5° plate, (top) $U_\infty = 5$ m/s, (bottom) $U_\infty = 9$ m/s. δ_0 is taken at s = 1.362 m

layer at the two Reynolds numbers in this region of the flow.

Figure 4.11 shows the evolution of the streamwise turbulence intensity profiles for both velocities along the 1.5° plate. For both velocities, the standard near wall peak is not accessible as the first measurement point is

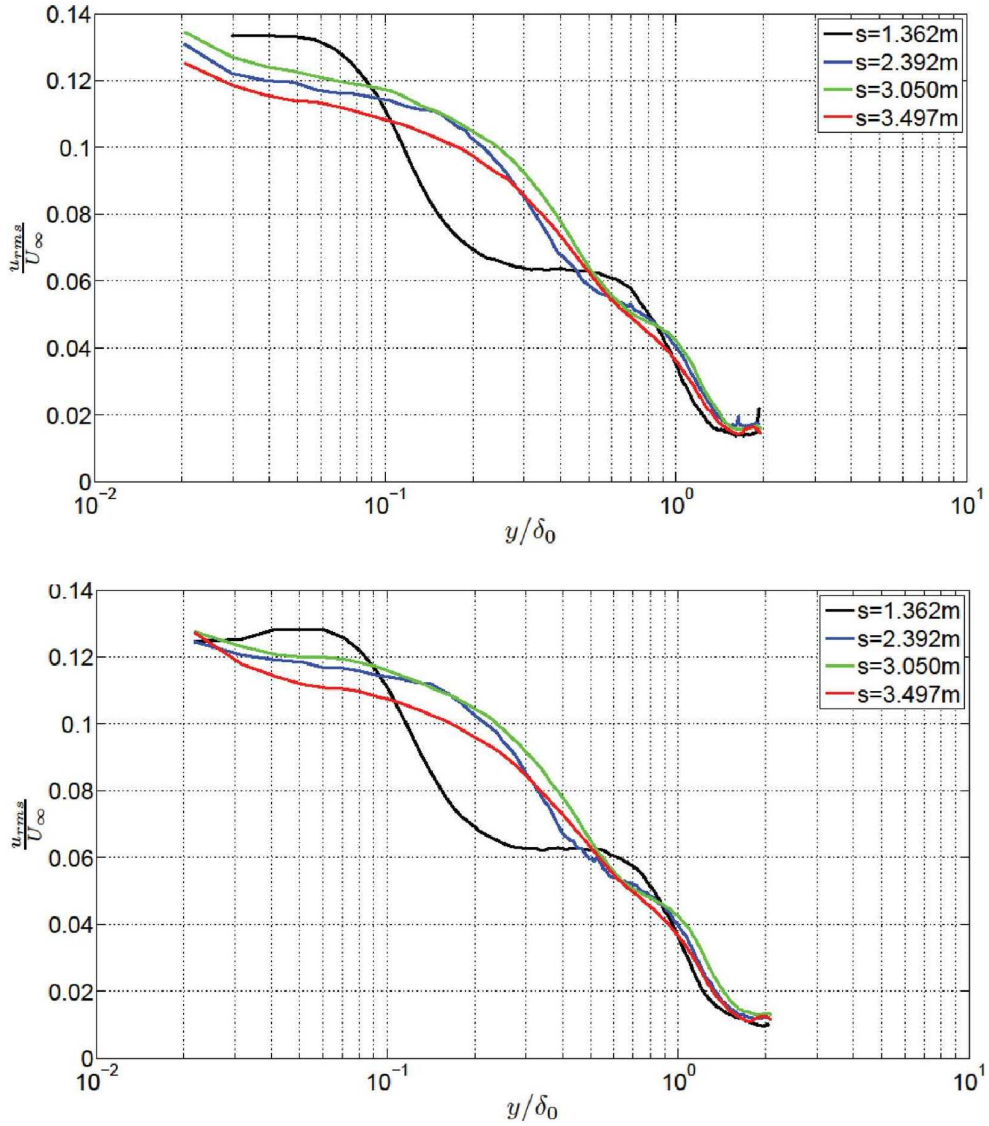

Figure 4.11: Evolution of the streamwise turbulence intensity profiles along the 1.5° plate, (top) $U_\infty = 5m/s$, (bottom) $U_\infty = 9m/s$. δ_0 is taken at s = 1.362m.

too far from the wall. The first profile at s = 1.362 m shows a small plateau close to $y/\delta_0 \sim$ 0.03-0.05. This plateau was also observed earlier by Cuvier et al. (2014) for a different configuration of the model. This phenomenon is probably due to the strong and short APG encountered at the end of

the converging part of the model (see Figure 4.3). In the outer part, a second plateau is clearly visible in the first profile, close to $y/\delta_0 \sim 0.5$, which progressively transforms into a vanishing kink at the following stations. This second plateau is probably linked to the external turbulence of the incoming boundary layer which is seriously attenuated by the strong FPG encountered in the converging part of the ramp. At s = 3.497 m, both the kinks are nearly smoothed out.

Figure 4.12 shows the evolution of the wall-normal turbulence intensity profiles for both velocities. At the first station, the shape is similar to the streamwise component, however the plateaus are replaced by well-defined peaks. At the following stations, the outer peak spreads out and nearly disappears while the one closer to the wall stays fairly visible.

Figure 4.13 shows the evolution of the Reynolds shear stress profiles for both velocities. The behaviour is strongly influenced by the wall-normal component of the fluctuations (see Figure 4.12).

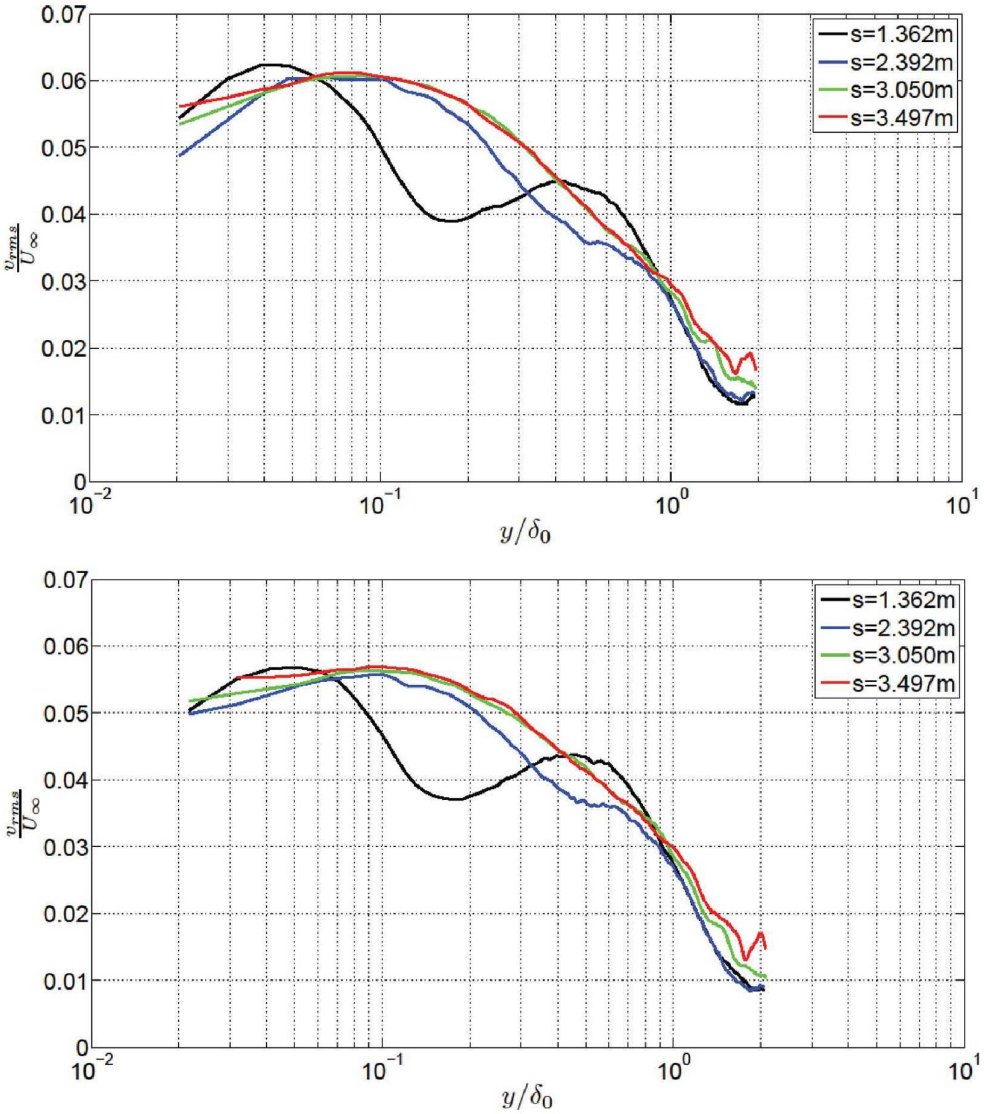

Figure 4.12: Evolution of the wall-normal turbulence intensity profiles along the 1.5° plate, (top) $U_\infty = 5$ m/s, (bottom) $U_\infty = 9$ m/s. δ_0 is taken at s = 1.362m.

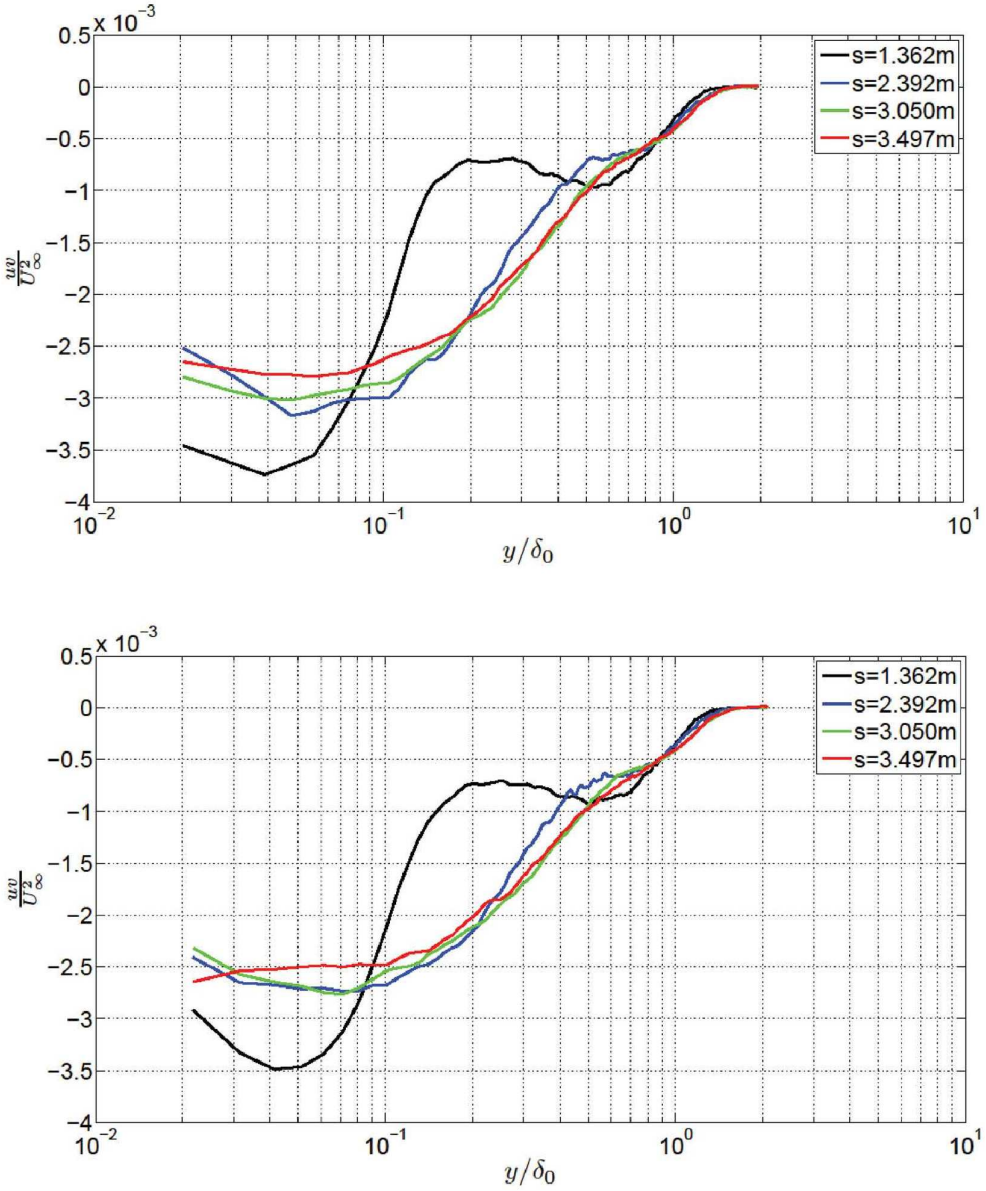

Figure 4.13: Evolution of the Reynolds shear stress profiles along the 1.5° plate, $U_\infty = 5$ m/s (top), $U_\infty = 9$ m/s (bottom). δ_0 is taken at s = 1.362 m.

4.4 APG ramp flow

4.4.1 PIV analysis

The large field 2D2C PIV measurements were performed in a streamwise wall-normal plane, 3.5 m long placed in the middle of the test section (XY

Figure 4.14: The set of 16 sCMOS cameras aligned in series and mounted on the side of the wind tunnel. The target used for calibration is placed along the centerline of the ramp

plane at Z = 0). The setup comprised of 16 sCMOS cameras built in order to study the boundary layer development in the region of an APG with a high spatial resolution while at the same time ensuring the possibility of capturing the very long turbulent structures ($\approx 14\delta$).

Figure 4.14 shows the 16 sCMOS cameras placed in series beside the wind tunnel test section. Out of these 16 cameras, 8 (number 1-8) were provided by UniBw, 6 (number 9-14) by DLR Gottingen, and 2 cameras (number 15 and 16) by LML. All the cameras were fixed on the same 3.5 m long X95 bench and mounted on Manfrotto 410 articulations to allow the tuning of the cameras normal to the side glasses and parallel to the ramp surface. The cameras were mounted at 90° so that the side of the sensor corresponding to 2560 pixels was aligned with the wall-normal direction. This was done in order to obtain the best resolution of 25 cm in height. The field of view of each camera was 230 mm along the wall and 273 mm in the wall normal direction. A common region of about 10 to 20 mm was set between each camera to obtain a continuous field. All but three cameras were equipped with macro

planar 100 mm Zeiss lens at a working distance of 1680 mm. To avoid the shadow of the side pillars of the wind tunnel (see Figure 4.14), camera 6 and 13 (with camera 1 being the first, upstream) were equipped with 85 mm Zeiss lens at a working distance of 1445 mm while camera 14 with a 50 mm Zeiss lens operating at a working distance of 1050 mm. The f number was #4 for all cameras except for cameras 6, 15 and 16 where it was fixed at 2.8, 4.8 and 4.8 respectively due to presence of the wind tunnel frame. The fields of view for all cameras were of the same order of approximately 230 mm in the streamwise direction and 255 mm in the wall normal direction. The LML BMI YAG laser system placed 11.6 m from the inlet of the test section with 2 x 200 mJ 532 nm was used to generate the light-sheet with a height of approximately 260 mm and a thickness of approximately 1 mm over a length of about 3 m. This laser light sheet was produced by passing the laser beam through a spherical lens with a focal length of 7500 mm and then through a diverging cylindrical lens having a focal length of -250 mm. This light sheet was introduced to the tunnel using a mirror placed at 45° downstream to the ramp model that directed the laser sheet vertically upwards. The second mirror was located inside the test section, 87 cm downstream of the end of the ramp. This mirror directed the laser sheet along the 3.5m long APG section (refer figure 4.15). The backside of the mirror was equipped with an aerodynamic profile to limit the vibration due to vortex shedding. A PEG smoke generator was used for all measurements to seed the whole flow with particles having a mean size of 1μm.

A total of 30 000 samples were recorded at a frequency of 4 Hz for two free stream velocities of 5 and 9 m/s.

The modified version of MatPIV toolbox by LML, under Matlab was used to process the acquired images. The magnification for each camera and the merging regions, was obtained by placing a calibration target across the field (refer figure 4.14). The images obtained of this target by the sixteen cameras were then processed to merge the target pictures of these cameras into one picture. The magnifcation of each camera together with the coordinates in this picture of the four extreme points of the fields of view of each camera was obtained. This entire target picture and these output parameters was used

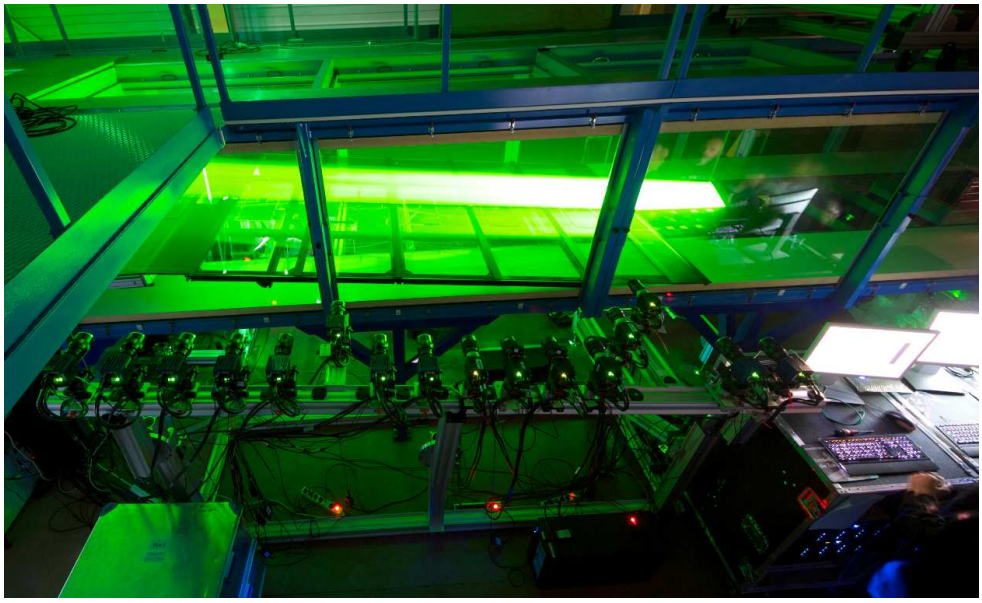

Figure 4.15: Photo of the large field 2D2C PIV experimental set-up showing the laser sheet parallel to the direction of flow

to create the mesh. The mean background images were first mapped using a basic pinhole model and the reflection (i.e wall position) was manually fitted with a line. A mesh was then built above this line in the mapped images (spacing of about 1.07 mm by 1.07 mm corresponding to 10 pixels by 10 pixels) and projected on each camera with the pinhole models. The analysis was then done with these projected grids. Four passes were used (first pass 64x64 pixels, second and third of 32x32 pixels and a final pass of 24x24 pixels with a mean overlap of 65%). Image deformation was used before the final pass with a cubic b-spline interpolation of the grey level and bilinear interpolation for the displacement to improve the result quality. Also background division was used to limit the effect of the laser reflection and the camera noise. The final grid then had 3250 points along the wall and 238 points in the wall-normal direction corresponding to a region 3.41 m long and 0.25 m high with a grid spacing of 1 mm.

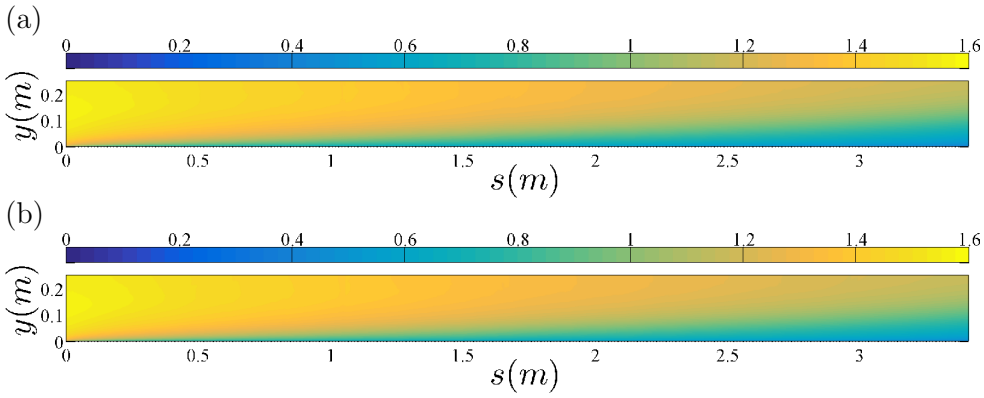

Figure 4.16: Mean streamwise velocity (U/U_∞) fields along the $-5°$ APG ramp (a) $U_\infty = 5$ m/s (b) $U_\infty = 9$ m/s.

4.4.2 Mean velocity and scaling

4.4.2.1 Mean flow development

Figure 4.16 (a) and (b) shows the evolution of the mean streamwise velocity normalised with the reference free-stream velocity U_∞ along the $-5°$ plate for both velocities studied. In this section, $s = 0$ now corresponds to the beginning of the 3.5 m long flat plate inclined at $-5°$ with respect to the horizontal. Due to the enlargement of the test section along the APG plate, the flow decelerates continuously but does not separate. As expected for a boundary layer subjected to an APG, the thickness of the boundary layer increases rapidly such that the ratio between the local free-stream velocity at the beginning and at the end of the 3.5 m long field is 1.45.

To obtain quantitative information on the evolution of the mean streamwise velocity, profiles for both free-stream velocities along the APG plate normalised by U_∞ and δ_0 are shown in Figure 4.17. As the flow has been accelerated on the convergent and the 2.14m long flat plate, the velocity is globally higher than the freestream for the first profile at $s = 3.5$m, located at the beginning of the ramp. The external velocity is then progressively reduced by the APG. It is also interesting to note the similarity in the profiles for the two test cases.

The velocity components are generally scaled based on the friction veloc-

(a)

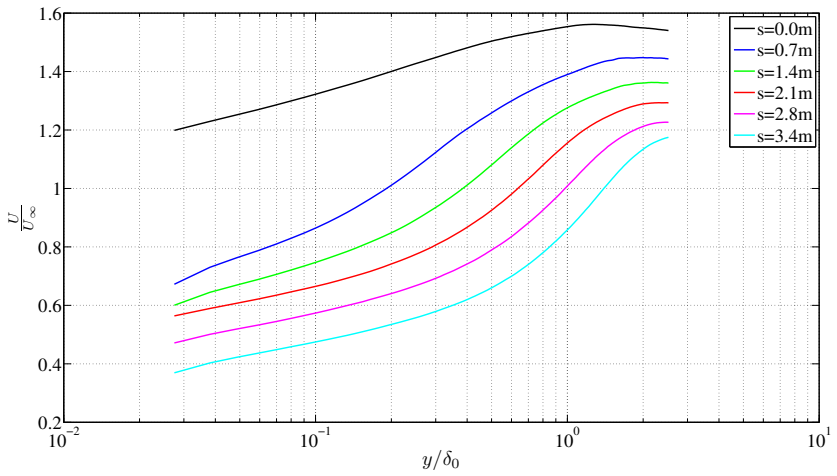

(b)

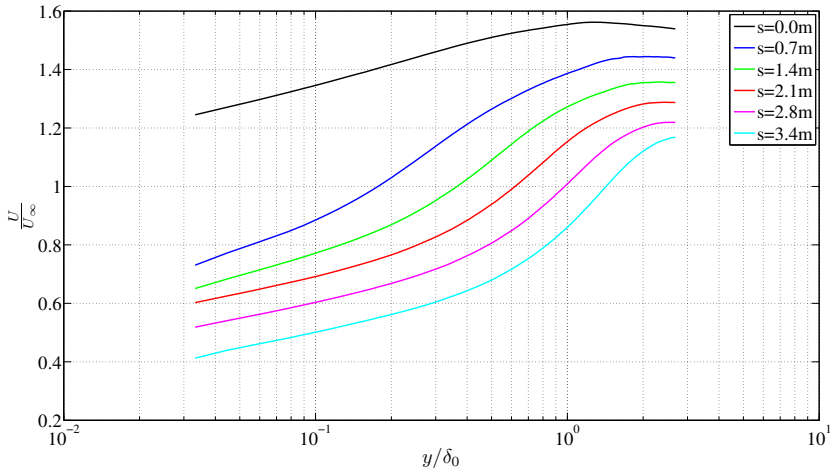

Figure 4.17: Evolution of the mean streamwise velocity profiles along the $-5°$ APG ramp (a) $U_\infty = 5$ m/s, (b) $U_\infty = 9$ m/s. δ_0 is 101 mm at 5 m/s and 95 mm at 9 m/s (see section 4.3.2)

ity (U_τ) and therefore it is important to use a proper method to estimate U_τ. We shall now see how the friction velocity, U_τ was determined.

4.4.2.2 Determination of friction velocity (U_τ)

The Clauser chart method (Clauser (1954)) has been traditionally used to determine the friction velocity, U_τ in wall-bounded flows. It relies on the existence of the log-law region near the wall, i.e by plotting U^+ vs y^+ on a semi logarithmic scale along the x-axis, the overlap region of the boundary layer plots as a straight line. This straight line relationship is known as the log-law as seen in Section 2.1, given by the relation

$$\frac{U(y)}{U_\tau} = \frac{1}{\kappa} log\left(\frac{yU_\tau}{\nu}\right) + B \tag{4.4}$$

The presence of the logarithmic region in APG flows is still a contentious issue (Anderson (2011), Monty et al. (2011)). In addition to ZPG flows, Monty et al. (2011) showed that the skin friction determined from the Clauser chart method agreed with that obtained from oil-interferometry for mild APG boundary layer flows at $Re_\theta = 11860$. Up to a $\beta < 3$, the skin friction obtained between both methods showed a good match. However beyond $\beta \approx 3$, the difference between both methods became significant, up to approximately 10% difference in C_f where

$$C_f = \frac{\tau_w}{\frac{1}{2}\rho U_\infty^2} = 2\frac{U_\tau^2}{U_\infty^2} \tag{4.5}$$

Thus, this study suggests that the Clauser chart method could be used for mild APG flows but should be used with caution for strong APG flows as inaccurate values of U_τ could lead to inaccurate conclusions concerning the scaling arguments for pressure gradient boundary layers.

From equation 4.4, $U(y)$ can be measured directly from experiments and assuming that ν, κ and B are constants, the only undetermined term is U_τ. This can be determined by using a least squared fit on the data between the region $30 \leq y^+ \leq 200$ (Cuvier et al. (2014)), beyond which a departure from the log-law was observed across the APG plate (refer figure 4.19). Figure 4.18 shows the development of U_τ across the APG ramp for both test cases. The solid lines indicate the value of U_τ for both test cases obtained using the Clauser chart method on the large field streamwise (LFStW) 2D2C PIV

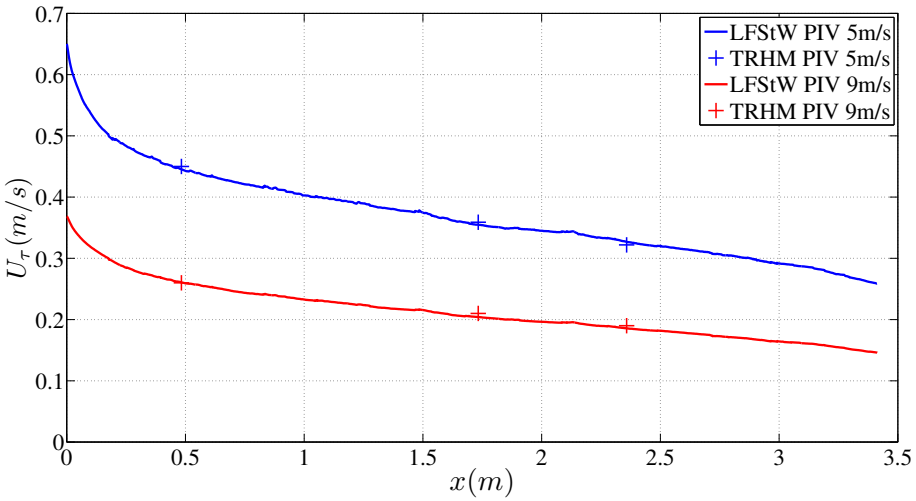

Figure 4.18: Distribution of the friction velocity, U_τ along the $-5°$ plate at $U_\infty = 5$ m/s and $U_\infty = 9$ m/s respectively. Symbols: '+' has been obtained from time resolved high magnification (TRHM) PIV and solid lines have been obtained from the Clauser chart method using the large field streamwise (LFStW) PIV data.

data while the crosses indicate U_τ obtained at the three stations using the time resolved high magnification (TRHM) PIV from Cuvier et al. (2017).

The friction velocity was obtained from the TRHM PIV by the wall-shear rate measurement technique developed by Willert (2015) that retrieves actual velocity data from the imaged sequences to estimate the mean wall-shear rate. The method relies on the one-dimensional cross-correlation of single, streamwise rows of pixels that are taken at the same wall-normal distance but separated by a few time steps (here 2–5 time steps). A one-dimensional Gaussian peak fit at the location of maximum correlation then provides sub-pixel accurate displacement information, which, in conjunction with magnification factor, M and time difference Δt, would yield an estimate of the streamwise velocity for the given wall distance. Then, estimates of the mean streamwise velocity for each wall distance are obtained by averaging the instantaneous velocity estimates over the entire length of the sequences. Finally, a least squares fitting to the linear portion of this data provided an

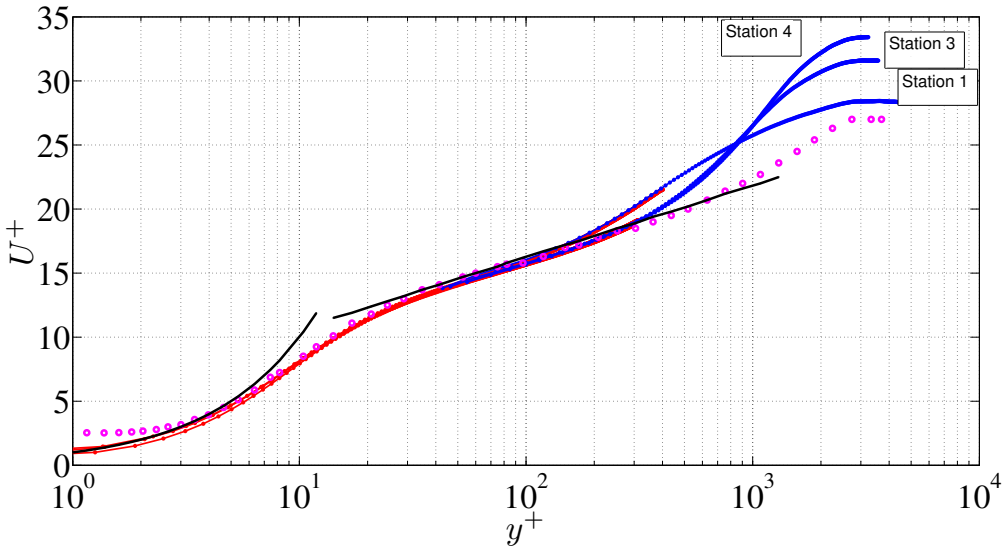

Figure 4.19: Mean streamwise velocity profiles at the three stations: 0.343 m (station 1), 1.733 m (station 3) and 2.358 m (station 4), on the $-5°$ plate at $U_\infty = 5$ m/s. Profile with the symbol 'o' corresponds to a ZPG flow case from Carlier and Stanislas (2005) at $Re_\theta = 8100$

estimate of the average wall shear rate that is directly proportional to the wall shear stress τ_w.

The values of U_τ estimated from TRHM PIV and LFStW PIV for the test cases at $U_\infty = 5$ m/s and $U_\infty = 9$ m/s are reported in tables 4.4 and 4.5. Also from figure 4.18, a good agreement on U_τ (within 3%) from the two methods is noted for both the test cases. This suggests that the Clauser chart technique could indeed be used to determine U_τ across the APG ramp with a fairly high accuracy.

We could make use of both techniques (TRHM PIV and LFStW PIV) to get an entire picture of the turbulent boundary layer at the three stations. Figure 4.19 shows the entire inner-scaled mean streamwise velocity, from the viscous sublayer to the wake region at these three stations for the test case at $U_\infty = 5$ m/s. ZPG data from Carlier and Stanislas (2005) at $Re_\theta = 8100$ is plotted with symbols for comparison. The near wall and part of the overlap region shown in red were obtained from the TRHM PIV while the overlap

	TRHM PIV U_τ (m/s)	LFStW PIV U_τ (m/s)
Station 1 (s = 0.48 m)	0.26	0.261
Station 3 (s = 1.73 m)	0.21	0.204
Station 4 (s = 2.35 m)	0.19	0.186

Table 4.4: Values of U_τ from TRHM (time resolved high magnification) PIV and LFStW (Large field streamwise) PIV at the measurement stations measured from the start of the APG ramp at $U_\infty = 5$ m/s

	TRHM PIV U_τ (m/s)	LFStW PIV U_τ (m/s)
Station 1 (s = 0.48 m)	0.46	0.445
Station 3 (s = 1.73 m)	0.36	0.355
Station 4 (s = 2.35 m)	0.32	0.327

Table 4.5: Values of U_τ from TRHM (time resolved high magnification) PIV and LFStW (Large field streamwise) PIV at the measurement stations measured from the start of the APG ramp at $U_\infty = 9$ m/s

and outer regions shown in blue were obtained from the LFStW PIV. A good agreement between both methods is noted. It is then interesting to observe a logarithmic region ($30 \lesssim y^+ \lesssim 300$) indicated by a solid black line on all APG profiles but with a limited extent compared to the ZPG flow. The mean velocity of the APG case also drops below the classical log law in the overlap region while it rises higher than the ZPG case (refer figure 4.19) in agreement with Monty et al. (2011).

4.4.2.3 Boundary layer parameters

The evolution of the mean streamwise velocity along the $-5°$ plate was shown earlier in figure 4.16. From these mean velocity profiles, boundary layer parameters can be obtained and are given in tables 4.6 and 4.7. The boundary layer thickness, δ is defined by the distance from the wall where the mean streamwise velocity, U reaches 99% of the local free-stream velocity, U_e. The displacement thickness (δ^*) and momentum thickness (θ) were obtained by integrating the profile using the trapezoidal rule. The shape factor is given by $H = \frac{\delta^*}{\theta}$. $Re_\theta = \frac{U_e \theta}{\nu}$ is the Reynolds number based on the momentum

s (m)	U_e (m/s)	δ (mm)	δ^* (mm)	θ (mm)	H	Re_θ	β
0	7.70	66	3.9	2.9	1.34	1470	-0.26
0.7	7.22	135	18.7	13.4	1.40	6430	1.42
1.4	6.81	161	26.1	18.0	1.45	8180	2.04
2.1	6.47	183	33.9	22.8	1.49	9840	2.01
2.8	6.13	205	44.2	28.4	1.56	11600	3.68
3.4	5.87	231	58.7	35.2	1.67	13790	-

Table 4.6: Boundary layer characteristics at different stations on the $-5°$ plate at $U_\infty = 5$ m/s.

thickness and $\beta = \frac{\partial P}{\partial s}\frac{\delta^*}{\rho U_\tau^2}$ is the non-dimensional pressure gradient parameter.

Although the profiles of the mean streamwise velocity are quite similar between the last station of the FPG (figure 4.10) and the first station of the APG (figure 4.16), a significant difference appears in the value of the shape factor. This indicates that the strong variations of the pressure gradient observed in figure 4.3 close to the articulation of the APG ramp significantly affects the near wall region. The reduction of the external velocity by a factor of about 1.3 along the 3.5m plate is accompanied by a notable increase of the boundary layer thickness by a factor of about 4. Figure 4.20 shows the evolution of δ, δ^* and θ along the APG ramp for the two test cases. In addition to the growth of δ, the integral parameters (δ^*, θ) also increase and the resulting values of the shape factor, H across the APG ramp indicates that the boundary layer is far from separation as the value of the shape factor reported in the literature for separation is about 2.7 (Alving and Fernholz (1996); Castillo et al. (2004); Kline et al. (1983))

4.4.2.4 Scaling of the mean flow

From a modelling perspective, the possibility of self-similarity of a boundary layer subjected to a pressure gradient has been an important issue. Methods for universally describing turbulent flows have long been sought after with a view to improve modelling and computational accuracy (Anderson et al. (2004)). Castillo and George (2001) addressed this issue by extending the equilibrium-type similarity analysis of George et al. (1997) for the outer part

s (m)	U_e (m/s)	δ (mm)	δ^* (mm)	θ (mm)	H	Re_θ	β
0	13.86	57	2.8	1.9	1.47	1720	-0.19
0.7	12.96	128	16.7	12.1	1.38	10490	1.53
1.4	12.20	154	23.3	16.5	1.41	13420	1.94
2.1	11.59	175	30.5	21.0	1.45	16240	2.27
2.8	10.97	196	39.5	26.3	1.51	19230	3.74
3.4	10.51	226	53.7	33.4	1.61	23430	-

Table 4.7: Boundary layer characteristics at different stations, 's' on the $-5°$ plate at $U_\infty = 9$ m/s.

of ZPG boundary layers to include boundary layers with pressure gradient. Through their analysis, they concluded that the local free-stream velocity, U_e is the appropriate scale for the mean velocity (refer section 2.3.2). Furthermore, Castillo and George (2001) showed how the mean deficit profiles of developing APG flows can be scaled with $U_e\delta^*/\delta$ of Zagarola and Smits (1998a). In this section, the scaling of the velocity deficit is presented in two different ways. Firstly, it is scaled with the CG scaling (Castillo and George (2001)), the free-stream velocity (U_e) and secondly with the ZS scaling (Zagarola and Smits (1998a)), $U_e\delta^*/\delta$. Finally, the equilibrium pressure gradient parameter developed by CG is tested on the APG data to corroborate the existence of self-similarity of boundary layers subjected to APG.

Contrary to internal flows, where the outer length scale δ is exactly defined through the geometry, the counterpart for semi-confined flows such as boundary layers "can hardly be exactly defined" (Rotta (1953)). The problem is commonly circumvented by using integral quantities such as the displacement thickness δ^*, e.g. through usage of the Rotta-Clauser outer scale $\Delta = U_\infty^+\delta^*$ (Vinuesa et al. (2016)). For complex turbulent boundary layer configurations such as the current study involving pressure gradients, the problem becomes even more apparent and even commonly used wake descriptions in the case of ZPG boundary layers are unable to accurately describe the data. Thus in addition to the standard definition of δ_{99} used in the previous section, δ_{95} (distance from the wall where the streamwise velocity U reaches 95% of the external velocity U_e) is also used as the outer length

(a)

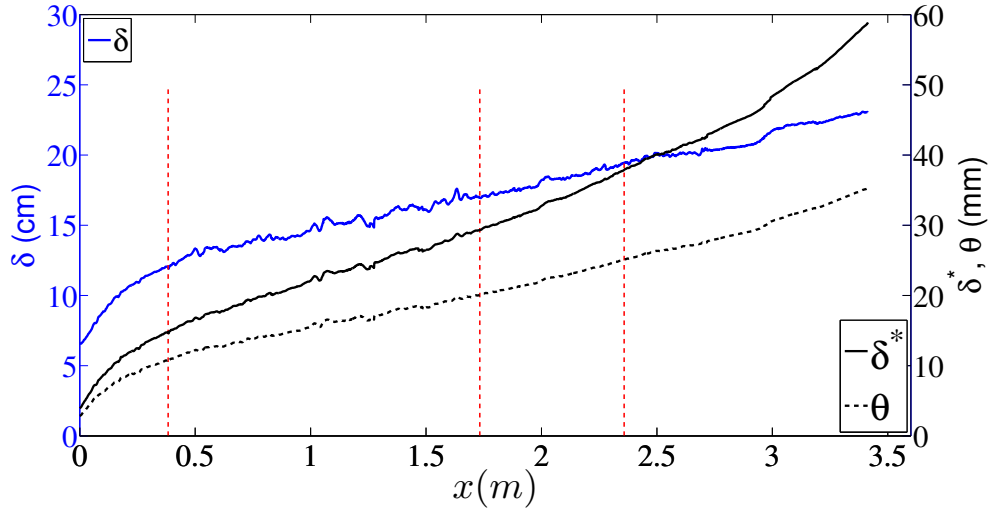

(b)

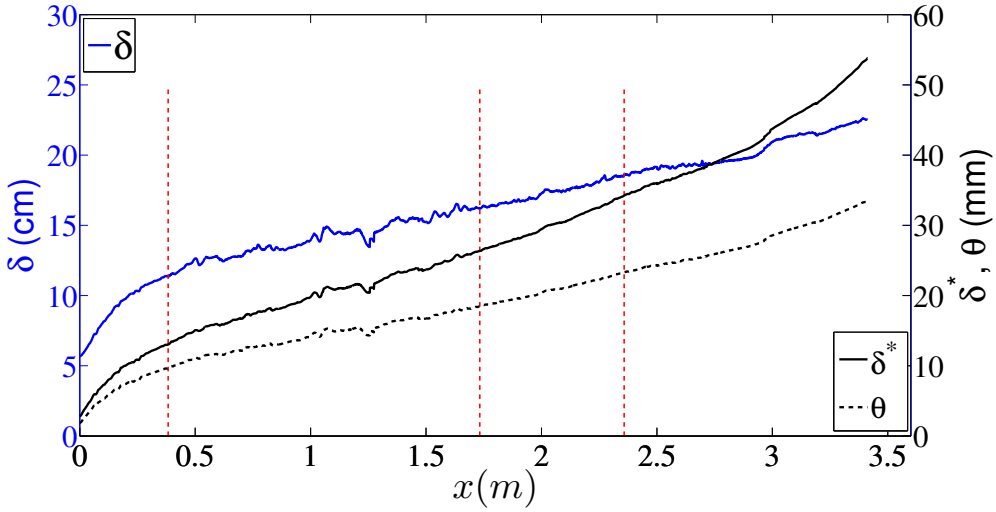

Figure 4.20: Evolution of δ, δ^*, θ along the $-5°$ APG ramp at (a) $U_\infty = 5$ m/s and (b) $U_\infty = 9$ m/s.

scale with perhaps less determination error following CG.

Figure 4.21 shows the velocity deficit scaled with the freestream velocity, U_e for the cases at $U_\infty = 5$ m/s and $U_\infty = 9$ m/s respectively. Both flows don't show a perfect collapse. The trends of the deficit profiles scaled with the CG scaling, U_e for both cases are that there is an increase in magnitude

(a)

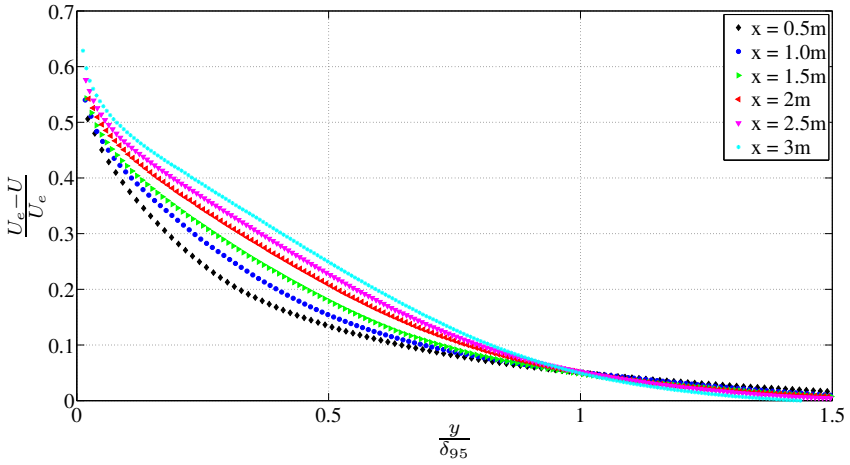

(b)

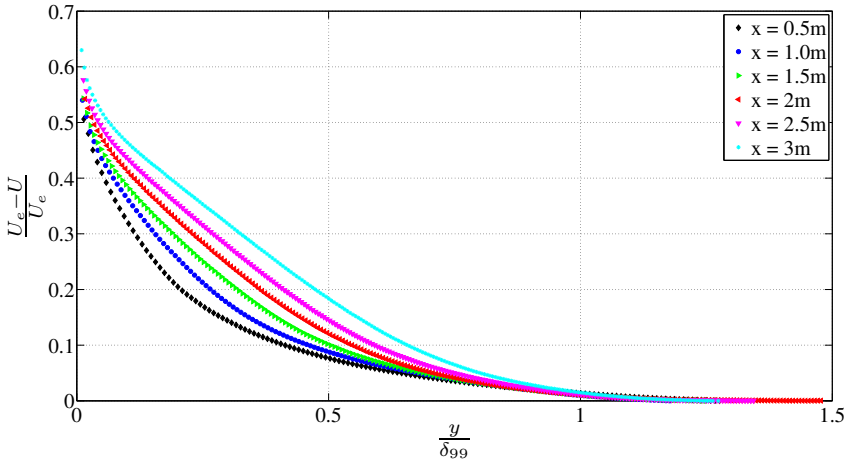

Figure 4.21: Mean velocity deficit scaled with the free-stream velocity U_e at $U_\infty = 9$ m/s, with the wall normal distance, 'y' normalised by (a) δ_{95} and (b) δ_{99}

with downstream location, such that the first streamwise profile has the lowest magnitude and the profile located furthest downstream, has the largest magnitude. However, it is important to keep in mind that using the CG scaling, U_e, the deficit profiles are not expected to collapse into a single curve. The profiles should converge towards an asymptote as the local Reynolds number increases (Castillo and George (2001)).

(a)

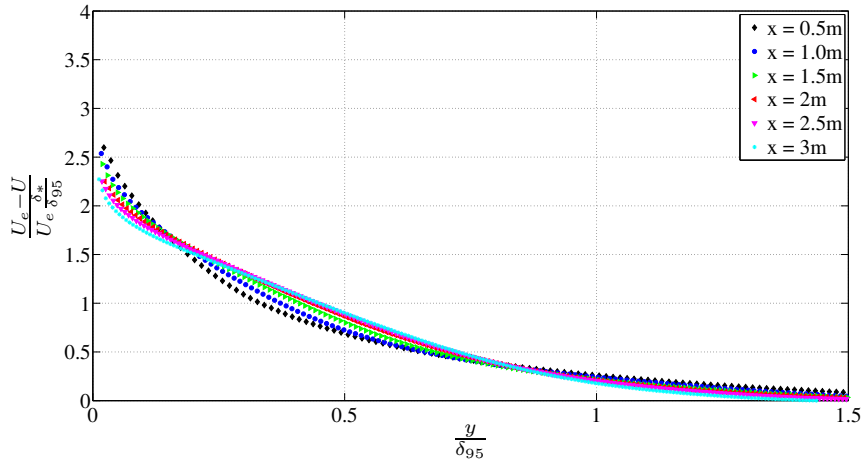

(b)

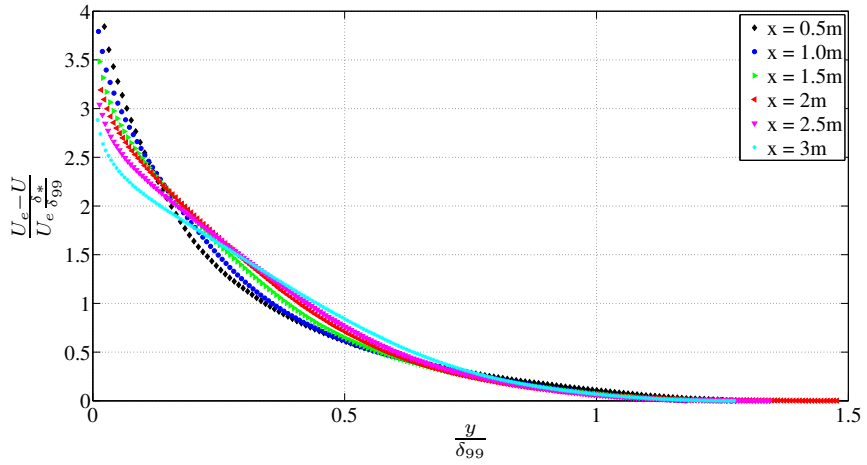

Figure 4.22: Mean velocity deficit scaled with the ZS scale $U_e\frac{\delta^*}{\delta}$ at $U_\infty = 9$ m/s, with the wall normal distance, 'y' normalised by (a) δ_{95} and (b) δ_{99}

In their study, CG also showed how the scaling of ZS collapsed the velocity profiles for the developing cases of pressure gradient flows. As described in section 2.3.2, ZS empirically determined a new scaling $U_e\delta^*/\delta$ for the velocity deficit in the outer region of a developing pipe or a channel flow (Zagarola and Smits (1998a)). They later showed that the velocity profiles collapsed for ZPG turbulent boundary layer on a smooth surface with this scaling (Zagarola and Smits (1998b)). Castillo and Walker (2002) showed that the

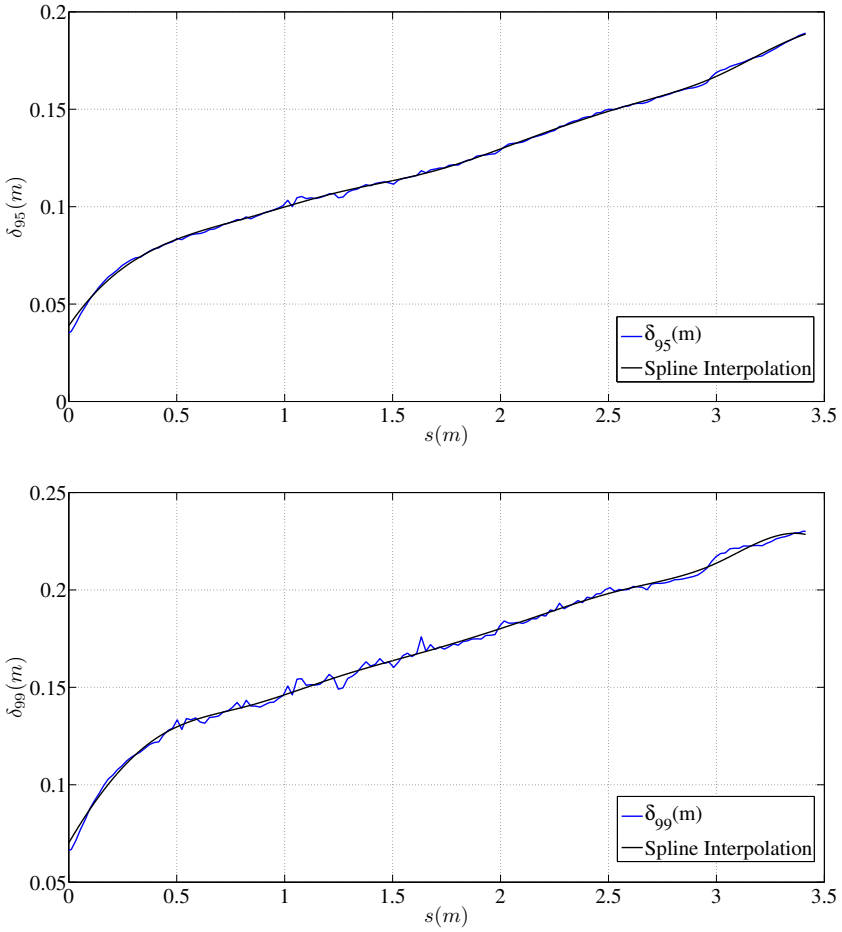

Figure 4.23: Evolution of the boundary layer thickness (a) δ_{95} (b) δ_{99} along the $-5°$ APG ramp as a function of the streamwise coordinate (blue). The black line is a smoothed profile obtained by least square spline interpolation.

ZS scaling successfully removes the Reynolds number dependence in the outer flow and it leads to only three basic velocity profiles: one each for APG, FPG and ZPG boundary layers consistent with the results for CG based on studies of equilibrium conditions on the pressure gradient parameter, $\Lambda = (-\frac{\delta}{\rho U_\infty^2 d\delta/ds}\frac{dP_\infty}{ds})$.

Figure 4.22 shows the velocity deficit data scaled with the ZS scaling, $U_e\delta^*/\delta$ for the test cases at $U_\infty = 5$ m/s and $U_\infty = 9$ m/s respectively. As

mentioned earlier, applying the ZS scaling to mean velocity deficit profiles can remove the Reynolds number dependence, and it is expected to result in a collapse of profiles. Compared to the CG scaling shown in figure 4.21, we observe a much better collapse of the profiles for both test cases. The profiles corresponding to the streamwise location of 0.5m and 1m do not fall within the bandwidth of collapse compared to the other streamwise stations. This might be as a result of the flow in this region still being under transition from FPG to APG and thus, the region on the -5° ramp encompassing these two streamwise locations do not have a typical APG behaviour; i.e, whilst all these flows are APG flows, FPG behaviour is also evident and flow development is causing this spread. Only after the flow reaches equilibrium, a good collapse of the data is observed from 1.5m up to 3m. The pressure gradient parameter, Λ is used to further confirm this equilibrium flow state.

As discussed in section 2.3.2, CG defined the boundary layer equilibrium state differently compared to Clauser (1954), $\beta = \frac{\partial P}{\partial s}\frac{\delta^*}{\rho U_\tau^2} =$ constant. In the sense of CG, a boundary layer under equilibrium is one where the pressure gradient parameter, $\Lambda =$ constant and when $(\Lambda \neq 0)$, $\delta \sim U_e^{-1/\Lambda}$. The value of the constant, Λ depends on the upstream conditions (Castillo and George (2001)).

The constant, Λ is obtained by fitting the slope of U_e vs δ in a log-log plot. In order to get a better fit, the evolution of δ along the APG ramp that was shown earlier in figure 4.20, was smoothed out using a least square spline interpolation. The profiles of δ_{95} and δ_{99} obtained after a spline interpolation are shown in black in figures 4.23 which were then used to plot U_e vs $\delta_{95/99}$. From figure 4.24, it is clear that the significant region of constant Λ are in excellent agreement with the equilibrium similarity requirement of CG. The region exhibiting the equilibrium range is shown by the line in magenta. A constant of $\Lambda = 0.27$ and $\Lambda = 0.38$ is obtained when δ_{95} and δ_{99} are used, implying that the value of Λ is also sensitive to the definition of δ. From figures 4.24, the range on the APG ramp over which flow equilibrium is exhibited can be estimated between 1 m to 3.4 m on the APG ramp as indicated in figure 4.24. For the first meter of the ramp, a region of constant Λ isn't observed. This might be due to the fact that the flow is still in

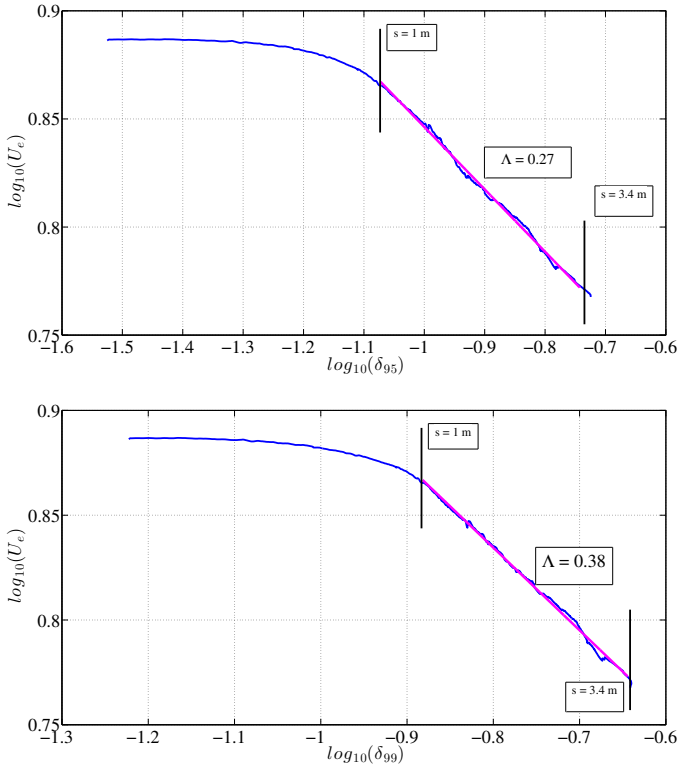

Figure 4.24: Pressure gradient parameter, Λ and δ along the -5° APG ramp at $U_\infty = 5$ m/s. (a) δ_{95} (b) δ_{99}. The line in magenta shows the region exhibiting the equilibrium range (Λ = constant) and the vertical black lines indicate the ranges over which equilibrium is exhibited

transition from FPG to APG and needs a certain distance to develop into a complete APG flow. This would then explain why the mean velocity profiles scaled by the ZS variable didn't show a reasonable collapse upto this region on the ramp. Thus, the behaviour of the Λ parameter according to CG should be a constant to enable the successful application of scaling given by ZS.

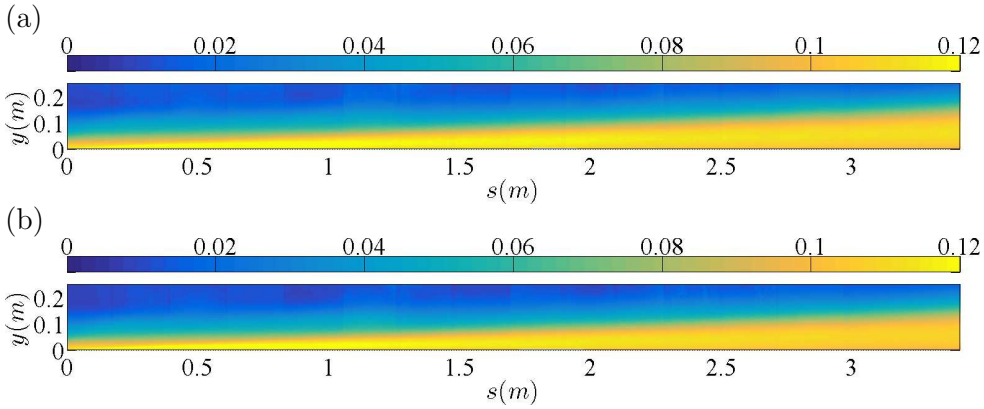

Figure 4.25: Streamwise turbulence intensity (u'/U_∞) fields along the $-5°$ APG ramp (a) $U_\infty = 5$ m/s (b) $U_\infty = 9$ m/s

4.4.3 Turbulence statistics

4.4.3.1 Turbulence intensity

Figure 4.25 shows the evolution of the streamwise turbulence intensity field along the APG plate for both velocities studied and normalised with U_∞. Looking at the contour plots, a good continuity is observed between the fields of view of the 16 cameras assembled in this set-up. This is a testament to the high quality of data acquired. As generally observed in all APG flows with and without separation (Cuvier et al. (2014); Simpson (1989); Webster et al. (1996); Wu and Squires (1998)), a region of high streamwise turbulence intensity reaching about 13% of U_∞ develops above the wall, that both spreads and moves away from it while developing downstream.

Figures 4.26 (a) and (b) show the evolution of the streamwise turbulence intensity profiles in the APG region at the same stations as in figure 4.16. The profiles at the first station is similar to the profile located at the last streamwise position on the FPG (see figure 4.11) with a slight reduction of level which is more apparent near the wall, at the highest Reynolds number. At the second station (s = 0.7 m), a weak outer peak located at about $y/\delta_0 = 0.15$, is induced by the change in sign of the pressure gradient. Moving downstream, this peak moves away from the wall with the peak magnitude

(a)

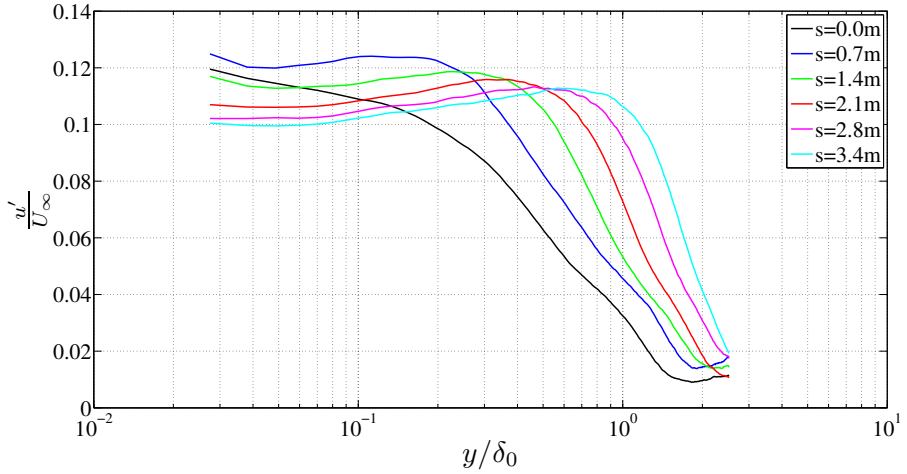

(b)

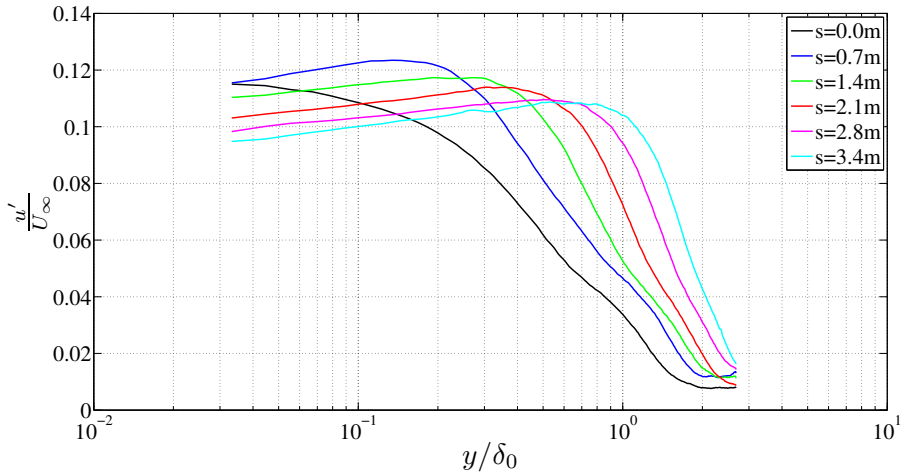

Figure 4.26: Evolution of the streamwise turbulence intensity (u'/U_∞) profiles along the $-5°$ APG ramp (a) $U_\infty = 5$ m/s, (b) $U_\infty = 9$ m/s. δ_0 as mentioned in section 4.3.2.

decreasing along the APG. At the last station, it is localised at about $y/\delta_0 = 0.7$ corresponding to about 30% of the local boundary layer thickness δ. The inner near wall peak of the streamwise turbulence intensity is not observed as it is located too close to the wall to be captured by the PIV measurement even for the 5 m/s case.

Figures 4.27 (a) and (b) show the evolution of the wall-normal turbulence

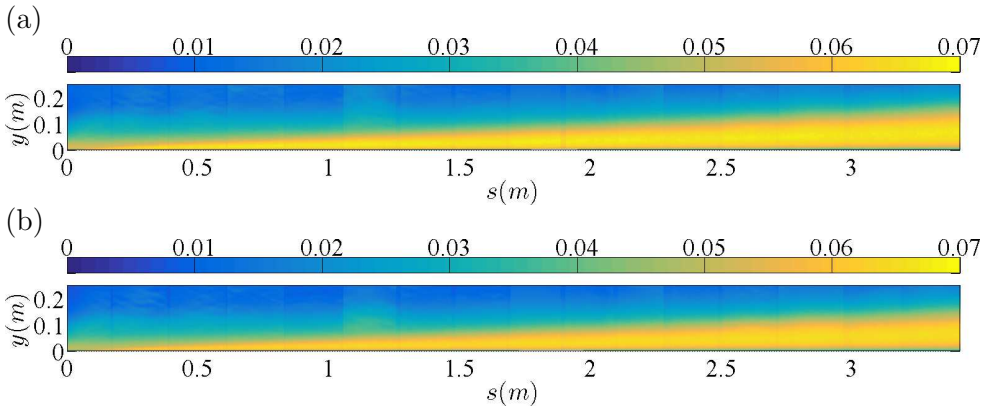

Figure 4.27: Wall-normal turbulence intensity (v'/U_∞) fields along the $-5°$ APG ramp (a) $U_\infty = 5$ m/s (b) $U_\infty = 9$ m/s

intensity field along the APG plate for both external velocities. Similar to the streamwise component shown in figure 4.25 (a) and (b), the wall-normal component of the turbulence intensity appears to move away from the wall while developing downstream. To get a clearer picture, the wall-normal turbulence intensity profiles at the same stations shown earlier is plotted in figures 4.28 (a) and (b). As mentioned earlier, it appears that the APG induces a peak that moves away from the wall with increasing streamwise direction. The y/δ_0 locations of peaks for v_{rms} are similar to the outer peak of u_{rms} shown in figures 4.26 (a) and (b). However, moving downstream, the peak can be observed to grow in strength with an increase in the peak magnitude that is clearly seen for the highest velocity studied. (refer figure 4.28 (b)). This behaviour was also observed by Cuvier et al. (2014) for an APG flow with separation.

Figures 4.29 and 4.30 show the evolution of the Reynolds shear stress intensity along the APG ramp. Similar to the streamwise and wall-normal turbulence intensities, the shear stress profiles exhibit a negative outer peak that moves away from the wall along the direction of flow. The magnitude of this peak decreases as we move downstream similar to the streamwise component shown in figure 4.26.

To get a global view of the development of the turbulence intensities, the inner region of the wall made accessible by the TRHM PIV data from Cuvier

(a)

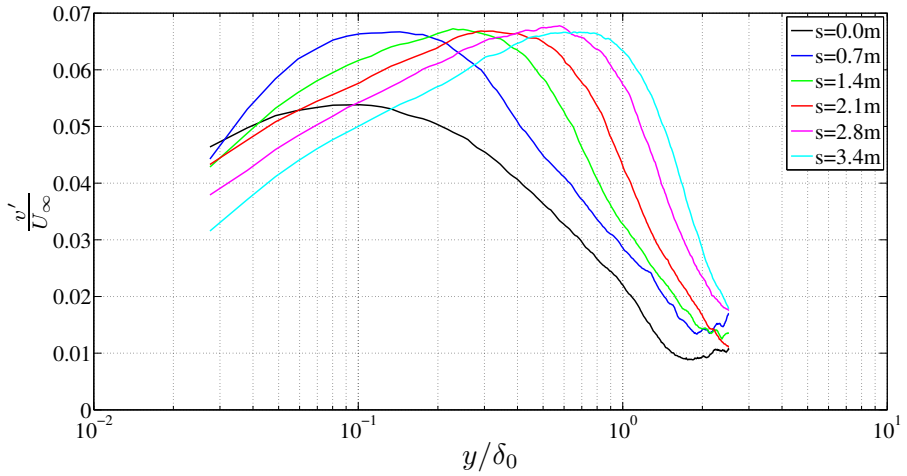

(b)

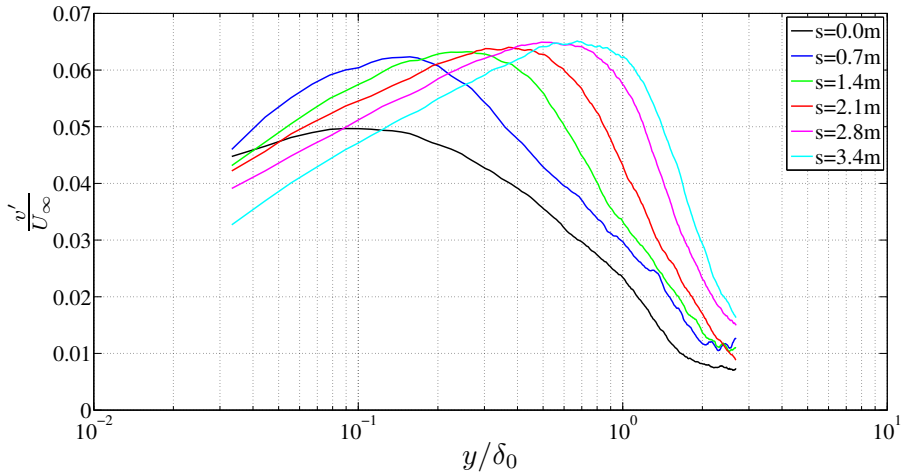

Figure 4.28: Evolution of the wall-normal turbulence intensity (v'/U_∞) profiles along the $-5°$ APG ramp (a) $U_\infty = 5$ m/s, (b) $U_\infty = 9$ m/s. δ_0 as mentioned in section 4.3.2

et al. (2017) is utilised. The turbulence intensity profiles scaled in inner units are shown in detail in figures 4.31 - 4.33 for the test case at $U_\infty = 5$ m/s. The vertical height, 'y' is normalised by the local inner units and plotted in a semi-logarithmic scale to emphasize the near wall region of the profiles. Furthermore, the profile marked by the symbol 'o' in black corresponds to a ZPG flow case from Carlier and Stanislas (2005) at $Re_\theta = 8100$. The

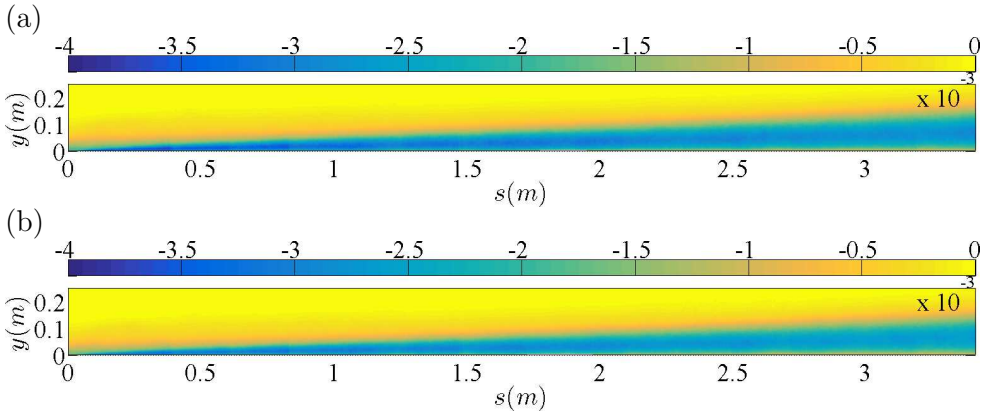

Figure 4.29: Reynolds shear stress ($u'v'/U_\infty^2$) fields along the $-5°$ APG ramp (a) $U_\infty = 5$ m/s (b) $U_\infty = 9$ m/s

respective Re_θ at the APG stations 1, 3 and 4 at $U_\infty = 5m/s$ are 5830, 8860 and 10630 respectively.

As illustrated in figure 4.31, the TRHM PIV resolves the near wall peak of the streamwise velocity fluctuations, which is present at its usual position of $y^+ \sim 15$. The presence of this near wall peak is an indication of the existence of near wall streaks all along the APG region. In this inner units representation, the near wall peak is observed to change very little at the measurement stations, while the outer peak develops and reaches a level comparable to the near wall peak at station 4. Based on Re_θ, the APG profile at station 3 is similar to the ZPG case plotted in black. It is clear that the turbulence intensity is highest throughout the flow for the APG case compared to the ZPG flow. The contrasting difference occurs in the outer region, where an outer peak is not observed in the ZPG data. This outer peak is related with the large-scale structures' energy of the flow (Hutchins and Marusic (2007); Monty et al. (2011)) suggesting consequences on the coherent structure statistics between both flows.

The profiles of the wall normal component of the turbulence intensity are shown in 4.32. In the inner region, the profiles collapse fairly well for the APG flows but do not collapse onto the ZPG profile. Additionally, the outer peak increases and also moves out from the wall whereas no such peak is

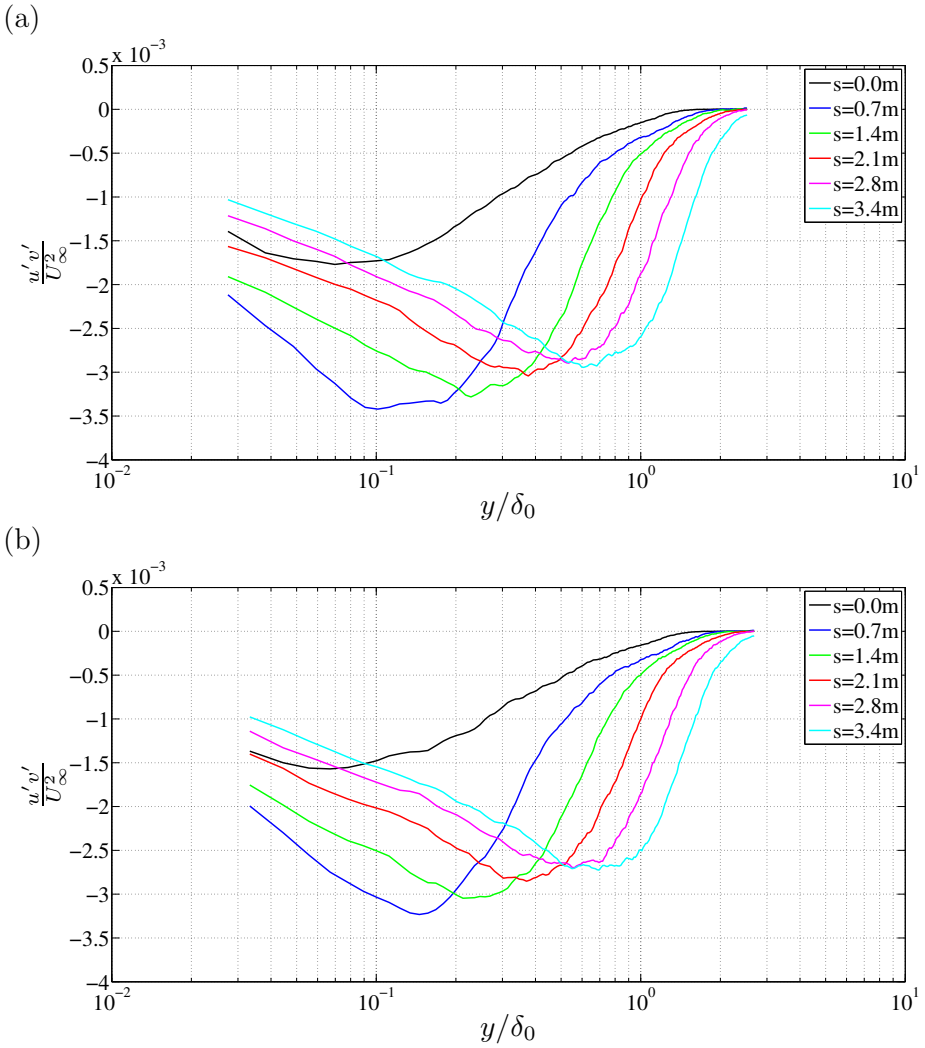

Figure 4.30: Evolution of the Reynolds shear stress ($u'v'/U_\infty^2$) profiles along the $-5°$ APG ramp (a) $U_\infty = 5$ m/s, (b) $U_\infty = 9$ m/s. δ_0 as mentioned in section 4.3.2

visible in the ZPG data.

The Reynolds shear profiles are shown in figure 4.33. Similar to the two other stress components, only the outer peak is clearly visible and is located at a wall position similar to the two other components. It is growing as well downstream along the APG ramp. In the inner region of a boundary layer subjected to an APG, the Reynolds shear stress can be expressed by equation

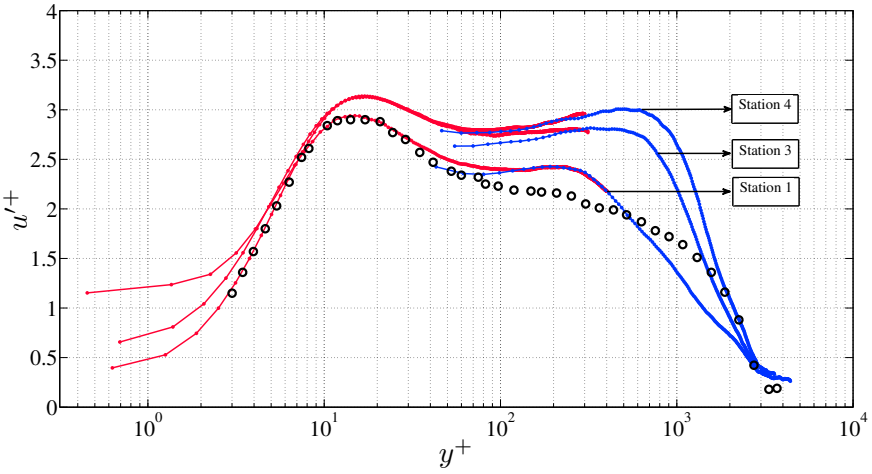

Figure 4.31: Distribution of the streamwise turbulence intensity profiles at the measurement stations 1, 3 and 4 on the $-5°$ APG ramp for $U_\infty = 5$ m/s symbols: Red line shows data from TRHM PIV, blue line from LFStW PIV and black 'o' corresponds to a ZPG flow at $Re_\theta = 8100$ from Carlier and Stanislas (2005)

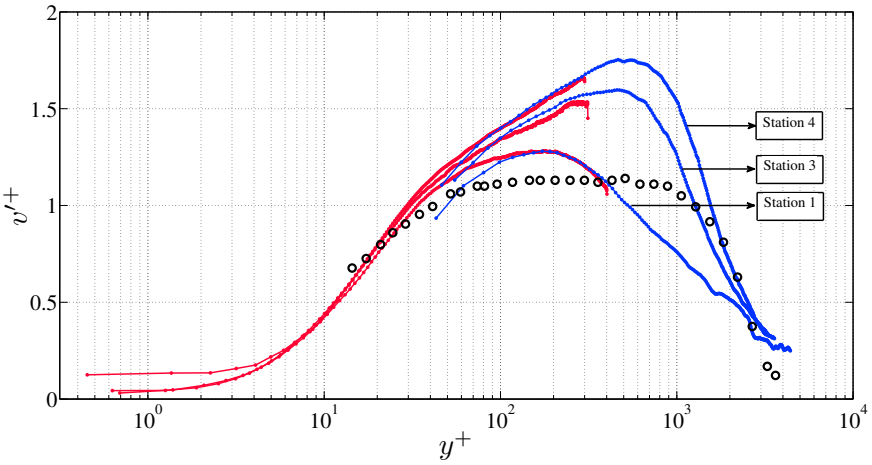

Figure 4.32: Distribution of the wall-normal turbulence intensity profiles at the measurement stations 1, 3 and 4 on the $-5°$ APG ramp for $U_\infty = 5$ m/s symbols: same as figure 4.31

4.6. From figure 4.33, we observe a good match for the theory (equation 4.6) at stations 3 and 4. Station 1 is located where the flow is still under transition

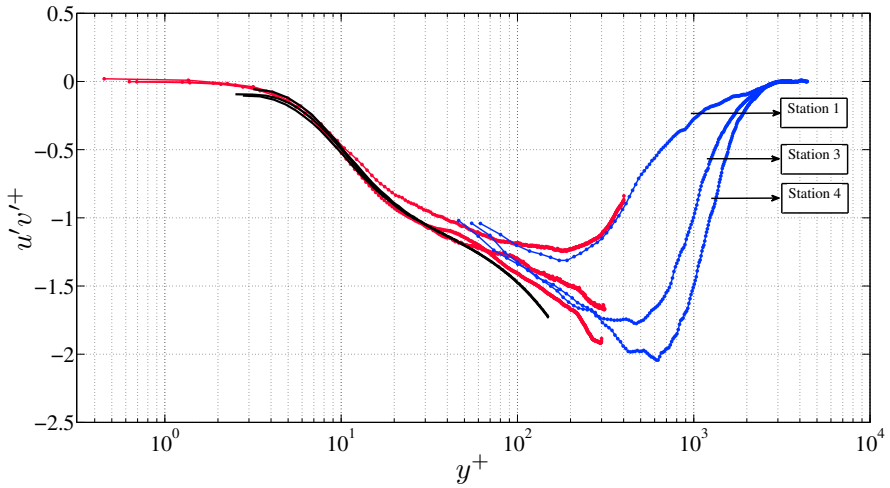

Figure 4.33: Distribution of the Reynolds shear stress profiles at the measurement stations 1, 3 and 4 on the $-5°$ APG ramp for $U_\infty = 5$ m/s
Symbols: Red line shows data from TRHM PIV, blue line from LFStW PIV and black line corresponds to the Reynolds shear stress obtained from equation 4.6

from the FPG to the APG. The strong variations of the pressure gradient observed in figure 4.3 close to the articulation of the APG ramp significantly affects the near wall region explaining why the profile obtained from equation 4.6 doesn't quite follow the data obtained from TRHM PIV at station 1.

$$\overline{u'v'}^+ = \frac{dU^+}{dy^+} - 1 - \frac{\nu}{U_\tau^3}\frac{1}{\rho}\frac{dP}{ds}y^+ \tag{4.6}$$

4.4.3.2 Skewness and flatness

The third moment of a quantity, such as $\overline{u^3}$ scaled by $(\sqrt{\overline{u^2}})^3$, describes the skewness $S(u)$ or asymmetry of the probability distribution of u (refer equation 4.7). The probability density function is symmetric about the origin, $S(u) = 0$, if $\overline{u^3} = 0$. A positive value of $S(u)$ implies that large positive values of u are more frequent than large negative values. For a Gaussian distribution, $S(u) = 0$. The fourth moment or Flatness, $F(u)$ of the u distribution is given by $\overline{u^4}$ scaled by $(\sqrt{\overline{u^2}})^4$, and is a measure of the frequency

of occurence of events far from the axis (refer equation 4.8). If these are relatively frequent, $F(u)$ will take greater values than the Gaussian value of 3 (Dengel and Fernholz (1990)).

$$S(u) = \frac{\overline{u^3}}{\overline{u^2}^{3/2}} \tag{4.7}$$

$$F(u) = \frac{\overline{u^4}}{\overline{u^2}^2} \tag{4.8}$$

Figure 4.34 shows the skewness as a function of wall normal distance in inner scaling. The crosses in black were obtained from the hot wire ZPG data of Carlier and Stanislas (2005) corresponding to a Re_θ of 11500. For completeness, data from TRHM PIV was used to throw light on the near wall region inaccessible from the LFStW PIV measurements. Station 3 at $U_\infty = 5$ m/s corresponding to Re_θ of 10630 was selected to compare the behaviour of APG with the ZPG flow.

For the zero pressure gradient case in figure 4.34, the skewness is negative in the lower part of the traditional logarithmic region ($20 < y^+ < 80$). Further from the wall ($0.017 < y/\delta < 0.06$ or $80 < y^+ < 400$), the pdf of streamwise velocity closely follows a Gaussian distribution (i.e., $S \sim 0$). From figure 4.34, it becomes clear that the influence of the pressure gradient is to increase the skewness over most part of the boundary layer, which was also reported by Nagano and Houras (2002). For the inner region, Nagano and Houras (2002) suggested that the rise in skewness is caused by 'structural changes in the near-wall' region due to pressure gradient. Monty et al. (2011) proposed that for high Reynolds number ($Re_\tau \approx 2000$), the change in skewness with pressure gradient is due to the increased large-scale influence in the near-wall region that earlier thought to be associated with increased β. They also pointed out a similar conjecture made by Metzger and Klewicki (2001) who compared low Reynolds number laboratory data with that from a high Reynolds number atmospheric boundary layer. At lower Reynolds number, it was found that in the inner region of $y^+ < 100$, the skewness was negative, while for the high Reynolds number data from the geophysical flow,

(a)

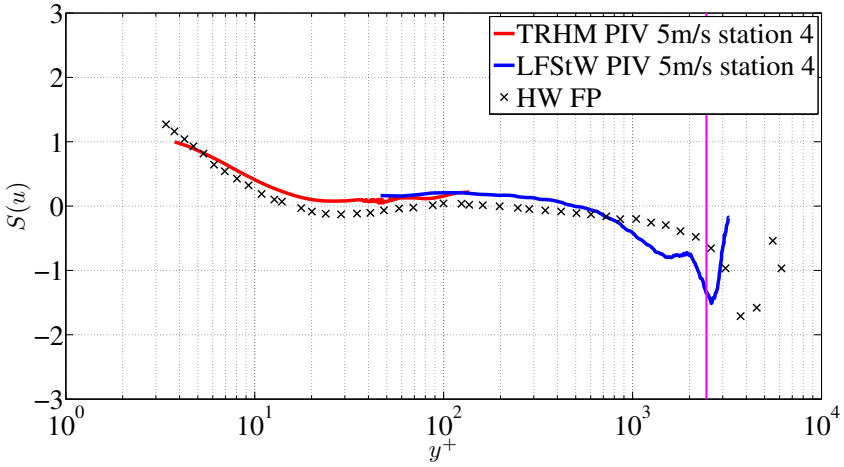

(b)

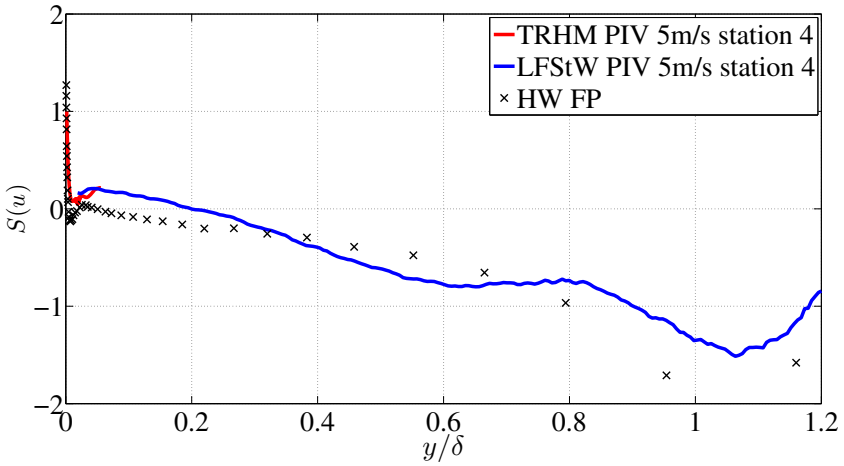

Figure 4.34: Distribution of skewness at station 4 for $U_\infty = 5$ m/s scaled in (a) inner and (b) outer units. Hot-wire (HW FP) profiles from Carlier and Stanislas (2005) for ZPG flows at $Re_\theta = 11500$. Vertical line in magenta indicates the boundary layer thickness δ

the skewness remained positive in the same region. Upon applying a high-pass filter to the streamwise velocity component to separate low-frequency, large-scale motions, it was concluded that the increased energy of large-scale structures caused the increase in skewness from a negative to a positive value.

Figure 4.35 shows the flatness, F, of the streamwise velocity fluctuations

(a)

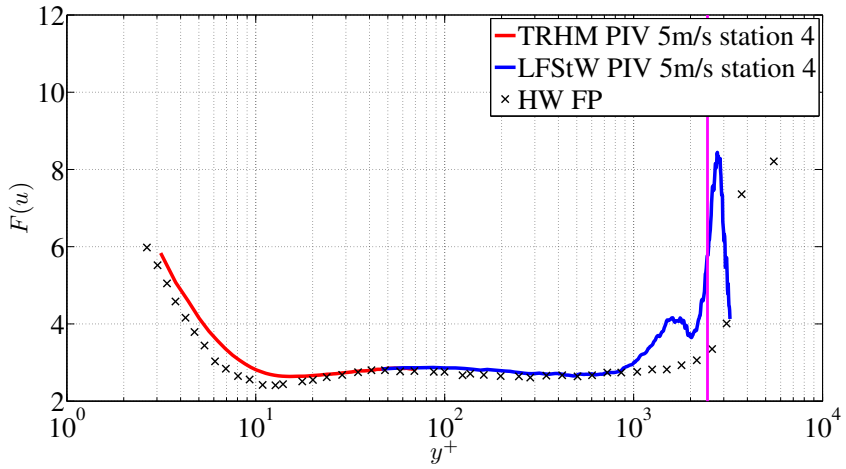

(b)

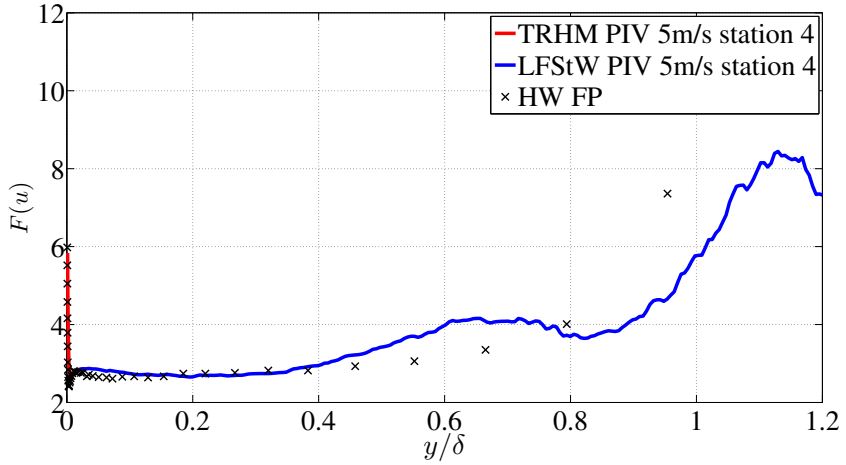

Figure 4.35: Distribution of flatness at station 4 for $U_\infty = 5$ m/s scaled in (a) inner and (b) outer units. Hot-wire (HW FP) profiles from Carlier and Stanislas (2005) for ZPG flows at $Re_\theta = 11500$. Vertical line in magenta indicates the boundary layer thickness, δ

at the same station and Reynolds number based on the momentum thickness shown in figure 4.34. It is clear from the figure 4.35 that the zero pressure gradient flow has the lowest value of flatness in the near-wall region. Monty et al. (2011) stated that in general, the flatness increases with pressure gradient. In the outer region till about $y/\delta \approx 0.4$ or $y^+ = 1000$, the flatness is

nearly invariant comparing both the APG and ZPG flows. A rise in flatness is often attributed to a rise in intermittency (Dengel and Fernholz (1990)). This interpretation leads to the conclusion that there is weakly increasing intermittency in the near-wall region as well as the near wake region where $F(u)$ rises to quite high values in a boundary layer subjected to an APG.

4.4.3.3 Turbulence production

For a 2D stationary flow, the production terms for the Reynolds stress $\overline{u_i u_j}$ are given by equation 4.9 while those for the turbulent kinetic energy are given by equation 4.10.

$$-\overline{u_i u}\frac{\partial U_j}{\partial x} - \overline{u_i v}\frac{\partial U_j}{\partial y} - \overline{u_j u}\frac{\partial U_i}{\partial x} - \overline{u_j v}\frac{\partial U_i}{\partial y} \tag{4.9}$$

$$-\overline{uu}\frac{\partial U}{\partial x} - \overline{uv}\frac{\partial U}{\partial y} - \overline{uv}\frac{\partial V}{\partial x} - \overline{vv}\frac{\partial V}{\partial y} \tag{4.10}$$

Figures 4.36 and 4.37 show the distribution of $-\overline{uv}\frac{\partial U}{\partial y}$ and $-\overline{u^2}\frac{\partial U}{\partial x}$ normalised by U_∞^3/δ_0 (δ_0 defined in section 4.3.2). These terms correspond to the production terms accessible in half the streamwise Reynolds stress ($\frac{1}{2}\overline{u^2}$) and also present in the production terms of the turbulent kinetic energy.

The production of the turbulent kinetic energy is dominated by $-\overline{uv}\frac{\partial U}{\partial y}$. From figure 4.36 it becomes apparent that the most striking difference between the APG flow and the ZPG case is that strong turbulent production does not only occur in the wall region but is also found in the outer part of the boundary layer. This would then affect the terms in the turbulent energy budget for e.g., the transport of the kinetic energy by diffusion receives its main contribution from $\frac{\partial \overline{vk}}{\partial y}$.

The second order production terms ($-\overline{uu}\frac{\partial U}{\partial x} - \overline{vv}\frac{\partial V}{\partial y}$) is not taken into account in ZPG flows as they don't contribute to production. However, in the case of APG flows this isn't the case, since the streamwise derivatives increase ($-\overline{vv}\frac{\partial V}{\partial y}$ could be written as $\overline{vv}\frac{\partial U}{\partial x}$). As shown in figure 4.37, the term $-\overline{uu}\frac{\partial U}{\partial x}$ is present in the outer part of the current boundary layer, continously growing and should therefore be not neglected. The case of the ZPG isn't

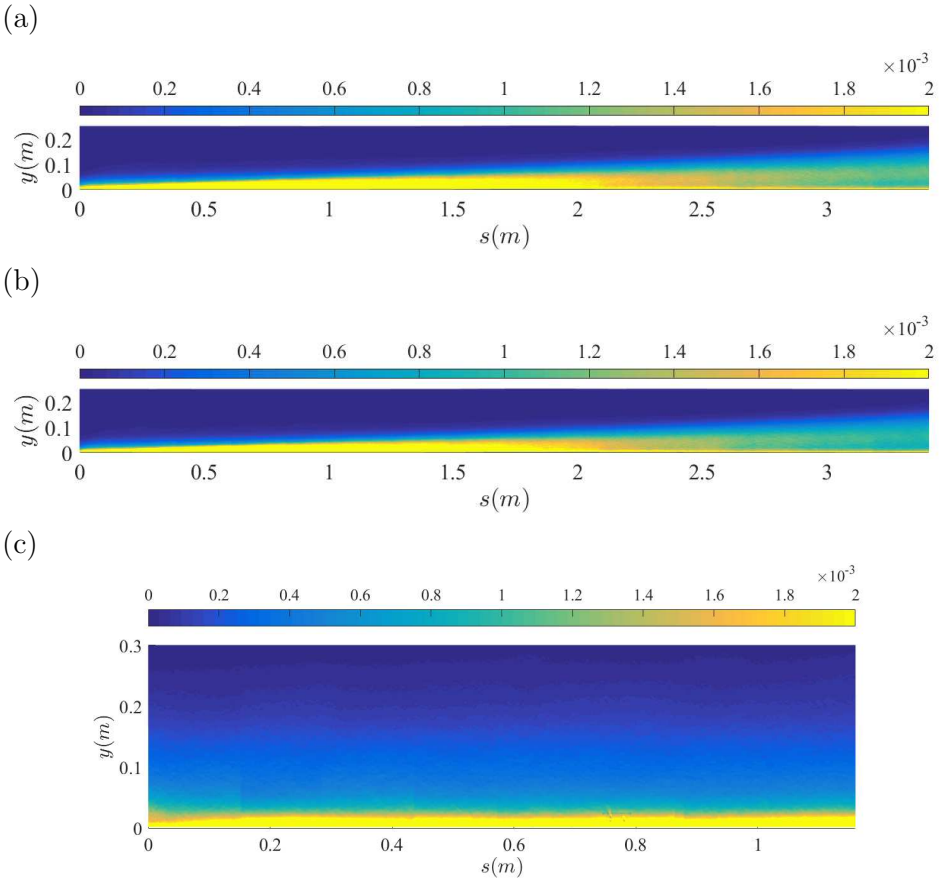

Figure 4.36: Production term $-\overline{uv}\frac{\partial U}{\partial y}$ of $\frac{1}{2}\overline{u^2}$ along the (a) APG at $U_\infty = 5$ m/s (b) APG at $U_\infty = 9$ m/s (c) ZPG at $U_\infty = 10$ m/s corresponding to $Re_\theta \approx 20600$

shown here as there wasn't any contribution by this term.

The production terms accessible for the wall-normal Reynolds stress ($\frac{1}{2}\overline{v^2}$) are $-\overline{uv}\frac{\partial V}{\partial x}$ and $-\overline{v^2}\frac{\partial V}{\partial y}$. The term $-\overline{uv}\frac{\partial V}{\partial x}$ was found to be negligible compared to the production terms of the streamwise component. The term $-\overline{v^2}\frac{\partial V}{\partial y}$ is about 10 times lower than $-\overline{uv}\frac{\partial U}{\partial y}$.

Concerning the four production terms of the Reynolds shear stress accessible with the PIV set-up used, it was found that $\overline{v^2}\frac{\partial U}{\partial y}$ largely dominates the three others. The strong similarity between distributions of v^2 and $-uv$ can

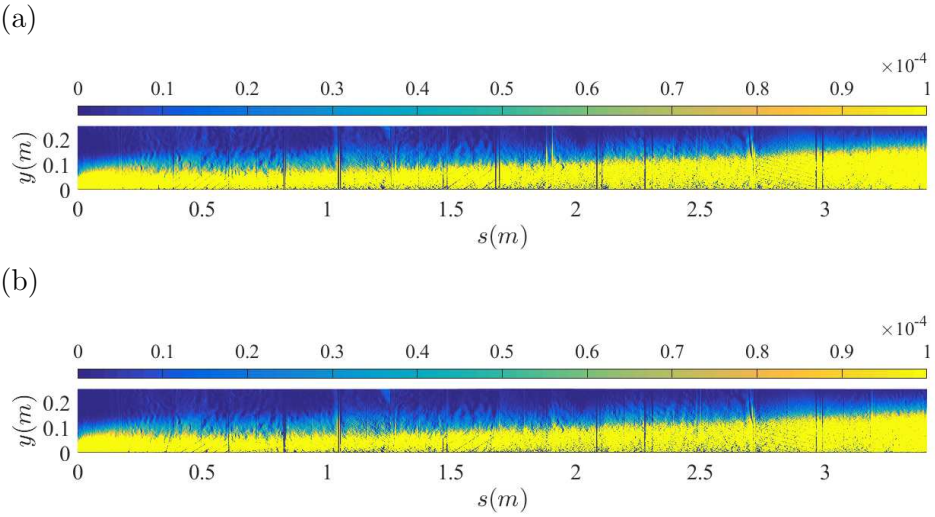

Figure 4.37: Production term $-\overline{u^2}\frac{\partial U}{\partial x}$ of $\frac{1}{2}\overline{u^2}$ along the APG at (a) $U_\infty = 5$ m/s (b) $U_\infty = 9$ m/s

then be explained by this term which produces Reynolds shear stress from the-wall normal Reynolds stress and this process is found in boundary layers.

Figure 4.38 shows the turbulence production term $-\overline{uv}\frac{\partial U}{\partial y}$ of $\frac{1}{2}\overline{u^2}$. The effect of the pressure gradient in the case of a mild APG is noticeable. The APG leads to an increased inner peak in the production profile and a moderate increase in production in the outer region as Reynolds number increases. Furthermore, there is a weak emergence of a second peak in the case of APG which moves outward. Skåre and Krogstad (1994) also observed 2 peaks in the production term while studying a strong APG flow with $\beta \approx 20$. In their study, they claimed that the inner peak was due to the mean strain as the wall was approached while the outer peak in the turbulent stresses which they noted was caused by the strong APG in their experiment. In figure 4.38, the profile marked in black shows the production term obtained from the large field PIV (refer chapter 4) at $Re_\theta \approx 8100$ in a ZPG turbulent boundary layer. Although the near wall region below $y^+ < 40$ isn't captured by the measurement, it is expected to be lower than the APG case. Globally though, it is clear that production in an APG turbulent boundary layer is higher than that of a ZPG.

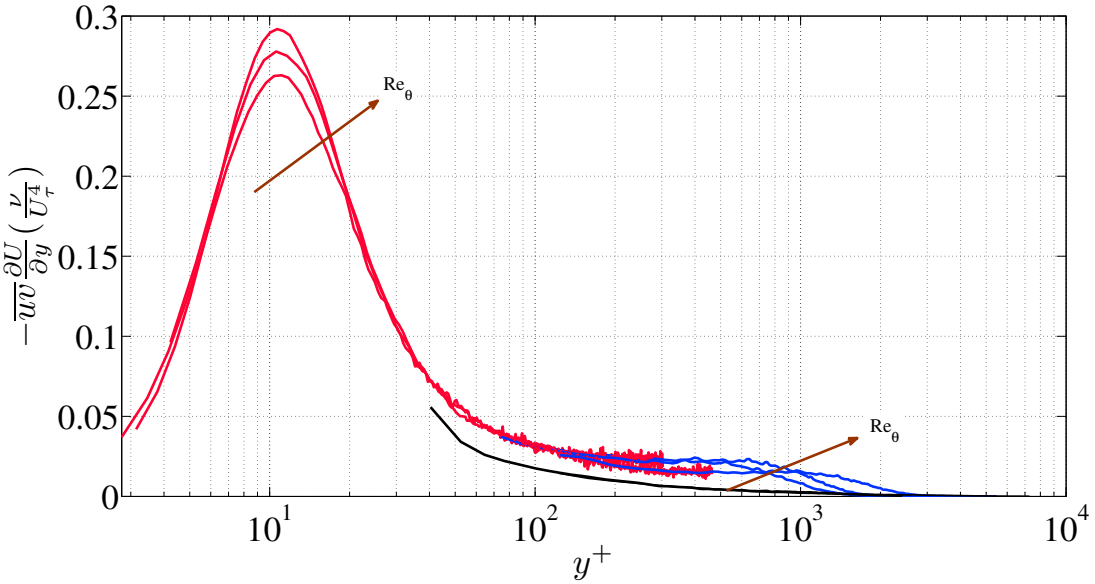

Figure 4.38: Turbulence production term $-\overline{uv}\frac{\partial U}{\partial y}$ of $(\frac{1}{2}\overline{u^2})$. Symbols: Red line - TRHM PIV, blue line - LFStW PIV. Data correspond to $Re_\theta = 8860$ (station 1 $U_\infty = 5$ m/s), 10630 (station 3, $U_\infty = 5$ m/s), 14560 (station 4, $U_\infty = 9$ m/s). Black line corresponds to PIV data at $Re_\theta = 8100$ (Refer chapter 3).

4.4.3.4 Quadrant analysis

In the previous section we observed that the production increases due to the APG. The production in a turbulent boundary layer is strongly linked to the negative contributions of $\overline{uv}$ and for that reason, Wallace et al. (1972) introduced the idea of quadrant analysis of the u and v velocity fluctuations to examine the structure of turbulence. They classified the product of these fluctuations into four categories: Q1($u > 0, v > 0$), Q2($u < 0, v > 0$), Q3($u < 0, v < 0$) and Q4($u > 0, v < 0$) which later were called the quadrants of the Reynolds shear stress plane.

In the log region of a ZPG flow, Q2 is the most contributive part of the Reynolds shear stress followed by Q4 and these motions dominate the contributions of Q1 and Q3. This behaviour was also observed in pipe flow (Nagano and Tagawa (1988)) and is considered to be a characteristic of canonical wall

flows. On the other hand in the APG flow, the situation is remarkably different from that in the ZPG flow. This is shown in figure 4.39 where the weighted joint pdf of $-\overline{uv}$ is plotted. The plots give the individual contribution to the total Reynolds shear stress of each quadrant. Figure 4.39a illustrates the contributions of sweep motions becomes larger than that of ejections in the log region. The locations of the peak values in Q2 and Q4 specify the values of u and v that contribute the most to the Reynolds shear stress at this location in the flow; however, these are not the most extreme values of the velocity fluctuations (Wallace et al. (1972)). Furthermore, the increased activity in these quadrants is coupled with higher contributions from both Q1 and Q3 motions. Q1, known as outward motion, represents transport of high speed fluid away from the wall, while the inward motion from Q3 motions tends to bring low speed fluid back to the surface. Krogstad and Skåre (1995) found that these quadrants are at least twice as high near the wall when the APG is applied than when the gradient is absent. Nagano et al. (1998) also found the contribution of sweep motions larger than that of ejections in an APG flow compared to a ZPG flow (refer figure 4.40) and noted the outward and wallward motions increase near the wall. They concluded that this indicated a change in coherent structures between ZPG and APG flows. For the outer region (refer figure 4.39b), contributions from Q2 are clearly dominant which is also the trend observed in ZPG flows (Krogstad and Skåre (1995)).

4.4.4 Influence on large-scale structures

Sections 4.4.2 and 4.4.3 dealt with a detailed characterisation of a turbulent boundary layer subjected to a pressure gradient. Through two-point correlation functions and structure detection techniques, the study is continued looking at how the coherent structures are influenced in the presence of a pressure gradient.

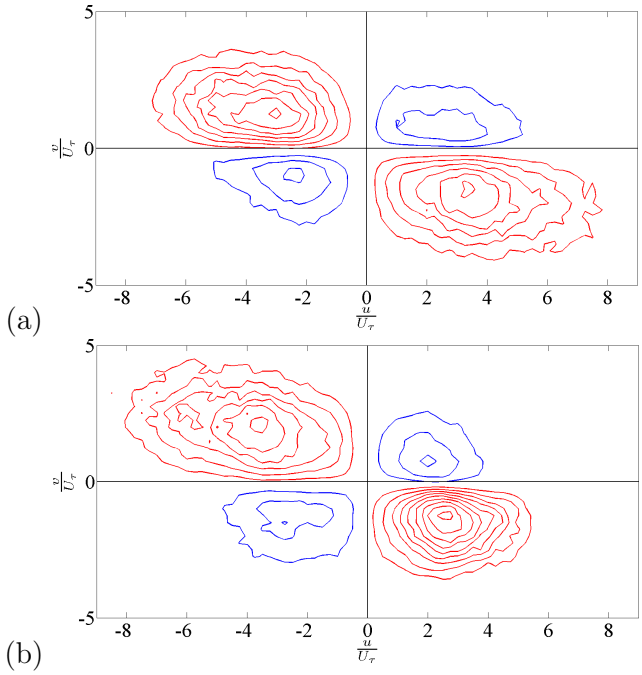

Figure 4.39: Weighted probability density functions of $-\overline{uv}$ in an APG flow at station 3 for $U_\infty = 5$ m/s at (a) $y^+ = 100$ (b) $y/\delta = 0.4$. In the contour maps, blue and red lines represent positive and negative values respectively, starting at 0.01 with a 0.01 interval between successive contour lines.

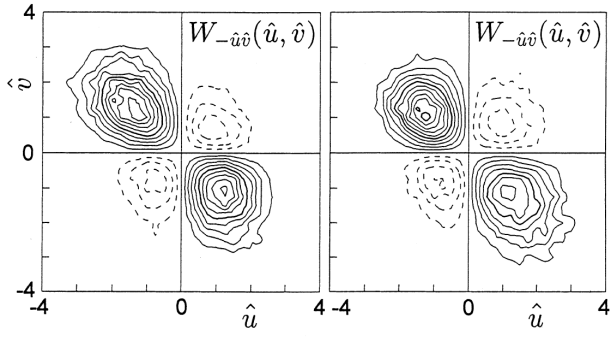

Figure 4.40: Weighted probability density functions of $-\overline{uv}$ in the log region ($y^+ = 50, y/\delta = 0.1$). the interval between contour lines is 0.01. (a) ZPG flow ($P^+ = 0$) (b) APG flow with $P^+ = 3.08 \times 10^{-2}$. Plot reproduced from Nagano et al. (1998)

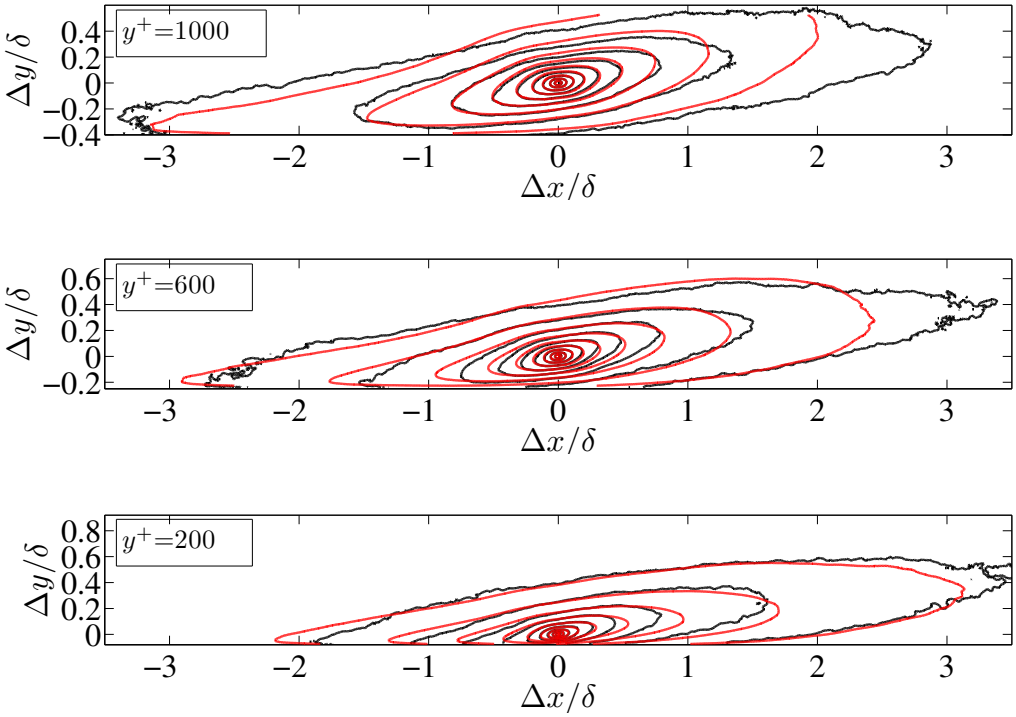

Figure 4.41: Two-point spatial correlation function of the streamwise velocity fluctuations (R_{uu}) with varying wall distance at station 3 along the APG ramp corresponding to $Re_\theta = 8860$ at $U_\infty = 5$ m/s in black contours compared to a ZPG flow at $Re_\theta = 8100$. The contours range from 0.1 to 1 with an increment of 0.1.

4.4.4.1 Spatial velocity correlations

It was shown in Chapter 3 on ZPG flows that the correlation function could be used to investigate the large-scale structures. In the following section, the correlation function will be used to analyse the effect of the mild pressure gradient in the near-wall and outer regions on the streamwise and wall-normal correlations.

Figure 4.41 shows the outer scale two-point spatial correlation for the streamwise velocity fluctuation R_{uu} at three wall-normal locations, at station 3 for $U_\infty = 5$ m/s. Similar to the ZPG case (refer figure 3.10), the correlation iso-contours are plotted as functions of $\Delta x/\delta$ and $\Delta y/\delta$. A lack

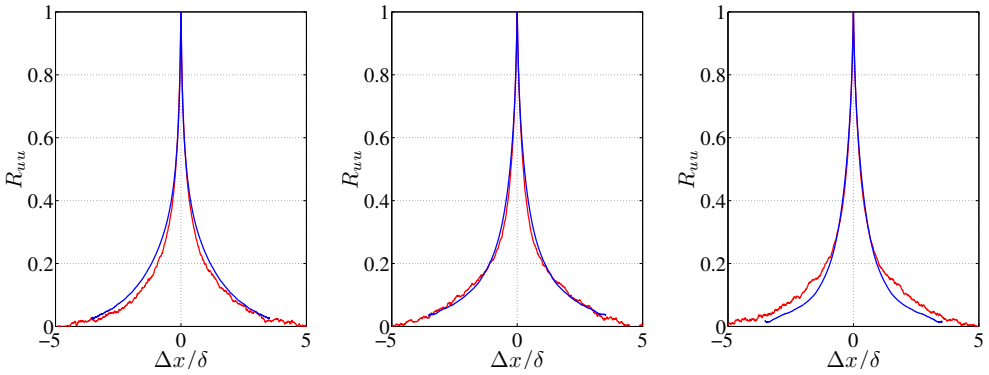

Figure 4.42: Streamwise two-point spatial correlation function (R_{uu}) at station 3 along the APG ramp corresponding to $Re_\theta = 8860$ at $U_\infty = 5$ m/s and $\delta = 0.17$ m (red line) and ZPG flow at $Re_\theta = 8100$ and $\delta = 0.34$ m (blue line). (a) $y^+ = 200$; (b) $y^+ = 600$ and (c) $y^+ = 1000$. .

of convergence can be observed, linked to the fact that the homogeneity of the flow can not be used anymore to increase the number of samples. The spatial correlation extends over a streamwise distance of 5δ at the various wall-normal locations based on a 0.1 correlation value. The general trend that can be observed from figure 4.41 is that the correlation function appears approximately as an ellipse and is strongly elongated in the streamwise direction. Compared to a ZPG flow, the correlations are slightly more inclined in the APG case at $y^+ = 200$ and they become broader and less inclined when moving from the wall. The largest structures also seem longer in APG.

To gauge the effect of the pressure gradient, a slice of R_{uu} at $\Delta y = 0$ or the auto-correlation at four selected wall distances as shown in 4.42 are compared to the ZPG flow at $Re_\theta = 8100$ described in Chapter 3. The plots in figure 4.42 indicate that the streamwise length of the correlations are comparable at all investigated wall-normal positions. The correlation with APG being shorter at $y^+ = 200$ in agreement with Nagano and Tagawa (1988) and Monty et al. (2011) and as shown in figure 4.41, the correlation of the longest structures seem longer in the outer region at $y^+ = 1000$ corresponding to $y/\delta \approx 0.4$ for this Reynolds number.

There isn't a clear picture in the turbulence community regarding the

influence of APGs on the streamwise length of large-scale structures. Lee (2017) recently suggested that the strength of the APG, characterised by β may be important in determining the large-scale features in the outer layer. In his review, he observed that when β is suficiently large, e.g. $\beta = 20$ (Krogstad and Skåre (1995)) and $\beta = 8.5$ (Rahgozar (2013)), the streamwise lengths of the large-scale motions are shorterned by the APG. On the other hand, they are more energized with longer streamwise coherence for relatively small values of β, e.g. $\beta = 1.74$ (Harun et al. (2013)), $\beta = 0.82$ (Monty et al. (2011)), $\beta = 1.68$ (Lee and Sung (2008)).

4.4.4.2 Structure detection

The case of a ZPG boundary with a 1.16 m long field of view was studied in chapter 3. In that case, turbulence statistics was assumed to be quasi-homogeneous. However in the case of an APG, we saw in the preceeding chapter that parameters such as U_τ and δ vary significantly along the direction of flow. Thus, before directly applying the structure detection tools described in section 3.2.2.2 for ZPG on the APG data, few steps are necessary to modify our detection algorithm.

In figure 4.31, the growth of an outer peak in the streamwise turbulence intensity was observed. Thus, a threshold u_{th} equal to $-0.4u'_{300^+}$ where (u'_{300^+} is u' at $y^+ = 300$) would no longer be a constant along the streamwise direction of the ramp. In order to take this into account, at each grid point along the streamwise direction, the local u' at $y^+ = 300$ is used for the threshold.

Once the threshold has been applied on the streamwise fluctuating velocity fields, one more step is needed before the results can be analysed. The variation of δ and its effect on the structures needs to be taken into account. Said otherwise, the structures detected at the beginning of the ramp might not have the same physics with that found towards the end. Thus, it was decided to create ranges with almost constant value of δ. A variation of 20% in δ was chosen to have a sufficiently long region to capture the large-scale structures. This results for $U_\infty = 9$ m/s to four ranges. The beginning,

Region	Start (m)	End (m)	Length (m)	δ_{mid} (m)
1	0	0.23	0.23	0.08
2	0.231	1.301	1.07	0.13
3	1.302	2.481	1.18	0.17
4	2.482	3.411	0.93	0.20

Table 4.8: The start, end and length of the four regions obtained through the structure detection algorithm at $U_\infty = 9$ m/s. δ_{mid} corresponds to the value of δ at the middle of the respective regions.

end and length of these regions is reported in table 4.8. The value of δ at the midsection of these regions is also tabulated. The strong variation in δ upstream of the ramp explains why the first region is of shorter length compared to the other three. Also, regions 3 and 4 fall under the equilibrium zone established through the Castillo and George pressure parameter (refer section 4.4.2.4). With an interest of studying APG flows under equilibrium, regions 3 and 4 are of interest. Covering a longer distance, region 3 is taken to analyse the statistics of the structures detected.

Through the detection procedure, the midpoints of the structures are stored. Instead of neglecting the structures that touch the side borders of the investigated region that was carried out for the ZPG case where the data were available on a limited domain, structures that have their midpoints between this region are kept. Finally, the size of the filter used on the APG data was chosen to be equal to the ZPG case in y^+. The value of U_τ varies only by about 20% in the equilibrium region, therefore the filter would vary by the same extent within this region.

Figure 4.43 shows a power law dependence on λ between about 0.5δ upto 6δ in all cases in what can be defined as the log region. For all cases, the PDF of λ/δ with a functional form $-C_1 + C_2(\lambda/\delta)^{-r}$. The values taken by the exponent r for the wall distances plotted in figure 4.43 are reported in table 4.9. The fit shown in figure 4.43 with an exponent of -1 to show the behaviour of the streamwise length distribution. The constants C_1 and C_2 are remain fairly constant over the range of wall distances (refer table 4.9). Returning now to the ZPG case, the difference in the distribution of

y^+	100	200	400	600
C_1	0.09	0.07	0.10	0.09
C_2	0.46	0.45	0.45	0.46
r	1.4	1.3	1.2	0.9

Table 4.9: Values of C_1, C_2 and r in the form $-C_1 + C_2(\lambda/\delta)^{-r}$ of the PDF of λ/δ from figure 4.43 at $U_\infty = 9$ m/s

the streamwise length of the attached structures is apparent as shown in figure 4.44. While the most probable length appears to be 0.5δ for both, their streamwise extents aren't distributed in the same way. From figure 3.16, it was observed that in the case of a ZPG turbulent boundary layer, the streamwise lengths of the long structures followed a power law, with an exponent -2 over a long range of y^+. However, from figure 4.43 and table 4.9, it is clear that the streamwise lengths of structures in an APG boundary layer aren't distributed in a similar manner as the exponent r decreases as we move away from the wall. While the reason for this difference is not known at present, certain hints could be obtained from the two-point spatial correlation function (refer figure 4.41). As mentioned earlier, the largest structures appear longer in an APG compared to a ZPG flow and are also inclined differently at distances from the wall. These differences in the characteristics of the large structures may be assumed to be the reason that the distribution of streamwise lengths aren't the same in both flows. Future study on this behaviour would be needed to have a conclusive evidence.

However, while figure 4.44 shows a difference of structure's length between the two flows, it is important to keep in mind certain caveats. The fields of view of the ZPG (1.16 m) and APG (3.41 m) set-up are not the same and hence extracting structures under similar conditions is difficult as the statistics of very long structures can be affected even if this effect has been tested on the ZPG case. While the threshold for the APG was chosen to be the value of u' at $y^+ = 300$, the same criterion set for ZPG, from figure 4.31 it is evident that the streamwise turbulence intensity profiles do not behave the same way for both flows. Thus, while the trends seen in the correlation of

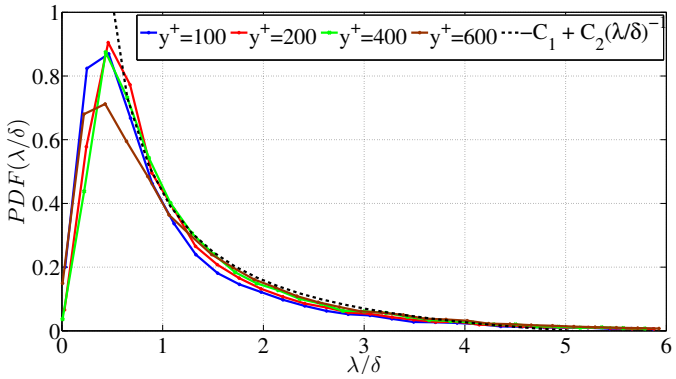

Figure 4.43: PDFs of streamwise lengths λ of wall-attached structures at selected wall distances for $U_\infty = 9$ m/s in the third region

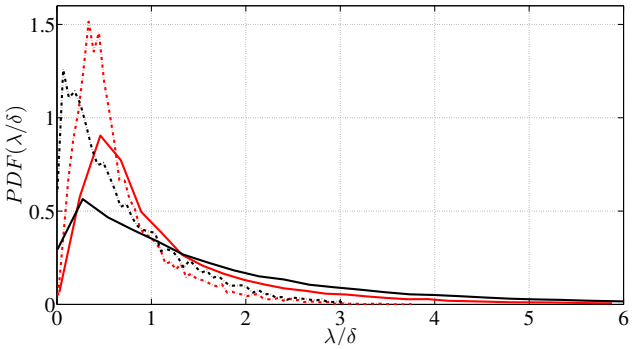

Figure 4.44: PDFs of streamwise lengths λ of wall-attached structures at wall distances of $y^+ = 200$ indicated in red and $y^+ = 1000$ indicated in black. Solid lines show region 3 of the APG at $U_\infty = 9$ m/s and dashed lines show $Re_\theta = 20600$ for the ZPG case

APG (refer figure 4.42) can be explained but the structure detection criteria for ZPG doesn't fully reflect what we see in the correlation.

Additionally, similar to the ZPG case, we plot $\overline{a^2}$ versus λ/δ where we have included best fits of power law curves in the plots. These best fits are indicated in the inserts of each plot and provide an estimation of the exponents p such as $\overline{a^2} \sim (\lambda/\delta)^p$. Although we do not have access to the exponent q from the spectra due to the non-homogeneous nature of the APG along the direction of flow , it would be worthwhile to observe how p evolves.

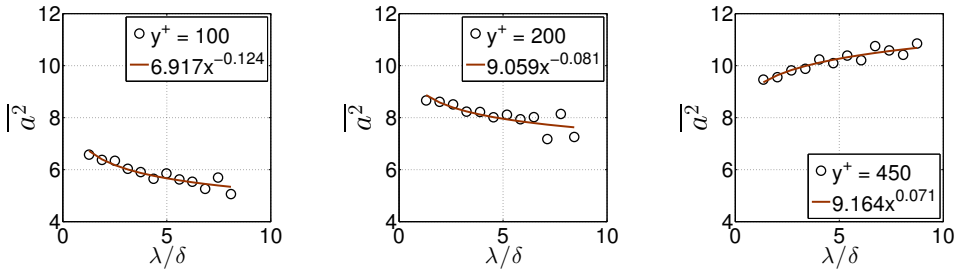

Figure 4.45: Plots of $\overline{a^2}$ versus λ/δ (left) and streamwise energy spectra plotted at wall distances $y^+ = 100$, 200 and 400 (from top to bottom) at $U_\infty = 9$ m/s.

Compared to the ZPG flow, it is perhaps remarkable that p is still negative (figure 4.45) for y^+ up to 400 beyond which p becomes positive as seen for $y^+ = 450$. Furthermore, this dependence varies with height like in the ZPG case: $\overline{a^2}$ decreases with increasing λ/δ up to $y^+ = 400$, and increases with increasing λ further up. This suggests that the shorter structures are more energetic compared to the ZPG flow and retain this behaviour at distances greater to the wall. Only after $y^+ = 450$, we observe a transition similar to the ZPG flow.

CHAPTER 5

Conclusion and outlooks

5.1 Summary of findings

The aim of the present work was to study a boundary layer subjected to a pressure gradient and to compare it with a ZPG at high Reynolds numbers. Within this framework, focus is laid on the behaviour of large-scale coherent structures. Due to their large streamwise extent, these structures are not easy to extract and characterize using standard measurement techniques. For this reason, specific experimental set-ups using PIV in the streamwise/wall-normal planes was designed to capture the large-scale structures and to gain more insight into the mechanisms governing the dynamics of these flows. The achievements of the present investigation can be divided into two parts. The first part revisits the results obtained on a ZPG turbulent boundary layer while the second focuses on the effect of the boundary layer subjected to a pressure gradient.

To begin with, a well-resolved PIV data of a flat plate turbulent boundary layer in a large field of view at two medium to high Reynolds numbers, $Re_\theta = 8100$ and $Re_\theta = 20600$ is obtained (refer Chapter 3). The database is validated though the analysis of single point statistics and power spectra that were compared with reference hot-wire data showing good agreement with the reference profiles. The aim here is to probe the origin of a k_x^{-1} spectral range in a turbulent boundary layer. To this end, a simple model which can

in principle be applied to various wall-bounded turbulent flows is proposed from a new perspective based on the work of Townsend-Perry.

A direct inspection of the streamwise energy spectrum (refer figure 3.17) would suggest $E_{11}(k_x) \sim U_\tau^2 k_x^{-1}$ in the range $2\pi/(4\delta) < k_x < 0.63/y$. However, a closer look assisted by relation (3.16)-(3.17) reveals a significantly subtler behaviour. This relation introduces a specific data analysis which involves the extraction of wall-attached elongated streaky structures from PIV data. The concurrent analysis of streamwise energy spectra and of the relation between the turbulence levels inside streaky structures and the length of these sructures offers strong support for (3.16)-(3.17) over a significant range of length-scales. This range covers LSMs and is comparable to the range where one might have expected the Townsend-Perry attached eddy model spectra to be present. Even though k_x^{-1} spectra are not, strictly speaking, validated by our data, the streaky structures which account for the scalings of $E_{11}(k_x)$ do need to be wall-attached for relation (3.16)-(3.17) to hold. Our conclusions agree with the experiments of Vallikivi et al. (2015) which suggest that the Townsend-Perry k_x^{-1} spectrum cannot be expected even at very high Reynolds numbers. The revised Townsend-Perry streamwise energy spectral form (3.16)-(3.17) with $p = p(y^+)$ given by figure 3.23 appears to extend the validity of the attached eddy concept and its revised consequences to a wider range of Reynolds numbers and a wider range of wall distances.

Finally, we stress that relation (3.16)-(3.17) is predicated on these wall-attached streaky structures being space-filling, i.e. $D = 1$ in the notation of section 3.1. The pdf of the streamwise length of the educed streaky structures does indeed follow a power law with exponent $-1 - D = -2$ over the range of scales which corresponds to the one where (3.16)-(3.17) holds. This work has shed some new light on the streamwise turbulence spectra of wall turbulence by revealing that some of the inner structure of wall-attached eddies is reflected in the scalings of these spectra via $p(y^+)$. An important implication of this inner structure is that the friction velocity is not sufficient to scale the spectra.

Chapters 4 dedicated to the study of flows subjected to a mild pressure gradient far from separation at external velocities. The fundamental aim of

this project is to improve the understanding of turbulence under APG by performing a complete characterisation of the flow. Emphasis is laid on the characteristics of the structures (length, scaling, energetic contribution and their wall normal distribution). The analysis is also extended to compare the behaviour of APG with the ZPG case at fairly high Reynolds numbers.

Analysis of the single point statistics show that the boundary layer behaves differently compared to a ZPG boundary layer even when subjected to a mild pressure gradient. Although the wake region grows substantially, the logarithmic law of the wall remains valid along the APG ramp for such mild pressure gradients. The study confirms the occurence of an enhanced outer peak of turbulence develops on all the Reynolds stresses suggesting an apparent consequence on the characteristics of the large-scale coherent structures while the near wall peak of the streamwise component indicating the presence of near-wall streaks is still visible.

Of primary interest was to build an APG ramp long enough for the flow to develop and reach a state of quasi-equilibrium where scaling laws can be relevant. Using Castillo and George's pressure parameter, Λ lead to the determination of an equilibrium region along the APG ramp. It is shown that in this zone of equilibrium, the mean velocity deficit profiles display an acceptable collapse. The value of Λ is seen to be constant from $s = 1$ m to $s = 3.4$ m along the APG ramp but clearly dependent on the definition of δ.

The two-point correlations show the presence of large structures existing in a boundary layer subjected to a mild pressure gradient. The APG increases the structural inclination angle and the streamwise length of the correlation is decreased in the inner layer. The same method used in ZPG flows to detect the large-scale structures on the fluctuating streamwise velocity component has been applied on this flow with APG. The evolution of the lengths of wall-attached streamwise velocity structures along the wall-normal direction show a power law dependence on λ, however, with a power law exponent (refer table 4.9) different to that of a ZPG boundary layer (-2). The exponent p also behaves differently when compared to the ZPG flow at comparable wall distances suggesting that the structural organization in an APG boundary layer is different to the classical ZPG case.

5.2 Future work

The findings of this thesis provide new avenues for further research and improvements. Based on the results in chapter 3 focussing on the ZPG boundary layer, as a short term perspective, future work must now probe the inner structure of wall-attached eddies, attempt to explain it and extend analysis to higher Reynolds numbers so as to establish with certainty the ranges of the power laws (exponents p and q in equation 3.16-3.17). The model developed could also be tested with DNS data and is currently being investigated by a PhD student at LML but at a fairly lower Reynolds number. The structure detection methodology employed here is carried out by discarding structures that cut through the vertical borders because their streamwise extent is unknown. This step could be negated by carrying out the experiment with a larger field of view that is currently possible at LML.

As mentioned earlier in the case of the ZPG boundary layer, the pdf of the streamwise length followed a power law with an exponent -2 over the range of scales where equation 3.17 i.e $p + q = -1$ holds. However in the case of an APG boundary layer the power r and p changes and thus we could guess that the spectra behaves differently and equation 3.17 is no longer valid. Therefore, in the immediate future, in addition to understanding the cause of this behaviour, measures to obtain the spectra in a decelerating flow should be explored. This is particularly not evident as the streamwise homogeneity of the flow can no longer be exploited and thus the spatial spectrum obtained from PIV as in the ZPG case in chapter 3 is not valid. Although not performed due to time constraints, as a first approximation, obtaining a time spectra from hot-wire is planned. Furthermore, LML is also currently trying to study APG flows along a 2D bump at low Reynolds numbers using DNS in a configuration similar to that described in chapter 4. Thus, a specific study comparing the different spectra could be carried out. Another idea could be to apply similarity mapping through which the velocity field is scaled and transformed to a homogeneous field. This was done in a study by Wänström (2009) on jets that resulted in streamwise homogeneity in similarity coordinates. This experiment being a case of a

mild APG may serve as an opportunity to test this method and subject to satisfactory results, it could be applied on a stronger APG.

With a focus on the streamwise component of the structures in the current study, the spanwise structure of the flow in APG should also be characterized. This can be made possible in the immediate future through the readily availability database of spanwise/wall normal SPIV measurements at two streamwise positions of $s = 0.595$ m and $s = 2.192$ m on the APG ramp. Also, the interaction between turbulence structures such as ejections, sweeps (see section 4.4.3.4) in the regions of the boundary layer are quite complex and difficult to comprehend in APG flows. Thus the manner in which these structures interact in the boundary layer at high Reynolds numbers could be studied with the help of the current database.

Furthermore, while the presence of LSMs in APG boundary layer has been evidenced though this study, the existence of hairpins and hairpin packets has not been explored. The role of hairpin vortices and packets have been previously carried out for ZPG boundary layers (see section 2.2.1.1), however, there isn't a clear picture in APG flows. The size, swirl intensity, orientation and the effect of the pressure gradient on the hairpin and hairpin packets could be explored. Furthermore, studies in ZPG flows have shown the existence of LSM present in the outer region having an influence on the near wall region (Hutchins and Marusic (2007); Mathis et al. (2009)) It would be worth probing how the pressure gradient affects the modulation of the small scaled by the large scales.

To understand the effects of a strong pressure gradient on the single point statistics and on the coherent structures, the APG experiments can be conducted with the same model with a steeper angle of the ramp as a medium term perspective. This could be carried out at a location further upstream on the wind tunnel floor thereby facing in a smaller boundary layer thickness to keep a large ration of the APG length with respect to δ and therefore the possibility of the flow to remain in equilibrium. Finally, with the improvement of measurement techniques, it could be possible to have access to 3D data at a very large scale for both the APG and ZPG flows using the recent 3D time resolved Shake-the-box technique associated

with appropriate tracers like soap bubbles.

Appendices

APPENDIX A

Detection algorithm

A.1 Pre-filtering of raw data

When working with two-dimensional PIV images, we need to use the two-dimensional Gaussian function, which has the form:

$$g(x,y) = \frac{1}{2\pi\sigma^2} e^{\left(-\frac{x^2+y^2}{2\sigma^2}\right)} \tag{A.1}$$

The convolution kernel for the two-dimensional Gaussian filter was created using the function, "fspecial" from Matlab. The default value for the kernel size is [3 3] pixels (A pixel here refers to the grid spacing between velocity vectors in the PIV images) and the standard deviation, '$\sigma = 0.5$'. The value of σ dictates the shape and size of the kernel. Truncating the Gaussian kernel at [3 3] pixels creates a sharp border that will cause unwanted artefacts in the output image thus losing the properties of a Gaussian filter. Cutting a Gaussian at a point where it is close to zero happens around 3σ meaning that the size of the Gaussian kernel should be 6σ, cutoff at 3σ on either side of the origin. Proceeding on this track, two Gaussian filters: a moderate filter having a $\sigma = 1$ (kernel [6 6] pixels) and a strong filter having a $\sigma = 3$ (kernel [18 18] pixels) was chosen in the present study. The respective filtered images were then compared to a case without any filter being applied, to ensure that there is no significant bias in the results and to also ensure that the filter doesn't modify the overall shape of the turbulent structures at large.

(a)

(b)

(c)

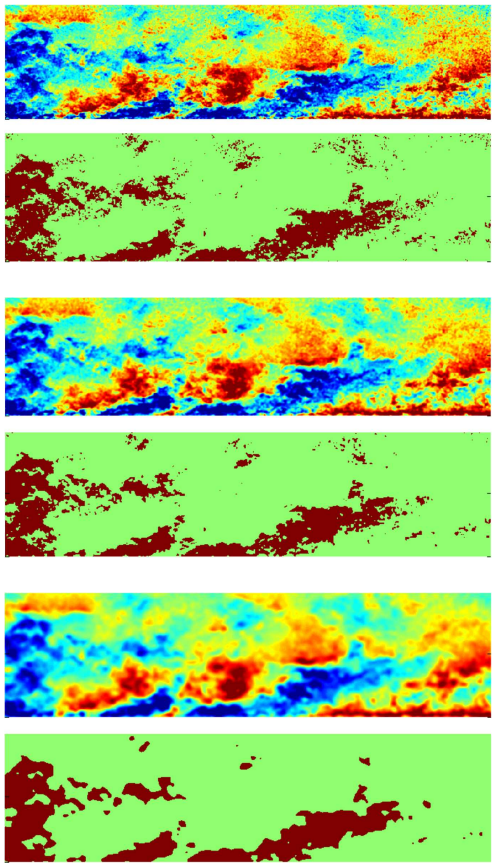

Figure A.1: (a) Image 11 from the instantaneous PIV snapshots recorded at $Re_\theta = 20600$. Effect of passing a (b) Moderate Gaussian filter (c) Stong Gaussian filter is shown. The contour in brown indicates the region where $u^* < -0.4u'_{300^+}$ with u'_{300^+} is u' at $y^+ = 300$ as seen in Chapter 3.

To visually examine the effect of filtering, the moderate and strong Gaussian filters were tested on a few PIV images. Figures A.1(a) and A.1(b)-(c) show the comparison of a resulting fluctuating streamwise velocity field after applying the Gaussian filters mentioned above on image number 11 for the $Re_\theta = 20600$ test case. From figure A.1(b), it is clear that the moderate Gaussian filter has not managed to remove much noise and connect many small structures that are disconnected with each other by a few pixels. On the other hand, the strong Gaussian filter shown in figure A.1(c) has worked

quite well in capturing the overall shape of the coherent structures and looks similar to what we expect while visually inspecting the thresholded PIV velocity fields.

A.2 Effects of threshold levels

Our results have no significant dependence on threshold u_{th} in the range $-0.2u'_{300^+}$ to $-0.6u'_{300^+}$. An example of this lack of threshold dependence can be seen in the PDFs of λ/δ which we plot in figure A.2. We also reported in table 3.1 the number of structures educed by the algorithm described in subsection 3.2.2.2 for the three negative threshold values $-0.2u'_{300^+}$, $-0.4u'_{300^+}$ and $-0.6u'_{300^+}$. Figures 3.19 to 3.22 have been obtained for $u_{th} = -0.4u'_{300^+}$ but we checked that they remain very similar without deviations from our conclusions if the threshold u_{th} is chosen in the range $-0.2u'_{300^+}$ to $-0.6u'_{300^+}$.

A.3 Behaviour of positive fluctuating streamwise velocity structures

As mentioned in subsection 3.2.2.2, this detection analysis can be repeated equally well on structures of positive streamwise fluctuating velocity. We provide examples of results obtained with $u_{th} = 0.4u'_{300^+}$ in figure A.3 and table A.1. There are indeed no significant differences in the results for the low and high speed attached flow regions, except for a lower but consistent value of C_1 and for a consistently lower value of C_2 in the lower Re_θ case. Figures 3.19 to 3.22 can be reproduced for this positive threshold $u_{th} = 0.4u'_{300^+}$ and show the exact same trend (refer figures A.4 to A.7) with p increasing while q is decreasing with increasing y^+ as shown in figure A.8. However, whereas p takes values similar to those for $u_{th} = -0.4u'_{300^+}$ in the lower Re_θ case, it does not do so in the higher Re_θ case. As a result $p + q$ is quite close to -1 in the lower Re_θ case but less so, and in fact closer to -1.1 on average, for the higher Re_θ.

(a)

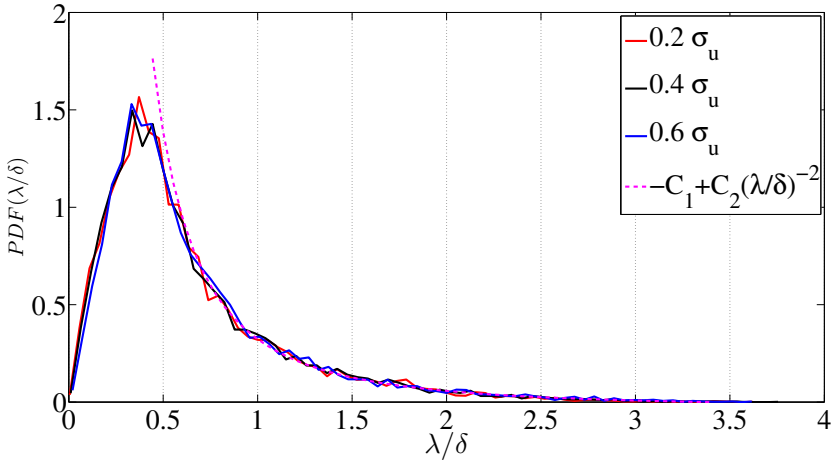

(b)

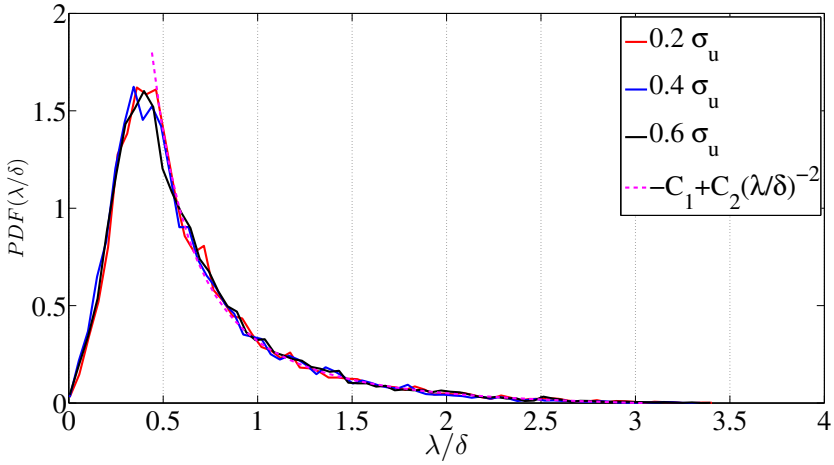

Figure A.2: PDFs of streamwise lengths λ of wall-attached structures at $y^+ = 195$ for (a) $Re_\theta = 20600$ and $y^+ = 125$ for (b) $Re_\theta = 8100$ over a set of thresholds

Re_θ	20600					8100				
y^+	90	195	305	450	630	52	88	125	198	306
C_1	0.02	0.02	0.01	0.02	0.02	0.02	0.02	0.02	0.03	0.02
C_2	0.35	0.36	0.34	0.38	0.37	0.28	0.29	0.28	0.31	0.29

Table A.1: Values of the constants C_1 and C_2 in the form $-C_1 + C_2(\lambda/\delta)^{-2}$ of the PDF of λ/δ.

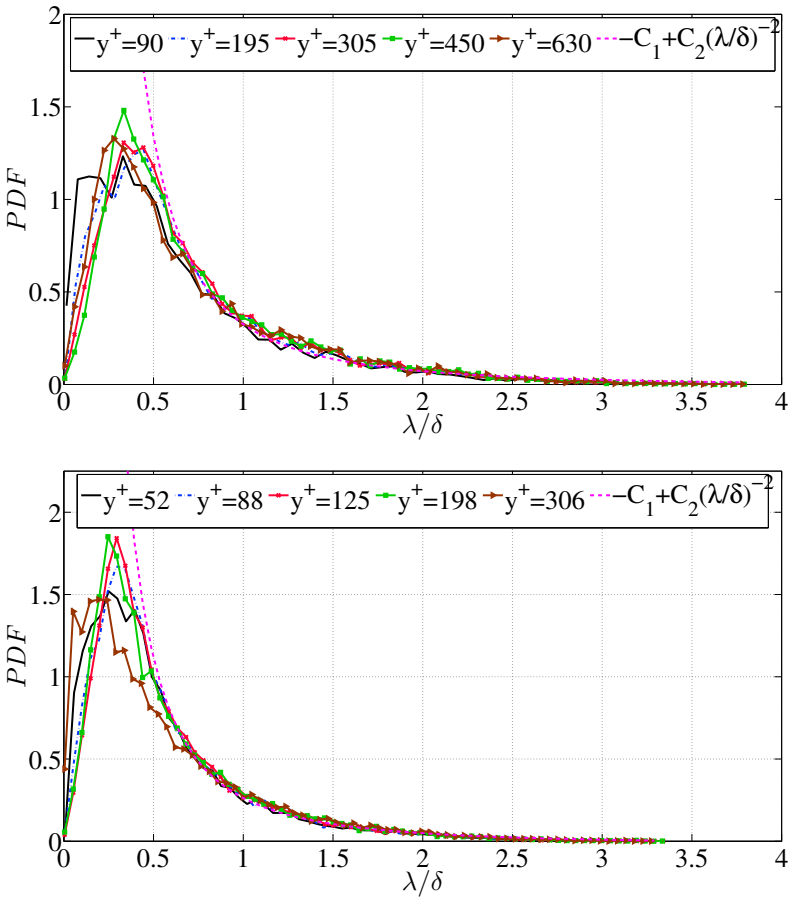

Figure A.3: PDFs of streamwise lengths λ of wall-attached structures at selected wall distances for (a) $Re_\theta = 20600$ and (b) $Re_\theta = 8100$. The fits shown here are for $y^+ = 195$ at $Re_\theta = 20600$ and $y^+ = 198$ at $Re_\theta = 8100$.

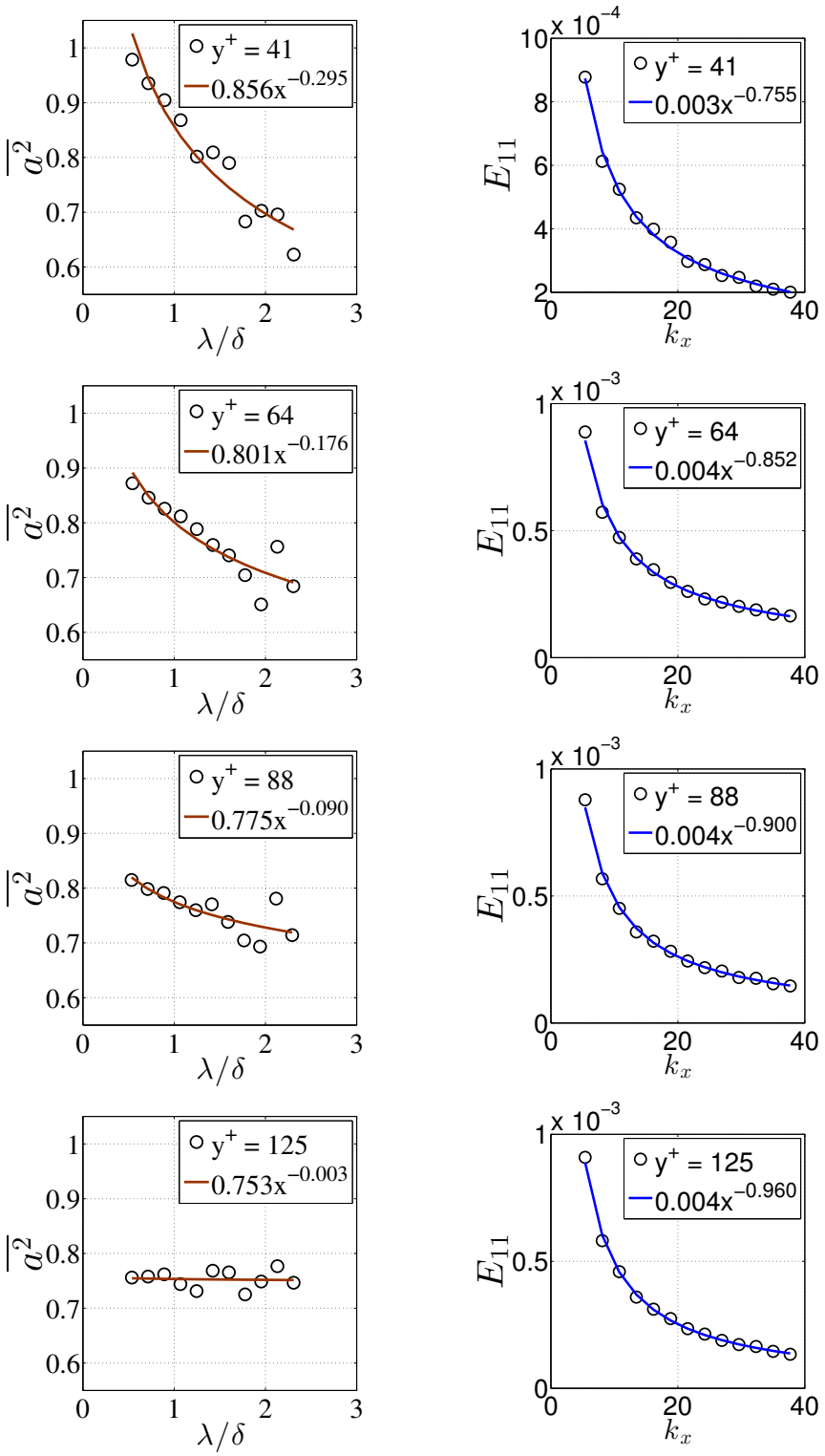

Figure A.4: Lin-lin plots of $\overline{a^2}$ versus λ/δ (left) and streamwise energy spectra plotted at wall distances $y^+ = 41$, 64, 88 and 125 (from top to bottom) at $Re_\theta = 8100$.

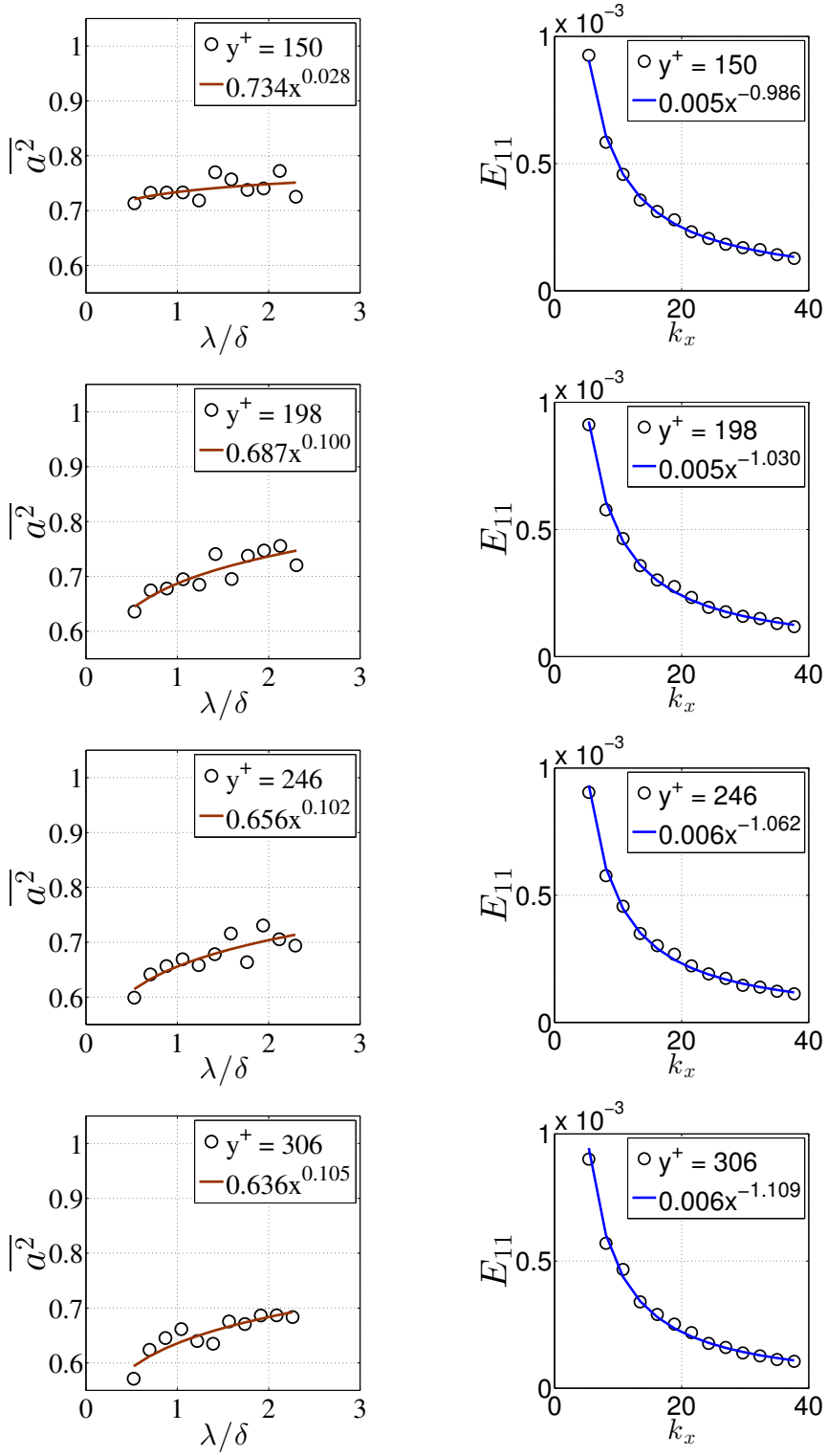

Figure A.5: Lin-lin plots of $\overline{a^2}$ versus λ/δ (left) and streamwise energy spectra plotted at wall distances $y^+ = 41$, 64, 88 and 125 (from top to bottom) at $Re_\theta = 8100$.

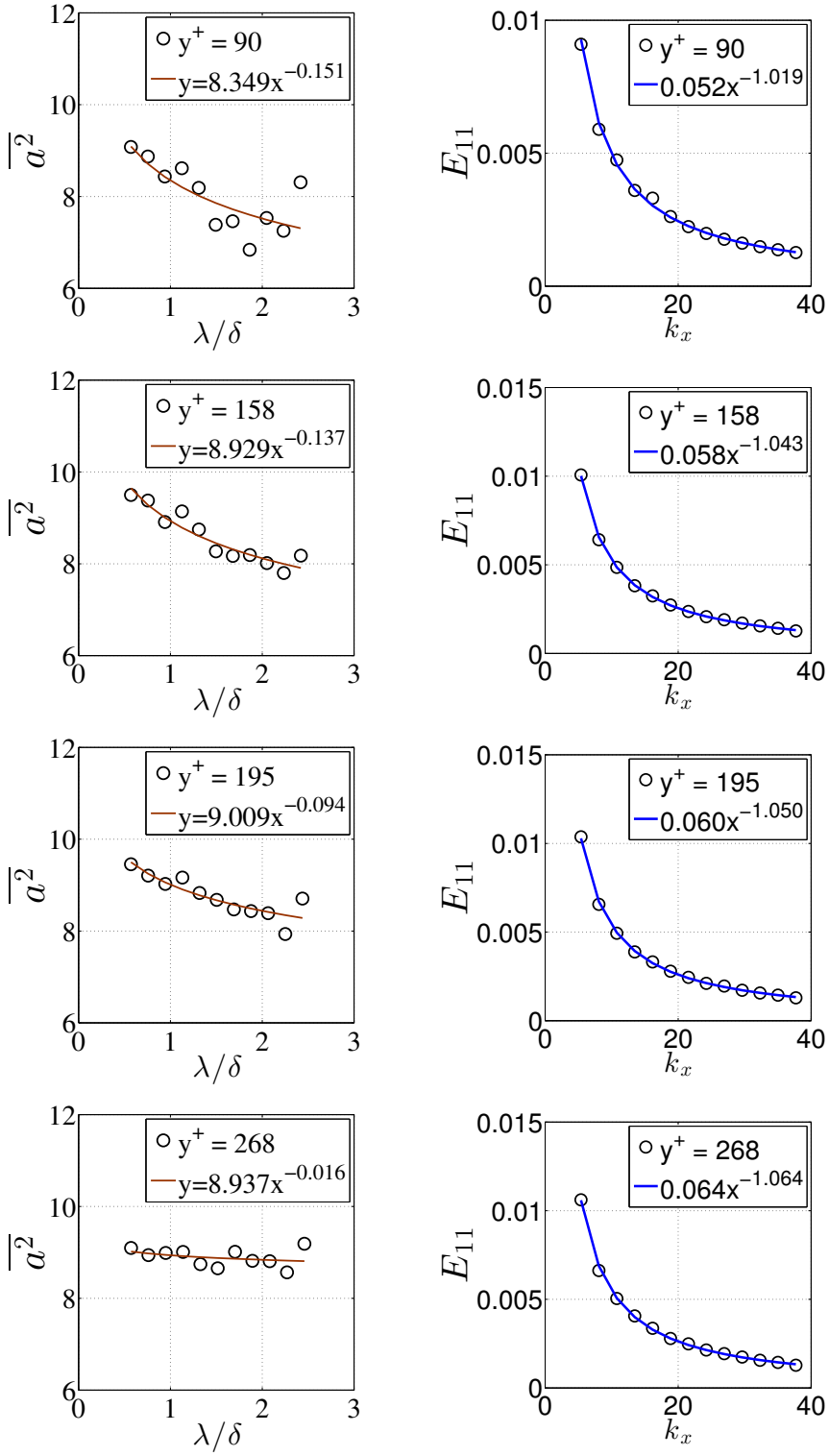

Figure A.6: Lin-lin plots of $\overline{a^2}$ versus λ/δ (left) and streamwise energy spectra plotted at wall distances $y^+ = 90$, 158, 195 and 268 (from top to bottom) at $Re_\theta = 20600$.

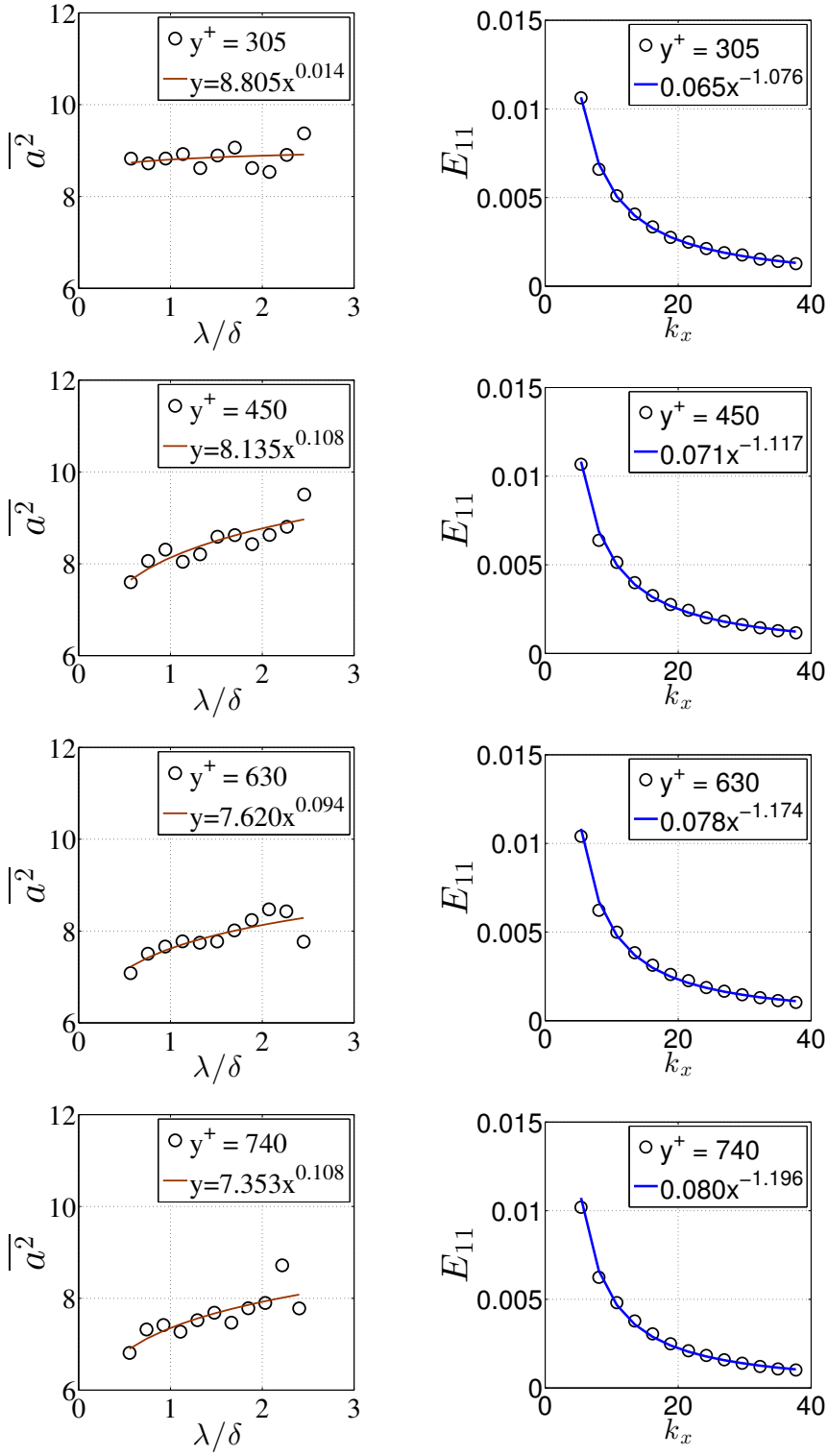

Figure A.7: Lin-lin plots of $\overline{a^2}$ versus λ/δ (left) and streamwise energy spectra plotted at wall distances $y^+ = 305$, 450, 630 and 740 (from top to bottom) at $Re_\theta = 20600$.

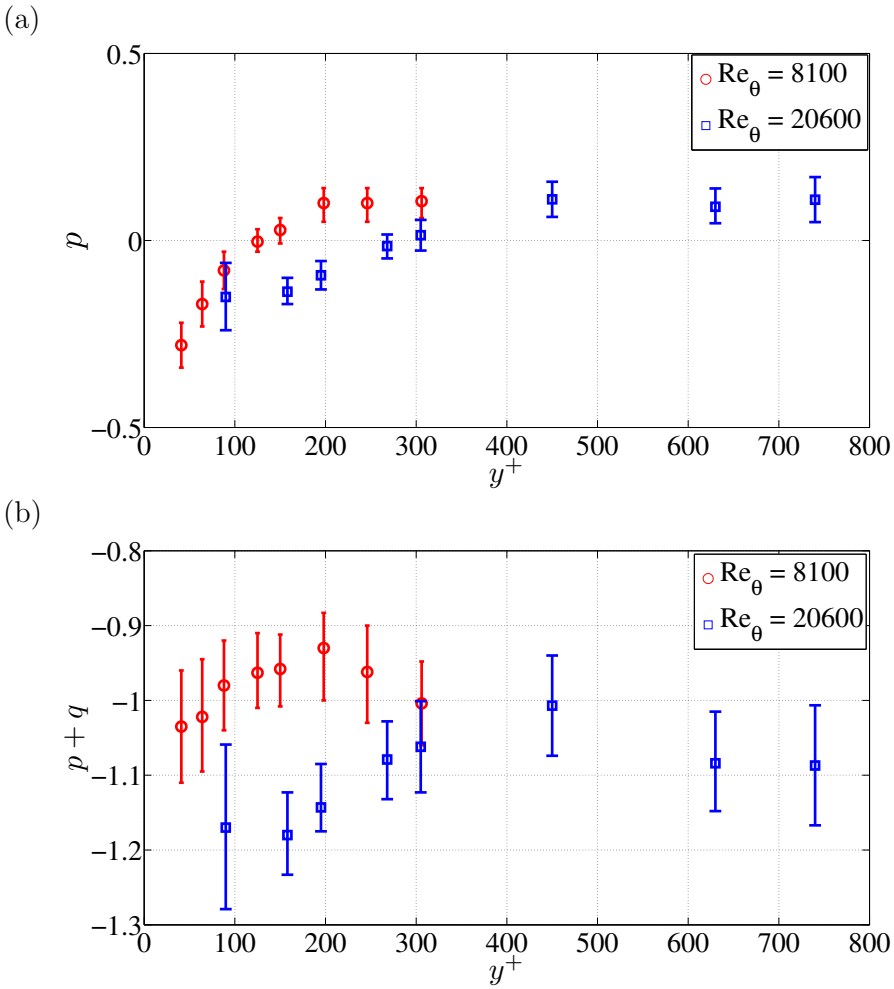

Figure A.8: (a) Exponents p obtained from the best power-law fit of $\overline{a^2} \sim (\lambda/\delta)^p$. (b) $p + q$ versus y^+. These fits are obtained over the range of scales investigated for the high-speed regions and the resulting exponents are plotted with the 95% confidence intervals for these fits. The y^+ positions and the two Reynolds numbers are those in figures A.4 to A.7.

APPENDIX B

RANS modeling of APG flow

In order to prepare the experiment described in Chapter 4, computational modelling using Reynolds-Averaged Navier-Stokes (RANS) was performed using the commercial CFD package, StarCCM+. Compared to ZPG turbulent boundary layer flows, additional complexities due to the variation of pressure gradient, curvature effects and flow separation in the case of APG turbulent boundary layer flows make the modelling of APG flows a challenge. A number of studies have been performed in the last few decades with an objective to predict the APG flow behaviour using RANS modelling (Menter (1994); Shih et al. (1995); Menter et al. (2003); de Jesus et al. (2013); Manceau (2015)). The standard $k-\epsilon$ model has generally failed to capture the physics of flows with pressure gradients. $k-\omega$ models have given better results than the standard $k-\epsilon$ models in APG flows and predicted the location of separation better. The recent work by de Jesus et al. (2013) presented comparative results from Large Eddy Simulations (LES) and RANS compared to available DNS data, in channel flows with an APG created by a two-dimensional bump. Although the RANS models that were tested did not perform on par with LES, results from the Reynolds-stress transport (RST) model showed the best performance among the RANS models evaluated. The transport equations in RST model contain the main physical mechanisms that drive turbulence. In particular, the production terms that are sufficient to explain many phenomena do not require modelling. It was thus decided to carry out the simulation of the APG flow using a RST model.

A steady-state, two-dimensional, incompressible pressure based solver is used with the default settings of the StarCCM+ package. The linear pressure-strain model developed by Gibson and Launder (1978) was used for this computation. Although not the most advanced model available, it is typical of models generally available in commercial packages. Other models may have produced better results for the stresses or mean flow or skin friction coefficient, however the idea here was to obtain a quick first guess of the flow behaviour using a commercially available software package. At the walls, the RST model used the enhanced wall treatment option which employs a two-layer formulation for the near wall region. The closure modelling techniques employed by StarCCM+ can be found in the StarCCM+ users manual.

Figure B.1 shows a sketch of the geometry over which the flow was to be simulated. The flat plate generating the FPG was set at an inclination of 1.5° while the plate generating the APG was set at -5° with respect to the wind tunnel floor. The dimensions of this geometry was set up to have the same physical dimensions as the wind tunnel flow, from the upstream to the final downstream location. A mesh was generated using the trimmer and prism layer meshers present in StarCCM+'s meshing tool. The prism layer mesher was used to capture the complex and intricate features near the wall. The inlet boundary conditions (U^+, k^+ and ϵ^+) were set from experimental data measured 7m (i.e 2.4m upstream of the ramp described in Chapter 4) from the entrance of the wind tunnel on the flat plate. The no-slip condition was used as the boundary condition for the top and bottom wall. The boundary conditions at the inlet and outlet were set as velocity inlet and pressure outlet respectively.

Figure B.2 shows the evolution of the mean streamwise velocity along the ramp. The plate inclined at 1.5° generated a slight favourable pressure gradient causing an acceleration of the flow. The $-5°$ plate generating the APG then decelerates the flow continuously but does not separate. This is also supported by looking at the plots of the skin friction coefficient, C_f along the ramp in figure B.3 which indicates that the flow is far from incipient separation. As expected for a boundary layer subjected to an APG, the thickness of the boundary layer, δ increased continuously along the APG

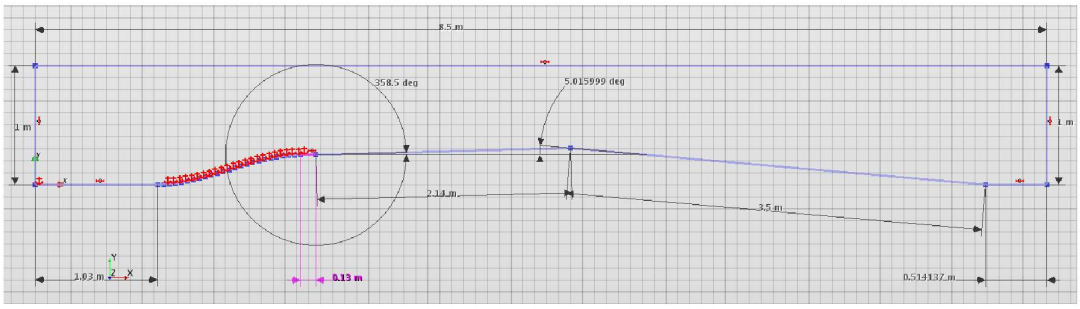

Figure B.1: Sketch of the ramp model

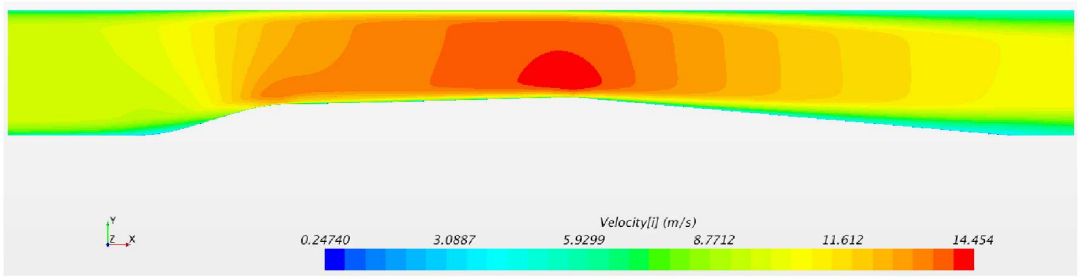

Figure B.2: Contour plot of the streamwise mean velocity along the ramp

ramp. The value of δ grew from 9cm at the beginning of the $-5°$ plate to 26cm at the end of the plate. The strength of the APG flow can be characterised by the pressure gradient parameter, $P^+ = \frac{dP}{dx}\frac{\nu}{\rho U_\tau^3}$ non-dimensionalised in viscous units. This was computed along the ramp as shown in figure B.4. Focussing on the APG flow region indicated in red on the ramp in figure B.4, a P^+ value between 0.005 to 0.01 was observed. Based on the classification (Patel (1965)) the flow developing across the 3.5m plate is a mild APG (for comparison, a strong APG has been classified as $P^+ > 0.09$). The peaks observed in figures B.3 and B.4 was due to surface kink which were not smoothened.

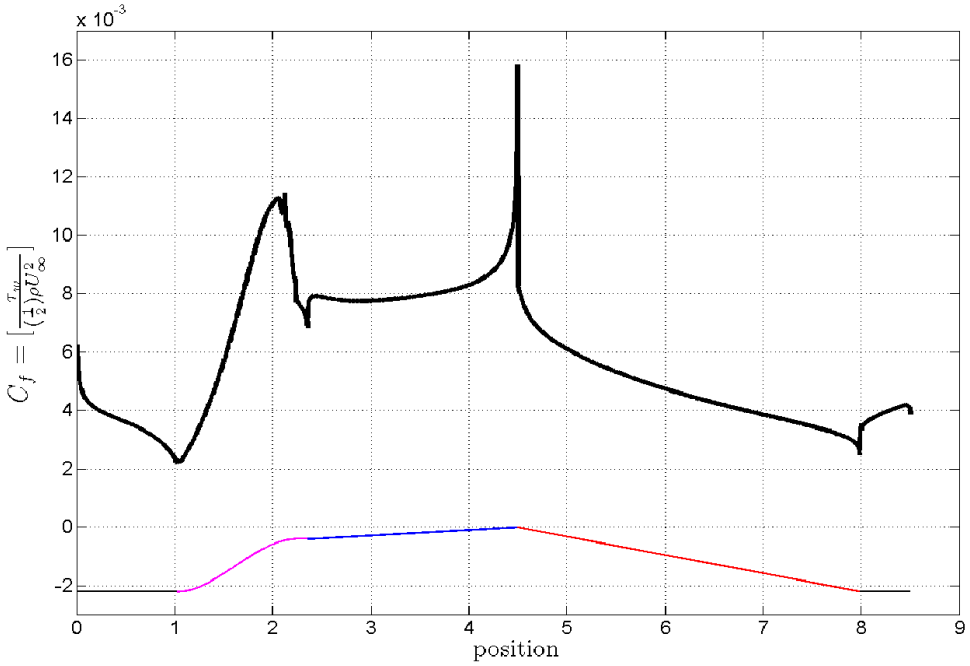

Figure B.3: Distribution of the skin friction coefficient, C_f along the ramp

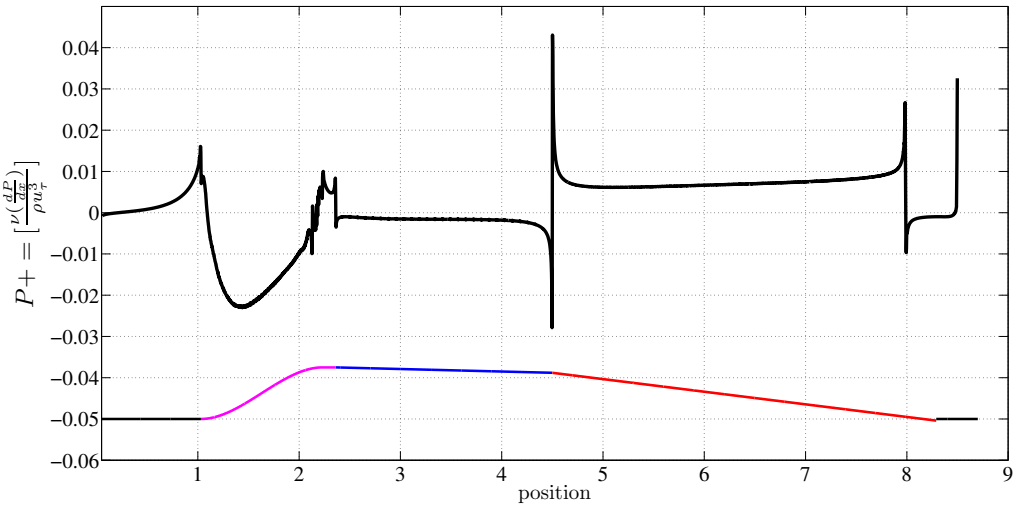

Figure B.4: Distribution of the viscous scaled pressure gradient parameter, P^+ along the ramp

APPENDIX C

Characterizing the corner vortices

Complementary to the main experiments described in chapter 4, characterisation of the corner flow that develops on the side walls of the wind tunnel was performed using a spanwise/wall-normal SPIV plane of 235 mm in height and 435 mm in width. The streamwise positions of the investigated plane were performed at two stations. The first station was located on the model at $s = 5595$ mm, i.e 2095 mm from the $-5°$ ramp articulation (APG region) and the second station was located upstream of the model, 6.8 m from the wind tunnel entrance.

Two Hamamatsu 2k by 2k cameras fitted with Nikon 50 mm lenses were used in Scheimpflug conditions and symmetric forward scattering. Figure C.1 shows a picture of the set-up used. The light sheet, about 2.5 mm in thickness, was introduced into the wind tunnel through the opposite wall and was normal to the wind tunnel floor. It was tuned tangent to the wall surface to minimize reflections. The cameras' aperture was $f_{\#} = 5.6$. As before, tests were performed for the two velocities of the experiment (5 and 9 m/s measured at the wind tunnel entrance). For each test case, 4000 velocity fields were acquired to ensure good convergence for the mean flow. The data was processed in similar way to the upstream conditions. The multigrid/multipass cross-correlation analysis (Willert and Gharib (1991); Soria (1996)) was also done with four passes starting with 48 x 64 pixels and ending with 16 x 24 pixels which was found to be the optimal size of the interrogation window. The final interrogation window corresponded to 3.5

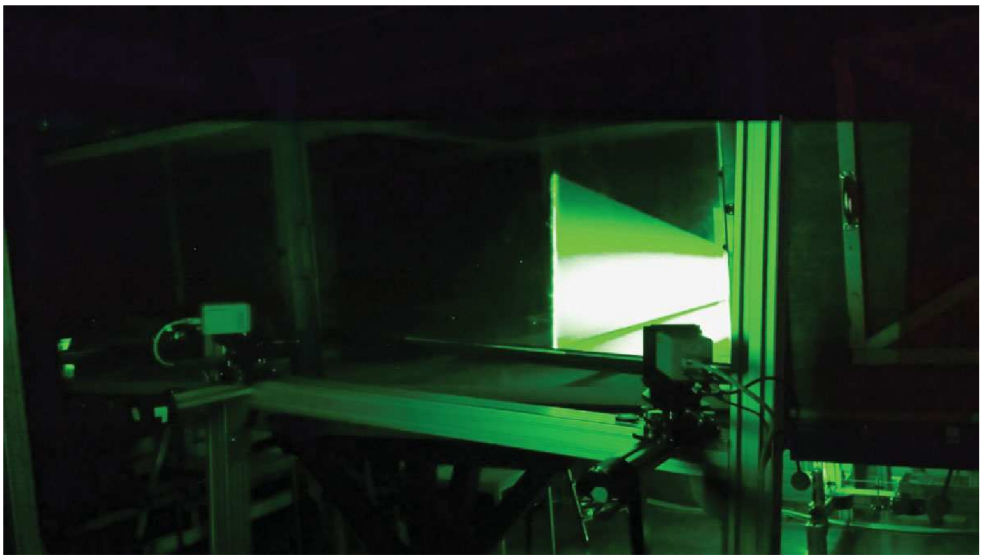

Figure C.1: Picture of the SPIV set-up used to characterise the corner flow upstream of the model and on the $-5°$ ramp.

mm^2 in physical space. The mesh spacing was 1.5 mm in both directions corresponding to an overlap of about 60%. This resulted in 156 points in the wall normal direction and 290 points in the transverse direction. A maximum displacement of 11 pixels was also chosen in the external region to ensure good results for the turbulence intensities.

Figure C.2 shows the mean streamwise velocity field U, the wall-normal (V) and spanwise (W) velocities obtained near the side-wall at $U_\infty = 9$ m/s measured at 6.8 m from wind tunnel entrance. The free-stream velocity shows a slight variation from Z = 0.55 m to Z = 0.8 m. Around Z = 0.7 m, it is slightly smaller (less than 1% difference but visible). The 'high speed extrema observed in the external regions' was attributed to the turning vanes which are located inside the plenum chamber of the wind tunnel (10 blades distributed on the 2 m width). The results for $U_\infty = 5$ m/s were similar to the 9 m/s case.

Figure C.3 shows the mean streamwise velocity field U, the wall-normal (V) and spanwise (W) velocities obtained near the side wall at $U_\infty = 9$ m/s on the $-5°$ ramp at s = 5595 mm. The corner vortex is clearly seen in this

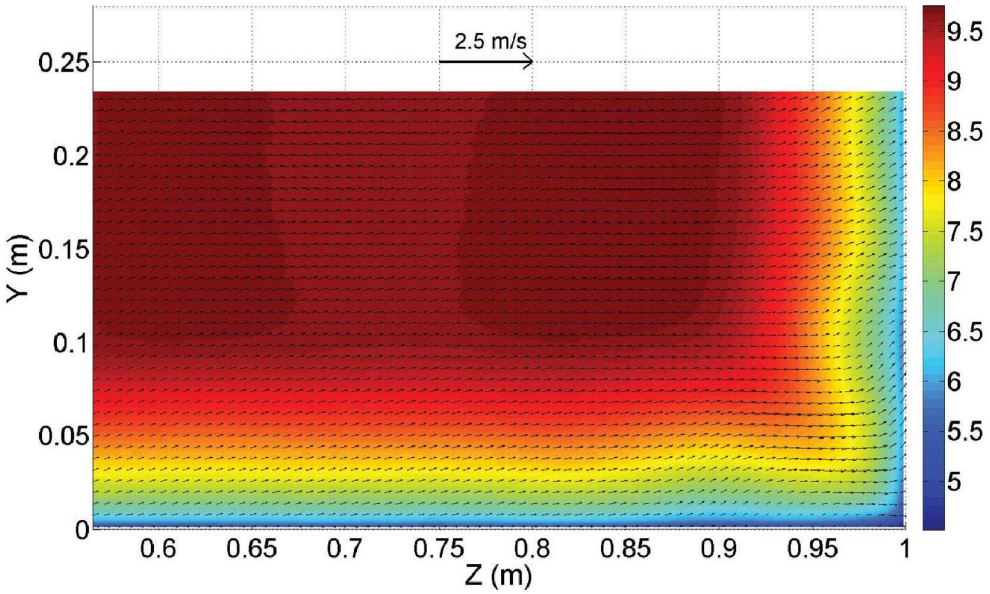

Figure C.2: Mean streamwise velociy U (colour plot), wall-normal (V) and spanwise (W) velocities (vectors plot) for U_∞ = 9 m/s measured at 6.8 m from wind-tunnel entrance.

figure, the centre of which is approximately located at z = 0.93 m and y = 0.03 m. At about 200 mm from the side wall, the influence of the vortex is very small. This is confirmed by mean streamwise velocity U (colour contour in Figure C.3). The spanwise variation of the free-stream velocity shown at 6.8 m from tunnel entrance has almost disappeared. Same conclusions were obtained for the 5 m/s case.

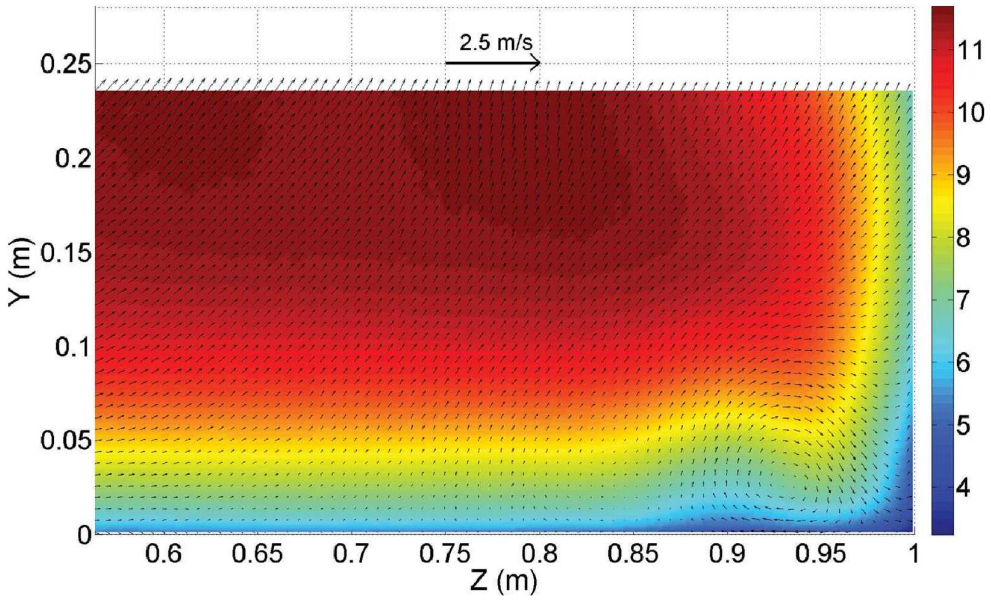

Figure C.3: Mean streamwise velociy U (colour plot), wall-normal (V) and spanwise (W) velocities (vectors plot) for $U_\infty = 9$ m/s on the $-5°$ ramp at s = 5595 mm.

APPENDIX D

Two-point correlation of wall-normal velocity component in APG ramp flow (R_{vv})

Figure D.1 shows the two-point spatial correlation for the wall-normal velocity fluctuation R_{vv} at four wall-normal locations, at station 3 for $U_\infty = 5$m/s. First, there are clear differences between R_{uu} (refer figure 4.41) and R_{vv}, in that, the correlations for R_{vv} are found to have limited spatial extent and they almost aligned with the y axis and slightly elongated in the vertical direction. This is attributed to the inhibiting influence of the wall on the wall-normal fluctuations, v (Krogstad and Skåre (1995); Krogstad and Antonia (1994)).

Comparing R_{vv} for ZPG and APG flows in figure 4.39, a striking similarity at $y^+ = 200$ is observed. The correlation for APG continues to have a slight overhang region in the streamwise direction up to 400 wall units while an overhang region is present in both the upstream and downstream directions for all wall distances in the ZPG flow. Also notable is the limited spatial extent of R_{vv} for APG compared to ZPG. This is clearly visible when the autocorrelation of R_{vv} is plotted in figure D.2. Up to $y^+ = 200$, R_{vv} shows a similar behaviour and as we move further away from the wall, the streamwise extent of the correlation increases for a ZPG flow compared to a flow with a pressure gradient.

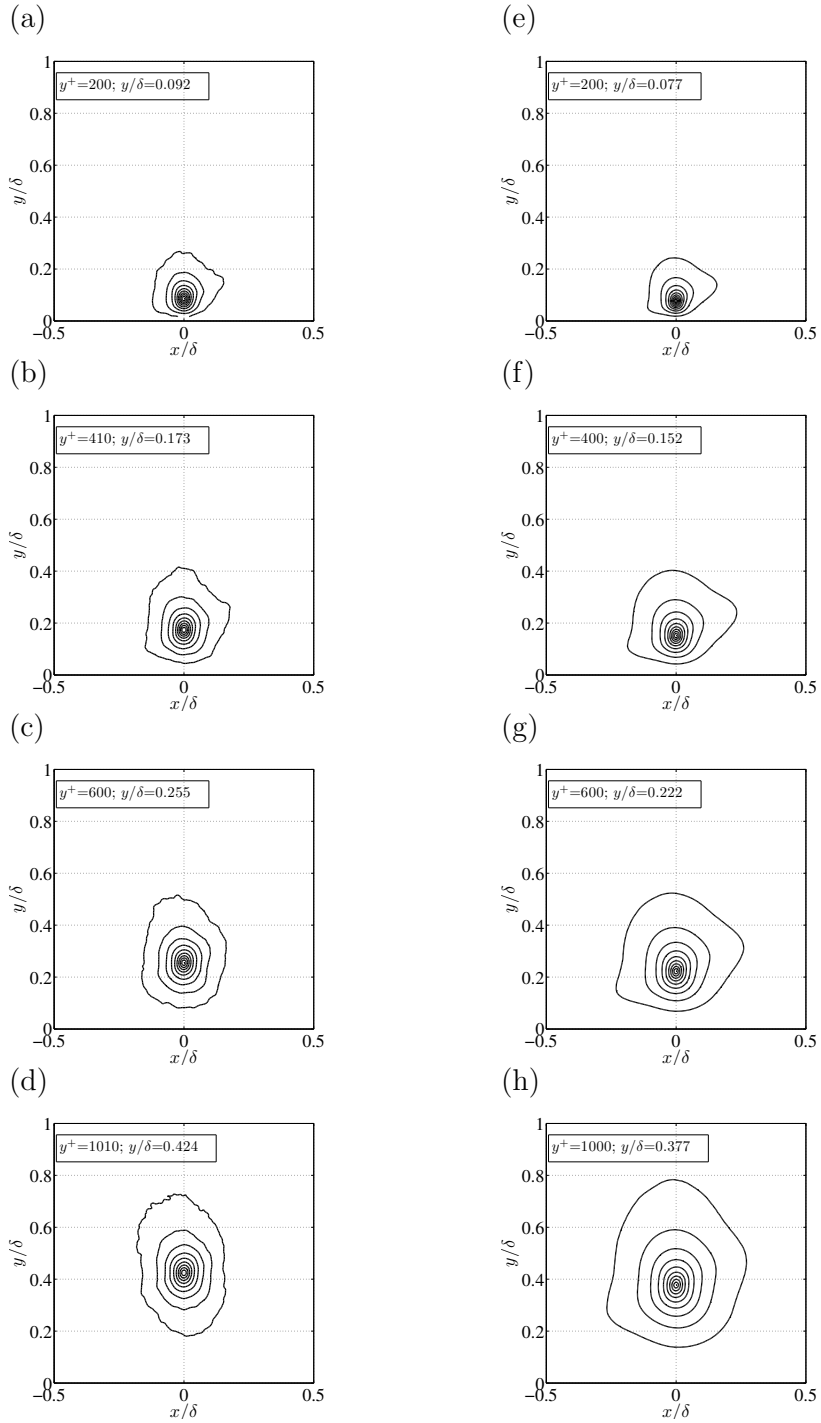

Figure D.1: Wall-normal two-point spatial correlation function (R_{vv}) with varying wall distances at station 3 along the APG ramp corresponding to $Re_\theta = 8860$ at $U_\infty = 5$m/s (left) and ZPG flow at $Re_\theta = 8100$ (right). The contours range from 0.1 to 1 with an increment of 0.1.

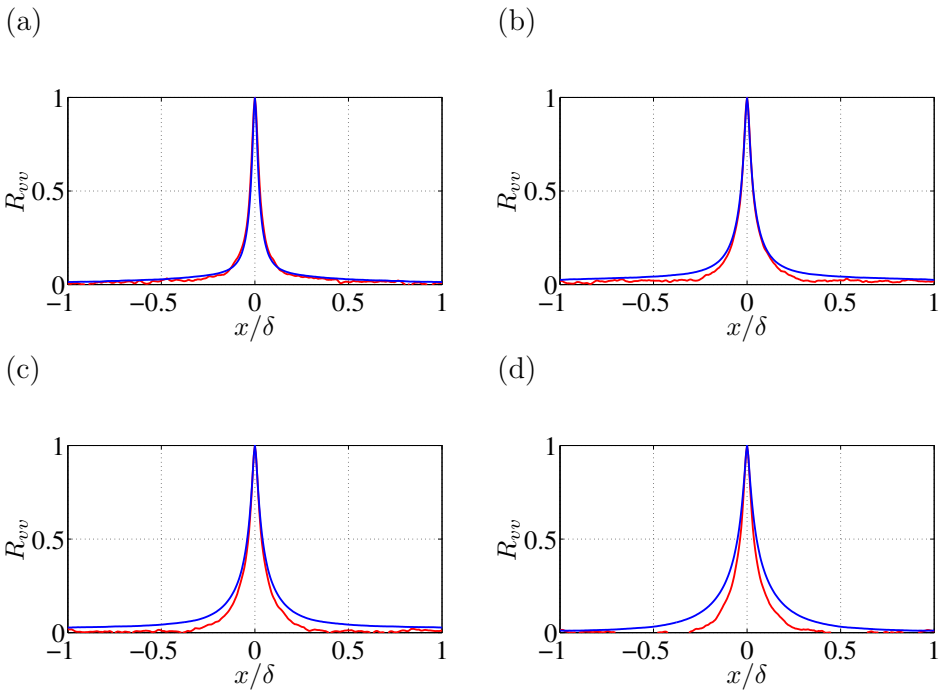

Figure D.2: Wall-normal two-point spatial correlation function (R_{vv}) at station 3 along the APG ramp corresponding to $Re_\theta = 8860$ at $U_\infty = 5$m/s (red line) and ZPG flow at $Re_\theta = 8100$ (blue line). (a) $y^+ = 200$; (b) $y^+ = 400$; (c) $y^+ = 600$ and (d) $y^+ = 1000$ ($y/\delta \sim 0.4$).

Bibliography

Adrian, R. J. (1991). Particle-imaging techniques for experimental fluid mechanics. *Annual review of fluid mechanics*, 23(1):261–304.

Adrian, R. J., Meinhart, C. D., and Tomkins, C. D. (2000). Vortex organization in the outer region of the turbulent boundary layer. *Journal of Fluid Mechanics*, 422:1–54.

Alving, A. E. and Fernholz, H. H. (1996). Turbulence measurements around a mild separation bubble and downstream of reattachment. *Journal of Fluid Mechanics*, 322:297–328.

Anderson, C., Brzek, B., Castillo, L., and Turan, O. (2004). An investigation of the outer flow scaling of developing adverse pressure gradient turbulent boundary layers: Part 1. Mean deficit and Reynolds stress behavior. In *APS Division of Fluid Dynamics Meeting Abstracts*.

Anderson, C. M. (2011). *Similarity in adverse pressure gradient turbulent flows*. PhD thesis, Victoria University.

Angele, K. P. and Muhammad-Klingmann, B. (2006). Piv measurements in a weakly separating and reattaching turbulent boundary layer. *European Journal of Mechanics-B/Fluids*, 25(2):204–222.

Balakumar, B. J. and Adrian, R. J. (2007). Large-and very-large-scale motions in channel and boundary-layer flows. *Phil. Trans. R. Soc. Lond.*, 365(1852):665–681.

Bradshaw, P. (1967). The turbulence structure of equilibrium boundary layers. *Journal of Fluid Mechanics*, 29(4):625–645.

Brown, G. L. and Thomas, A. S. (1977). Large structure in a turbulent boundary layer. *Phys. Fluids*, 20(10):S243–S252.

Carlier, J. and Stanislas, M. (2005). Experimental study of eddy structures in a turbulent boundary layer using particle image velocimetry. *J. Fluid Mech.*, 535:143.

Castillo, A. L. (2000). Application of Zagarola/Smits scaling in turbulent boundary layers with pressure gradient. *WIT Transactions on Engineering Sciences*, 29.

Castillo, L. and George, W. K. (2001). Similarity analysis for turbulent boundary layer with pressure gradient: outer flow. *AIAA journal*, 39(1):41–47.

Castillo, L. and Walker, D. J. (2002). Effect of upstream conditions on the outer flow of turbulent boundary layers. *AIAA journal*, 40(7):1292–1299.

Castillo, L., Wang, X., and George, W. K. (2004). Separation criterion for turbulent boundary layers via similarity analysis. *Journal of fluids engineering*, 126(3):297–304.

Clauser, F. H. (1954). Turbulent boundary layers in adverse pressure gradients. *J. aeronaut. Sci*, 21(2):91–108.

Coles, D. (1956). The law of the wake in the turbulent boundary layer. *Journal of Fluid Mechanics*, 1(2):191–226.

Cuvier, C., Foucaut, J.-M., Braud, C., and Stanislas, M. (2014). Characterisation of a high Reynolds number boundary layer subject to pressure gradient and separation. *Journal of Turbulence*, 15(8):473–515.

Cuvier, C., Srinath, S., Stanislas, M., Foucaut, J.-M., Laval, J.-P., Kähler, C. J., Hain, R., Scharnowski, S., Schröder, A., Geisler, R., Agocs, J., Röse, A., Willert, C., Klinner, J., Amili, O., Atkinson, C., and Soria, J. (2017). Extensive characterisation of a high Reynolds number decelerating boundary layer using advanced optical metrology. *Journal of Turbulence*, 18(10):929–972.

de Jesus, A. B., Azevedo, J. L. F., and Laval, J.-P. (2013). Large eddy simulations and RANS computations of adverse pressure gradient flows.

del Álamo, J. C. and Jiménez, J. (2003). Spectra of the very large anisotropic scales in turbulent channels. *Physics of Fluids*, 15(6):L41–L44.

del Álamo, J. C., Jiménez, J., Zandonade, P., and Moser, R. D. (2004). Scaling of the energy spectra of turbulent channels. *Journal of Fluid Mechanics*, 500:135–144.

Dengel, P. and Fernholz, H. H. (1990). An experimental investigation of an incompressible turbulent boundary layer in the vicinity of separation. *Journal of Fluid Mechanics*, 212:615–636.

Dennis, D. J. C. and Nickels, T. B. (2011a). Experimental measurement of large-scale three-dimensional structures in a turbulent boundary layer. Part 1. Vortex packets. *J. Fluid Mech.*, 673:180–217.

Dennis, D. J. C. and Nickels, T. B. (2011b). Experimental measurement of large-scale three-dimensional structures in a turbulent boundary layer. Part 2. Long structures. *J. Fluid Mech.*, 673:218–244.

Falco, R. E. (1977). Coherent motions in the outer region of turbulent boundary layers. *The Physics of Fluids*, 20(10):S124–S132.

Foucaut, J.-M., Carlier, J., and Stanislas, M. (2004a). PIV optimization for the study of turbulent flow using spectral analysis. *Meas. Sci. Technol.*, 15(6):1046.

Foucaut, J.-M., Coudert, S., Stanislas, M., and Delville, J. (2011). Full 3D correlation tensor computed from double field stereoscopic PIV in a high reynolds number turbulent boundary layer. *Exp. Fluids*, 50(4):839–846.

Foucaut, J.-M., Miliat, B., Perenne, N., Stanislas, M., et al. (2004b). Characterization of different piv algorithms using the europiv synthetic image generator and real images from a turbulent boundary layer. *Particle Image Velocimetry: Recent Improvements*, pages 163–185.

Ganapathisubramani, B., Hutchins, N., Hambleton, W. T., Longmire, E. K., and Marusic, I. (2005). Investigation of large-scale coherence in a turbulent boundary layer using two-point correlations. *J. Fluid Mech.*, 524(1):57–80.

Ganapathisubramani, B., Longmire, E. K., and Marusic, I. (2003). Characteristics of vortex packets in turbulent boundary layers. *Journal of Fluid Mechanics*, 478:35–46.

George, W. K. (2006). Recent advancements toward the understanding of turbulent boundary layers. *AIAA journal*, 44(11):2435.

George, W. K. (2007). Is there a universal log law for turbulent wall-bounded flows? *Philosophical Transactions of the Royal Society of London A: Mathematical, Physical and Engineering Sciences*, 365(1852):789–806.

George, W. K. (2013). Lectures in turbulence for the 21st century. *Chalmers University of Technology*.

George, W. K., Castillo, L., and Knecht, P. (1997). Zero-pressure-gradient turbulent boundary layer. *Applied Mechanics Reviews*, 50:689–730.

George, W. K., Stanislas, M., and Laval, J.-P. (2012). New insights into adverse pressure gradient boundary layers. In *Progress in Turbulence and Wind Energy IV*, pages 201–204. Springer.

Gibson, M. M. and Launder, B. E. (1978). Ground effects on pressure fluctuations in the atmospheric boundary layer. *Journal of Fluid Mechanics*, 86(3):491–511.

Guala, M., Hommema, S. E., and Adrian, R. J. (2006). Large-scale and very-large-scale motions in turbulent pipe flow. *J. Fluid Mech.*, 554:521–542.

Harun, Z., Monty, J. P., Mathis, R., and Marusic, I. (2013). Pressure gradient effects on the large-scale structure of turbulent boundary layers. *Journal of Fluid Mechanics*, 715:477–498.

Head, M. R. (1976). Equilibrium and near-equilibrium turbulent boundary layers. *Journal of Fluid Mechanics*, 73(1):1–8.

Head, M. R. and Bandyopadhyay, P. (1981). New aspects of turbulent boundary-layer structure. *Journal of Fluid Mechanics*, 107:297–338.

Herpin, S., Wong, C. Y., Stanislas, M., and Soria, J. (2008). Stereoscopic piv measurements of a turbulent boundary layer with a large spatial dynamic range. *Experiments in fluids*, 45(4):745.

Hinze, J. (1938). 0. 1975 turbulence.

Hultmark, M., Vallikivi, M., Bailey, S. C. C., and Smits, A. J. (2012). Turbulent pipe flow at extreme Reynolds numbers. *Phys. Rev. Lett.*, 108(9):094501.

Hutchins, N. and Marusic, I. (2007). Evidence of very long meandering features in the logarithmic region of turbulent boundary layers. *J. Fluid Mech.*, 579:1–28.

Indinger, T. and el Hak, M. H. B. M. G. (2006). Mean-velocity profile of turbulent boundary layers approaching separation. *AIAA journal*, 44(11):2465.

Jiménez, J., Alamo, J. C. D., and Flores, O. (2004). The large-scale dynamics of near-wall turbulence. *Journal of Fluid Mechanics*, 505:179–199.

Kim, K. C. and Adrian, R. J. (1999). Very large-scale motion in the outer layer. *Phys. Fluids*, 11(2):417–422.

Kline, S. J. (1978). The role of visualization in the study of the structure of the turbulent boundary layer. *Coherent Structure of Turbulent Boundary Layers*, pages 1–26.

Kline, S. J., Reynolds, W. C., Schraub, F. A., and Runstadler, P. W. (1967). The structure of turbulent boundary layers. *Journal of Fluid Mechanics*, 30(4):741–773.

Kline, S. J., Strawn, R. C., and Bardina, J. G. (1983). Correlation of the detachment of two-dimensional turbulent boundary layers. *AIAA Journal*, 21(1):68–73.

Kostas, J., Foucaut, J.-M., and Stanislas, M. (2005). Application of double spiv on the near wall turbulence structure of an adverse pressure gradient turbulent boundary layer. In *6th International Symposium on PIV, Pasadena, California*, pages 21–23.

Kovasznay, L. S. G., Kibens, V., and Blackwelder, R. F. (1970). Large-scale motion in the intermittent region of a turbulent boundary layer. *J. Fluid Mech.*, 41(02):283–325.

Krogstad, P. and Antonia, R. A. (1994). Structure of turbulent boundary layers on smooth and rough walls. *Journal of Fluid Mechanics*, 277:1–21.

Krogstad, P. and Kaspersen, J. H. (2002). Structure inclination angle in a turbulent adverse pressure gradient boundary layer. *Journal of fluids engineering*, 124(4):1025–1033.

Krogstad, P. and Skåre, P. E. (1995). Influence of a strong adverse pressure gradient on the turbulent structure in a boundary layer. *Physics of Fluids*, 7(8):2014–2024.

Laval, J.-P., Marquillie, M., and Ehrenstein, U. (2012). On the relation between kinetic energy production in adverse-pressure gradient wall turbulence and streak instability. *Journal of Turbulence*, (13):N21.

Laval, J.-P., Vassilicos, J. C., Foucaut, J.-M., and Stanislas, M. (2017). Comparison of turbulence profiles in high-Reynolds-number turbulent boundary layers and validation of a predictive model. *J. Fluid Mech.*, 814.

Lee, J., Lee, J. H., Lee, J.-H., and Sung, H. J. (2010). Coherent structures in turbulent boundary layers with adverse pressure gradients. *Journal of Turbulence*, (11):N28.

Lee, J. H. (2017). Large-scale motions in turbulent boundary layers subjected to adverse pressure gradients. *Journal of Fluid Mechanics*, 810:323–361.

Lee, J.-H. and Sung, H. J. (2008). Effects of an adverse pressure gradient on a turbulent boundary layer. *International Journal of Heat and Fluid Flow*, 29(3):568–578.

Lee, J. H. and Sung, H. J. (2011). Very-large-scale motions in a turbulent boundary layer. *J. Fluid Mech.*, 673:80–120.

Lee, J. H. and Sung, H. J. (2013). Comparison of very-large-scale motions of turbulent pipe and boundary layer simulations. *Physics of Fluids*, 25(4):045103.

Lin, J. (2006). *Etude détaillée des structures cohérentes de la zone tampon de la turbulence de paroi à l'aide de données de PIV stéréoscopique*. PhD thesis, Ecole Centrale de Lille.

Lögdberg, O., Angele, K., and Alfredsson, P. H. (2008). On the scaling of turbulent separating boundary layers. *Physics of fluids*, 20(7):075104.

Maciel, Y., Rossignol, K., and Lemay, J. (2006). Self-similarity in the outer region of adverse-pressure-gradient turbulent boundary layers. *AIAA journal*, 44(11):2450–2464.

Manceau, R. (2015). Recent progress in the development of the Elliptic Blending Reynolds-stress model. *International Journal of Heat and Fluid Flow*, 51:195–220.

Manhart, M., Peller, N., and Brun, C. (2008). Near-wall scaling for turbulent boundary layers with adverse pressure gradient. *Theoretical and Computational Fluid Dynamics*, 22(3):243–260.

Marusic, I. and Kunkel, G. J. (2003). Streamwise turbulence intensity formulation for flat-plate boundary layers. *Phys. Fluids*, 15(8):2461–2464.

Marusic, I., Uddin, A. K. M., and Perry, A. E. (1997). Similarity law for the streamwise turbulence intensity in zero-pressure-gradient turbulent boundary layers. *Phys. Fluids*, 9(12):3718–3726.

Mathis, R., Hutchins, N., and Marusic, I. (2009). Large-scale amplitude modulation of the small-scale structures in turbulent boundary layers. *Journal of Fluid Mechanics*, 628:311–337.

McKeon, B. J. and Morrison, J. F. (2007). Asymptotic scaling in turbulent pipe flow. *Phil. Trans. R. Soc. A*, 365(1852):771–787.

Mellor, G. L. and Gibson, D. M. (1966). Equilibrium turbulent boundary layers. *Journal of Fluid Mechanics*, 24(2):225–253.

Menter, F. R. (1994). Two-equation eddy-viscosity turbulence models for engineering applications. *AIAA journal*, 32(8):1598–1605.

Menter, F. R., Kuntz, M., and Langtry, R. (2003). Ten years of industrial experience with the SST turbulence model. *Turbulence, heat and mass transfer*, 4(1):625–632.

Metzger, M. and Klewicki, J. (2001). A comparative study of near-wall turbulence in high and low reynolds number boundary layers. *Physics of Fluids*, 13(3):692–701.

Millikan, C. B. (1939). A critical discussion of turbulent flow in channels and circular tubes. In *Proc. 5th Int. Congress on Applied Mechanics (Cambridge, MA, 1938)*, pages 386–392. Wiley.

Monty, J. P., Harun, Z., and Marusics, I. (2011). A parametric study of adverse pressure gradient turbulent boundary layers. *International Journal of Heat and Fluid Flow*, 32(3):575–585.

Monty, J. P., Stewart, J. A., Williams, R. C., and Chong, M. S. (2007). Large-scale features in turbulent pipe and channel flows. *Journal of Fluid Mechanics*, 589:147–156.

Morrison, J. F., McKeon, B. J., Jiang, W., and Smits, A. J. (2004). Scaling of the streamwise velocity component in turbulent pipe flow. *J. Fluid Mech.*, 508:99–131.

Nagano, Y. and Houras, T. (2002). Higher-order moments and spectra of velocity fluctuations in adverse-pressure-gradient turbulent boundary layer. *Experiments in fluids*, 33(1):22–30.

Nagano, Y. and Tagawa, M. (1988). Statistical characteristics of wall turbulence with a passive scalar. *Journal of Fluid Mechanics*, 196:157–185.

Nagano, Y., Tsuji, T., and Houra, T. (1998). Structure of turbulent boundary layer subjected to adverse pressure gradient. *International Journal of Heat and Fluid Flow*, 19(5):563–572.

Nickels, T. B., Marusic, I., Hafez, S., and Chong, M. S. (2005). Evidence of the k_1^{-1} law in a high-Reynolds-number turbulent boundary layer. *Phys. Rev. Lett.*, 95(7):074501.

Nickels, T. B., Marusic, I., Hafez, S., Hutchins, N., and Chong, M. S. (2007). Some predictions of the attached eddy model for a high Reynolds number boundary layer. *Phil. Trans. R. Soc. Lond.*, 365(1852):807–822.

Panton, R. L. (2001). Overview of the self-sustaining mechanisms of wall turbulence. *Progress in Aerospace Sciences*, 37(4):341–383.

Patel, V. C. (1965). Calibration of the Preston tube and limitations on its use in pressure gradients. *Journal of Fluid Mechanics*, 23(1):185–208.

Perry, A. E. and Abell, C. J. (1977). Asymptotic similarity of turbulence structures in smooth-and rough-walled pipes. *J. Fluid Mech.*, 79(04):785–799.

Perry, A. E., Bell, J. B., and Joubert, P. N. (1966). Velocity and temperature profiles in adverse pressure gradient turbulent boundary layers. *Journal of Fluid Mechanics*, 25(2):299–320.

Perry, A. E. and Chong, M. S. (1982). On the mechanism of wall turbulence. *J. Fluid Mech.*, 119:173–217.

Perry, A. E., Henbest, S., and Chong, M. S. (1986). A theoretical and experimental study of wall turbulence. *J. Fluid Mech.*, 165:163–199.

Perry, A. E. and Li, J. D. (1990). Experimental support for the attached-eddy hypothesis in zero-pressure-gradient turbulent boundary layers. *J. Fluid Mech.*, 218:405–438.

Perry, A. E. and Schofield, W. H. (1973). Mean velocity and shear stress distributions in turbulent boundary layers. *The Physics of Fluids*, 16(12):2068–2074.

Pope, S. B. (2001). Turbulent flows.

Raffel, M., Willert, C. E., Kompenhans, J., et al. (2007). *Particle image velocimetry: a practical guide*. Springer Science & Business Media.

Rahgozar, S. (2013). *Coherent structures in a turbulent boundary layer under a strong adverse pressure gradient*. PhD thesis, Université Laval.

Rahgozar, S. and Maciel, Y. (2011). Low-and high-speed structures in the outer region of an adverse pressure gradient turbulent boundary layer. *Experimental Thermal and Fluid Science*, 35(8):1575–1587.

Richard, R. D. and Adrian, R. J. (1992). Theory of cross-correlation analysis of piv images. *Applied scientific research*, 49(3):191–215.

Robinson, S. K. (1991). Coherent motions in the turbulent boundary layer. *Annual Review of Fluid Mechanics*, 23(1):601–639.

Robinson, S. K., Kline, S. J., and Spalart, P. R. (1989). A review of quasi-coherent structures in a numerically simulated turbulent boundary layer.

Rotta, J. (1953). On the theory of the turbulent boundary layer.

Samuel, A. E. and Joubert, P. N. (1974). A boundary layer developing in an increasingly adverse pressure gradient. *Journal of Fluid Mechanics*, 66(3):481–505.

Schofield, W. H. (1981). Equilibrium boundary layers in moderate to strong adverse pressure gradients. *Journal of Fluid Mechanics*, 113:91–122.

Shah, S.-I., Laval, J.-P., and Stanislas, M. (2011). A specific behaviour of adverse pressure gradient near wall flows. In *Progress in Wall Turbulence: Understanding and Modeling*, pages 257–265. Springer.

Shih, T.-H., Liou, W., Shabbir, A., Yang, Z., and Zhu, J. (1995). A new k-ϵ eddy viscosity model for high Reynolds number turbulent flows. *Computers & Fluids*, 24(3):227–238.

Sillero, J. A., Jiménez, J., and Moser, R. D. (2014). Two-point statistics for turbulent boundary layers and channels at Reynolds numbers up to $\delta^+ \approx 2000$. *Physics of Fluids*, 26(10):105109.

Simpson, R. L. (1983). A model for the backflow mean velocity profile. *AIAA journal*, 21(1):142–143.

Simpson, R. L. (1989). Turbulent boundary-layer separation. *Annual Review of Fluid Mechanics*, 21(1):205–232.

Skåre, P. E. and Krogstad, P.-å. (1994). A turbulent equilibrium boundary layer near separation. *Journal of Fluid Mechanics*, 272:319–348.

Skote, M. and Henningson, D. S. (2002). Direct numerical simulation of a separated turbulent boundary layer. *Journal of Fluid Mechanics*, 471:107–136.

Skote, M., Henningson, D. S., and Henkes, R. A. W. M. (1998). Direct numerical simulation of self-similar turbulent boundary layers in adverse pressure gradients. *Flow, turbulence and combustion*, 60(1):47–85.

Smith, C. R. (1984). A synthesized model of the near-wall behavior in turbulent boundary layers. Technical report, LEHIGH UNIV BETHLEHEM PA DEPT OF MECHANICAL ENGINEERING AND MECHANICS.

Smits, A. J., McKeon, B. J., and Marusic, I. (2011). High-Reynolds number wall turbulence. *Annu. Rev. Fluid Mech.*, 43:353–375.

Soloff, S. M., Adrian, R. J., and Liu, Z.-C. (1997). Distortion compensation for generalized stereoscopic particle image velocimetry. *Measurement science and technology*, 8(12):1441.

Soria, J. (1996). An investigation of the near wake of a circular cylinder using a video-based digital cross-correlation particle image velocimetry technique. *Experimental Thermal and Fluid Science*, 12(2):221–233.

Spalart, P. and Watmuff, J. H. (1993). Experimental and numerical study of a turbulent boundary layer with pressure gradients. *Journal of Fluid Mechanics*, 249:337–371.

Stanislas, M. (2016). Near wall turbulence: an experimental view. In *APS Meeting Abstracts*.

Stanislas, M., Carlier, J., Foucaut, J.-M., and Dupont, P. (1999). Double spatial correlations, a new experimental insight into wall turbulence. *Comptes Rendus de l'Académie des Sciences-Series IIB-Mechanics-Physics-Astronomy*, 327(1):55–61.

Taylor, G. I. (1938). The spectrum of turbulence. *Proc. R. Soc. Lond.*, 164(919):476–490.

Tennekes, H. and Lumley, J. L. (1972). *A first course in turbulence*. MIT press.

Theodorsen, T. (1952). Mechanism of turbulence. In *Proceedings of seconnd Midwestern Conference on Fluid Mech. anics, Ohio State University, Columbus, OH.*

Tomkins, C. D. and Adrian, R. J. (2003). Spanwise structure and scale growth in turbulent boundary layers. *Journal of Fluid Mechanics*, 490:37–74.

Townsend, A. A. (1951). The structure of the turbulent boundary layer. In *Mathematical Proceedings of the Cambridge Philosophical Society*, volume 47, pages 375–395. Cambridge University Press.

Townsend, A. A. (1956). The properties of equilibrium boundary layers. *Journal of Fluid Mechanics*, 1(6):561–573.

Townsend, A. A. (1961). Equilibrium layers and wall turbulence. *Journal of Fluid Mechanics*, 11(1):97–120.

Townsend, A. A. (1976). The structure of turbulent shear flow. *Cambridge UP, Cambridge*.

Tutkun, M., George, W. K., Delville, J., Stanislas, M., Johansson, P. B. V., Foucaut, J.-M., and Coudert, S. (2009). Two-point correlations in high Reynolds number flat plate turbulent boundary layers. *Journal of Turbulence*, (10):N21.

Vallikivi, M., Ganapathisubramani, B., and Smits, A. J. (2015). Spectral scaling in boundary layers and pipes at very high Reynolds numbers. *J. Fluid Mech.*, 771:303–326.

Vassilicos, J. C. and Hunt, J. C. R. (1991). Fractal dimensions and spectra of interfaces with application to turbulence. *Proc. R. Soc. Lond. A.*, 435(1895):505–534.

Vassilicos, J. C., Laval, J.-P., Foucaut, J.-M., and Stanislas, M. (2015). The streamwise turbulence intensity in the intermediate layer of turbulent pipe flow. *J. Fluid Mech.*, 774:324–341.

Vinuesa, R., Bobke, A., Örlü, R., and Schlatter, P. (2016). On determining characteristic length scales in pressure-gradient turbulent boundary layers. *Physics of fluids*, 28(5):055101.

Wallace, J. M., Eckelmann, H., and Brodkey, R. S. (1972). The wall region in turbulent shear flow. *Journal of Fluid Mechanics*, 54(1):39–48.

Wänström, M. (2009). *Spatial decompositions of a fully-developed turbulent round jet sampled with Particle Image Velocimetry*. Chalmers University of Technology.

Webster, D. R., DeGraaff, D. B., and Eaton, J. K. (1996). Turbulence characteristics of a boundary layer over a two-dimensional bump. *Journal of Fluid Mechanics*, 320:53–69.

Wieneke, B. (2005). Stereo-PIV using self-calibration on particle images. *Experiments in fluids*, 39(2):267–280.

Willert, C. and Gharib, M. (1991). Digital particle image velocimetry. *Experiments in fluids*, 10(4):181–193.

Willert, C. E. (2015). High-speed Particle image velocimetry for the efficient measurement of turbulence statistics. *Experiments in Fluids*, 56(1):17.

Wu, X. and Squires, K. D. (1998). Numerical investigation of the turbulent boundary layer over a bump. *Journal of Fluid Mechanics*, 362:229–271.

Wu, Y. (2014). A study of energetic large-scale structures in turbulent boundary layer. *Physics of Fluids*, 26(4):045113.

Zagarola, M. V. and Smits, A. J. (1998a). Mean-flow scaling of turbulent pipe flow. *Journal of Fluid Mechanics*, 373:33–79.

Zagarola, M. V. and Smits, A. J. (1998b). A new mean velocity scaling for turbulent boundary layers. *ASME paper no. FEDSM98-4950*.

Zhou, J., Adrian, R. J., Balachandar, S., and Kendall, T. M. (1999). Mechanisms for generating coherent packets of hairpin vortices in channel flow. *Journal of fluid mechanics*, 387:353–396.

Zhou, J., Meinhart, C. D., Balachandar, S., and Adrian, R. J. (1997). Formation of coherent hairpin packets in wall turbulence.

Prédiction et modélisation d'écoulements turbulents proches de parois

Le but de ce travail est d'étudier une couche limite soumise à un gradient de pression et de la comparer avec une couche limite de plaque plane à grands nombres de Reynolds. Dans ce cadre, l'accent est mis sur le comportement des structures cohérentes à grande échelle. En raison de leur grande longueur, ces structures ne sont pas faciles à extraire et à caractériser en utilisant des techniques de mesure standard. Pour cette raison, des dispositifs expérimentaux spécifiques utilisant la PIV dans les plans longitudinaux et parallèles à la paroi ont été conçus pour capturer les structures à grande échelle et pour mieux comprendre les mécanismes régissant la dynamique de ces écoulements. La première partie revisite les résultats obtenus sur une couche limite plaque plane en sondant l'origine d'une décroissance spectrale en k_x^{-1} dans la couche limite turbulente. Dans cette perspective, un modèle simpliste basé sur le travail de Townsend-Perry est proposé. La deuxième partie se concentre sur l'amélioration de la compréhension de la turbulence en gradient de pression adverse en effectuant une caractérisation complète d'un écoulement académique au dessus d'une géométrie. L'accent est mis sur les caractéristiques des structures (longueur, scaling, contribution énergétique et distribution selon la normale à la paroi) ainsi que sur l'influence du gradient de pression adverse sur les structures des grandes échelles. L'analyse permet de comparer le comportement d'une couche limite en présence de gradient de pression adverse avec le cas d'une plaque plane à grands nombres de Reynolds.

Mots clés: Couche limite turbulente, Structures cohérentes, Vélocimétrie par images de particules, Modélisation de la turbulence

---

Modelling and prediction of near wall turbulent flows

The aim of the present work is to study a boundary layer subjected to a pressure gradient and to compare it with a zero pressure gradient (ZPG) boundary layer at high Reynolds numbers. Within this framework, focus is laid on the behaviour of large-scale coherent structures. Due to their large streamwise extent, these structures are not easy to extract and characterize using standard measurement techniques. For this reason, specific experimental set-ups using PIV in the streamwise/wall-normal planes was designed to capture the large-scale structures and to gain more insight into the mechanisms governing the dynamics of these flows. The achievements of the present investigation can be divided into two parts. The first part revisits the results obtained on a ZPG turbulent boundary layer by probing the origin of a k_x^{-1} spectral range in a turbulent boundary layer. To this end, a simple model which can in principle be applied to various wall-bounded turbulent flows is proposed from a new perspective based on the work of Townsend-Perry. The second part focuses on improving the understanding of turbulence under an adverse pressure gradient (APG) by performing a complete flow characterisation of an academic test case on a large-scale geometry. Emphasis is laid on the characteristics of the structures (length, scaling, energetic contribution and their wall normal distribution) along with the influence of the APG on the large-scale structures. The analysis is also extended to compare the behaviour of APG with the ZPG case at high Reynolds numbers.

Keywords: Turbulent boundary layer, Coherent structures, Turbulence model, Particle Image Velocimetry